CNWRA 94-02S

NRC HIGH-LEVEL RADIOACTIVE WASTE RESEARCH AT CNWRA JULY—DECEMBER 1994

Prepared for

Nuclear Regulatory Commission
Contract NRC-02-93-005

Contributors

M.P. Ahola, R.G. Baca, F.P. Bertetti, A.H. Chowdhury, C.B. Connor, G.A. Cragnolino, D.S. Dunn, D.A. Ferrill, D.B. Henderson, B.E. Hill, S.M. Hsiung, D.D. Kana, R.V. Klar, P.C. Lichtner, R.H. Martin, S. Mohanty, A.P. Morris, W.M. Murphy, R.T. Pabalan, E.C. Pearcy, J.D. Prikryl, N. Sridhar, S.A. Stothoff, D.R. Turner, G.W. Wittmeyer

Edited by

Budhi Sagar

Center for Nuclear Waste Regulatory Analyses
San Antonio, Texas

February 1995

CNWRA 94-02S

NRC HIGH-LEVEL RADIOACTIVE WASTE RESEARCH AT CNWRA JULY–DECEMBER 1994

Prepared for

Nuclear Regulatory Commission
Contract NRC-02-93-005

Prepared by

Center for Nuclear Waste Regulatory Analyses
San Antonio, Texas

February 1995

PREVIOUS REPORTS IN SERIES

Number	Name	Date Issued
CNWRA 90-01Q	First Quarterly Research Report for 1990 January 1–March 30	May 1990
CNWRA 90-02Q	Second Quarterly Research Report for 1990 April 1–June 30	August 1990
CNWRA 90-03Q	Third Quarterly Research Report for 1990 July 1–September 30	November 1990
NUREG/CR-5817 Volume 1 CNWRA 90-01A	Report on Research Activities for Calendar Year 1990	December 1991
CNWRA 91-01Q	First Quarterly Research Report for 1991 January 1–March 30	May 1991
CNWRA 91-02Q	Second Quarterly Research Report for 1991 April 1–June 30	August 1991
CNWRA 91-03Q	Third Quarterly Research Report for 1991 July 1–September 30	November 1991
NUREG/CR-5817 Volume 2 CNWRA 91-01A	NRC High-Level Radioactive Waste Research at CNWRA Calendar Year 1991	May 1993
NUREG/CR-5817 Volume 3, No. 1 CNWRA 92-01S	NRC High-Level Radioactive Waste Research at CNWRA January–June 1992	May 1993
NUREG/CR-5817 Volume 3, No. 2 CNWRA 92-02S	NRC High-Level Radioactive Waste Research at CNWRA July–December 1992	July 1993
CNWRA 93-01S	NRC High-Level Radioactive Waste Research at CNWRA January–June 1993	August 1993
CNWRA 93-02S	NRC High-Level Radioactive Waste Research at CNWRA July–December 1993	February 1994
CNWRA 94-01S	NRC High-Level Radioactive Waste Research at CNWRA January–June 1994	September 1994

THIS PAGE INTENTIONALLY LEFT BLANK

THIS PAGE INTENTIONALLY LEFT BLANK

PREFACE

The Center for Nuclear Waste Regulatory Analyses (CNWRA), a Federally Funded Research and Development Center (FFRDC), conducts research on behalf of the Nuclear Regulatory Commission (NRC). The NRC-funded research at the CNWRA is focused on activities related to the NRC responsibilities defined under the Nuclear Waste Policy Act (NWPA), as amended. Progress for the period of July 1, 1994 to December 31, 1994 on nine of twelve research projects that are currently active is described in this report. Three research projects not reported here are the Thermohydrology, Subregional Hydrogeologic Flow and Transport Processes, and High-Level Waste Near-Field Processes and Variations. The final report for the Thermohydrology Research Project has been prepared and submitted for peer review. The Subregional Hydrogeologic Flow and Transport Processes and High-Level Waste Near-Field Processes and Variations Research Projects were initiated in December 1994 and February 1995, respectively, and have not progressed sufficiently for inclusion in this report. For a brief summary of the work performed during the reporting period, the reader is referred to the Executive Summary.

In addition to disseminating research results through publications in appropriate open literature (e.g., CNWRA topical reports, NRC documents, and journals) and at technical meetings, workshops, and symposia, the CNWRA produces these research reports twice yearly. A list of previous reports in this series is on page iii.

Each chapter in this semi-annual report summarizes the progress made in a particular research project and is authored by the researchers in that project. Since readers of this report may be interested only in a particular topic, each chapter is self-contained and can be read without reference to other chapters. Coverage in the semi-annual reports is limited to only the key aspects of progress made; greater detail is provided in topical reports that are produced during the course of the research or at its conclusion, as appropriate. The editor of this report ensures that each chapter is reviewed for its technical and programmatic content and that some uniformity as to the depth of descriptions is maintained across the various chapters.

The NRC evaluates its research needs continually as the research progresses. The research needs are based on user needs identified jointly by the NRC Offices of Nuclear Material Safety and Safeguards (NMSS) and Nuclear Regulatory Research (RES). Generally, the NMSS is the user in the sense that its staff applies the research results to strengthen its reviews of the submittals by the U.S. Department of Energy (DOE), including the License Application (LA) for the first High-Level Nuclear Waste (HLW) Repository. In their turn, the user needs are based on Key Technical Uncertainties (KTUs) identified during the process of developing strategies and methods for determining compliance with the applicable regulations—in this case, 10 CFR Part 60. Thus, the research is directed toward evaluation of the KTUs.

CONTENTS (Cont'd)

CONTENTS

CONTENTS (Cont'd)

CONTENTS (Cont'd)

CONTENTS (Cont'd)

THIS PAGE INTENTIONALLY LEFT BLANK

FIGURES

FIGURES (Cont'd)

FIGURES (Cont'd)

FIGURES (Cont'd)

FIGURES (Cont'd)

THIS PAGE INTENTIONALLY LEFT BLANK

TABLES

THIS PAGE INTENTIONALLY LEFT BLANK

ACKNOWLEDGMENTS

This report was prepared to document work performed by the Center for Nuclear Waste Regulatory Analyses (CNWRA) for the Nuclear Regulatory Commission (NRC) under Contract NRC-02-93-005. The activities reported herein were performed on behalf of the NRC Office of Nuclear Regulatory Research (RES), Division of Regulatory Applications (DRA). The report is an independent product of the CNWRA and does not necessarily reflect the views or regulatory position of the NRC.

Active support from several people during the production of this report is thankfully acknowledged. First and foremost, this report is possible only because of the wholehearted cooperation from the principal investigators and researchers within each project who kept to the tight schedule of the editor. Technical reviewers—A.C. Bagtzoglou, A.R. DeWispelare, D.A. Ferrill, A.B. Gureghian, B.E. Hill, W.M. Murphy, P.K. Nair, J.L. Russell, and D.R. Turner—provided substantive comments that materially improved the quality of the report. Programmatic reviews were performed by P.C. Mackin, W.C. Patrick, and the editor. Able secretarial support was provided by E.F. Cantu, B.L. Garcia, C. Garcia, L.F. Gutierrez, M.A. Gruhlke, L.G. Hearon, A. Ramos, R.A. Sanchez, and A. Woods. The overall support from E.F. Cantu and R.A. Sanchez in producing this document using FrameMaker is especially appreciated. R.L. Marshall's assistance in sorting out the graphic files for FrameMaker was a valuable contribution.

Southwest Research Institute (SwRI) Publications Services staff provided illustration, editorial, format adherence, printing, and binding support.

Finally, the valued interaction with NRC project officers—G.F. Birchard, L.A. Kovach, M.B. McNeil, T.J. Nicholson, J. Philip, and J.D. Randall—is gratefully acknowledged.

QUALITY OF DATA

DATA: Sources of data are referenced in each chapter. CNWRA-generated laboratory and field data contained in this report meet quality assurance (QA) requirements described in the CNWRA Quality Assurance Manual. Data from other sources, however, are freely used. For data from non-CNWRA sources, their referenced sources should be consulted for determining their level of QA.

ANALYSES AND CODES: Scientific/engineering computer codes used in analyses contained in this report are: UDEC and ABAQUS (Chapter 2), PORFLOW (Chapter 4), FITEQL and MINTEQA2 (Chapter 5), VTOUGH (Chapter 6), and ARC/INFO Geographic Information System (GIS) (Chapters 8 through 10). The computer codes UDEC, PORFLOW, FITEQL, and MINTEQA2 are presently controlled under the CNWRA Software Configuration Procedure TOP-018. The ABAQUS and ARC/INFO are commercial software, and only their object codes are available to the CNWRA.

THIS PAGE INTENTIONALLY LEFT BLANK

1 EXECUTIVE SUMMARY

1.1 INTRODUCTION

Progress from July 1 to December 31, 1994, on nine of twelve research projects underway at the Center for Nuclear Waste Regulatory Analyses (CNWRA) is discussed in this report. One of the three research projects not reported, namely Thermohydrology, has been completed with its final report (Green et al., 1995) submitted for external peer review. The Subregional Hydrogeologic Flow and Transport Processes and High-Level Waste Near-Field Processes and Variations Projects were initiated in December 1994 and February 1995, respectively, and have not progressed sufficiently for reporting in this report. The Integrated Waste Package Experiments Research Project is planned for completion during the next reporting period.

All research projects at the CNWRA are sponsored by the Nuclear Regulatory Commission (NRC) to fulfill its mandate under the Nuclear Waste Policy Act (NWPA), as amended. To understand the role of NRC-funded research, it is important to recognize that the NRC regulatory responsibilities are distinct from those of the U.S. Department of Energy (DOE), which is responsible for siting, constructing, and operating a repository for the permanent disposal of high-level waste (HLW). The DOE has undertaken the development and implementation of a broad range of techniques and methods to obtain information and to produce analyses necessary to determine site suitability, design the engineered portions of the repository, and complete a license application for review by the NRC. In fulfilling its responsibilities for assuring the radiological health and safety of the public, the NRC conducts confirmatory and exploratory (also referred to as anticipatory) research to

- Develop the licensing tools and technical bases necessary to judge the adequacy of the DOE license application
- Ensure a sufficient independent understanding of the basic physical processes taking place at the proposed geologic repository site
- Maintain an independent, but limited, confirmatory research capability to be used in evaluating DOE prelicensing and license application submittals

Figure 1-1 depicts the basic relationship between the NRC research program and licensing needs. Regulations applicable to the licensing of a HLW repository (primarily 10 CFR Part 60) are translated into regulatory requirements, each of which must be met before the NRC staff can recommend the issuance of a license. Strategies and methods for determining if DOE demonstration of compliance with the regulatory requirements is acceptable are currently being developed and documented in the NRC License Application Review Plan (LARP). Key technical uncertainties (KTUs) are defined based on the risk to compliance determination. Evaluation and reduction of those aspects of the KTUs that are the NRC responsibility are the primary objectives of the research undertaken by the NRC. Each chapter of this report outlines the specific KTUs being addressed by the research described in that chapter.

Each research project discussed herein is being conducted in accordance with approved research project plans, which were developed consistent with an associated NRC statement of work. These plans are the vehicle for establishing the objectives, technical approach, justification, and funding for each of the studies. They also describe the interrelationships among the various projects, which provide a sound basis for integrating research results across disciplines. Because the plans primarily address planning and management matters, they are not discussed further in this report.

This executive summary covers, in capsule form, the progress of each research project over the past 6 mo. The executive summary is followed by Chapters 2 through 10, representing each of the nine currently active research projects. Project objectives and a report of research activities and results to date, as appropriate, are given in each chapter. The progress toward fulfillment of identified research needs and the development of particular regulatory products are addressed in cases where such progress has been significant. In addition, commentary is provided on anticipated progress for each project in the ensuing 6-mo period.

1.2 ROCK MECHANICS

Long-term deterioration of emplacement drifts and potentially enhanced near-field fluid flow resulting from coupled processes are among the important concerns for safe high-level nuclear waste (HLW) disposal. Repetitive seismic loads and thermal loads generated by

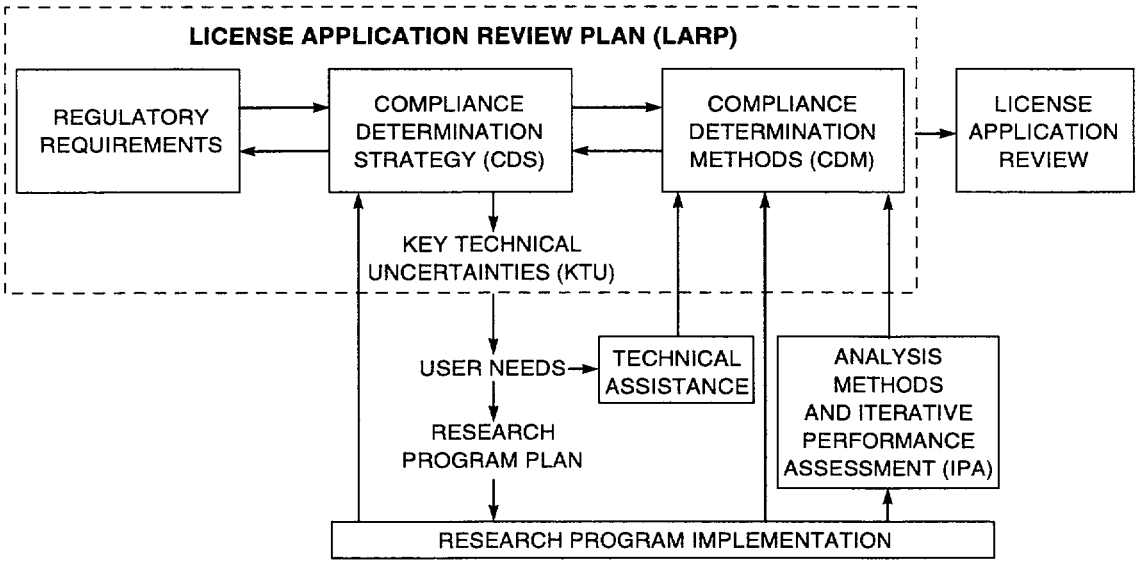

Figure 1-1. Relationship of the NRC HLW Research Program to licensing needs

decay of the emplaced waste are among the factors that could potentially cause rock degradation or change near-field flow patterns due to joint normal and shear deformations. Evidence in the literature indicates that the most likely significant effect of earthquakes on hydrology is changes in fracture permeability.

A key technical uncertainty (KTU) that could pose a high risk of noncompliance with the performance objectives of 10 CFR Part 60 has been described in the License Application Review Plan (LARP). This KTU has the ability to predict the long-term effects of repetitive seismic load and high temperatures on the degradation of emplacement drifts. These long-term effects may have implications on the performance of the Engineered Barrier Systems (EBS), retrievability of waste, and long-term waste isolation, especially if some of the openings to the HLW repository are left unfilled at closure. The objective of the Rock Mechanics Research Project is to develop techniques that could be used to predict the response of the near-field rock mass at the proposed repository at the Yucca Mountain (YM) site when it is subjected to repetitive seismic loads and high-temperature conditions. The knowledge gained through laboratory, field, and theoretical analyses in this project has supported the development and implementation of portions of the License Application Review Plan (LARP) and prelicensing activities, including reviews of Exploratory Studies Facility (ESF) design packages. The results of ongoing activities in Tasks 4 and 9 are reported herein.

Task 4 activities during this reporting period included assembly and dynamic experiments of a small-scale model of jointed rock mass. This scale model consisted of approximately 670 cast simulated-rock ingots aligned within a testing frame at 45 degrees to the horizontal. In the center of the simulated rock mass was a 15.2-cm circular tunnel. The simulated-rock ingots were fabricated with appropriate physical and surface (interface) roughness properties to simulate those of naturally jointed Apache Leap welded tuff with a scale of 1/15. However, the density of the simulant material did not strictly follow the similitude requirements due to the need for this material to remain brittle and exhibit surface wear properties approximately similar to those of the prototype material. This physical distortion is judged not to have much effect on the validity of the experimental results for use in verifying of computer codes in predicting rock-mass responses to repetitive dynamic loads and in obtaining a better understanding of rock mass dynamic behavior around underground openings. The ingredients included in the rock-simulant material are Type I Portland cement, barite, water, bentonite, DARACEM-100 (plasticizer), vinsol resin (air entrainment), and Ivory Liquid Soap. Test procedures were based on what can be called an "incremental fragility level" philosophy. Test runs were started at a very low

peak excitation displacement level, and this amplitude was incrementally increased as the runs progressed. The excitation displacement input signal was derived from an accelerogram measured at the Guerrero array for the September 1985 Mexico City earthquake using a 1/15-scale. The data acquisition system was centered with a 486 (66 MHz) personal computer and consisted of 50 data channels. The sampling rate for each channel was 2,800 data points/second for a duration of 10 seconds for each run. The measurements for the dynamic scale model experiments included ingot deformation (strain), accelerations, interface (joint) normal and shear displacements, variations of cable loads that provided the initial stress boundary condition for the scale model, and opening convergencies. Significant amounts of data were collected for the dynamic scale model experiments and are being analyzed.

The third phase of Task 9, the **DE**velopment of **CO**upled models and their **VAL**idation against **EX**periments (DECOVALEX), is nearing completion. The numerical modeling of the Big-Ben Experiment (TC3) using the finite element code ABAQUS has been completed. This work involved analyzing the coupled thermal-hydrologic-mechanical (THM) behavior of a partially saturated bentonitic buffer material surrounding a heater system within a simulated rock (concrete). Simulated fractures were also present in the system so that water could be injected into the partially saturated buffer. The purposes of the test were to evaluate the water uptake within the buffer as well as to determine the degree of moisture-induced swelling and expansion under heated conditions and water injection. The experiment involved many complex coupled processes, some of which could not be modeled with the ABAQUS code (Version 5.3) used by the Center for Nuclear Waste Regulatory Analyses (CNWRA). One such process was the heat and moisture flow within the vapor. Even so, the CNWRA results using ABAQUS appear to agree, for the most part, with the experimental measurements as well as with numerical results from other codes. One exception to this agreement is in the higher temperature regions of the buffer adjacent to the heater in which the CNWRA results did not account for the drying within the bentonite. Also, with regard to the mechanical stress state, the effective stress principle as implemented in ABAQUS needs to be further investigated to determine if it is appropriate to use in partially saturated materials over all ranges of saturation. This concern is due to the strong fluid suction versus saturation relation apparently measured for the buffer in the laboratory and provided as input for the analysis. This strong relation resulted in the ABAQUS analysis predicting very high magnitudes of mechanical stress within the buffer. Experimental measurements, as well as results from other codes, showed much lower stress magnitudes.

1.3 INTEGRATED WASTE PACKAGE EXPERIMENTS

The Nuclear Regulatory Commission (NRC) in 10 CFR 60.113 requires that waste packages for high-level nuclear waste provide substantially complete containment of radionuclides for a minimum period of 300 to 1,000 yr. As stated in the License Application Review Plan (LARP) Section 5.4, the key technical uncertainties (KTUs) associated with the assessment of Engineered Barrier System (EBS) compliance with performance objectives include the prediction of environmental effects on the performance of waste packages and the EBS, and the extrapolation of short-term laboratory and prototype test results to predict long-term performance of EBS components. The goal of the Integrated Waste Package Experiments (IWPE) program is to provide a critical evaluation of the information available for assessment of compliance with regulatory requirements pertaining to the EBS by a suitable combination of literature surveys and critical experiments. To achieve its objectives, the IWPE program is divided into six tasks: Task 1–Corrosion, Task 2–Stress Corrosion Cracking, Task 3–Materials Stability, Task 4–Microbiologically Influenced Corrosion, Task 5–Other Degradation Modes, and Task 6–Report Preparation and Peer Review. The results of ongoing activities in Tasks 1, 2, and 3 are reported here.

Two of the key parameters in long-term life prediction of container materials under localized corrosion environments are the initiation and repassivation potentials. In performance assessment calculations, a single critical potential, which is the experimentally determined repassivation potential, is proposed for predicting the occurrence of localized corrosion of waste package containers. The assumption of a single critical potential is supported by the results reported in Chapter 3. Long-term localized corrosion tests (up to 14 months) show that the use of repassivation potential for deep pits or crevices is more conservative than the use of localized corrosion initiation potentials. The initiation potentials for pitting and crevice corrosion were found to decrease with time and approach the repassivation potential after long-term exposures. In addition, specimens held at po-

tentials more negative than the repassivation potential have not yet shown any indication of localized corrosion. Further tests along this line are recommended to gain greater confidence in the use of this parameter for performance assessment.

The applicability of critical potentials for localized corrosion for predicting stress corrosion cracking (SCC) is being studied using slow strain rate and constant deflection tests on type 316L stainless steel (SS) and alloy 825. The results generated thus far are consistent with the assumption that the repassivation potential for localized corrosion constitutes a lower bound for the critical potential for SCC. However, the occurrence of SCC is apparently dependent on test technique. In contrast to slow strain rate tests in which SCC of type 316L SS was only observed at high chloride concentrations, SCC was observed using U-bend specimens in constant deflection tests conducted in either concentrated chloride solutions or in more dilute solutions with and without the addition of thiosulfate. Cracking was confined to the region above the solution/vapor interface for U-bend specimens in both a normal orientation, with the apex of the bend immersed in solution, and an inverted orientation, with the apex of the bend just above the solution/vapor interface. On creviced specimens, formed by using a double U-bend specimen, cracks were always located near the apex of the bend, independent of the specimen orientation. No differences in SCC susceptibility were observed with the two heats of type 316L SS currently being tested in the IWPE program. In the case of alloy 825, no apparent discrepancies were observed by comparing the results of the slow strain rate tests with those of constant deflection tests under environmental conditions similar to those used for testing type 316L SS. For alloy 825, SCC was observed only in a highly concentrated chloride solution (approximately 14 molal) in both slow strain rate and U-bend tests. However, since alloy 825 is far more resistant to SCC than type 316L SS, additional studies are needed to reach a conclusion. The need to further study the effect of crevice conditions and concentration processes at the vapor/solution interface on the initiation of cracks is emphasized to explore the full range of environmental and electrochemical conditions that can cause cracking of these alloys in chloride-containing solutions at temperatures close to the boiling point.

The thermal stability of alloy 825 was investigated and compared to the well-characterized type 304 SS. Sensitized alloy 825 has a high corrosion rate in standard boiling nitric acid tests but not in ferric sulfate/sulfuric acid tests. These results indicate that there is significant precipitation of high chromium-containing phases at the grain boundaries but comparatively little chromium depletion in the adjacent grains. Scanning transmission electron microscopy investigations of the sensitized material confirmed the results obtained in these standard corrosion tests. Chromium-rich $M_{23}C_6$ precipitates were found along the grain boundaries of the sensitized material, but unlike type 304 SS, no significant chromium-depleted regions near the grain boundaries could be detected. The precipitates were determined to contain as much as 71 wt percent chromium, in general agreement with literature values for $M_{23}C_6$ precipitates in Fe-Cr-Ni based materials. Cyclic potentiodynamic polarization tests conducted in 100 ppm chloride indicate that the repassivation potential, which has previously been shown to be sensitive to chromium depletion, decreased as the degree of sensitization increased. Further characterization of the precipitates and near-grain boundary regions of thermally treated alloy 825 is necessary for a comprehensive evaluation of the mechanism and effects of sensitization.

1.4 GEOCHEMICAL ANALOG OF CONTAMINANT TRANSPORT IN UNSATURATED ROCK

The technical objective of the Geochemical Natural Analog Research Project is to develop an understanding of the utility and limitations of natural analog studies in support of a license application for a high-level waste (HLW) repository and to provide fundamental data on the long-term behavior of a HLW repository. Natural systems that have evolved for periods of time comparable to that required for HLW disposal (i.e., 10^3 to 10^4 yr and greater) (U.S. Environmental Protection Agency, 1989) provide unique opportunities to obtain observational knowledge of the behavior of HLW repository subsystems. Such information is important in support of long-term predictive models of repository performance (Nuclear Regulatory Commission, 1987).

Qualitative and quantitative comparisons are made between field data for contaminant transport at Delta 3 in the Akrotiri, Santorini natural analog site, and a corresponding numerical flow and transport model. The archaeologic site has many features that are analogous to the proposed repository at Yucca Mountain (YM): silicic volcanic rocks, chemically oxidizing environment; partially saturated hydrology, semiarid climate,

well constrained source of contaminant material, and a time scale of burial (approximately 3,620 yr) comparable to the regulatory period. Field samples have been collected and analyzed to detect and document the contaminant plume that emanated from bronze Minoan artifacts buried in silicic volcanic materials. Other meteorologic, hydrologic, geologic, and geochemical data have been collected to characterize the site to support numerical unsaturated flow and transport modeling. The flow and transport model was developed using data collected at the site, laboratory data on site materials, and literature data. Although site characterization data from Akrotiri are subject to considerable practical limitations, both the data and the limitations reflect fundamental facets of the development of performance assessments for the YM repository. Similarly, modeling presented in this report was conducted without knowledge of the character and extent of the contaminant plume at Akrotiri.

Cu is a primary component of the bronze artifacts and occurs in large concentrations in visible corrosion products located only immediately adjacent to artifacts. Cu occurs at slightly elevated concentrations associated with Mn in packed earth material. Zn shows a systematic pattern of decreasing concentration with depth in Hole IV. Both Zn and Cu show elevated concentrations in the deepest sample from Hole IV, suggesting a heterogeneous path to this point. Pb associated with the carbonate fraction reveals considerable heterogeneity. Relatively high values for Pb commonly occur in the top 15 cm, but never occur below 20 cm. Pb is also significantly enriched in Hole VII, which is adjacent to a major fracture.

The vertical, one-dimensional (1D) model system extends from the pre-excavation ground surface to the groundwater table at a depth of 24 m. At the top is a flux boundary with yearly sinusoidal infiltration reflecting the Mediterranean climate at the site. Four vertically disposed zones in the model correspond to the overlying Minoan tuff, the zone of Minoan deposits enclosing artifacts, a zone of packed earth floor material immediately beneath the zone of artifacts, and a zone of underlying Cape Riva tuff. No fractures or other heterogeneities are incorporated explicitly in the model. Porosity, hydraulic conductivity, moisture retention curve parameters, and distribution coefficients were assigned to the unsaturated matrix materials in the simulations. These data were determined in part from property values measured in the field and in the laboratory on samples from the Akrotiri site. Cu transport from the artifacts was modeled. The Cu source was fixed in the model by specifying a constant solubility-limited concentration in the zone containing artifacts.

Steady-state conditions are achieved rapidly in the model and correspond for most of the profile to initial conditions. The low permeability, highly sorptive packed earth layer has a dominant effect on modeled flow and transport. Sinusoidal infiltration has a small effect on steady-state hydraulic oscillations, which is detectable only above the packed earth. Aqueous Cu concentrations computed in the model show that concentrations beneath the source zone equal the constant value of the source over the time scale of millennia. Constant distribution coefficients in the model therefore produce no gradient in sorbed Cu over the same distances, except where the distribution coefficient changes for different materials.

Although some results from the field are qualitatively consistent with model results, important discrepancies result from poor representation of heterogeneity in the model and poorly constrained model parameters. System components that appear to have had major impacts on distribution of contaminants (i.e., Mn minerals in packed earth and the fracture adjacent to Hole VII) were neglected in the model. Identification of such components in relevant systems is confirmed as a major contribution that analog studies can make in support of repository modeling. Major assumptions, were required in the base model concerning both water chemistry and its control on the source term, retardation, and infiltration. Future data collection and interpretation will be used to refine these assumptions and tests will be performed to examine the sensitivity of model results to such parameters. This process may resolve discrepancies between field data and model results such as the apparent remaining transient nature of the Zn and Cu plumes in the field and the over prediction of sorption on packed earth in the model.

1.5 SORPTION MODELING FOR HIGH-LEVEL WASTE PERFORMANCE ASSESSMENT

To develop an understanding of radionuclide sorption processes and the important physical and chemical parameters that affect sorption behavior in the Yucca Mountain (YM) environment, experiments are being conducted to investigate the sorption behavior of U and other actinides on geologic media. During the second

half of 1994, experiments were completed to determine the effects of pH, solid-mass to solution-volume (M/V) ratio, and U concentration on the sorption of uranium(6+) on quartz, which is a widespread and major rock-forming mineral at YM. The experiments were conducted using initial solution concentrations of 5, 50, or 500 ppb U, solution pH from 2 to 9, and M/V equal to 2, 20, or 50 g/L. The results show that uranium sorption on quartz is strongly dependent on pH. At an M/V ratio equal to 20 g/L and initial U concentration equal to 50 ppb, uranium sorption increases sharply at pH values above 4 ("adsorption edge"), reaches a maximum at pH approximately 6.8, and decreases sharply at pH greater than about 7.5 ("desorption edge"). Sorption data at M/V equal to 50 g/L indicate that, at a higher M/V ratio, the "sorption envelope" broadens, that is, the adsorption edge shifts to lower pH whereas the desorption edge shifts to higher pH, and the sorption maximum increases to higher values. Similar effects on the sorption envelope are observed when the initial uranium concentration is lowered (e.g., from 50 to 5 ppb). The experiments were conducted in a manner such that the amount of uranium sorbed on the quartz and the experimental containers could be independently quantified.

Modeling of uranium(6+) sorption on quartz was performed using a surface complexation modeling approach. A simplified diffuse-layer model (DLM) was used to reproduce the experimentally observed sorption behavior of uranium and to predict its sorption behavior under differing experimental conditions. Results of the modeling indicate that the sorption data could be fitted well by a simple DLM, but that at least two complexation reactions were required to appropriately model all data. Even in its simplified form, the DLM is capable of accounting for the effects of changing physicochemical conditions such as M/V or pH.

Results of the laboratory experiments and modeling activities provide the Center for Nuclear Waste Regulatory Analyses (CNWRA) with an understanding of the important parameters that control the sorption behavior of an actinide element. Because of the strong dependence on pH and sorbent-surface-area/solution-volume ratio, modeling of sorption processes will likely require that changes in groundwater chemistry and in rock/fluid ratio be properly accounted for in performance assessment calculations if retardation by sorption processes is included. However, the success of the surface-complexation model (SCM) in describing and predicting uranium sorption on quartz and other minerals suggests that SCMs offer a scientifically defensible approach that may be useful for performance assessment calculations.

The similarity in the pH-dependence of uranium sorption on quartz observed in experiments reported in this report and those reported previously for minerals such as α-alumina, montmorillonite, and clinoptilolite is important. It may help identify simplified approaches to modeling sorption and thus help in the development of Compliance Determination Methods (CDMs) relevant to the Key Technical Uncertainties (KTUs) identified in License Application Review Plan (LARP) Section 5.1 and in developing conceptual models related to the Performance Assessment Research Project and the Iterative Performance Assessment Phase 3. The information derived from the laboratory experiments may also help interpret data on uranium distribution and migration at the Peña Blanca field site of the Geochemical Analog of Contaminant Transport in Unsaturated Rock Research Project.

1.6 PERFORMANCE ASSESSMENT RESEARCH

In this research project, three general and interrelated technical objectives are being pursued. The first of these objectives is to provide modeling technology that will directly benefit the Nuclear Regulatory Commission (NRC) Iterative Performance Assessment (IPA) activity and be used in Compliance Determination Methods (CDMs). The second, and equally important, objective is to address Performance Assessment (PA) topics (e.g., conceptual models, mathematical models, model parameters, future system states, and model validation), which are designated as Key Technical Uncertainties (KTUs) in the License Application Review Plan (LARP). The third objective is to provide the technical basis for formulating guidance to the U.S. Department of Energy (DOE) in the specific areas of PA modeling approaches, particularly in the areas of disruptive scenarios and model validation. Studies conducted under the PA Research Project are divided among the following three major tasks: Task 1–Conceptual Model Development, Task 2–Computational Model Development, and Task 3–Model Evaluation. In this reporting period, research emphasis was on topics associated with Tasks 1 and 3. As part of Task 1, a detailed study was conducted of multiphase flow and reactive transport models for the near-field zone. Under Task 3, a computer modeling study was performed to examine the relation between

model predictive reliability and sampling schemes used to obtain data in heterogeneous media. Work was also performed on: (i) benchmark testing of DOE and NRC/Center for Nuclear Waste Regulatory Analyses (CNWRA) thermohydrologic codes, (ii) evaluating the Parallel Virtual Machine (PVM) computing technology, (iii) completing documentation on the new infiltration model for use in IPA Phase 3, and (iv) completing documentation of the analysis of hydraulic characteristics of tuff samples from the Peña Blanca site.

A study of near-field conceptual and mathematical models was given high priority to better position the NRC to review and critique the current DOE thermal loading strategy, which is referred to as the "extended-dry concept." The study involved a detailed technical review of the theoretical basis currently used in thermohydrologic models and codes. The review was conducted in a manner that identified the limitations and ranges of applicability of thermohydrologic models to unsaturated tuff. In addition, this review examined methods of estimating porosity and permeability changes that may occur in the thermohydrologic environment as a result of changes in pore fluid chemistry. This activity resulted in a CNWRA technical report (Lichtner, 1994) that is expected to be published as a NUREG/CR. In this semi-annual report, one aspect of that near-field study is highlighted, namely, an analysis of hydrochemical effects on porosity and permeability. A conservative hydrochemical model was formulated to estimate, as a function of temperature, the extent of mineral dissolution in the tuff. This model was then applied to bound adverse porosity and permeability changes in the tuff. For the case in which the K-feldspar completely dissolves, the model predicts that the matrix permeability could increase by one to two orders of magnitude, depending on pore-fluid temperature.

A hydrologic modeling study of predictive reliability and sampling design was also given high priority because of its potential benefits to addressing the related issues of conceptual model uncertainty and model validation. In the study, soil hydraulic data from the Las Cruces trench experiment were used to define properties of the hydrostratigraphy, assuming various sampling configurations. Predictions of water content obtained from a flow model were compared to *in situ* water content measurements for a long-term infiltration experiment. A single geometric representation of the layering was used in which the hydraulic properties were assigned to each zone using both purely random and stratified-random sampling configurations. For each sampling configuration, 10 infiltration simulations were performed to obtain estimates of the mean prediction error. Two measures are used to compare the predicted and observed moments of the infiltrated moisture plume. Both measures indicate a general improvement in the accuracy of the model predictions as the number of samples is increased, although the marginal increase in accuracy decreases rapidly as more samples are taken.

Based on the mean squared error measure, the purely random sampling configuration produced the most accurate predictions. This activity, which is highlighted in this semi-annual report, resulted in the paper by Wittmeyer et al. (1994), which has been submitted for journal publication.

1.7 VOLCANIC SYSTEMS OF THE BASIN AND RANGE

Investigations in the Volcanic Systems of the Basin and Range Research Project are directed primarily toward development of probability models of potential volcanic events in the Yucca Mountain Region (YMR), based as far as possible on geologic insight into tectonic processes and geological controls on small volume basaltic volcanism. The project is directed toward addressing several key technical uncertainties (KTUs) including: (i) prediction of future system states (disruptive scenarios), and (ii) development and use of conceptual tectonic models of igneous activity. During the last 6 months, work has included a critical review of the Volcanism Geographic Information System (GIS) database (delivered as a Major Milestone in January 1995), peer review of volcanism research projects (results delivered as an Intermediate Milestone in January 1995), and development of two new nonparametric models of the probability of volcanic disruption of the proposed repository (submitted as a contribution to the *Journal of Geophysical Research*).

Research at the Center for Nuclear Waste Regulatory Analyses (CNWRA) into the probability of volcanic disruption of the proposed repository has led to recognition of several scales of spatial and temporal patterns in cinder cone volcanism that must be incorporated into any viable probability model. The patterns include: (i) shifts in the location of volcanism, either by migration or more abrupt changes in the locus of volcanism; (ii) development of clusters; and (iii) development of regional alignments and local vent alignments. Research in this

project has documented and quantified these aspects of vent distribution in a comprehensive fashion for the first time. Recognition of these aspects of basaltic volcano distribution provides the Nuclear Regulatory Commission (NRC) with a direct means of assessing the utility and applicability of any volcanism probability model. A model that cannot capture these aspects of basaltic volcano distribution may not be adequate in the formulation of disruptive scenarios unless conservative results can be assured.

Planned research is now essentially complete on the development and implementation of nonparametric, nonhomogeneous probability models, which includes spatio-temporal nearest-neighbor, kernel, and nearest-neighbor kernel models. This research represents the first application of nonparametric and nonhomogeneous probability models to volcanism in the YMR, and the first time these models have been developed for use in volcanic fields in general. Together, these models indicate that the probability of volcanic disruption of the repository is between 1×10^{-4} and 5×10^{-4} in 10,000 yr. These estimates encompass broad uncertainty in the ages and number of volcanic events in the YMR. However, currently these models take only extrusive volcanic events into account. Development of these models has provided insight into the spatial scale of probability variation in the YMR that was not otherwise available. Although probability estimates of volcanic disruption of the proposed repository based on nonparametric, nonhomogeneous models are broadly similar to those based on simpler techniques, such as homogeneous models, they also indicate that probability varies by more than two orders of magnitude within 20 km of the center of the repository block, due to the position of the repository at the edge of the Crater Flat Cluster. Thus, these models show that much of the uncertainty in prediction of the probability of disruptive scenarios lies in the constraints that can be placed on this spatial scale of variation.

Several broad and preliminary statements can be made regarding the utility of structural models in igneous disruptive scenario modeling, based on literature review and development of the Volcanism GIS. Correlation between regional rates of extension and volcanism is clear; yet, given available data, this correlation does not, in itself, provide insight in the likelihood of continuing volcanism in the YMR on the spatial and temporal scales of most concern. Rates of deformation are poorly known compared with geochronological data available for most volcanic fields. Episodes of volcanism may occur synchronously with episodes of extension, but this occurrence has not been demonstrated conclusively in any western Great Basin volcanic field. On a regional scale, volcanism in the western Great Basin is sometimes localized in pull-apart zones and similar structures. Broad, regional fault patterns in the YMR may be consistent with this relationship. However, the scale of this correlation, for example, in the Coso volcanic field, is coarse compared with the proximity of the repository to Crater Flat. Fault and dike interaction is a viable means of focusing magmatism, particularly in areas like the YMR, where regional fault patterns and principal stress orientations are sympathetic. Therefore, the fault pattern should be considered in formulating probabilistic models on a detailed local scale, such as in Iterative Performance Assessment (IPA). Yet little data are available related to the extent to which this interaction controls the ascent and localization of basaltic magmas. One conclusion from these observations is that current probability models based on structural control are tentative at best. It is questionable whether these models have a predictive value on the temporal and spatial scales of interest for volcanic disruptive scenarios. Nonetheless, incorporation of structural and tectonic data does remain as one of the most likely avenues for introducing a mechanistic basis for probability models development and evaluation.

1.8 TECTONIC PROCESSES IN THE CENTRAL BASIN AND RANGE REGION

The primary objectives of the Tectonics Research Project are to compile and integrate tectonic data for the Central Basin and Range and Yucca Mountain (YM) regions, and to develop and assess models of tectonic processes. The purpose of the project is to evaluate the adequacy of existing data, methods, and models for determining compliance with regulatory requirements involving tectonics. Of particular concern is the adequacy of existing and anticipated data for quantitatively evaluating compliance with waste-isolation performance objectives and design criteria for a geologic repository operations area. Data and references compiled by Tectonics Research Project staff have been used to develop Compliance Determination Strategies (CDSs) on Structural Deformation [License Application Review Plan (LARP) Section 3.2.1.5], Evidence of Igneous Activity (LARP Section 3.2.1.9), and Structural Deformation and Groundwater (LARP Section 3.2.2.8). Digital terrain and boundary data, and visualization methods developed for

tectonics research are also being used in the Regional Hydrogeologic Processes and Volcanism Research Projects.

Significant technical accomplishments by the Tectonics Research Project to date include: (i) development of digital terrain models of the YM and central Basin and Range regions; (ii) production of integrated maps of Quaternary faults, Quaternary basaltic volcanic fields, historic earthquake seismicity and *in situ* stress data using the Tectonics Geographic Information System (GIS); (iii) compilation of an initial database of geodetically measured regional strain and geologically determined slip rates for individual fault systems; (iv) evaluation of historic earthquakes with emphasis on the relationships between earthquakes and mapped faults, temporal and spatial clustering of earthquakes, and the 1992 Landers earthquake sequence in the southern Mojave desert; (v) sampling at Bare Mountain, Nevada, for fission track analyses; (vi) reconnaissance field work in the Black Mountains, California; (vii) participation in the NRC/CalTech YM/Death Valley Global Positioning System (GPS) Survey; and (viii) conducting collaborative research, with the Regional Hydrogeologic Processes Research Project, on the effects of *in situ* stress on transmissivity and regional groundwater flow in the Death Valley region.

Significant accomplishments since the last semi-annual report include: (i) development of an interactive computer program to analyze slip tendency and dilation tendency for mapped faults and fractures; (ii) performance of slip tendency analyses of existing fault sets (including YM faults) to evaluate relative risk of slip in contemporary stress state; (iii) dilation tendency for faults and fractures to investigate potential for magmatic intrusion of faults/fractures and to evaluate potential effects of *in situ* stress on transmissivity and regional groundwater flow; (iv) field research on fault and dike interaction along the Mesa Butte Fault in the San Francisco Volcanic Field, Arizona; (v) sampling at Bare Mountain, Nevada, for paleomagnetic, microstructural, and additional fission track analyses; (vi) participation in the 1994 campaign of the NRC/CalTech YM/Death Valley GPS Survey; and (vii) continued collaborative research, with the Regional Hydrogeologic Processes Research Project, on the effects of *in situ* stress on transmissivity and regional groundwater flow.

1.9 FIELD VOLCANISM

The Field Volcanism Research Project is designed to better characterize the effects of basaltic igneous activity on repository performance. This characterization will be possible through investigations of the (i) mechanics of basaltic eruptions, (ii) extent and characteristics of shallow hydrothermal systems and diffuse degassing associated with basaltic volcanoes, and (iii) nature of basaltic intrusive geometries in the shallow subsurface. Successful completion of the Field Volcanism Research Project, which began in April 1993, will require study of Plio-Quaternary basaltic volcanoes in the western Great Basin (WGB) and comparison with historically active basaltic volcanoes located elsewhere. Key technical uncertainties (KTUs) related to the Field Volcanism Research Project are (i) low resolution of exploration techniques to detect and evaluate igneous features, (ii) inability to sample igneous features, (iii) development and use of conceptual tectonic models as related to igneous activity, and (iv) prediction of future system states (disruptive scenarios).

Activities designed to address issues related to the probability and consequence of igneous activity in the Yucca Mountain Region (YMR) that have been initiated or completed during the last 6 months include:

- An independent expert-panel review of the Center for Nuclear Waste Regulatory Analyses (CNWRA) volcanism research projects
- Extensive field work at Tolbachik volcano, Kamchatka
- Initial comparisons of YMR and Tolbachik eruption products
- Continued modeling of temperature and soil-gas data from Parícutin volcano, Mexico
- Continued modeling of fault-dike interactions

The details of the expert-panel review are reported in an Intermediate Milestone, Expert-Panel Review of CNWRA Volcanism Research Programs (Hill, 1995), which was completed during this reporting period. In addition, some results of fault-dike modeling studies (Draper et al., 1994) and degassing studies at Cerro Negro, Nicaragua (Conway et al., 1994), were presented as posters at the Annual Meeting of the Geological Society of America. CNWRA contributions to melt-inclusion research at Cerro Negro, Nicaragua, were presented at the Fall Meeting of the America Geophysical Union (Roggensack et al., 1994). A paper on the significance of amphibole crystals in Quaternary YMR basalts, which

was reported in Connor and Hill (1994), also was accepted for presentation at the 1995 International High Level Radioactive Waste Management Conference.

The main conclusions of the peer review were: (i) CNWRA volcanism research projects are scientifically defendable, relevant to addressing important geological problems in the YMR, and are being undertaken by well-qualified personnel; (ii) increase the scope of studies of basaltic volcanism in the YMR, including Miocene basaltic activity associated with waning stages of caldera magmatism; (iii) conduct independent physical volcanological studies of Quaternary YMR basaltic volcanoes and supplement these studies with data from other appropriate Basin and Range and modern analog volcanoes; (iv) continue to evaluate the relationships between YMR and modern analog volcanoes as data from planned studies becomes available; (v) prioritize project goals to focus on the most urgent tasks; and (vi) allocate more time for in-depth studies that result in peer-reviewed journal publications by decreasing the number of administrative reports.

The 1975 eruption of Tolbachik volcano, Russia, had a relatively large range in explosivity throughout the eruption. Earlier phases of the eruption sustained columns of ash to over 10 km high and dispersed that material hundreds of kilometers from the vent. In contrast, later stages of the eruption had intermittent ash columns only several kilometers in height and of limited dispersal. However, the cinder-fall deposits from all phases of this eruption have characteristics that are classically defined as low energy (i.e., strombolian). This contradiction indicates that commonly applied definitions of basaltic eruption energetics may be inaccurate, when determined from cinder-fall deposits. A limited sampling of the Lathrop Wells cinder-fall deposits shows that these deposits have granulometric and crystallographic characteristics that are similar to the 1975 Tolbachik deposits. Quaternary volcanoes in Crater Flat also have crystallographic characteristics of the Tolbachik deposits, but their cinder-fall deposits have not yet been sampled. The 1975 eruption of Tolbachik volcano thus appears very analogous to Quaternary eruptions in the YMR. Ongoing research will continue to investigate the possibility that YMR volcanoes may have had periods of highly explosive and dispersive eruption activity.

Degassing and thermal studies conducted at the Tolbachik volcano support initial work at the Parícutin volcano. These studies show that degassing occurs over a broad area at cooling cinder cones, for at least decades after cessation of the eruption. In addition, the detailed thermal studies at Tolbachik and Parícutin are being used to evaluate the Sandia National Laboratories (SNL) Total-System Performance Assessment (TSPA) models that simulate cooling of igneous features. Initial results of this analysis are that the numerical models used in the SNL TSPA analysis predict a rate of cooling that is much faster than observed at the Tolbachik volcano.

1.10 REGIONAL HYDROGEOLOGIC PROCESSES OF THE DEATH VALLEY REGION

Yucca Mountain (YM) has been proposed as a potential high-level nuclear waste (HLW) repository, in part because of the favorable geochemical and hydrologic environment provided by its 700-m-thick unsaturated zone. Siting the repository in the unsaturated zone may limit the potential for waste canister corrosion and dissolution of the waste form. Low water fluxes which are postulated to exist in the unsaturated zone, limit the likelihood that dissolved radionuclides will be rapidly transported to the accessible environment. One mechanism that may saturate the repository horizon and compromise favorable conditions at the YM site would be an increase in the elevation of the regional water table. Elevation of the water table may occur due to increased recharge to the regional hydrogeologic system from areas up to 100 km to the north and northeast of YM. Even if elevation of the regional water table does not saturate the repository block, the reduced thickness of the unsaturated zone may significantly diminish travel times in the vadose zone. The research project on Regional Hydrogeologic Processes of the Death Valley Region was initiated to improve understanding of the saturated groundwater flow regime at YM and to assess the influence of the regional flow system on the height of the water table beneath YM. The objectives of this research project are to analyze existing conceptual models and develop new conceptual models of the regional hydrogeologic flow regime in the Death Valley region that contains YM, and to construct numerical models of regional flow that may be used to assess the potential for the water table beneath YM to rise in response to wetter climatic conditions.

Predictions made with numerical models will be used by the U.S. Department of Energy (DOE) in its license application to demonstrate that the YM site meets the overall performance standards outlined in 10 CFR

60.112 and the geologic subsystem performance standard defined in 10 CFR 60.113(a)(2). In addition, the DOE may choose to use numerical models to demonstrate the absence or influence of potentially adverse conditions including: (i) the effects of future pumping on the regional flow system [10 CFR 60.122(c)(2)]; the potential for deleterious changes to the hydrologic system [10 CFR 60.122(c)(5)]; (ii) the potential for changes to the hydrologic conditions resulting from climate change [10 CFR 60.122(c)(6)]; (iii) the potential for water table rise [10 CFR 60.122(c)(22)]; and (iv) the presence and influence of favorable conditions, including the clear absence of fully saturated pathways connecting the repository to the water table [10 CFR 60.122(b)(8)(ii)]. Understanding of the regional hydrogeologic system developed from this project will be used to guide the review of the DOE license application and to assess the adequacy of the models used by the DOE to demonstrate compliance with the regulatory requirements and environmental standards.

During the past 6 mo, efforts focused on developing alternative conceptual models of flow in the Death Valley region and the constructing and calibrating of numerical models of flow and transport, respectively. An accurate steady-state water level map has been prepared, and a straightforward procedure for estimating the areal distribution of average annual precipitation and average annual recharge has been developed. Work on obtaining prior estimates of the mean values and variances of model parameters, such as hydraulic conductivity and areal recharge, that are required for statistically based model calibration procedures has also progressed. The work presented in this semi-annual report details the development of a new geostatistical procedure for estimating average annual precipitation and recharge in the Death Valley region.

Obtaining reasonably accurate initial estimates of the distribution and magnitude of natural recharge is essential for constructing and calibrating numerical models of the regional flow system. The areal distribution of recharge will be used to define the number and extent of the areal source terms in the numerical flow model. In addition, estimates of the magnitude of recharge are needed to provide the prior information used to stabilize the inverse problem, as well as to provide initial parameter estimates for the optimization algorithm used in the automatic calibration routine. The spatial variation of average annual precipitation within the Death Valley region is caused by mesoscale and synoptic effects. The predominant mesoscale effect is orographic precipitation resulting from the extreme relief of Basin and Range topography. Two separate synoptic scale effects cause the average annual precipitation in the western and northwestern portions of the Death Valley region to be less than that in the southern and southeastern portions, at any specified elevation. The predominant synoptic scale effect is the rain shadow produced in the lee of the Sierra Nevada during the winter months when low-pressure centers generated in the western Pacific Ocean and Gulf of Alaska are driven onshore by the Canadian High. A secondary synoptic effect is caused by the Southwest Monsoon, which produces summertime convective storms in the southern and southeastern portions of the Death Valley region.

Coefficients of a logarithmic equation describing the mesoscale orographic effect are estimated by regressing measured average annual precipitation against the elevation of the precipitation stations. Residuals obtained by subtracting the average annual precipitation predicted by this logarithmic equation from the measured average annual precipitation exhibit a spatial structure indicative of both the Sierra Nevada rain shadow and the Southwest Monsoon effects. Previous researchers have taken advantage of the strong correlation of precipitation with elevation and the relative abundance of elevation data to cokrige the spatial distribution of average annual rainfall. However, geostatistical analysis conducted in this report suggests that neither the precipitation field nor the elevation field is stationary, and thus calls into question the validity of using cokriging. A new co-estimation procedure for average annual precipitation is described in this semi-annual report. The new procedure makes use of the relative abundance of elevation from digital elevation maps (DEMs), and combines residual kriging in the presence of an external drift function with polynomial trend surface fitting. An especially appealing aspect of the procedure is its use of drift and trend models that explicitly represent the orographic precipitation effect and the combined leeward rain shadow and Southwest Monsoon effects. Moreover, because the trend in the residuals caused by the synoptic effects is removed by fitting a polynomial trend surface, the resulting random field is stationary, and straightforward kriging can be used. Initial estimates of recharge within the Death Valley region are obtained by using the empirical Maxey-Eakin formula, which specifies that recharge is a fixed percentage of average annual precipitation.

1.11 REFERENCES

Connor, C.B., and B.E. Hill. 1994. Field Volcanism Research. *NRC High-Level Radioactive Waste Research at CNWRA, January–June 1994*. B. Sagar, ed. CNWRA 94-01S. San Antonio, TX: Center for Nuclear Waste Regulatory Analyses: 161–187.

Conway, F.M., A.W. Macfarlane, C.B. Connor, P.C. Lafemina, and M. Reimer, 1994. Degassing at a young cinder cone: Volcan Cerro Negro. *Geological Society of America Abstracts with Program—1994 Annual Meeting*. Boulder, CO: Geological Society of America: 26(7): 435.

Draper, G., Z. Chen, M. Conway, C.B. Connor, and C. Condit. 1994. Structural controls of magma pathways in the upper crust: Insights from the San Francisco Volcanic Field, Arizona. *Geological Society of America Abstracts with Program—1994 Annual Meeting*. Boulder, CO: Geological Society of America: 26(7): 115.

Green, R.T., F.T. Dodge, S.J. Svedeman, R.D. Manteufel, G. Rice, K.A. Meyer, and R.G. Baca. 1995. *Thermally Driven Moisture Redistribution in Partially Saturated Porous Media*. CNWRA 95-005. San Antonio, TX: Center for Nuclear Waste Regulatory Analyses.

Hill, B.E. 1995. *Expert-Panel Review of CNWRA Volcanism Research Programs*. CNWRA 95-002. San Antonio, TX: Center for Nuclear Waste Regulatory Analyses.

Lichtner, P. 1994. *Multi-Phase Reactive Transport Theory*. CNWRA 94-018. San Antonio, TX: Center for Nuclear Waste Regulatory Analyses.

Nuclear Regulatory Commission. 1987. *Disposal of High-Level Radioactive Wastes in Geologic Repositories*. Title 10, Energy, Part 60. Washington, DC: U.S. Government Printing Office.

Roggensack, K., S.N. Williams, R.L. Hervig, S.B. McKnight, C.B. Connor, and M. Navarro. 1994. Evidence of polybaric fractionation: Melt inclusions in 1992 eruption of Cerro Negro volcano, Nicaragua. *EOS, Transactions of the American Geophysical Union* 75(44): 747.

U.S. Environmental Protection Agency. 1989. *Environmental Radiation Protection Standards for Management and Disposal of Spent Nuclear Fuel, High-Level and Transuranic Radioactive Wastes*. Title 40, Protection of the Environment, Part 191. Washington, DC: U.S. Government Printing Office.

Wittmeyer, G., B. Sagar, and M. Cruse. 1994. Network Design and Accurate Prediction of Infiltration at the Las Cruces Trench Site. Submitted to the *Journal of Groundwater*.

2 ROCK MECHANICS

by Simon M. Hsiung, Mikko P. Ahola, Daniel D. Kana, Asadul H. Chowdhury, and Sitakanta Mohanty

Investigators: Mikko P. Ahola, Asadul H. Chowdhury, Amitava Ghosh, Simon M. Hsiung, Sitakanta Mohanty, Goodluck I. Ofoegbu (CNWRA); Daniel D. Kana (SwRI)

NRC Project Officer: Jacob Philip

2.1 TECHNICAL OBJECTIVES

The Rock Mechanics Research Project is developing techniques that can be used to predict the response of the near-field jointed rock mass at the proposed high-level waste (HLW) repository at Yucca Mountain (YM), Nevada, when it is subjected to repetitive seismic conditions (including earthquakes and nuclear explosions at the Nevada Test Site) and thermal loads. The near-field response includes the response at both the emplacement borehole and the emplacement drift scales. The laboratory, field, and theoretical analyses conducted as a part of this project are designed to develop a better understanding of near-field rock mass behavior under repetitive seismic and thermally induced loads. The testing is designed to obtain data on the seismic and thermal effects that can be used to validate predictive models and to verify computer codes for review of repository design [10 CFR 60.131(b)(1), 60.133(e)(1), 60.133(e)(2), 60.133(i), and 60.134], waste retrievability [10 CFR 60.111, 60.133(c), 60.133(e)(1), 60.133(i), and 60.134], and postclosure performance assessment (10 CFR 60.112, 60.113). Many factors that control the effect of seismic and thermally induced loads on the near-field jointed rock mass behavior of the proposed repository are poorly understood. The problem is further complicated when the potential coupled effects of thermal loads are considered.

Information developed within the Rock Mechanics Research Project is being used under the technical assistance program at the Center for Nuclear Waste Regulatory Analyses (CNWRA) to support development of specific portions of the License Application Review Plan (LARP) (Nuclear Regulatory Commission, 1994) and prelicensing activities, including reviews of Exploratory Studies Facility (ESF) design packages. Detailed laboratory and field studies on the stability of underground openings were used to provide a basis for development and implementation of portions of the LARP relating to Section 4.3, Assessment of Compliance with Design Criteria for Shafts and Ramps, and will be used for Section 4.4, Assessment of Compliance with Design Criteria for the Underground Facility; Section 4.5.2, Retrievability of Waste; and Section 5.3, Assessment of Compliance with the Design Criteria for the Postclosure Features of the Underground Facility. Knowledge regarding the prediction of long-term stability of vertical emplacement boreholes and emplacement drifts (for in-drift emplacement) and potential near-field fluid flow resulting from coupled effects (including repetitive seismic effects) will support implementation of Section 5.4, Assessment of Engineered Barrier System (EBS) Compliance with the Performance Objectives. Furthermore, knowledge of effects of repetitive seismic and thermal loads (including long-term deterioration of underground openings in the emplacement area) on near-field hydraulic conductivity changes and on the potential to create preferential pathways that may compromise the waste isolation capability of the proposed repository will provide input for Iterative Performance Assessment.

The Compliance Determination Strategies (CDSs) for the LARP sections noted previously have been identified as having several Key Technical Uncertainties (KTUs) posing a high risk of noncompliance with performance objectives. The KTU topics that will be addressed by the Seismic Rock Mechanics Research Project include the ability to predict the effects of thermal and repetitive seismic loads on the stability of emplacement drifts and emplacement boreholes and on the retrievability of waste. For instance, it has already been determined through field experimental studies that repetitive lower magnitude seismic events can have a much greater influence on the degree of damage to underground openings than a single large-magnitude event (Hsiung et al., 1992).

The Rock Mechanics Research Project is an integrated effort combining expertise in rock mechanics, mining engineering, engineering geology, and hydrology. The integration includes the exchange of

research results among Rock Mechanics, Thermohydrology, Integrated Waste Package Experiments (IWPE), and Performance Assessment (PA) Research Projects in the prediction of opening stability and changes in near-field hydraulic conductivity. The rock mechanics and thermohydrology projects have complemented each other in developing techniques to predict near-field hydraulic conductivity and the flow and transport environment, taking into account matrix flow and mechanical effect-dependent fracture flow under thermal conditions. The rock mechanics research will assist in evaluating the mechanical loads that may cause stress corrosion cracking or structural failure of waste packages, which is a component of EBS evaluations. The combined research and modeling efforts of the Rock Mechanics and Thermohydrology Research Projects have been useful in evaluating the presence of aqueous environments near the waste package for IWPE research and the near-field flow and transport environment for PA research.

Specific Nuclear Regulatory Commission (NRC) research needs that may be met through this project include attainment of a better understanding of dynamic response of a jointed rock mass; evaluation of existing rock-joint constitutive models; evaluation of scale effects such that laboratory results can be applied to the field; assessment of potential effects of repetitive seismic loads on change of hydrological properties; identification, through a better understanding, of coupled thermo-mechanical-hydrological (TMH) processes that are relevant to the unsaturated environment; and verification of selected computer code(s) that will be used in the LARP for seismic analyses and prediction of coupled TMH effects on near-field rock mass response. Research within the Rock Mechanics Research Project includes: characterization of dynamic behavior of single-joint rock in the laboratory using tuff natural joint specimens from Apache Leap near Superior, Arizona; performance of scale-model experiments of a jointed rock mass subjected to scaled earthquake loads; assessment of analytical models and computer codes; performance of field studies on the effects of mining-induced seismicity and local hydrology; collection of ground shock data on the rock mass near underground openings; participation in the **DE**velopment of **CO**upled models and their **VAL**idation against **EX**periments (DECOVALEX) program for evaluation of computer codes capable of simulating coupled TMH processes; and identification and understanding of important thermally induced coupled processes in an unsaturated environment through laboratory studies. Earlier reports in this series documenting progress to date include Hsiung et al. (1992, 1993a-e, 1994a,b), Ahola et al. (1992, 1993), Hsiung and Chowdhury (1991, 1993), Kana et al. (1990, 1991), Brady et al. (1990), and Brandshaug et al. (1990). This Semi-Annual report describes the results of activities in the Rock Mechanics Research Project during the second half of 1994.

2.2 SIGNIFICANT TECHNICAL ACCOMPLISHMENTS

2.2.1 Dynamic Scale-Model Experiment on a Jointed Rock Mass

In this study, a scale model consisting of an aggregate of simulated rock material blocks was used to simulate the earthquake response of a larger segment of the reference repository rock mass. This model was a follow-on to direct shear experiments on single, naturally jointed, welded tuff fractures that were used to determine the joint normal and shear response under both cyclic pseudostatic and dynamic loadings. The direct shear tests on single, natural-welded tuff joints have been discussed fully in previous reports (e.g., Hsiung et al., 1993d,e) including the comparison with numerical predictions obtained from the distinct element code UDEC. For this period of reporting, a brief description of the design related to the scale-model experiment is presented. A detailed discussion regarding the scale-model design will be provided in a report entitled "An Experimental Model Study of Seismic Response of an Underground Opening in Jointed Rock" (IM 5704-034-095-002) that is scheduled to be submitted to NRC on March 3, 1995.

A two-dimensional conceptual diagram of an underground rock mass with a central opening is shown in Figure 2-1. It is assumed that the rock mass consists of various sets of fractures or joints. The square cross-section (1×1) rock mass is assumed to be influenced by the overburden mass, M_0, and lateral boundary masses, M_1. The value of M_0 was determined by an assumed overburden height of 42.67 m (140 ft), and the value of M_1 was approximated by assuming that M_1 also consists of a square cross-section. The earthquake excitation was assumed to be purely horizontal and to have a wavelength much greater than the length of the affected rock-mass segment. Under these conditions, the excitation could be represented by a spatially uniform displacement motion. Values for some dimensions were

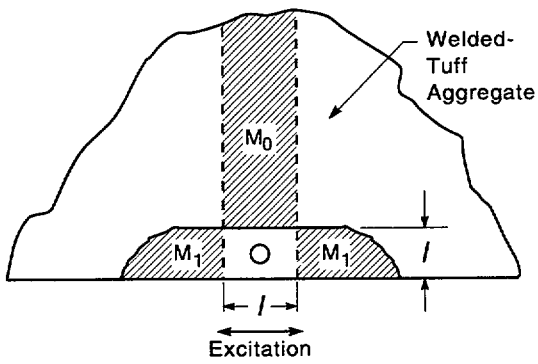

Figure 2-1. Conceptual model of underground rock mass with opening

selected in order to be a reasonable representation of a practical physical problem, and at the same time to allow scaling for a 1/15-scale model system to be described later. The dimensions and weight capacity of the seismic simulator had to be compatible with these values. The exact nature of the effective boundary conditions had to be estimated.

A similitude analysis of the model in Figure 2-1 results in the following nondimensional equation for shear and relative displacement response:

$$\left(\frac{\sigma}{\rho lg}, \frac{u}{l}\right) = F\left(\frac{E}{\rho lg}, \phi, \nu, \frac{\sigma_n \phi}{\rho lg}, \frac{M_0}{\rho l^3}, \frac{M_1}{\rho l^3}, \frac{a}{l}, \frac{x_0}{l}, \frac{\omega^2 l}{g}, \omega t\right) \quad (2\text{-}1)$$

where a is the thickness of the model, M_0 is the overburden mass, l is the rock mass dimension, E is the material Young's Modulus, ν is the material Poisson's ratio ρ, is the material density, M_1 is the effective boundary mass, σ is the normal stress on rock mass, σ_n is the shear stress, u is the relative shear displacement, ϕ is the friction factor, g is the gravity, x_0 is the excitation displacement, ω is the excitation frequency, and t is the time duration. Potential coupling between M_0 and M_1 is not included in Eq. (2-1) for simplicity.

Note that it is possible to make the nondimensional numbers more meaningful by presenting them as the following ratios.

$$\left(\frac{\sigma_n \phi}{\rho lg}\right)\left(\frac{la}{la}\right) = \frac{\text{Overburden Shear Force}}{\text{Segment Inertia Force}} \quad (2\text{-}2)$$

$$\left(\frac{M_0}{\rho l^3}\right)\left(\frac{lg}{ag}\right) = \frac{\text{Overburden Shear Force}}{\text{Segment Inertia Force}} \quad (2\text{-}3)$$

$$\left(\frac{M_1}{\rho l^3}\right)\left(\frac{lg}{ag}\right) = \frac{\text{Lateral Boundary Inertia Force}}{\text{Segment Inertia Force}} \quad (2\text{-}4)$$

Thus, system boundaries (overburden and lateral boundaries of the square cross-section rock mass in Figure 2-1) were replaced with normal and lateral pressures and masses, and σ_n is the effective hydrostatic pressure of the overburden. This concept of replacing the system boundaries was the one on which the scale model design was based. It was desirable to design the scale model with as little distortion of similitude as possible, consistent with dimensions and force capacity of the available seismic simulator. As in any scale model design, several independent variables were chosen, and others were then determined by satisfying similarity requirements. It was decided that a 1/15 geometric scale would be feasible. Therefore, if s is the scale factor and is equal to ls, then

$$\frac{l_m}{l_p} = \frac{1}{s} \quad (2\text{-}5)$$

where l_m and l_p are the rock mass dimensions for the model and prototype, respectively. Furthermore, we let

$$\frac{\phi_m}{\phi_p} = \frac{1}{k} \quad (2\text{-}6)$$

where k is equal to 2.0, which was determined by comparison of the shear test results of the rock simulant interfaces and actual rock joints. Finally,

$$\frac{\rho_m}{\rho_p} = \frac{1}{q} \quad (2\text{-}7)$$

where q is equal to 6.67, which was determined based on the preliminary tests of potential rock simulant samples. With these independent parameters, the following similarity requirements resulted:

$$\sigma_{nm} = \frac{k}{qs}\sigma_{Np} = 0.02 \text{ MPa (2.9 psi)} \quad (2\text{-}8)$$

$$M_{om} = \frac{1}{qs^3}M_{op} = 762 \text{ kg (1,680 lb)} \quad (2\text{-}9)$$

$$M_{1m} = \frac{1}{qs^3}M_{1p} = 327 \text{ kg (720 lb)} \quad (2\text{-}10)$$

$$E_m = \frac{1}{qs}E_p = 400 \text{ MPa } (57,971 \text{ lb/in.}^2) \quad (2\text{-}11)$$

$$\rho_m = \frac{1}{q}\rho_p = 360 \text{ kg/m}^3 \text{ (22.5 lb/ft}^3) \quad (2\text{-}12)$$

The parameters above necessitated that the rock simulant effective density be significantly reduced over that for the prototype tuff material. This requirement would be very useful for controlling overall model weight. However, such an approach generally requires a change of rock simulant material or a hollowing out of simulated rock centers which is impractical. Furthermore, it was felt that the simulant material needed to remain brittle and exhibit surface wear properties approximating those of the prototype material. Therefore, as a practical compromise, it was decided to use simulated rock of solid material and a density ratio, q, of 1.43, which would be applied for the rock simulant within the rock-mass segment only. The original ratio of 6.67 would be applied to the material outside the segment. This simulation effectively produced a model whose exterior masses were more manageable in terms of seismic simulator capacity, but at the same time, caused the interior rock mass too be 4.67 times too high. Although this condition was an obvious physical distortion, the result should still be useful for providing a better understanding of the seismic effects on a simulated rock mass and for providing a database for verification of computer codes. Furthermore, since the greatest shear load on the interior segment was anticipated to result from the overburden mass lateral moment, it was felt that the effects of mass exaggeration within the interior segment would be less pronounced on the dynamic response. Therefore, the overburden mass, M_0, was maintained as discussed above, but the boundary masses were reduced in order to maintain total model mass within the shaker table capacity, and, in some measure, to counteract the effects of exaggerated interior segment mass. Confirmation of these assertions was established by the analysis of a preliminary discrete element analytical model of the system.

The final physical design and associated dimensions are given in Figure 2-2. The model consisted of an aggregate of many stacked rock simulant ingots, each 61 cm long, with the interfaces oriented at a 45° angle to the horizontal. The ingot cross-sections varied from 5×5 cm square for basic ingots, to half-section ingots at the boundaries, to curved-section ingots around the center circular opening. This opening was 15.2 cm in diameter. The four boundaries of the stack were interfaced with 6.4-mm thick rubber, which is bonded to the rock on the inside and lubricated with silicone at the interface with the confining box boundaries. These boundaries were a very stiff construction of welded aluminum plates and 10.2-cm I-beam frames. The proper pressure, σ_n, was maintained on the system by eight vertical cables and eight horizontal cables. The two end structures were hinged to the bottom support structure at the baseplate and were held against top rollers at each upper corner. Therefore, the end structures could pivot laterally, while the top structure can pivot and float up and down as necessary to follow the confined rock motion.

As noted earlier, although several rock properties were identified as being important for modeling purposes, it was felt that the brittle nature and associated wear properties of the jointed interfaces were the most important for model characterization. Furthermore, it was recognized that an exact modeling of welded tuff behavior was probably neither possible nor was actually

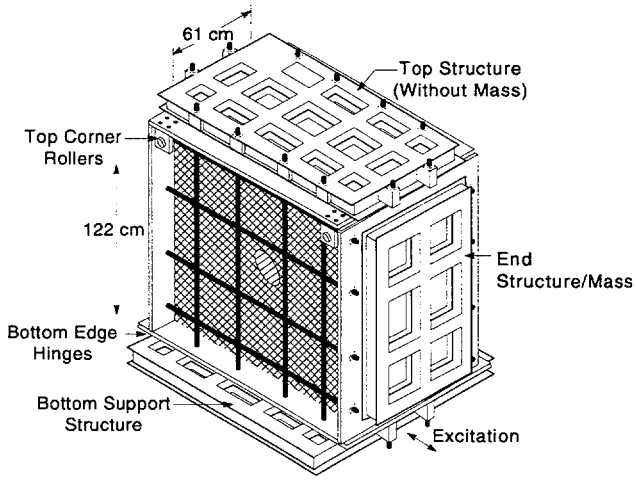

Figure 2-2. Physical design of scale-model rock mass with opening

necessary for a successful verification of computer codes. Therefore, the technical approach adopted for development of a suitable rock simulant consisted of following the previously presented similitude guidelines as much as practical, but allowing distortions so long as they could be quantified.

Initial development of the rock simulant was based on repeated trials of various constituent mixtures and testing of material properties of cylindrical specimens cast from these mixtures. The specimens were cast as 5.0-cm (2-in.) diameter by 10.0-cm (4-in.) long specimens that were instrumented with strain gages and tested in uniaxial compression test machines. Table 2-1 lists the ingredients that were ultimately found to provide a material having the appropriate properties.

Generally, it was recognized that relative normal and shear displacement at the rock interfaces, and overall structure motions were of interest, and that the transducers used for such measurements should offer negligible resistance to rock interface movement. Therefore, several types of transducers were selected for measurement of these responses. These transducers included accelerometers, strain gages, specially designed cantilever beam shear displacement measurement devices, Bentley proximeters, and linear variable differential transducers. The data from these transducers were collected via a 486 (66 MHz) computer. The sampling rate was 2,800 data points/second. A total of 50 data channels was used during the tests. It was also recognized that relatively large displacements for the blocks around the opening might be expected due to repetitive shaking. The transducers mentioned above were not expected to function under large displacements. Consequently, one video camera at each side of the scale model apparatus was mounted axially with the opening to capture large displacements.

Test procedures were based on what can be called an "incremental fragility level" philosophy. Test runs were started at a very low peak excitation displacement level, and this amplitude was incrementally increased as the runs progressed. The excitation displacement input signal used for the dynamic scale-model experiments was derived from an accelerogram measured at the Guerrero array for the September 1985 Mexico City earthquake, a well-characterized seismic event, using a 1/15 scale. Both videotape and digital data were acquired for each run. At the end of each run, all 50 channels were converted to engineering units, and a preliminary review of the data was performed visually on the 486 computer monitor. When transducer or other component malfunction occurred, reopens and adjustments were performed prior to the next run. Furthermore, some shifting of filter channels or transducer locations was performed as response information was acquired and evaluated in order to ensure the fidelity of the data acquired.

Table 2-1. Properties of rock simulant specimen

Material Constituents (Percent by Weight)	
25.2	Type I Portland Cement
45.9	Barite
25.2	Water
3.4	Bentonite
0.3	DARACEM-100 (Plasticizer)
8.6×10^{-3}	Vinsol Resin (Air Entrainment)
4.6×10^{-2}	Ivory Liquid Soap
Uniaxial Compressive Strength	
10.35 (MPa) (1,500 lb/in.^{2})—13.79 MPa (2,000 lb/in.^{2})	
Material Density	
1,682 kg/m^3 (105 lb/ft^3)	
Roughness Data	
Averag Peak:	±0.2 mm (0.008 in.)
Average Wave Length:	6.4 mm (0.25 in.)

This section describes the design, fabrication, and test of a relatively complex scale model for studying the seismic response in the vicinity of an underground opening. By all observations during the test sequence, it appears that instrumentation and associated data acquisition systems performed as expected. The scale-model experiment produced data that can be used for evaluating the adequacy of computer codes for assessing the performance of underground openings subjected to earthquake impacts. Analysis of the results for the scale-model experiments is underway. The limited preliminary analysis indicates a general response that is entirely plausible for the seismic excitation employed.

2.2.2 Thermal-Mechanical-Hydrological Coupled Modeling (DECOVALEX)

The purpose of this research activity is to increase the understanding of TMH processes for evaluating rock mass stability and radionuclide release and transport from a geologic repository to HLW through NRC/CNWRA participation in the international DECOVALEX project. DECOVALEX was organized by the Swedish Nuclear Power Inspectorate (SKI). Eleven funding organizations are currently involved, each supporting one or more research teams. In the DECOVALEX project, modeling is being used to design validation tests of TMH-coupled processes, which are expected to lead to the development and validation of coupled TMH models for use in the licensing of an HLW repository.

The final report for Phase II of DECOVALEX is being published as an SKI technical report. This Phase II report will present detailed comparisons of results among the various research teams, including the CNWRA, for one benchmark test (BMT) and one Test Case (TC) problem. These study problems for Phase II are the Near-Field Repository Model (BMT3) and the revised Coupled Stress-Flow Model (TC1).

2.2.2.1 DECOVALEX Phase III Experimental and Modeling Studies

The experimental and modeling work for Phase III of DECOVALEX is continuing. The results of DECOVALEX Phases I and II were reported elsewhere (Ahola et al., 1992 and 1993; Jing et al., 1993 and 1994). Of the five TC problems proposed for Phase III, the CNWRA has proposed one, namely, the Direct Shear-Flow Test (TC5). In addition to conducting the experiment, the CNWRA team is using the computer code ABAQUS to model the TC5 experiment. Also, the CNWRA team used ABAQUS to model the Big-Ben Experiment (TC3) as proposed by the Japanese participants. ABAQUS results from modeling the Big-Ben Experiment are presented in the next section, followed by a summary of the experimental results completed for the Direct Shear-Flow Test.

2.2.2.2 Big-Ben Experiment (TC3)

The Big-Ben Experiment was designed to evaluate the EBS for the current Japanese radioactive waste disposal concept. The experiment was conducted by the Japanese team with the objectives of better understanding the heat transfer, water uptake, and swelling behavior in an EBS for underground disposal of HLW, and also of evaluating the ability of mathematical models to accurately predict the observed phenomena. The experimental EBS is composed of an electric heater, carbon steel overpack, buffer material, and concrete containment simulating the surrounding host rock. The reinforced concrete containment has an outside diameter of 6 m and is 5 m in height. A borehole, approximately 1.7 m in diameter and 4.5 m in depth, is located in the center of the concrete. An electric heater with several cartridge heaters, all set in a carbon steel overpack, which is about 1 m in diameter and about 2 m in height, was placed in the borehole. A buffer material was packed between the overpack and concrete containment. This particular experiment consisted of uniform heating as well as water injection under constant pressure into the partially saturated buffer. A full description of the experiment and proposed test case is given by DECOVALEX (1993).

Figure 2-3 shows a view of the buffer material region within the TC3 experiment. The buffer itself is composed of a mixture of 70 percent bentonite and 30 percent quartz sand. It is partially saturated, having an initial saturation of approximately 0.63 (i.e., 63 percent). Around the inner and outer edges of the bentonite lie two thin, highly permeable quartz sand layers a few centimeters thick. During the experiment, water was injected through a tube directly into the outer quartz sand layer at a constant pressure of 50 kPa throughout a 5-mo period to simulate water flowing in from the surface of the borehole through a fracture. Over this same 5-mo period, the heater was operated at a constant power output of 0.8 kW. The TMH coupling effects thus consisted of water being imbibed into the buffer material, creating an increase in saturation and swelling of the buffer material. In addition, the heating caused thermal expansion within the different engineered materials, and created some vapor-driven moisture flow outward, thus desaturating the inner portions of the buffer material. During the experiment, periodic measurements of temperatures, strains, water content, and swelling pressures were taken.

In addition to the experimental measurements conducted by the Japanese, the Big-Ben Experiment was modeled numerically by three separate DECOVALEX research teams. These teams included the NRC-funded research team (CNWRA), the Japanese Power Reactor and Nuclear Fuel Development Corporation-funded research team from Kyoto Univer-

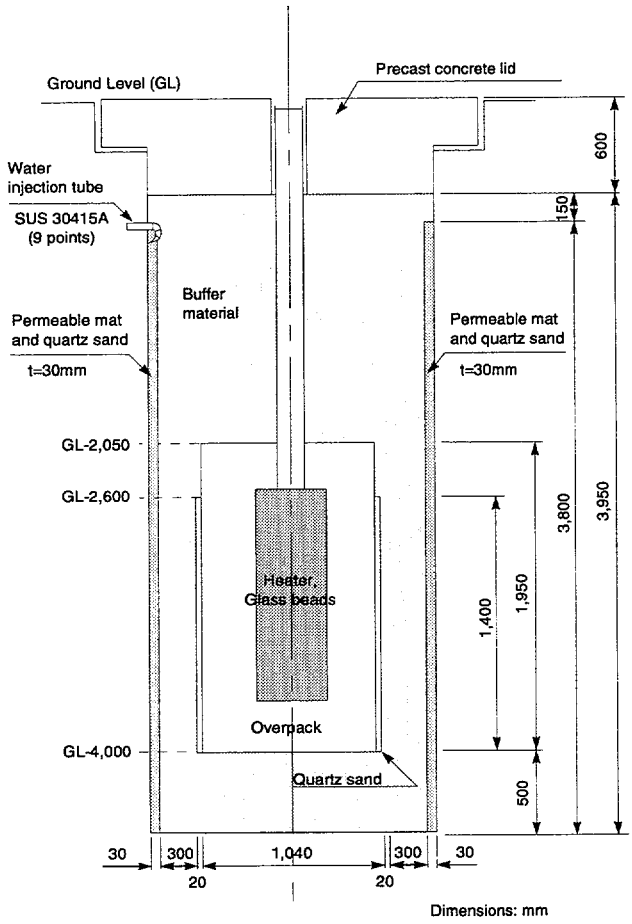

Figure 2-3. Schematic view of buffer region (Test Case 3)

sity (KPH), and the Swedish Nuclear Fuel and Waste Management Company-funded research team (Clay Technology AB). Both the CNWRA and Clay Technology teams utilized the finite element code ABAQUS for the modeling analysis. However, the version of ABAQUS used by the Swedish team was somewhat enhanced to take into account the heat transfer and moisture redistribution in the vapor phase (Börgesson and Hernelind, 1994) that was not available in the CNWRA version of ABAQUS (i.e., Version 5.3). The Japanese KPH team utilized its three-dimensional finite element code THAMES (Ohnishi et al., 1985).

Figure 2-4 shows the temperature distribution at three different elevations within the buffer as measured experimentally and calculated numerically by the different modeling teams after a period of 5 mo (i.e., end of the experiment). This figure shows that both the CNWRA and Clay Technology results obtained using ABAQUS agree very well with the experimental measurements. The KPH research team results using THAMES somewhat underestimated the experimental measurements of temperature throughout the buffer. Some slight discrepancies in the calculated results are likely due to the fact that certain boundary condition and material property uncertainties required varying assumptions to be made by the different teams.

The distribution of water content after 5 mo is shown in Figure 2-5 at the same three elevations within the buffer. In portions of the buffer, for example, above the heater and to some extent along the heater midplane, the computed results agree well with the experimental measurements of water content. Near the base of the heater, all three computed results underestimate the water content, especially toward the outer region of the buffer. Along the two horizontal sections through the buffer nearest the heater (i.e., along the heater midplane and base), the amount of heating in the buffer is greater. The results calculated by the CNWRA (using the original Version 5.3 of ABAQUS) and those by Clay Technology (using an enhanced Version 5.3 of ABAQUS) begin to deviate toward the innermost portion of the buffer. The reason for this deviation is that the Clay Technology results are better able to account for the moisture redistribution in the vapor, which leads to drying in the buffer adjacent to the heater. As a result, the slope of the water content curve obtained by Clay Technology along these two lower elevations in the buffer track the experimentally measured values better than the CNWRA results. The CNWRA results begin to cross above the measured values, indicating that in the higher temperature regions, the enhancement to the ABAQUS code is necessary. The THAMES code is also able to account for the heat and moisture flow in the vapor, and the results obtained by the KPH team agree well with the Clay Technology results. However, the water content at the innermost calculated point near the heater is somewhat underestimated.

Finally, a comparison of the distribution of radial (total) stress within the bentonite is provided in Figure 2-6. There is a considerable discrepancy between the CNWRA results and those obtained by both KPH and Clay Technology. The reason for the large (and most probably unrealistic) stresses calculated by the CNWRA is that ABAQUS takes into account the fluid suction pressure for calculation of stresses. The component added to the mechanical stress from the suction pressure depends on the level of saturation at that particular

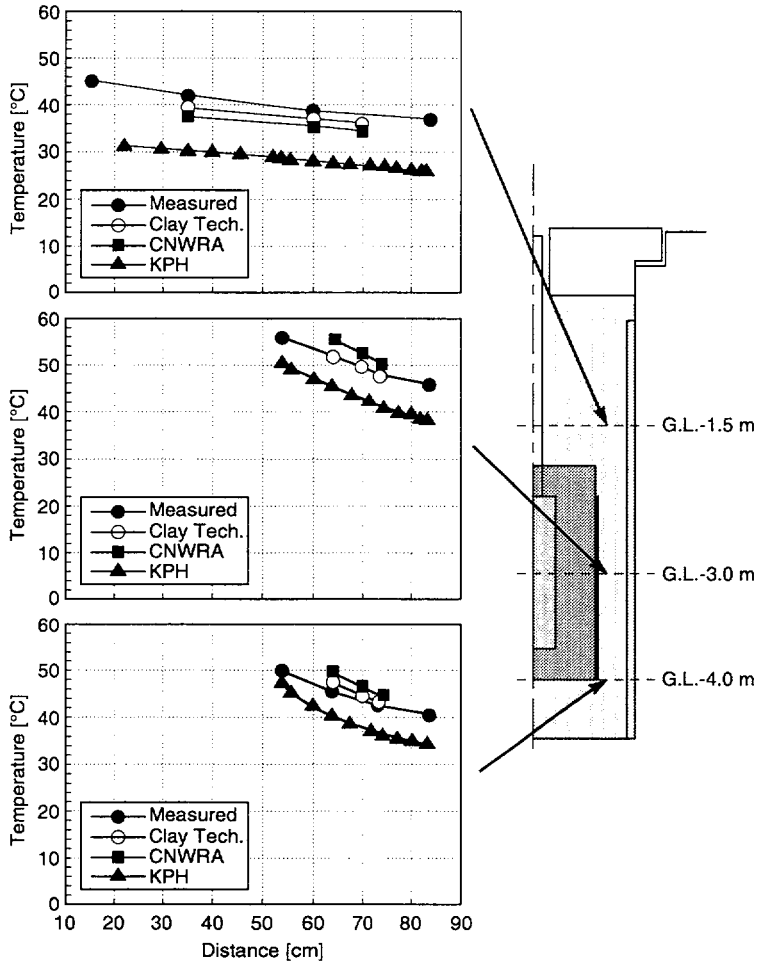

Figure 2-4. Distributions of temperature after 5 months

point. In ABAQUS, the effective stress principle is applied, in which the portion of fluid suction pressure contributing to mechanical stress is set equal to the suction pressure multiplied by the degree of saturation. In this particular TC3 problem, the fluid suction pressures provided by the Japanese team were experimentally measured to be very high within the bentonite buffer. These high suction pressures lead to high mechanical states of stress in the buffer as shown in the CNWRA results (Figure 2-6). The version of THAMES used for this analysis does not account for the fluid suction pressure in the mechanical equilibrium equations, and thus the maximum stress is only a few tenths of a megapascal. Although the Clay Technology team used ABAQUS, they opted to use much lower fluid suction or retention curve values for the buffer than those provided to the CNWRA team based on some of their own laboratory measurements of similar material. Consequently, even though both versions of ABAQUS used the same effective stress principle, mechanical stress states were very different. Experimental measurements of stress were only available from a few pressure cells attached to the concrete on the outermost edge of the buffer. The pressure cell mounted to the concrete along the midplane elevation of the heater (i.e., G.L.-3.0 m in Figure 2-6) measured approximately 0.4 MPa radial stress at the end of 5 mo. Again, the induced stress is a combination of swelling and thermal expansion of the buffer. The KPH and Clay Technology results in the center plot in Figure 2-6 appear to agree more closely with the experimental stress than the CNWRA results. More work is apparently needed to better understand the extent to which the fluid suction contributes to the overall stress state. For example, the effective stress principle applied to partially saturated clay buffers may be acceptable at higher degrees of

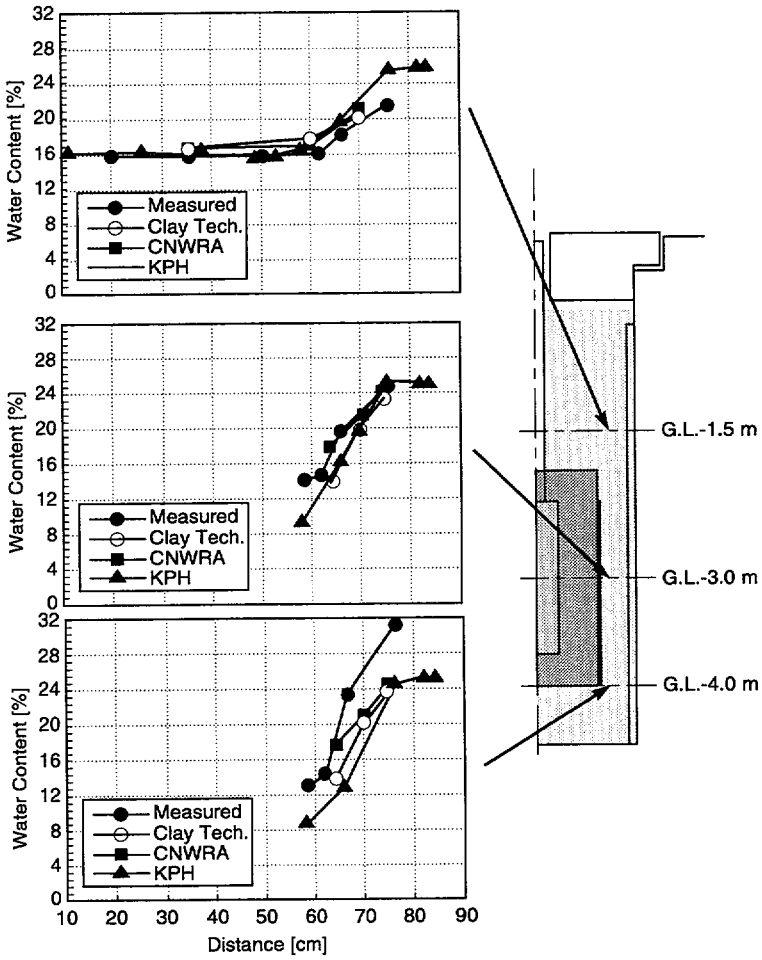

Figure 2-5. Distributions of water content after 5 months

material saturation, but be unrealistic at lower degrees of saturation.

2.2.2.3 Direct Shear-Flow Test (TC5)

The overall objectives of the coupled TMH laboratory experiments are to understand the key parameters affecting mechanical-effect-dependent fracture flow and to provide a database that can be used to evaluate current capabilities for calculating such fracture flow. In FY93, the coupled experimental program was initiated on an exploratory basis with the radial flow study of the mechanical-hydrological (MH) coupled effects on a single-jointed Apache Leap tuff specimen. In subsequent years, this program will be followed by selected two-process coupled experiments and, finally, coupled TMH experimental studies. The scope of this work encompassed MH experiments on a single-jointed Apache Leap tuff specimen including both linear and radial flow tests. However, the primary emphasis is on linear flow experiments. The MH experimental activities include (i) development of experimental techniques, (ii) radial flow experiments under normal load, (iii) linear flow experiments under normal load, and (iv) linear flow experiments under combined normal and shear loads. Details of the work can be found in Mohanty et al. (1994). Results for coupled shear and flow experiments using a linear flow configuration are presented in this report.

In order to perform direct dynamic shear tests on single-jointed rock specimens, a test apparatus with combined normal and shear loading capability was designed, fabricated, and assembled at Southwest Research Institute (Hsiung et al., 1994b). This direct shear test apparatus was modified for conducting the MH experiments. Detailed discussion regarding the modification is provided in a separate report (Mohanty et al., 1994).

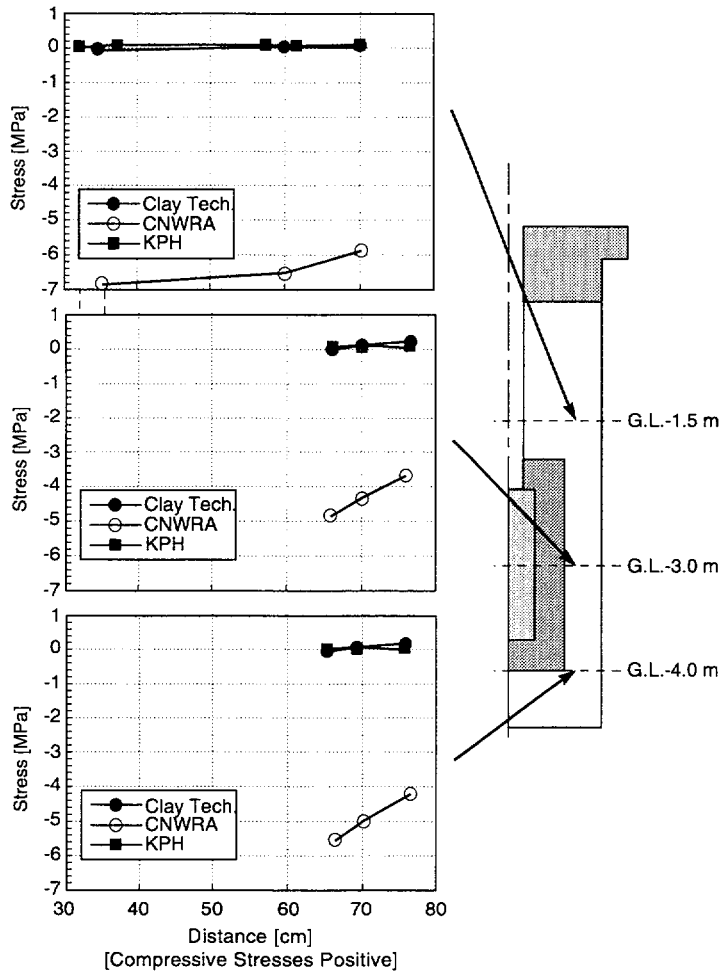

Figure 2-6. Distributions of radial stress after 5 months

For the linear hydrologic flow method, the faces parallel to the overall flow direction were sealed with grout. Special modifications were necessary for the grouted faces. The fluid was injected across the fracture cross section using a positive displacement pump, and the fluid produced from the fracture cross section at the opposite end was collected. The pressure drop across the specimen was measured by using a differential pressure transducer.

During the shear process, an increase in the fracture void volume was anticipated. The 0.45-m outlet end tubing served as a water accumulator, from which water, through suction, filled the additional void created during the shearing process. In order to prevent the liquid head in the outlet tubing from falling below its entry level to the collection chamber, a three-way connector was attached to the inlet end of the specimen holder. An additional water reservoir was connected to the three-way connector via a valve. The water reservoir was maintained at such a height that water would flow at a pressure head of 3 m of water. The purpose of this arrangement was to avoid change in the flow rate setting of the positive displacement pump so as to compensate for the falling head in the outlet tubing when shear takes place.

For the shear load experiments, 150 s (2.5 min) elapsed before moving from one load setting to another. Then data were acquired for 240 s (4 min) at each load and displacement setting. Also, 150 s (2.5 min) were allowed for a rock displacement of 6.35×10^{-3} m (0.25 in.).

The rock was subjected to four cycles of shear load under 2 MPa normal stress prior to the collection of the data presented in Table 2-2. In this table, the data are

presented for conditions under 2, 4, and 5 MPa normal stress. Conducting shear experiments at more than 5 MPa normal stress would have required replacement of the horizontal actuator, which is intended for use in future experiments.

Shear tests were conducted in test runs T38HYD12.DAT, T38HYD13.DAT, T38HYD14.DAT, and T38HYD15.DAT. Test run T38HYD12.DAT was abandoned at the end of a shear cycle at 2 MPa normal stress because a sudden rise in pressure was observed toward the end of the cycle. It was suspected that the rubber shoe of the upper grout box was obstructing flow into the collection groove. Therefore, it was decided that the reverse displacement in the shearing cycle would be limited to 1.905×10^{-2} m (0.75 in). In test run T38HYD13.DAT, surprisingly, similar pressure buildup occurred at 1.905×10^{-2} m (0.75 in.) in the reverse displacement. These pressure buildups caused leaks that were later sealed. This test run indicated that the flow-path blockage was not due to the rubber shoe of the upper box, but rather to the formation of fine materials while shearing. Attempts to remove the blockage of the flow path were made by using high-velocity forward and reverse flushing. The method worked with only occasional success because the pressure in the flowing fluid was not high enough to dislodge the accumulated particles without damaging the fluid seal. Test run T38HYD14.DAT was intended to be run at 1.905×10^{-2} m (0.75 in.) shear displacement at 2, 5, and 8 MPa normal stresses. Analysis of the data revealed that rock displacement did not take place at 5 and 8 MPa normal stress. Therefore, a higher capacity horizontal actuator (50,000 lb) was used. As a precautionary measure, the next test run (T38HYD15.DAT) was conducted at 2, 4, and 5 MPa normal stress.

The data presented in Table 2-2 were measured by using water as the flowing fluid. Due to slack in the grout box, the actual displacement was always smaller than the specified displacements. During the shear cycle under 2 MPa normal stress, the mean aperture was observed to be 0.1314 mm with a maximum change in aperture of 39 percent. At the end of the displacement cycle at 5 MPa normal stress, a maximum change in effective hydraulic aperture of 370 percent was observed. The differential pressure transducer used in the experiment was adequate for measuring a permeability change for the specified specimen through three orders of magnitude. The absolute pressure transducers were rated at 3.45×10^{4} Pa (5 psig). Therefore, the readings from these transducers were used when the pressure drop could not be measured by using the more precise differential pressure transducer.

The constricted flow effect due to the production and accumulation of fine particles did not occur in any definite pattern. Attempts were made to dislodge the blockage of flow through reverse flushing. This procedure helped clear the flow paths in only a few instances. At the end of the steady-state experiment at each displacement, particle accumulation was removed by lowering the exit end of the outlet tube, tapping the tube, and permitting flow from the water reservoir to dislodge the accumulated fine particles. Figure 2-7 gives evidence of the dense deposition of the dislodged fine particles in the joint while flushing the deposits at the outlet valve. Data acquisition was interrupted until the hydrologic conditions were suitable for the steady-state runs after flushing. Fortunately, at the water injection rate of $6.66\times10^{-8}m^3/s$ (4 cm^3/min), there was no significant suspension of particles in the flowing fluid. Thus, change in water viscosity was not considered significant.

At the end of the experiment, the experimental apparatus was dismantled in order to visually inspect the changes in the rock joint. A much larger amount of fine deposits was observed in the joint than could be interpreted from the amount of fine deposits migrating during the flow experiment. The fine particles existed as a thick paste. It could not be determined if these fine particles existed in the same thick paste form during the flow experiment or if the drying of water before the dismantling of the apparatus gave a paste-like texture to the aggregate. The rock surfaces were allowed to dry to room temperature, and then the fine particles were collected for further analysis. The fines that migrated with flowing fluid were collected along with the effluent. Then the effluent was evaporated in a constant temperature oven to recover the solids. A total of 3.81×10^{-2} kg of fine solids were dislodged from the rock during four displacement cycles under normal stresses of 2 MPa, and one cycle at 4 and 5 MPa each, over a displacement of approximately 1.905×10^{-2} m (0.75 in.).

The modification of the apparatus for confining pressure performed marginally during both normal and shear load experiments. The leaks that impaired data acquisition at a few shear displacement increments were caused by the slack distortion of the grout box while shearing. In order to facilitate the grouting process, the boxes were constructed of steel plates held together by

Table 2-2. Shear displacements and corresponding aperture during forward and reverse cycles at 2, 4, and 5 MPa normal stress

Movement F: Forward R: Reverse	Normal Stress (MPa)	Specified Shear Displacement (in.)	Actual Shear Displacement m (in.)	Aperture ($\times 10^{-3}$ m)
F	2	6.35×10^{-3} (0.25)	3.23×10^{-3} (0.172)	0.12
F	2	0.0127 (0.5)	0.0105 (0.416)	0.14
F	2	0.01905 (0.75)	0.0166 (0.656)	0.14
F	2	0.0254 (1.00)	0.0227 (0.894)	0.15
R	2	0.01905 (0.75)	0.0161 (0.633)	0.14
R	2	0.0127 (0.50)	0.0093 (0.386)	0.13
R	2	6.335×10^{-3} (0.25)	0.0036 (0.141)	0.10
F	4	6.35×10^{-3} (0.25)	0.0036 (0.142)	0.09
R	4	0.01905 (0.75)	0.0167 (0.661)	0.15
R	4	0.0127 (0.50)	0.0109 (0.431)	0.13
F	5	0.0127 (0.50)	0.007 (0.28)	0.04
R	5	0.0254 (1.00)	0.0184 (0.725)	0.18
R	5	0.01905 (0.75)	0.0172 (0.679)	0.15
R	5	0.0127 (0.50)	0.0114 (0.449)	0.04

bolts. It was observed that during the shearing process, the bolted plate interfaces opened up, causing severe leaks. The 1.5875×10^{-3} m (1/16 in.) thick silicone coating on the rock block separating the rock from the cement did not work as desired to prevent leaks. It is likely that the severe shearing process to which the silicone rubber seal had been subjected punctured the seal, causing leaks to develop. However, these leaks stopped after the displacement was complete, except in some cases. In order to maintain sufficient head of water downstream, the injected fluid was allowed to flow at high rates during the shearing; no air was expected to enter into the rock joint during such leaks.

It should be noted that shear testing is a destructive method of testing. It is clearly evident that the damage of the rough surface produces a significant amount of fine particles. Therefore, it is necessary to separate the effect of dilation on the flow from the effect of fine particles on the flow. However, from the data acquired during the first displacement cycle under 2 MPa normal stress, before a significant amount of fine particles was formed, qualitative statements could be made on the effect of dilation. Maximum increase and decrease in the permeability of the fracture during 0.0254-m (1-in.) shear displacement was observed to be nearly 40 and 20 percent, respectively.

The current experiment was interrupted by leaks, malfunctioning of the transducers for water-saturated experiments, breakdown of the cylinder-switching valve, and a synchronization of the piston

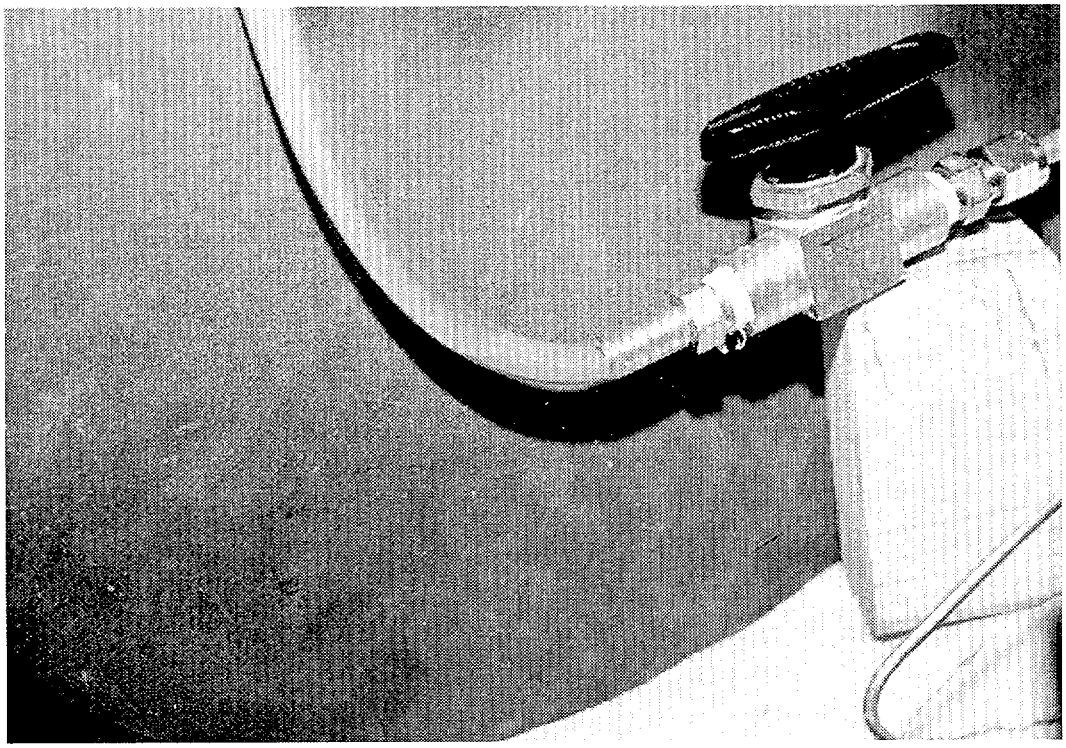

Figure 2-7. The fine particle accumulation due to settling. This material must be removed before data recording for steady-state flow.

movement with the driving motor. Difficulties were also experienced in the airflow measurements at both high- and low-flow rates. At low-flow rates, the bubble flowmeter was affected by the interfacial tension at the glass wall, whereas at high-flow rates, creation of multiple bubbles forced the experiment to be repeated several times.

2.3 ASSESSMENT OF PROGRESS TOWARD MEETING PROJECT OBJECTIVES

The primary objective of the Rock Mechanics Research Project is to identify seismic-related key technical issues that will affect repository design and performance and to develop techniques that could be used to predict the response of near-field jointed rock mass at the proposed HLW repository at YM, Nevada, when it is subjected to repetitive seismic (including earthquakes and nuclear testing at the Nevada Test Site) and thermal loads. This objective is being accomplished through laboratory and field experiments as well as computer modeling studies. Several seismic-related issues have been addressed. For instance, it has been determined through field experimental studies that repetitive, lower- magnitude seismic events can cause greater damage to underground tunnels than a single large-magnitude event, due to the cumulative effects of joint slip around the tunnels. Such cumulative effects will again be demonstrated through the small-scale dynamic load experiments of a simulated rock mass. Most designs today consider only the maximum credible seismic event. The cumulative effect results have been presented to the Nuclear Waste Technical Review Board (NWTRB), and the NWTRB has incorporated these findings in its annual report as guidance for the U.S. Department of Energy (DOE) to consider in its ESF and repository design (Nuclear Waste Technical Review Board, 1992). The findings on the effects of repetitive seismic events have also directly supported the development of the Compliance Determination Method (CDM) for shafts and ramps design, specifically with regard to establishing review method steps for assessing protection against natural phenomena and environmental conditions [10 CFR 60.131(b)(1)]. Also, based on the field experiments performed at the Lucky

Friday Mine, Mullan, Idaho (Task 5), both the magnitude and duration of water pressure changes due to seismic events were observed to be small (Hsiung et al., 1993f). These results would tend to indicate that significant changes in the water pressure below the proposed repository site due to seismic events of large magnitude may not be credible.

Through laboratory experiments and modeling studies, it has been found that the rock-joint models presently incorporated in the computer codes under consideration for use in seismic design in jointed rock masses do not correctly simulate anticipated cyclic pseudostatic and dynamic rock-joint behavior. The development of a new rock-joint model based on the research finding that can adequately predict the joint behavior under cyclic shear loading condition is currently underway under Task 2.3 of the RDCO Program Element. Through identification of these problems and subsequent enhancement of the rock-joint models, the staff will be better able to review the DOE repository seismic design and to support the assessment of repository performance. In addition, several of the design-related CDMs have KTUs related to the impact of repetitive seismic motion on long-term performance of seals. Furthermore, observed deficiencies in the rock-joint model will be used as a basis for developing acceptance criteria in the CDMs relevant to design review of subsurface facilities. A verified code for seismic analysis will increase the staff capabilities for performing independent detailed safety reviews regarding these issues.

The objective of DECOVALEX (Task 9) TMH modeling and coupled experiments is to address KTUs related to the impact of coupled TMH processes on repository design and performance. Preliminary investigation has suggested a significant change in permeability due to displacement under shear load. It is expected that further change in permeability can be recorded by expanding the range of the instrumentation and increasing the pressure rating of the sample holder. These data could directly be used in the model validation exercises. These activities are to evaluate methodologies including model validation and code verification for coupled TMH modeling of jointed rocks. The work being done in this task supports development by the technical assistance program of a compliance determination code for simulating coupled processes. This code will be used by the NRC and the CNWRA for determination of DOE compliance with NRC regulations on thermal and repetitive seismic loads. The results of seismic research have also been used for Site Characterization Plan reviews and are currently being used for ESF Title II Design reviews.

2.4 PLANS FOR NEXT REPORTING PERIOD

The results of the dynamic scale-model experiments will be analyzed during the next reporting period. These results are expected to provide a better understanding of jointed rock-mass behavior subjected to repeated earthquake loads and will generate a data set for code verification. Work on DECOVALEX Phase III modeling and the MH experiments will continue. Other work will include preparation of the three chapters for the manuscript of the DECOVALEX, preparation of peer review on the TMH modeling and experimental program, and the Final Project Report for the Rock Mechanics Research Project. The Final Project Report will document the results obtained from the Rock Mechanics Research Project on seismic-related issues and will make recommendations on the use of these results.

2.5 REFERENCES

Ahola, M.P., S.M. Hsiung, L.J. Lorig, and A.H. Chowdhury. 1992. *Thermo-Hydro-Mechanical-Coupled Modeling: Multiple Fracture Model BMT2, Coupled Stress-Flow Model TC1, DECOVALEX—Phase I.* CNWRA 92-005. San Antonio, TX: Center for Nuclear Waste Regulatory Analyses.

Ahola, M.P., L.J. Lorig, A.H. Chowdhury, and S.M. Hsiung. 1993. *Thermo-Hydro-Mechanical Coupled Modeling: Near-Field Repository Model, BMT3, DECOVALEX—Phase II.* CNWRA 93-002. San Antonio, TX: Center for Nuclear Waste Regulatory Analyses.

Börgesson, L., and J. Hernelind. 1994. *Calculation of Test Case 3—Big Ben Experiment.* DECOVALEX Phase III. Draft Report. Lund, Sweden: Clay Technology AB.

Brady, B.H.G., S.M. Hsiung, and A.H. Chowdhury. 1990. *Qualification Studies on the Distinct Element Code UDEC Against Some Benchmark Analytical Problems.* CNWRA 90-004. San Antonio, TX: Center for Nuclear Waste Regulatory Analyses.

Brandshaug, T., B. Dasgupta, B.H.G. Brady, S.M. Hsiung, and A.H. Chowdhury. 1990. *Qualification Studies on the Finite Element Code HONDO II Against Some Benchmark Analytical Problems.* CNWRA 90-006. San Antonio, TX: Center for Nuclear Waste Regulatory Analyses.

DECOVALEX. 1993. *Phase 3 Test Case 3, Big Ben, DECOVALEX Doc 93/124.* DECOVALEX Secretariat. Stockholm, Sweden: Royal Institute of Technology.

Hsiung, S.M., and A.H. Chowdhury. 1991. *Report on Research Activities for Calendar Year 1990.* W.C. Patrick, ed. NUREG/CR-5817. Washington, DC: Nuclear Regulatory Commission.

Hsiung, S.M., and A.H. Chowdhury. 1993. *NRC High-Level Radioactive Waste Research at CNWRA For Calendar Year 1991.* W.C. Patrick, ed. NUREG/CR-5817. Washington, DC: Nuclear Regulatory Commission.

Hsiung, S.M., A.H. Chowdhury, W. Blake, M.P. Ahola, and A. Ghosh. 1992. *Field Site Investigation: Effect of Mine Seismicity on a Jointed Rock Mass.* CNWRA 92-012. San Antonio, TX: Center for Nuclear Waste Regulatory Analyses.

Hsiung, S.M., M.P. Ahola, and A.H. Chowdhury. 1993a. *NRC High-Level Radioactive Waste Research at CNWRA January–June 1992.* W.C. Patrick, ed. NUREG/CR-5817, CNWRA 92-01S. Washington, DC: Nuclear Regulatory Commission.

Hsiung, S.M., M.P. Ahola, A. Ghosh, and A.H. Chowdhury. 1993b. *NRC High-Level Radioactive Waste Research at CNWRA July–December 1992.* W.C. Patrick, ed. NUREG/CR-5817, CNWRA 92-02S. Washington, DC: Nuclear Regulatory Commission.

Hsiung, S.M., M.P. Ahola, A. Ghosh, and A.H. Chowdhury. 1993c. *NRC High-Level Radioactive Waste Research at CNWRA January–June 1993.* W.C. Patrick, ed. CNWRA 93-01S. San Antonio, TX: Center for Nuclear Waste Regulatory Analyses.

Hsiung, S.M., D.D. Kana, M.P. Ahola, A.H. Chowdhury, and A. Ghosh. 1993d. *Laboratory Characterization of Rock-Joints.* CNWRA 93-013. San Antonio, TX: Center for Nuclear Waste Regulatory Analyses.

Hsiung, S.M., A. Ghosh A.H. Chowdhury, and M.P. Ahola. 1993e. *Evaluation of Rock-Joint Models and Computer Code UDEC Against Experimental Results.* CNWRA 93-024. San Antonio, TX: Center for Nuclear Waste Regulatory Analyses.

Hsiung, S.M., A.H. Chowdhury, W. Blake, and J. Philip. 1993f. Field investigation of mining-induced seismicity on local geohydrology. *Proceedings of the Fourth Annual International Conference on High-Level Radioactive Waste Management.* La Grange Park, IL: American Nuclear Society: 913–920.

Hsiung, S.M., M.P. Ahola, A. Ghosh, and A.H. Chowdhury. 1994a. *NRC High-Level Radioactive Waste Research at CNWRA July–December 1993.* W.C. Patrick, ed. CNWRA 93-02S. San Antonio, TX: Center for Nuclear Waste Regulatory Analyses.

Hsiung, S.M., M.P. Ahola, S. Mohanty, and A.H. Chowdhury. 1994b. *NRC High-Level Radioactive Waste Research at CNWRA January–June 1994.* B. Sagar, ed. CNWRA 94-01S. San Antonio, TX: Center for Nuclear Waste Regulatory Analyses.

Jing, L., J. Rutqvist, O. Stephansson, C.F. Tsang, and F. Kautsky. 1993. *DECOVALEX—Mathematical Models of Coupled THM Processes for Nuclear Waste Repositories—Report of Phase I.* Stockholm, Sweden: Swedish Nuclear Power Inspectorate.

Jing, L., J. Rutqvist, O. Stephansson, C.F. Tsang, and F. Kautsky. 1994. *DECOVALEX—Mathematical Models of Coupled THM Processes for Nuclear Waste Repositories—Report of Phase II.* Stockholm, Sweden: Swedish Nuclear Power Inspectorate.

Kana, D.D., D.C. Scheidt, B.H.G. Brady, A.H. Chowdhury, S.M. Hsiung, and B.W. Vanzant. 1990. *Development of Rock-Joint Dynamic Shear Test Apparatus.* CNWRA 90-005. San Antonio, TX: Center for Nuclear Waste Regulatory Analyses.

Kana, D.D., B.H.G. Brady, B.W. Vanzant, and P.K. Nair. 1991. *Critical Assessment of Seismic and Geomechanics Literature Related to a High-Level Nuclear Waste Underground Repository.* NUREG/CR-5440. Washington, DC: Nuclear Waste Regulatory Commission.

Mohanty, S., A.H. Chowdhury, S.M. Hsiung, and M.P. Ahola. 1994. *Single Fracture Flow Behavior of Apache Leap Tuff Under Normal and Shear Loads.* CNWRA 94-024. San Antonio, TX: Center for Nuclear Waste Regulatory Analyses.

Nuclear Regulatory Commission. 1994. *License Application Review Plan for a Geologic Repository for Spent Nuclear Fuel and High-Level Radioactive Waste Draft Review Plan.* NUREG-1323. Rev. 0. Washington, DC: Nuclear Regulatory Commission.

Nuclear Waste Technical Review Board. 1992. *Fifth Report of the U.S. Congress and the U.S. Secretary of Energy.* Washington, DC: Nuclear Regulatory Commission.

Ohnishi, Y., H. Shibata, and A. Kobayashi. 1985. Development of finite element code for the analysis of coupled thermo-hydro-mechanical behavior of saturated-unsaturated medium. *Proceedings of the International Symposium on Coupled Processes Affecting the Performance of a Nuclear Waste Repository.* Berkeley, CA: 263–268.

3 INTEGRATED WASTE PACKAGE EXPERIMENTS

by Darrell S. Dunn, Narasi Sridhar, and Gustavo A. Cragnolino

Investigators: ***Gustavo A. Cragnolino, Darrell S. Dunn, Narasi Sridhar (CNWRA), and Yi-Ming Pan (Consultant)***

NRC Project Officer: ***Michael B. McNeil***

3.1 OVERALL TECHNICAL OBJECTIVES

The overall technical objectives of the Integrated Waste Package Experiments (IWPE) Project are to:

- Conduct waste package experiments to scope and study the key parameters affecting long-term material performance
- Assess waste package materials and designs selected by the U.S. Department of Energy (DOE) and provide independent evaluation for reasonable assurance of long-term performance
- Support the Office of Nuclear Regulatory Research (RES) in addressing the needs of the Division of Waste Management (DWM)

Several Key Technical Uncertainties (KTUs), developed as part of the Compliance Determination Strategy related to waste package performance and listed in the License Application Review Plan (LARP), Sections 5.2 and 5.4 (Nuclear Regulatory Commission, 1994), are addressed in the IWPE program. These KTUs are:

- The extrapolation of short-term laboratory and prototype test results to predict long-term performance of waste packages and engineered barrier systems (EBSs)
- The prediction of environmental effects on the performance of waste packages and the EBS
- The prediction of release path parameters such as size, shape, and distribution of penetrations of waste packages due to thermomechanical, environmental, or criticality effects
- The prediction of thermomechanical effects on the performance of waste packages

To address the above objectives and KTUs, the IWPE project is divided into six tasks: Task 1—Corrosion; Task 2—Stress Corrosion Cracking, Task 3—Materials Stability, Task 4—Microbiologically Influenced Corrosion, Task 5—Other Degradation Modes, and Task 6—Report Preparation and Peer Review.

Results generated within the IWPE project are being used to provide input parameters to waste package performance assessment models, as well as to verify the model assumptions and predictions. A key area of continued integration between the IWPE project and other projects involving thermohydrology and geochemistry is in the prediction of the environmental evolution very near the waste packages. The fundamental assumption in the waste package corrosion studies reported here is the presence of an aqueous environment, at least episodically. This assumption is conservative because the corrosion rate in a dry steam or dry air environment at anticipated repository temperatures is negligible (Farmer et al., 1991). However, the aqueous environment near the container can have a wide range of compositions. The results from experimental research and modeling efforts within the thermohydrology and geochemistry-related projects will assist evaluations of the presence and chemistry of aqueous environments near the waste package. The results of the IWPE project will help identify the environmental factors of importance to waste package performance and thus guide the investigations of rock-water interactions in the geochemistry-related projects. Another aspect of the near-field environment is the effect of corrosion of containers/waste forms on the environment chemistry. This aspect is especially important in occluded regions such as crevices between the container and the rock.

3.2 SIGNIFICANT TECHNICAL ACCOMPLISHMENTS

3.2.1 Background

In the United States geologic disposal program, horizontal drift emplacement of a multiple-wall container has been proposed (Doering, 1993). A multi-purpose canister (MPC) concept has evolved as the baseline design (Sridhar et al., 1994a) for handling spent fuel from the reactor site through intermediate storage and eventually to the disposal facility. The MPC is proposed to be contained in disposal overpacks. It has also been proposed that high thermal loading via horizontal drift emplacement of large waste packages, containing up to 21 pressurized water reactor fuel assemblies, be used to create a dry-out zone around the EBS for thousands of years that will minimize corrosion and nongaseous radionuclide transport (Ruffner et al., 1993; Buscheck et al., 1993). However, the drying-out process may create deposition of solids rich in Ca and Si (Beavers et al., 1992; Murphy and Pabalan, 1994). In addition, backflow of the condensate through fractures may result in an aqueous environment around the container, as indicated by the results of some field heater tests (Patrick, 1986; Zimmerman et al., 1986; Ramirez, 1991). The evaporation of water may cause the formation of solutions rich in chloride and sulfate (Abraham et al., 1986; Beavers et al., 1992; Walton, 1993). Hence, a conservative approach to MPC life prediction is to assume the presence of aqueous conditions surrounding the containers. The chemical composition of such an aqueous environment is not known, and a range of concentrations of various species has been investigated (Sridhar et al., 1993a).

The approach used in the example analysis of the "substantially complete containment" rule (Cragnolino et al., 1994a) and in the Engineered Barrier System Performance Assessment Codes (EBSPAC) activities for the prediction of performance of container materials (Sridhar et al., 1993b) assumes that corrosion failure modes of importance to life prediction are determined by the corrosion potential (E_{corr}). The E_{corr} of the container material, which is a mixed potential dictated by the kinetics of the anodic and cathodic reactions at the surface exposed to the repository environment, changes with time in response to factors such as radiolysis, pH, temperature, and oxygen concentration (Macdonald and Urquidi-Macdonald, 1990). If the E_{corr} exceeds the pit-initiation potential (E_p), pits initiate and propagate into the container wall. If the E_{corr} drops below E_p, pits already initiated continue to grow, but no new pits initiate. Finally, if the E_{corr} drops below the repassivation potential (E_{rp}), all pits repassivate and cease to grow. After repassivation, the corrosion of the container continues in a uniform manner at a low rate determined by the passive current density. This concept of critical potentials has been well established in the literature for pitting and crevice corrosion (Szklarska-Smialowska, 1986). Both E_p and E_{rp} are distributed values and depend on both material and environmental factors. Although two potentials, E_p and E_{rp}, are defined, in long-term prediction, E_p and E_{rp} may coincide with one critical potential (Tsujikawa et al., 1987; Thompson and Syrett, 1992). Similar parameters have been used to characterize the crevice corrosion behavior of these alloys (Okayama et al., 1987). The concept of critical potential has been applied to SCC of several alloy-environment combinations (Cragnolino and Sridhar, 1992a), but there are only limited data for the alloys and environments of interest to the Yucca Mountain (YM) repository. Other environmental degradation phenomena such as hydrogen embrittlement also depend on the E_{corr}, but do not exhibit a critical potential.

The fabrication and closure operations of the disposal packages are expected to result in redistribution of alloying elements within welds during solidification and in the heat-affected-zone (HAZ) due to precipitation of secondary phases along the grain boundaries. The precipitation of secondary phases along the grain boundaries can be further exacerbated by the long-term exposure to repository thermal conditions (aging). The effect of aging at various temperatures on corrosion (sensitization) of alloy 825 is being evaluated in the IWPE project. The aging temperatures employed thus far (800 to 600 °C) are much higher than the anticipated repository temperatures. However, the higher temperatures accelerate the kinetics of the sensitization process, thus facilitating laboratory studies within a reasonable time frame.

3.2.2 Previous Reports

The crucial questions in the measurement and use of E_{rp} are its dependence on the extent of prior pitting corrosion, measurement technique, environmental parameters, and microstructural characteristics. The research results reported previously (Cragnolino and Sridhar, 1992b; Sridhar and

Cragnolino, 1992a,b; Sridhar et al., 1993a,c; Sridhar et al., 1994c) have addressed some of these questions for pitting. To a limited extent, it was shown that E_{rp} for alloy 825 was not dependent on the pH or the concentration of species such as sulfate, bicarbonate, and silica. However, the E_{rp} was observed to decrease logarithmically with an increase in chloride concentration. It has been shown that the E_{rp} measured on polished specimens is lower (more conservative) than the potentials required to grow pits on a Cr-depleted surface (Dunn et al., 1993a,b). The effect of external potential on the changes in the chemistry of crevice solutions was examined in a previous report (Sridhar et al., 1994b). This investigation indicated the importance of critical potential on changes in crevice chemistry and provided a basis for future improvement in crevice corrosion modeling. A comparison of pitting and crevice corrosion has revealed that, for deep penetrations, both the E_{rp} and the repassivation potential for crevice corrosion, E_{rcrev}, are virtually identical and independent of increased penetration depth (Cragnolino et al., 1994b).

Studies on the effects of environmental factors and potential on the SCC of type 316L stainless steel (SS) and alloy 825 using slow strain rate and constant deflection tests were reported previously (Cragnolino et al., 1994c). The results of these tests were consistent with the assumption that E_{rp} defines a lower-bound value for the critical potential for SCC in chloride-containing environments at temperatures around 95 °C and above. However, selection of the test technique was found to be an important factor since SCC of type 316L SS was observed at lower chloride concentrations (0.028 molal) in constant-deflection tests than in slow strain rate tests. It was observed that alloy 825 is significantly more resistant to SCC than type 316L SS over a wide range (0.028–10 molal) of chloride concentrations. In slow strain rate tests, SCC of alloy 825 only occurred in 40 percent $MgCl_2$ (14 molal Cl^-) solution at 120 °C.

The effects of high temperature exposures on the intergranular corrosion susceptibility of alloy 825 in boiling 65 percent nitric acid, a standard test solution, were reported previously (Cragnolino and Sridhar, 1993). An apparent activation energy of about 290 kJ/mole was found for the sensitization of alloy 825, which is similar to the activation energy for the diffusion of Cr in an austenitic matrix.

3.2.3 Present Report

The relationship between the E_p and the initiation potential for crevice corrosion, E_{crev}, is examined in this report. The values of the E_{rp} and the E_{rcrev} obtained in short-term tests are compared to the initiation potentials measured in long-term tests. The concept of a unique potential, E_u, defined as the potential above which localized corrosion can occur and below which the material is immune from localized attack, is supported by the results of experimentally determined localized corrosion initiation and repassivation times as a function of applied potential. The results of ongoing constant-deflection (U-bend) SCC tests on type 316L SS and alloy 825 are reported and compared with data published previously. The thermal stability of alloy 825 is also addressed in this report. The basis for the sensitization kinetics, in terms of grain boundary chromium depletion in the material, is examined. Type 304L SS was used as a benchmark material in this study because of the large body of literature on this alloy. Additionally, the relationship between the results of the boiling nitric acid test and repository performance is examined in the present report. The effect of sensitization on the E_{rp} is compared with the results of boiling nitric acid tests as well as with the boiling ferric sulfate/sulfuric acid tests. The composition of precipitates formed as a result of sensitization, and the compositional profile around the sensitized grain boundaries were analyzed using a scanning transmission electron microscope (STEM) and compared to those of type 304L SS.

3.3 LONG-TERM CORROSION TESTS

3.3.1 Experimental Procedures

The validity of using E_{rp} and E_{rcrev}, obtained in short-term tests as a parameter to determine the long-term initiation of localized corrosion, was evaluated by potentiostatically polarizing test specimens to potentials above and below the repassivation potential for an extended period. In order for the E_{rp} to be a valid long-term predictor of localized corrosion, pitting or crevice corrosion should only occur when the specimen is maintained at a potential higher than this critical potential. The specimen geometries used for the localized corrosion tests allowed a comparison of pitting corrosion on polished and mill-finished surfaces. Test specimens were machined from a 12.5-mm-thick plate,

the chemical composition of which has been reported previously (Sridhar et al., 1993a). These specimens were completely immersed, exposing the crevice formed at the specimen gasket interface to the test solution. In addition, crevice corrosion on polished surfaces was investigated using a specimen geometry reported elsewhere (Cragnolino et al., 1994a). A variation of the crevice specimen incorporating the mill-finished surfaces was also used to determine the effect of the Cr-depleted layer on the initiation of crevice corrosion. Crevices were created on the specimen surfaces by bolting polytetraflouroethylene (PTFE) serrated washers to the specimens using an initial torque of 0.28 N·m (40 in.-oz). A PTFE-coated alloy C-276 bolt and nut were used along with a PTFE bushing to prevent electrical contact with the specimen. The specimens were partially immersed in the solution such that the cylindrical post was outside the solution. The rest of the experimental apparatus and procedure has been described previously (Cragnolino et al., 1994b). The results of initiation time tests were compared to the repassivation time for pitting corrosion as a function of potential and pit depth on cylindrical polished specimens. The test procedures used for measuring repassivation time have been previously reported (Sridhar and Cragnolino, 1993).

All specimens were tested in a solution containing 1,000 ppm Cl^-, 85 ppm HCO_3^-, 20 ppm SO_4^{2-}, 10 ppm NO_3^-, and 2 ppm F^- as sodium salts at 95 °C. Long-term tests conducted in 28-d intervals were carried out in closed test cells that were not deaerated. Under potentiostatic conditions, the low dissolved oxygen concentration is not expected to influence the results significantly. The test cells were equipped with either a platinum or graphite counter electrode and a saturated calomel reference electrode (SCE). The weights of all specimens were recorded prior to the start of each test interval. Specimens were potentiostatically polarized while immersed in the test solution. The current and potential were monitored throughout the course of the test. The initiation of localized corrosion was indicated by an increase in current. Following the 28-d test interval, the solution was changed, and the specimen was dried, reweighed, and examined using a 70 × stereoscope for signs of localized corrosion. Shorter tests, which typically lasted for less than 7 d, were conducted using a similar setup to measure the localized corrosion initiation time at higher potentials. These tests were terminated after the initiation of pitting or crevice corrosion was observed.

3.3.2 Results and Discussion

Short-term cyclic potentiodynamic polarization (CPP) tests have previously shown (Dunn et al., 1995) that the E_p of alloy 825 in 1,000 ppm Cl^- is greater than 600 mV_{SCE} and the E_{crev} is slightly less, approximately 500 mV_{SCE}. The repassivation potentials, E_{rp} and E_{rcrev}, were measured to be 160 mV_{SCE} and 35 mV_{SCE}, respectively. The variability of the initiation and repassivation potentials observed in CPP testing was typically 50 mV. Pitting and crevice corrosion initiation times obtained from potentiostatic tests and pitting repassivation times are plotted in Figure 3-1 as functions of applied potential for alloy 825 in a 1,000 ppm Cl^- solution at 95 °C. In this figure, the arrows indicate that either initiation, for the adjacent triangles, or repassivation, for the adjacent circles, did not occur in the range of times tested. Pitting corrosion was initiated at 600 mV_{SCE} in a time of less than 200 s as shown by the dark triangle in this figure. However, the pitting corrosion initiation time increased to times longer than 2 d at 500 mV_{SCE}. For specimens with a controlled crevice on polished surfaces, created by attaching PTFE crevice blocks to the surface with an insulated C-276 bolt, the initiation time of crevice corrosion was also observed to be dependent on the applied potential. The results of these tests, shown as the open triangles, indicate that crevice corrosion was initiated in less than 1 d for the specimen tested at 300 mV_{SCE}. As the applied potential was increased, the initiation time for crevice corrosion decreased. It may be observed from this figure that, at 500 mV_{SCE} the initiation time for crevice corrosion is much shorter than that for pitting corrosion.

The initiation of crevice corrosion at the specimen-PTFE gasket interface was previously reported for a specimen held at 200 mV_{SCE} (more than 100 mV above the repassivation potential) after 139 d of testing (Cragnolino et al., 1994b). The onset of crevice corrosion was indicated by a prolonged average current density greater than 10^{-5} A/cm^2. Significant weight loss was also observed for this specimen at the conclusion of the last test segment. On the contrary, no localized corrosion has been observed on an identical specimen tested under the same conditions for a total test time of 140 d. However, the crevice created at the specimen-PTFE gasket interface is not completely reproducible in terms of tightness or lateral depth. Hence, the lack of crevice corrosion on the duplicate specime to date is not surprising. No localized corrosion

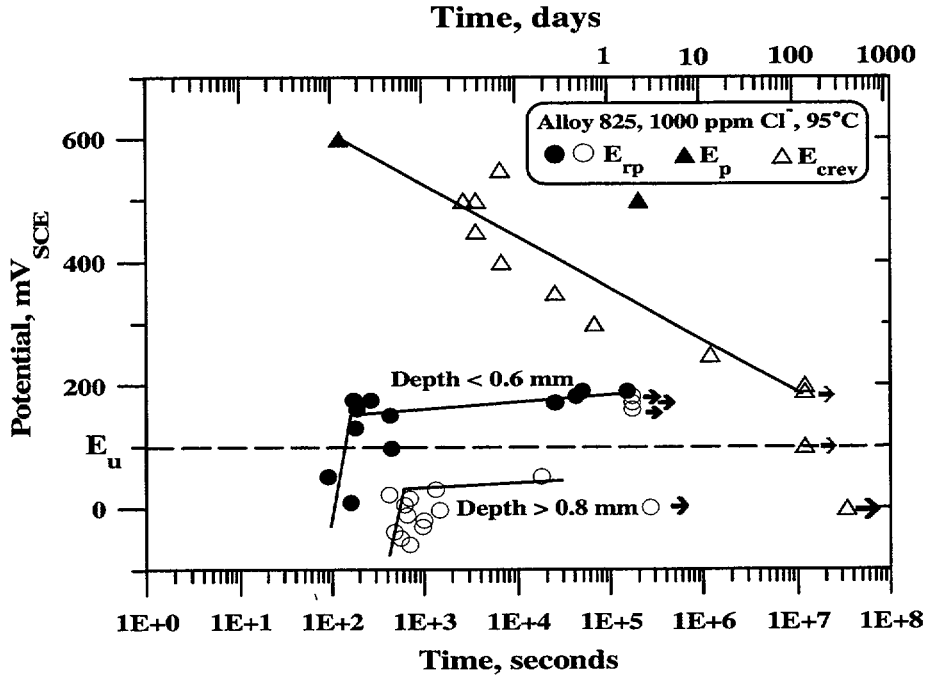

Figure 3-1. The effect of applied potential on localized corrosion initiation and repassivation kinetics of alloy 825 in 1,000 ppm Cl^- solution at 95 °C. E_u is defined as a "unique Potential" as suggested by Thompson and Syrett (1992).

has been observed on the specimens held at either 100 mV_{SCE} for a cumulative test time of 140 d or at 0 mV_{SCE} over a test time of 392 d.

The repassivation time for pits was observed to be dependent on both the depth of the pit and the applied potential. For pits less than 0.6 mm deep, shown as the dark circles in Figure 3-1, the repassivation time increased rapidly above an applied potential of 170 mV_{SCE}. At lower potentials, the repassivation time was observed to be less than 500 s. For pits deeper than 0.6 mm, represented by the open circles, the repassivation time increased above applied potentials of 20 mV_{SCE}. Below 20 mV_{SCE}, the repassivation time was in the range of 500 to 2,000 s. If repassivation is assumed to be related to the outward diffusion of Cl^-, then at potentials below the E_{rp} the repassivation time, t_r, should be (Strehblow, 1984)

$$t_r = \frac{r^2}{2D} \qquad (3\text{-}1)$$

where r is the pit radius and D is the diffusivity of chloride ion. Assuming hemispherical pits, r is the pit depth and a diffusivity of 5×10^{-6} cm^2/s, the repassivation time for pits 0.6 mm deep should be 360 s. The difference between the calculated and measured values may be a result of slight variations in the actual pit depth or to a diffusional boundary layer at the mouth of the pit, increasing the effective pit radius (Strehblow, 1984).

The chromium-depleted surface of alloy 825 was previously shown to be more susceptible to pitting than polished, bulk composition surfaces (Sridhar et al., 1993c). Crevice corrosion was observed at 200 mV_{SCE} on the creviced, mill-finished surfaces almost immediately after the start of the test. Penetration of the corrosion front through the chromium-depleted layer into the bulk material was observed after 112 d of testing. However, no crevice corrosion has been observed on the creviced, mill-finished surfaces following 140 d when the specimens were held below the repassivation potential for deep pits (0 mV_{SCE} and −100 mV_{SCE}).

The results of potentiostatic tests support previous reports that the critical potentials for localized corrosion are time dependent (Szklarska-Smialowska, 1986). Crevice corrosion that occurred preferentially to pitting corrosion was initiated at potentials as low as 200 mV_{SCE}, which was only 10 mV greater than the highest observed E_{rp} for shallow pits. It is apparent that the E_{rp} for shallow pits is neither a useful long-term predictive parameter nor a conservative estimate of the E_u which defines the lowest potential at which localized corrosion can be initiated. The E_{rp} for deep pits, which has been shown to be constant and equal to the E_{rcrev} for deep penetration depths (Cragnolino et al., 1994b), is a better estimation of the E_u and a conservative, long-term localized corrosion performance parameter.

3.4 STRESS CORROSION CRACKING STUDIES

3.4.1 Experimental Procedures

The chemical compositions of the heats of type 316L SS and alloy 825 used in this study were reported elsewhere (Cragnolino et al., 1994c). Cold-rolled and mill-annealed sheets were used for the preparation of specimens for constant-deflection tests. U-bend specimens were machined from these sheets and stressed without any heat treatment. Specimen preparation and additional experimental details have been previously reported (Cragnolino et al., 1994c). As before, two U-bend specimens were tested simultaneously in each glass cell. One of the specimens was exposed to the solution at a controlled anodic potential, whereas the second one was maintained under open-circuit conditions. In addition to the single U-bend specimens previously used, several tests were conducted using double U-bend specimens to create a crevice environment at the apex of the inner U-bend where the tensile stresses reached the highest values. To compare the behavior in the constant-deflection tests of the two heats of type 316L SS, U-bend specimens were prepared from the heat named A, which was used previously for slow strain rate tests only (Cragnolino et al., 1994c). For this purpose, specimens were machined after a piece of the 12.7-mm plate was reduced in thickness to 3.175 mm (0.125 in.).

The constant deflection tests were conducted in chloride-containing solutions similar to those used previously. Type 316L SS was tested in a solution containing 1,000 ppm chloride prepared with NaCl reagent and high purity water, with the addition of 0.01 molar $Na_2S_2O_3$. The pH of this solution was adjusted to 4.0 by the addition of HCl. Alloy 825 was tested in 40 percent $MgCl_2$ solution because this highly concentrated chloride solution (14.0 molal) was the single environment in which SCC was observed in slow strain rate tests. The temperature of the solutions were maintained constant at 95 °C during the course of the tests that were conducted in successive periods of 28 d. At the end of each period, the specimens were optically examined at about 70 × magnification. If no signs of SCC or severe localized corrosion were detected, the same specimens were exposed, using freshly prepared solutions, to identical environmental conditions for an additional time interval.

3.4.2 Results and Discussion

Table 3-1 summarizes the results of constant-deflection tests using U-bend specimens of type 316L SS in dilute chloride solutions (1,000 ppm Cl^-) containing thiosulfate at 95 °C. After 672 h (28 d) of testing, no signs of SCC were detected on the six specimens tested, including those from heat A and those with a mill-finished surface, as well as the double U-bend specimens. Only minor pitting corrosion was observed on the specimens under open-circuit conditions as well as on those under anodic overvoltage. Therefore, the same specimens were tested through a subsequent period of 28 d. In the second test period, extensive localized corrosion was observed on all the specimens, but both double U-bend specimens exhibited SCC on the inner U-bend specimen near the apex, which was located below the vapor/solution interface and, therefore, exposed to the aqueous solution. As noted in Table 3-1, some small cracks were detected on heat A specimens under the zirconia washers located above the vapor/solution interface in this test period.

New specimens were used in the third test period. All specimens were placed in an inverted position with the apex of the U-bend exposed to the environment above the vapor/solution interface. As indicated in Table 3-1, all specimens, regardless of the heat, surface finish, existence of a crevice in the double U-bend, or application of an anodic potential, experienced SCC on the apex of the U-bend, corresponding to the area at which the highest tensile stress can be expected in the outer fiber of the constant-deflection specimen. Nevertheless, SCC was

Table 3-1. Summary of U-bend test results for type 316L stainless steel in 1,000 ppm chloride solutions containing 0.01 M $Na_2S_2O_3$ at 95 °C

Specimen	E_{corr} (mV_{SCE})	$E_{applied}$ (mV_{SCE})	Current (Amps)	Initial pH	Final pH	Test time (hr)	Results
Heat A	−62 −39	O.C. O.C.	—	4.0 4.0	3.8 3.9	672 672[a]	Pitting. No sign of SCC. Localized corrosion. Small cracks.
Heat A	−66 −39	−53/−186 25/−219	$-10^{-5}/10^{-4}$ $-6.2\times10^{-5}/2.4\times10^{-4}$	4.0 4.0	3.8 3.9	672 672[a]	Pitting. No sign of SCC. Localized corrosion. Small cracks.
Mill-finish	−128 −129	O.C. O.C.	—	4.0 4.0	4.9 5.0	672 672[a]	Pitting. No sign of SCC. Localized corrosion.
Mill-finish	−147 −107	−60/−166 −98/−187	$-10^{-5}/10^{-4}$ $-7.8\times10^{-5}/1.9.4\times10^{-4}$	4.0 4.0	4.9 5.0	672 672[a]	Pitting. No sign of SCC. Localized corrosion.
Double U-bend	−228 −188	O.C. O.C.	—	4.0 4.0	5.1 6.0	672 672[a]	Pitting. No sign of SCC. SCC in inner U-bend.
Double U-bend	−163 −198	−150/−227 −142/−187	$-10^{-5}/10^{-4}$ $-2.7\times10^{-5}/1.2\times10^{4}$	4.0 4.0	5.1 6.0	672 672[a]	Pitting. No sign of SCC. SCC in inner U-bend.
Heat A Inverted	−102	O.C.	—	4.0	5.2	672	SCC and pitting on apex above V/S interface
Heat A Inverted	−136	−178/−100	$-10^{-4}/1.9\times10^{-4}$	4.0	5.2	672	SCC and pitting on apex above V/S interface
Mill-finish Inverted	−104	O.C.	—	4.0	5.1	672	SCC and pitting on apex above V/S interface
Mill-finish Inverted	−122	−159/−108	$-10^{-4}/1.7\times10^{-4}$	4.0	5.1	672	SCC and pitting on apex above V/S interface
Double U-bend Inverted	−134	O.C.	—	4.0	6.5	672	SCC on apex of inner U-bend. SCC and pitting on apex above V/S interface
Double U-bend Inverted	−121	−205/−2	$-2.7\times10^{-4}/5.4\times10^{-4}$	4.0	6.5	672	SCC on apex of inner U-bend. SCC and pitting on apex above V/S interface

O.C.: open circuit. V/S : vapor/solution [a]: Second test period after initial test period of 672 hours.

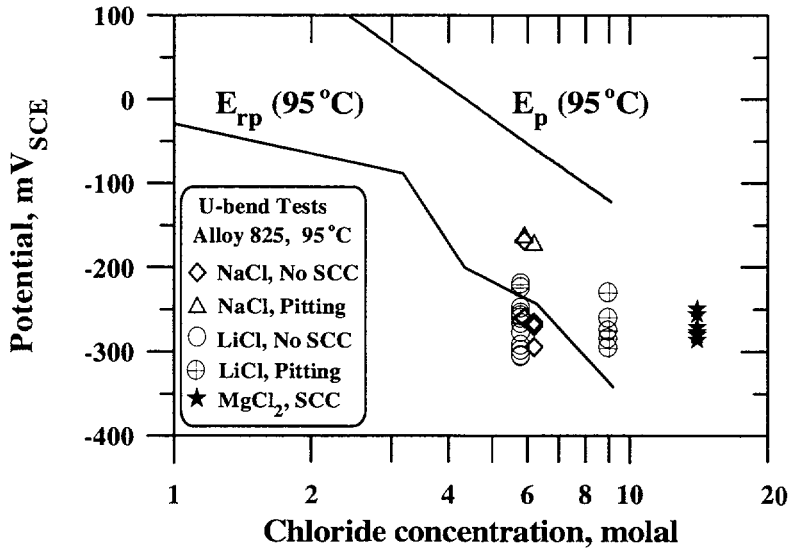

Figure 3-2. The effect of chloride concentration and potential on the stress corrosion cracking of alloy 825 in constant deflection(U-bend) tests. The E_p and E_{rp} lines were obtained separately on unstressed specimens.

accompanied by severe localized corrosion in all the specimens tested.

The results of these tests show that in dilute chloride solutions, even in the presence of thiosulfate, SCC of type 316L SS occurred predominantly above the vapor/solution interface, indicating that the local environment created as a liquid film on the specimen surface appears to be more detrimental than the bulk liquid environment. SCC was observed in specimens from both heats of material used in this study, indicating that the difference between the results of slow strain rate and constant-deflection tests reported in (Cragnolino et al., 1994c) cannot be the result of heat-to-heat variability. No detectable effect on the SCC susceptibility attributed to variations in surface finish (mill-finished versus polished and nitric acid treated surfaces) was observed.

As reported previously (Cragnolino et al., 1994c), no SCC of alloy 825 occurred, in some cases for a total testing time of 4,536 hr (189 d), in concentrated chloride solutions (pH 4.0) at 95 °C, with chloride concentrations ranging from 5.8 to 9.0 molal. However, SCC was found to occur in a more concentrated chloride solution (14 molal), using slow strain rate tests in 40 percent $MgCl_2$ at 120 °C. Since no constant-deflection tests were previously conducted in that environment, six specimens of alloy 825 were tested in 40 percent $MgCl_2$ solution at 95 °C for a total time of 2,016 hr (84 d). These specimens included those with polished and with mill-finished surfaces, as well as double U-bend specimens. All specimens were tested under both open-circuit and anodic potentials. No SCC was observed visually after two consecutive periods of 28 d, although the double U-bend specimens were not disassembled to examine the apex of the inner U-bend at a higher magnification at the end of each period. Nevertheless, localized corrosion was noted. In the third consecutive period, however, SCC and localized corrosion were observed in all the specimens tested at open-circuit or applied-anodic potentials. The potentials at which SCC was observed are plotted in Figure 3-2. Data reported earlier for less concentrated chloride solutions (Cragnolino et al., 1994c) are also included in Figure 3-2 for comparison.

The results of these constant-deflection tests confirmed previously reported results of slow strain rate tests of alloy 825. It was found that SCC occurred only in 40 percent $MgCl_2$ solution at a chloride concentration equal to 14.0 molal. This observation suggests that, for alloy 825, the results obtained in slow strain rate tests are equivalent to those of constant-deflection tests. The slow strain rate tests were conducted at 120 °C, whereas

the constant-deflection tests reported here were carried out at 95 °C. SCC was observed in slow strain rate tests after 100 to 120 hr of testing, whereas exposures to the solution for times longer than 1,300 hr were required to induce visible cracks in the constant deflection tests. The microchemical modifications associated with chromium depletion in the mill-finished surfaces (Dunn et al., 1993a,b) do not appear to enhance the susceptibility to SCC.

3.5 MATERIALS STABILITY

3.5.1 Experimental Procedure

The chemical compositions of the heats of alloy 825 and type 304L SS used in this study are shown in Table 3-2. The alloy 825 specimens (12.5-mm plate) were solution annealed at 1,200 °C for 10 min and water quenched before further heat treatment at lower temperatures. The specimens from type 304L SS plate were heat treated in the as-received condition at 621 °C for 24 hr, followed by water quenching as recommended in American Society for Testing and Materials (ASTM) G 108 (American Society for Testing and Materials, 1992). The heat-treated specimens of alloy 825 were subjected to ASTM A 262 Practice C corrosion tests in boiling 65 percent nitric acid for five 48-hr periods and A262 Practice B tests using a boiling mixture of 50 percent H_2SO_4+42 g/L $Fe_2(SO_4)_3 \cdot 4\ H_2O$ for 120 hr (American Society for Testing and Materials, 1992). The procedure for these tests is given in a previous report (Cragnolino and Sridhar, 1993). Selected specimens were also tested in a 100 ppm Cl^- solution containing 85 ppm HCO_3^-, 20 ppm SO_4^{2-}, 10 ppm NO_3^-, and 2 ppm F^- using the CPP technique. The procedure for the CPP tests has been described before (Sridhar et al., 1993a). The heat-treated type 304L SS specimens were subjected to the electrochemical potentiokinetic reactivation (EPR) test as described in ASTM G 108 (American Society for Testing and Materials, 1992). The solution used was 0.5M H_2SO_4+0.01M KSCN at 30 °C. After the corrosion tests, the specimens were examined under an optical microscope for intergranular attack. The precipitate structure and associated chromium depletion were examined using a Phillips EM420 STEM. Slices approximately 1,000 μm thick were cut from bulk specimens and polished mechanically to approximately 40 μm thickness. Discs 3 mm in diameter were punched from these slices and further thinned in a jet electrochemical polisher until a small perforation was detected. The area around the perforation is transparent enough to electrons to perform microscopy.

Several jet-polishing solutions were used in this investigation. The commonly used solution of 80 mL $HClO_4$+180 mL $HOCH_2CH_2OH$+300 mL CH_3OH did not yield a large, thin area for analysis. Subsequent analyses were conducted on specimens polished in 15 percent HNO_3+CH_3OH, with a typical voltage of 14 V and current of 30 mA.

The quantitative x-ray microanalyses were carried out using a 20-nm electron beam diameter. The instrument is capable of going down to a 1-nm probe size, however, the problems of beam location and low x-ray intensities resulted in a lower limit of 2-nm probe size. The x-ray intensities were converted to concentration of species using the Cliff-Lorimer procedure (Goldstein and Williams, 1981). In this procedure, the ratio of concentration of species is assumed to be proportional to the ratio of their x-ray intensities; x-ray fluorescence and absorption are assumed to be negligible due to the thinness of the sample. This relationship is expressed as:

$$\frac{C_{Cr}}{C_{Ni}} = k_{CrNi}\left(\frac{I_{Cr}}{I_{Ni}}\right) \qquad (3\text{-}2)$$

where C_{Cr} and C_{Ni} refer to the concentrations of Cr and Ni respectively, and I_{Cr} and I_{Ni} refer to their respective x-ray intensities. The factor, k_{CrNi}, is calculated by conducting the analysis at a location remote from the grain boundary and using the known bulk chemical composition of the alloy. Since Ni is a major alloying element in alloy 825, it was used as the basis for calculating other alloying elements. For type 304L SS, Fe was used as the basis for calculating the concentrations of the other alloying elements. The errors associated with the Cliff-Lorimer procedure have been discussed by Goldstein and Williams (1981). Their method of estimating the errors (2σ confidence limits) on the calculated composition consists of adding the relative errors of k and I values in Eq. (3-2). Because of the Gaussian nature of the x-ray intensities, the relative errors of the measured intensities are assumed to be proportional to $2(I)^{-0.5}$. In the present study, the root mean squares of all the relative errors are used, as shown in Eq. (3-3), rather than the sum of the relative errors (Coleman and Steele, 1989)

Table 3-2. Bulk chemical compositions of alloy 825 and type 304L SS in weight percent as reported by the vendor. Minor elements are not shown in this table.

Alloy and Heat No.	C	Cr	Fe	Mo	Ni	Ti
Alloy 825 HH4371FG	0.01	22.09	30.41	3.21	41.06	0.82
Type 304L SS T0954	0.022	18.27	70.54	—	9.14	—

$$\varepsilon_{Cr} = \{ (\varepsilon_k)^2 + (\varepsilon_{I_{Ni}})^2 + (\varepsilon_{I_{Cr}})^2 \}^{0.5} \quad (3\text{-}3)$$

where the ε values are the relative errors (95 percent confidence interval/average value) of the various terms in Eq. (3-2) and the error in the matrix Ni concentration, which is used to normalize the other concentrations, is ignored. In Eq. (3-3), k is not a directly measured quantity, but is calculated from analyses of the matrix far from the grain boundaries, in both sensitized and solution-annealed specimens. Based on a number of measurements on alloy 825, the 2σ relative error in k_{Cr} is about 2.8 percent. Using Eq. (3-3), the relative error in Cr concentration was calculated to be about 15 percent. Generally, however, the error calculated by Eq. (3-3) is larger than the errors estimated from replicate measurements of the same specimen (Hall and Briant, 1984). In the present work, the errors in the concentration of the alloying elements measured by energy dispersive x-ray spectroscopy (EDS) were calculated as the 95 percent confidence interval/average value of 4 to 12 measurements instead of using Eq. (3-3).

3.5.2 Results

3.5.2.1 Corrosion Tests

The results of intergranular corrosion tests in boiling 50 percent H_2SO_4+42 g/L $Fe_2(SO_4)_3 \cdot 4\ H_2O$ and 65 percent nitric acid test solutions are shown in Figure 3-3 for solution annealed and aged specimens. It can be seen that the nitric acid test is more sensitive to the grain boundary precipitation than the ferric sulfate test. These differences are the result of the different sensitivities of these tests to grain boundary chemistry, as discussed by Streicher (1978). The ferric sulfate test is sensitive to the extent of the chromium-depleted region, both its microstructural width and the minimum Cr concentration. In contrast, the nitric acid test is sensitive to both the Cr depletion and the presence of Cr^{6+}. It has been shown (Streicher, 1978) that in nitric acid solutions containing Cr^{6+}, the higher Cr-containing phases demonstrate higher rates of corrosion. If the grain boundary region has a small Cr depletion, preferential corrosion occurs initially in this region in the nitric acid. However, once sufficient Cr^{6+} is generated in this corroded-region then accelerated corrosion occurs in the grain boundary where there is a higher Cr phase. The accumulation of Cr^{6+} within pits created by the dissolution of TiC particles has been shown to accelerate the corrosion of even nonsensitized SSs (Streicher, 1978). Hence, the observed differences in the corrosion rates of aged alloy 825 to nitric acid and ferric sulfate is indicative of a very narrow region of Cr depletion in this alloy. This finding is in accordance with previous results of Brown (1969) on alloy 825 with a much higher carbon (0.03 percent) and slightly lower Cr (21.24 percent) concentration.

The disadvantages of the nitric acid test are that the test takes 10 d to conduct, and large amounts of waste acid are created. Also, the data obtained are in terms of average weight loss and are not direct measures of the degree of sensitization. Hence, alternative tests were explored. The EPR test has become an accepted test for detecting sensitization of type 304L SS (American Society for Testing and Materials, 1992). This test, with some modifications, has also been used for type 316L SS, duplex SSs, and some Ni-base alloys such as alloys 600 and 800. Therefore, this alternative test was explored at the Center for Nuclear Waste Regulatory Analyses (CNWRA). Initial benchmark tests using type 304L SS aged at 621 °C for 24 hr were conducted and yielded results in reasonable agreement with the results of round-robin tests published in ASTM standards. However, when the same procedures were applied to alloy 825, solution annealed and aged at 750 °C for 15 hr, no sensitization was detected.

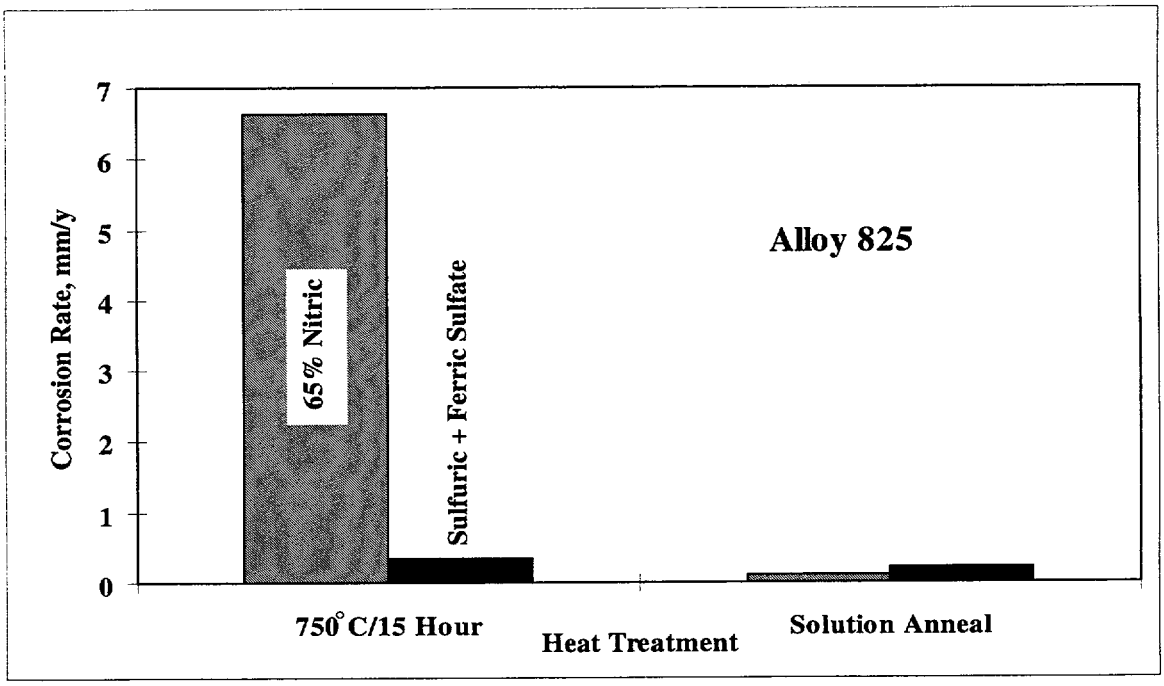

Figure 3-3. A comparison of the corrosion rates of sensitized and solution annealed alloy 825 in boiling 65% nitric acid and boiling 50% H_2SO_4 + 42 g/L $Fe_2(SO_4)_3$ • 4 H2O. Both tests were conducted on speciments obtained from the unstressed portions of U-bend samples.

Additional tests using more concentrated sulfuric acid, higher temperatures, or higher concentrations of thiocyanate did not yield useful results in terms of detecting sensitization in alloy 825.

The effect of sensitization on localized corrosion was examined using CPP tests conducted in simulated groundwater solutions containing a range of chloride concentrations. CPP tests conducted in a solution containing 100 ppm chloride at 95 °C were found to be sensitive to grain boundary precipitation. The correlation between the nitric acid test results and the repassivation potential, E_{rp}, is shown in Figure 3-4. The E_{rp} values were derived from tests in which pitting was initiated at high potentials. Heat treatment conditions that led to a high corrosion rate in 65 percent HNO_3 also resulted in a lower E_{rp}. The specimens that, whereas the nonsensitized specimens showed random pitting, mainly in the grain interior. It is also important to note that the E_{rp} for mill-annealed material is lower than that for the solution-annealed material, whereas the nitric acid test indicates no significant difference. The mill-annealed microstructure still has some intragranular and intergranular precipitates, which are a combination of TiC and $M_{23}C_6$, whereas the solution annealing essentially dissolves all the precipitates (Raymond, 1968; Shaikh et al., 1992). These microstructural features are discussed later. The decrease in E_{rp} with sensitization was observed only in the 100 ppm Cl^- solution and also only when the polarization scan reached very high potentials (above 1 V_{SCE}). If pits were initiated potentiostatically at 800 mV_{SCE}, no significant effect on E_{rp} was observed.

3.5.2.2 Analytical Electron Microscopy

As discussed previously, the differences in the sensitivity of the nitric acid and ferric sulfate tests have been attributed to formation of sigma phase (Streicher, 1978). Segregation of impurity elements such as phosphorus has also been shown to increase the corrosion rate in nitric acid (Briant, 1987). In this study, electron diffraction patterns of grain boundary precipitates in alloy 825 for various aging conditions did not indicate the presence of sigma phase. As shown in

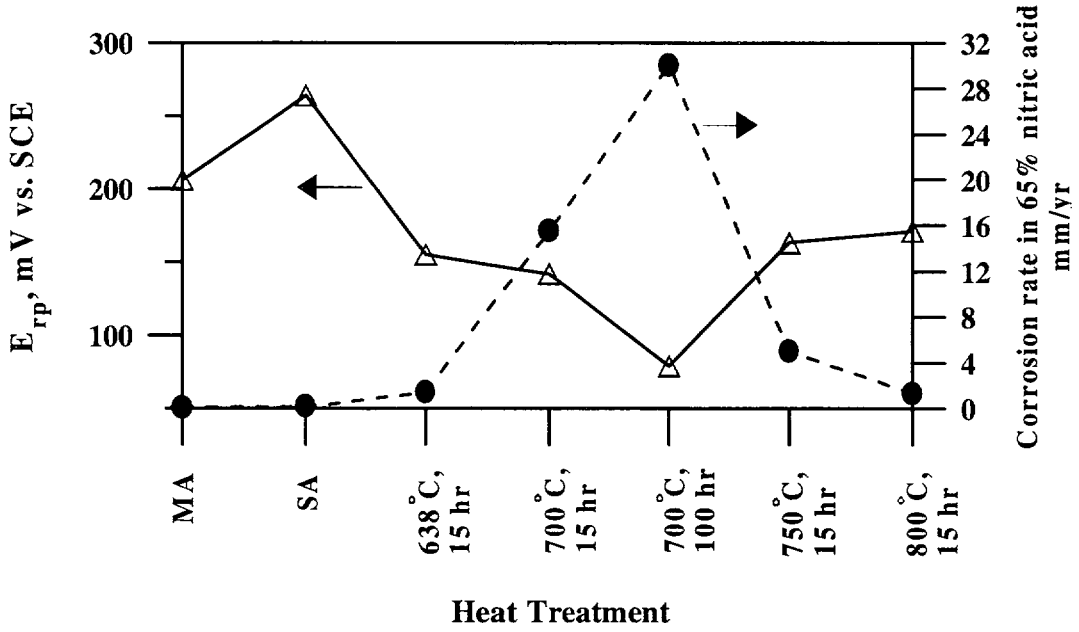

Figure 3-4. A comparison of the repassivation potential measured in a 100 ppm Cl solution at 95 °C, shown as triangles, (scan rate: 0.167 mV/sec) and the corrosion rate in boiling 65% nitric acid, shown as circles, of variously heat-treated alloy 825

Figures 3-5 and 3-6, only $M_{23}C_6$-type carbides were observed.

The chromium depletion near the grain boundary was measured using the EDS analysis capability of the STEM. The location of the probe with respect to the grain boundary is indicated in Figure 3-6 by arrows T and B that are used to differentiate between analyses on either side of this boundary. In order to gain confidence in the analytical procedure, type 304L SS, aged in the as-received condition at 621 °C for 24 hr, was analyzed prior to analyzing alloy 825.

Electron diffraction patterns showed the grain boundary precipitate in type 304L SS to be $M_{23}C_6$ carbide, which is consistent with the literature (e.g., Mulford et al., 1983). The grain-boundary carbide composition in type 304L SS is shown in Table 3-3. While the Cr content of the carbide is relatively high (about 42 weight percent), it is lower than the Cr concentration reported in the literature for other alloys (Table 3-3). Additionally, the concentrations of Fe and Ni in the grain boundary carbide were higher than reported in the literature. This is especially true for alloy 825 where very high Ni content was found in the carbide on specimens electropolished in a HNO_3+CH_3OH mixture at high anodic potentials. This particular electropolishing procedure may have led to preferential dissolution of Cr in the transpassive regime and a resultant enrichment of Ni and Fe. An analysis conducted on a specimen of alloy 825 polished in $HClO_4$+CH_3OH mixture confirms this hypothesis. As shown in Table 3-3, the carbide in the specimen polished in perchloric acid mixture showed a much higher Cr content and lower Ni content, which is consistent with most of the literature. Another contributing factor for the lower Cr content of most of the carbides analyzed in the present study may be matrix dilution. In one case in which the edge of a carbide particle was probed, the Cr content was considerably lower than indicated in Table 3-3.

The associated Cr profile on either side of the grain boundary between two carbide particles is shown in Figure 3-7. The Cr concentration near the grain boundary dips to about 13 weight percent, which is consistent with the literature (Mulford et al., 1983). The minimum value would be expected to be lower if the analysis were taken closer to one of the carbide particles, rather than in between the particles. The EDS Cr profiles near the grain boundary for two different heat treatments of alloy 825 are shown in Figure 3-8 in comparison to the Cr profile on a solution-annealed

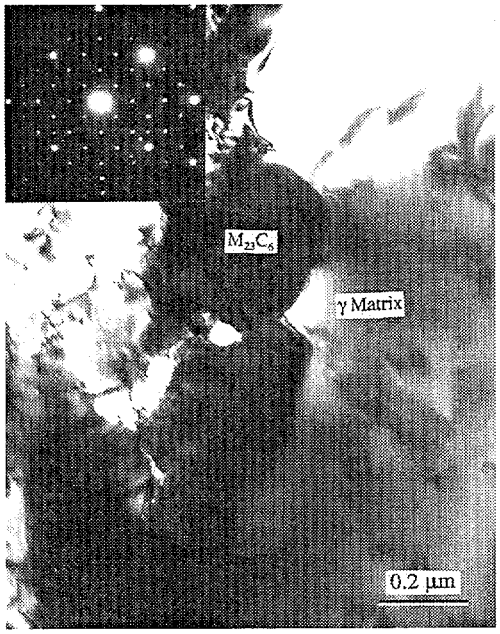

Figure 3-5. Bright-field transmission electron microscope (TEM) image of alloy 825 solution annealed and aged at 750 °C for 15 hr. Also shown in the inset is the selected area diffraction pattern of the austenite grain in the [001] zone axis and the grain boundary carbide oriented in the [001] zone axis.

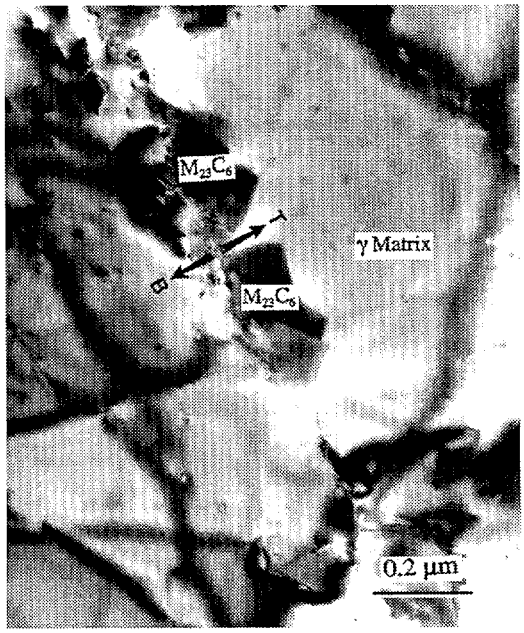

Figure 3-6. Bright field TEM image of alloy 825 solution annealed and aged at 750 °C for 15 hr showing the nanoprobe analysis area. The incident electron beam diameter was 20 nm. T and B indicate nanoprobe location for analysis on either side of the grain boundary.

Table 3-3. Chemical composition of grain boundary carbides determined in the present study in comparison to literature findings. The ± sign indicates the 95-percent confidence interval based on replicate measurements.

Alloy (Carbide)	Fe (wt%)	Ni (wt%)	Cr (wt%)	Reference
304L SS ($M_{23}C_6$)	48.3±7.3	7.1±0.7	42.5±5.8	Present work (nitric + methanol polish)
alloy 825($M_{23}C_6$)	28.3±0.9	39.4±2.3	32.3±3.1	Present work (nitric + methanol polish)
alloy 825($M_{23}C_6$)	10.5±1.8	10.3±2.2	70.9±3.96	Present work (perchloric + methanol polish)
316LN ($M_{23}C_6$)	19	3	65	Hall and Briant, 1984
alloy 690 ($M_{23}C_6$)	2.1	7.7	88.5	Angeliu and Was, 1990
17Cr-12Ni SS ($M_{23}C_6$)	21.2	3.3	74.1	Thorvaldsson et al., 1981
In 939 ($M_{23}C_6$)	—	—	98.2	Smith et al., 1981
316LN	17.3	2.3	63.1	Mulford et al., 1983
308 SS	—	4	75	Chen et al., 1990
Nimonic 80 ($M_{23}C_6$)	—	6.1	88.4	Voice and Faulkner, 1985

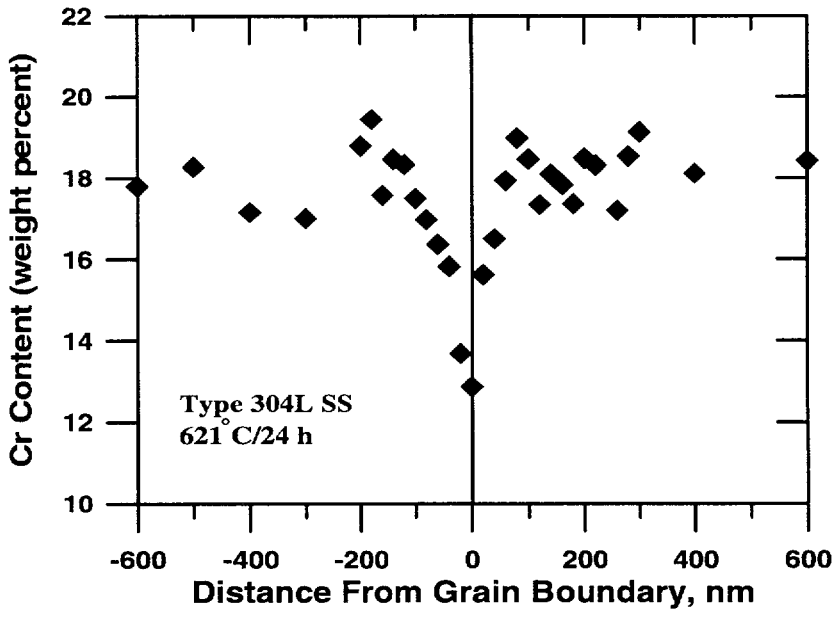

Figure 3-7. Chromium concentration profile near one of the grain boundaries in type 304L SS containing $M_{23}C_6$ carbides. Specimen aged at 621 °C for 24 hours. The calculated 95 percent-confidence interval is ±2%. Incident electron beam was 20 nm in diameter.

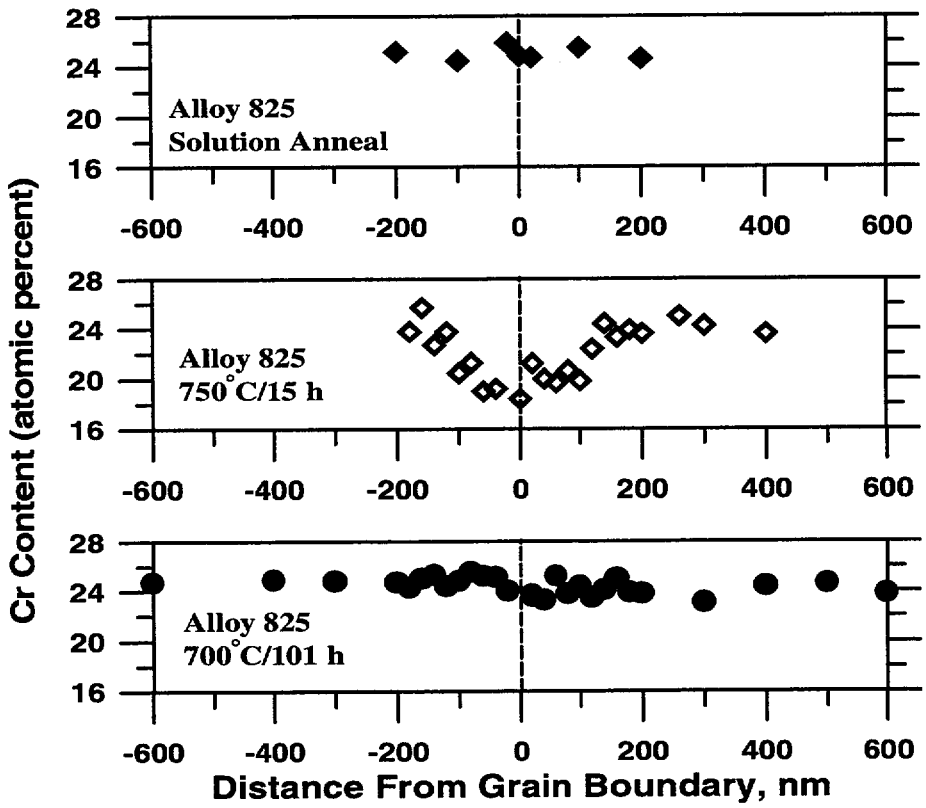

Figure 3-8. Chromium concentration profile across a grain boundary of alloy 825 containing $M_{23}C_6$ carbides for the two different aged specimens and no precipitates in the solution-annealed condition. The incident electron beam diameter was 20 nm.

material. It can be seen that the extent of Cr depletion for alloy 825 is considerably less than that for type 304L SS. Surprisingly, the 750 °C aged specimen showed a lower Cr concentration near the grain boundary than the 700 °C aged specimen. Preliminary analysis indicates that the Cr profile near the grain boundary is not significantly affected by the polishing procedure, unlike the carbide analysis. However, this finding needs to be further verified.

3.5.3 Discussion

Both the corrosion tests and the analytical electron microscopy results suggest that there is a significant Cr depletion near the grain boundaries in sensitized type 304L SS, but not so in sensitized alloy 825. The high corrosion rates measured for the sensitized alloy 825 are, more probably, due to the high Cr phase in the grain boundary rather than Cr depletion near the grain boundary. This supposition is further strengthened by other experimental observations. The ferric sulfate test, which is sensitive to Cr depletion but not to high Cr phase, did not show high corrosion rate. The EPR test, which has been successfully employed for other SSs and Ni-base alloys such as alloy 600, did not indicate grain boundary sensitization in alloy 825. On the other hand, the repassivation potential, which has been shown to depend on surface Cr depletion (Dunn et al., 1993a,b), decreased with sensitization. This decrease was observed only when the pitting was initiated at very high potentials (over 1 V_{SCE}), well in the transpassive dissolution regime. It is possible that the Cr-depleted region is very narrow and beyond the resolution of the 20-nm probe. A nanoprobe analysis using a 1-nm probe was conducted and did not find any significant depletion of Cr. However, the analysis is inconclusive because the x-ray intensities are very low,

resulting in large uncertainties. Hence, the grain boundary composition changes in alloy 825 due to carbide precipitation need to be understood better in order to quantify the degree of sensitization in alloy 825 as a function of thermal exposure.

The phenomenon of sensitization induced by Cr depletion is controlled by both thermodynamic and kinetic factors. Quantitative modeling of these factors to predict the degree of sensitization of a given alloy exposed to a given thermal cycle has been discussed in relation to the SSs (Bruemmer, 1990; Fullman, 1982) and Ni-base alloys (Was and Kruger, 1985). A brief description of the considerations involved in the quantitative prediction of sensitization follows. Under equilibrium conditions, the formation of $M_{23}C_6$ can be represented by

$$23M + 6C \Leftrightarrow M_{23}C_6 \tag{3-4}$$

and the equilibrium constant for the reaction is given by

$$K = \frac{1}{(\gamma_C X_C)^6 (\gamma_{Cr} X_{Cr})^{23}} \tag{3-5}$$

where M is assumed to be essentially 100 percent Cr; K is the equilibrium constant for the reaction given in Eq. (3-4); and γ_C, X_C and γ_{Cr}, X_{Cr} are the activity coefficients and concentrations of carbon and chromium in the solid solution, respectively. The activity coefficient of carbon has been determined as a function of alloying elements, and it is generally assumed that the activity of carbon becomes equal throughout the matrix because its diffusion rate is about ten orders of magnitude greater in comparison to Cr (Bruemmer, 1990). Hence, the equilibrium concentration of Cr at the carbide-matrix interface can be determined if the equilibrium constant and activity coefficient of Cr are known as functions of temperature and alloying element. While the equilibrium constant is reasonably well established in Fe-Cr-Ni-C systems as a function of temperature, the γ_{Cr} dependence on alloying element and temperature is known only for some ranges of composition (Bruemmer, 1990; Was and Kruger, 1985; Hillert and Qui, 1991). Current experimental evidence and review of the Fe-Ni-Cr-C system thermodynamics (Hillert and Qui, 1991) indicate that the concentration of Cr in equilibrium with $M_{23}C_6$ is higher than that with M_7C_3, but is considerably lower than that found as the interfacial Cr concentration in alloy 825. Since Ni is not very soluble in $M_{23}C_6$, it is not expected to affect the concentration of Cr in equilibrium with the carbide (Bruemmer, 1990; Hillert and Qui, 1991). Hence, under equilibrium considerations, a much lower Cr is expected at the carbide-matrix interface in sensitized alloy 825. It is also surprising that a lower interfacial Cr concentration was observed at 750 °C than at 700 °C, whereas the opposite would be expected under equilibrium conditions (Bruemmer, 1990).

The change in the Cr concentration with time and distance from the grain boundaries is determined by

$$\frac{dC_{Cr}}{dt} = D_{Cr}\nabla^2 C_{Cr} \tag{3-6}$$

where the C_{Cr} is the concentration and D_{Cr} is the diffusion coefficient of Cr. For simplicity, the diffusion of other species such as C and Ni is not considered above, although this must occur in a multicomponent system. Finite difference-based modeling has been performed to calculate the Cr-concentration profile as a function of time and temperature (Was and Kruger, 1985), and these calculations indicate that the width of the Cr-depletion profile at 700 °C in Ni-base alloys such as alloy 600, which precipitates M_7C_3-type carbides, is more than 1,000 nm. While the depletion width and depth for the $M_{23}C_6$ is expected to be smaller (Bruemmer, 1990), the lack of Cr depletion in the present study on alloy 825 is puzzling. Electropolishing in nitric acid may tend to lessen the Cr gradient because the higher Cr regions dissolve faster and selectively leach Cr. However, preliminary analysis of alloy 825 did not indicate any significant difference in the Cr-depletion profile between using the $HClO_4$+CH_3OH polishing solution and the HNO_3+CH_3OH solution. Further analysis is in progress.

3.6 CONCLUSIONS

The initiation potential for localized corrosion decreases and approaches the repassivation potential during prolonged exposures. Long-term performance predictions using the initiation potentials measured in short-term tests may significantly overestimate the lifetime of high-level nuclear waste containers in a potentially corrosive environment. The repassivation potential for localized corrosion tends to increase with time and is unaffected by the presence of near-surface imperfections and compositional variations. The repassivation potential for deep pits and crevices is a

conservative value that can be obtained in relatively short-term tests and is the most appropriate parameter for predicting the long-term container performance.

The present results confirm the applicability of critical potentials for localized corrosion for predicting SCC, but the occurrence of this phenomenon is dependent on test technique in the case of type 316L SS. In this material, cracking in dilute chloride solutions under constant-deflection conditions occurs predominantly above the vapor/solution interface after prolonged exposure time (>1,000 hr), suggesting that concentration of the solution in a thin-liquid film formed on the metal surface is more detrimental than the bulk environment.

For alloy 825, SCC only occurs in highly concentrated chloride solutions, in which the chloride concentration is equal to 14.0 molal, in either slow strain rate or constant-deflection tests. Only very prolonged tests, in which heat transfer devices can be used to introduce the influence of heat transfer in addition to chloride concentration effects, may provide an answer to the question of susceptibility to SCC in the presence of chloride salts (e.g., NaCl) that can be expected under repository conditions. It should be noted that the maximum chloride concentration than can be attained in this case is approximately 6 molal.

The corrosion tests indicate that increased corrosion rate of sensitized alloy 825 occurs mainly in the nitric acid test, which is sensitive to the high-Cr phase formed on the grain boundaries and not to Cr depletion. Increased corrosion was not observed in the sulfuric acid + ferric sulfate test, which is sensitive to Cr depletion. The EPR test is not sensitive to intergranular precipitation in alloy 825, unlike the case for type 304L SS. On the other hand, the repassivation potential measured by the CPP test in a 100 ppm chloride solution at 95 °C is sensitive to precipitation and correlates well with the nitric acid test results. At higher chloride concentrations, the E_{rp} is no longer sensitive to precipitation in alloy 825.

In order to predict whether sensitization and increased susceptibility to localized corrosion or stress corrosion cracking can occur for alloy 825 in the long time periods, the mechanism of sensitization must be understood. The analytical microscopy conducted thus far on alloy 825 indicates that a high-Cr $M_{23}C_6$-type carbide precipitates during thermal treatment of the alloy, but no significant Cr depletion is associated with it. In contrast, type 304L SS shows a significant Cr depletion near the grain boundary upon sensitization, which is consistent with the literature.

3.7 PROGRESS TOWARD MEETING PROJECT OBJECTIVES

The approach that is currently being used in waste package performance assessment (Cragnolino et al., 1994a) involves a single critical potential with an associated range for all three localized degradation modes: pitting, crevice corrosion, and SCC. The experimental results reported thus far indicate that, at least for pitting and crevice corrosion, this assumption is viable. The E_{rp} from short-term tests is conservative and may be used as a lower bound parameter for predicting the long-term initiation of localized corrosion.

Constant deflection tests were used to confirm that slow strain rate tests are not appropriate to evaluate the SCC resistance of type 316L SS in dilute chloride solutions. Differences previously observed cannot be the result of heat-to-heat variability. The superior resistance to SCC of alloy 825 was confirmed through both slow strain rate and constant-deflection tests, which are entirely consistent in the case of this alloy.

The experimental approach used in Task 3 in assessing the sensitization of alloy 825 is consistent with mechanistic models developed for sensitization and parameters developed for long-term prediction of localized corrosion, E_{rp}. Thus far, the experimental results have shown that alloy 825 is highly resistant to sensitization by Cr depletion. The corrosion tests seem to be consistent with analytical electron microscopy findings. The analytical studies have confirmed the precipitation of $M_{23}C_6$-type carbides in this alloy, but no significant Cr depletion has been detected. On the other hand, confidence in the analytical procedure has been gained by the results on type 304L SS, which are consistent with literature results. The lack of Cr depletion in alloy 825 is puzzling, however, and needs further analysis.

3.8 PLANS FOR THE NEXT REPORTING PERIOD

The IWPE project will be concluded at the end of FY95. A project final report has been planned for delivery in May 1995, followed by an external peer

review of the report. The peer review panel selection process is underway, and final selection of the panelists will be concluded in the next reporting period. After the peer review of the report, a workshop to discuss future areas of research in waste-package performance has been planned. The workshop, as well as previous reports on alternate container materials/designs, will result in specific recommendations for future research.

One area of continuing activity beyond FY95 will be the long-term testing to gain confidence in the methodologies employed for extrapolating short-term data to long-term prediction. Long-term tests under controlled potentials, anticipated to continue for time periods ranging from a few months to 5 yr, are necessary to verify several of the concepts discussed previously. These tests, which are continuing, will verify whether the E_{rp} for deep pits is a conservative parameter for predicting pit initiation and repassivation for all surface conditions. Tests with creviced specimens under potentiostatic control will also be continued to verify if the E_{rp} for deep pits can be used to predict initiation and repassivation of crevice corrosion. In conjunction with these controlled-potential tests, tests under naturally aerated conditions will also be conducted in which the E_{corr} will be monitored. Results of these tests will be reported in future semi-annual reports.

Using a fracture mechanics approach, pre-cracked specimens will be used in the next reporting period to determine the validity of the repassivation potential as critical potential for SCC of type 316L SS in chloride solutions. Both the threshold stress intensity and the critical potential for arresting a propagating crack are expected to be determined using this approach. Long-term SCC tests will be continued for periods extending from a few months to several years.

In order to understand the long-term behavior of container materials, their microstructural changes as a result of thermal exposure need to be understood. These studies are being performed for alloy 825 in Task 3. As part of this task, methods to quantify the grain boundary sensitization of alloy 825 are being developed. While such test techniques exist for SS such as type 304L, no method for rapidly and sensitively estimating grain boundary chromium depletion of alloy 825 exists. The results from these studies will be presented in the next semi-annual report as a basis for further studies in this area and will be applied to the evaluation of the effect of thermal treatments on SCC.

3.9 REFERENCES

Abraham, T., H. Jain, and P. Soo. 1986. *Stress Corrosion Cracking Tests on High-Level Waste Container Materials in Simulated Tuff Repository.* NUREG/CR-4619. Washington, DC: Nuclear Regulatory Commission.

Angeliu, T.M., and G.S. Was. 1990. Grain boundary chemistry and precipitation in controlled purity alloy 690. *Environmental Degradation of Materials in Nuclear Power Systems-Water Reactions.* D. Cubicciotti, ed. Houston, TX: NACE International: 5-64–5-78

ASTM. 1992. Standard V.03.02. Wear and erosion: Metal corrosion. *Annual Book of ASTM Standards.* Philadelphia, PA: American Society for Testing and Materials.

Beavers, J.A., N.G. Thompson, and C.L. Durr. 1992. *Pitting, Galvanic, and Long-Term Corrosion Studies on Candidate Container Alloys for the Tuff Repository.* NUREG/CR-5709. Washington, DC: Nuclear Regulatory Commission.

Briant, C.L. 1987. Grain boundary segregation of phosphorus and sulfur in types 304L and 316L stainless steel and its effect on intergranular corrosion in the Huey test. *Metallurgical Transactions* 18A: 691–699.

Brown, M.H. 1969. The relationship of heat treatment to the corrosion resistance of stainless alloys. *Corrosion* 25(11): 438–443.

Bruemmer, S.M. 1990. Quantitative modeling of sensitization development in austenitic stainless steel. *Corrosion* 46(9): 698–709.

Buscheck, T.A., D.G. Wilder, and J.J. Nitao. 1993. Large-scale *in situ* heater tests for hydrothermal characterization at Yucca Mountain. *Proceedings of the Fourth Annual International High-Level Radioactive Waste Management Conference.* La Grange Park, IL: American Nuclear Society: 1,854–1,872.

Chen, J-S, V. Radmilovic, and T.M. Devine. 1990. A comparison of the chromium concentration on grain boundaries in sensitized stainless steel measured by analytical electron microscopy and an electrochemical technique. *Corrosion Science* 30(4/5): 477–494.

Coleman, H.W., and W.G. Steele, Jr. 1989. *Experimentation and Uncertainty Analysis for Engineers.* New York City, NY: John Wiley & Sons.

Cragnolino, G.A., and N. Sridhar. 1992a. *A Review of Stress Corrosion Cracking of High-Level Nuclear Waste Container Materials—I.* CNWRA 92-021. San Antonio, TX: Center for Nuclear Waste Regulatory Analyses.

Cragnolino, G.A., and N. Sridhar. 1992b. Integrated waste package experiments. *NRC High-Level Radioactive Waste Research at CNWRA January–June 1992.* W.C. Patrick, ed. CNWRA 92-01S. San Antonio, TX: Center for Nuclear Waste Regulatory Analyses.

Cragnolino, G.A., and N. Sridhar. 1993. *Long-Term Stability of High-Level Nuclear Waste Container Materials: I–Thermal Stability of Alloy 825.* CNWRA 93-003. San Antonio, TX: Center for Nuclear Waste Regulatory Analyses.

Cragnolino, G.A., N. Sridhar, J. Walton, R. Janetzke, J. Wu, and P. Nair. 1994a. *Substantially Complete Containment—Example Analysis of a Reference Container.* CNWRA 94-003. San Antonio, TX: Center for Nuclear Waste Regulatory Analyses.

Cragnolino, G.A., N. Sridhar, and D. Dunn. 1994b. *Integrated waste package experiments. NRC High-Level Radioactive Waste Research at CNWRA January–June 1994.* B. Sagar, ed. CNWRA 94-01S. San Antonio, TX: Center for Nuclear Waste Regulatory Analyses.

Cragnolino, G.A., D. Dunn, and N. Sridhar. 1994c. *Environmental Effects on Stress Corrosion Cracking of Type 316L Stainless Steel and Alloy 825 as High-Level Nuclear Waste Container Materials.* CNWRA 94-028. San Antonio, TX: Center for Nuclear Waste Regulatory Analyses.

Doering, T.W. 1993. Robust waste package concept (multibarrier). *Proceedings of the Fourth Annual International High-Level Radioactive Waste Management Conference.* La Grange Park, IL: American Nuclear Society: 551–557.

Dunn, D.S., N. Sridhar, and G.A. Cragnolino. 1993a. The effect of surface conditions on the localized corrosion of a candidate high-level waste container material. Corrosion control for low-cost reliability. *Proceedings of the Twelfth International Corrosion Congress.* Houston, TX: NACE International: 5B: 4,021–4,030.

Dunn, D.S., N. Sridhar, and G.A. Cragnolino. 1993b. Effects of surface conditions on the localized corrosion of alloy 825 high-level waste container *'94.* Houston, TX: NACE International.

Dunn, D.S., N. Sridhar, and G.A. Cragnolino. 1995. Long-term prediction of localized corrosion of alloy 825 in high-level nuclear waste repository environments. Paper No. 95-423. *Corrosion '95.* Houston, TX: NACE International.

Farmer, J.C., G.E. Gdowski, R.D. McCright, and H.S. Ahluwalia. 1991. Corrosion models for performance assessment of high-level radioactive waste containers. *Nuclear Engineering and Design* 129: 57–88.

Fullman, R.L. 1982. A thermodynamic model of the effects of composition on the susceptibility of austenitic stainless steels to intergranular stress corrosion cracking. *Acta Metallurgica* 30: 1,407–1,415.

Goldstein, J.L., and D.B. Williams. 1981. X-ray microanalysis of thin specimens. *Quantitative Microanalysis with High Spatial Resolution.* G.W. Lorimer et al., eds. London, U.K.: The Metals Society: 5–14.

Hall, E.L., and C.L. Briant. 1984. Chromium depletion in the vicinity of carbides in sensitized austenitic stainless steels. *Metallurgical Transactions* 15A: 793–811.

Hillert, M., and C. Qui. 1991. A thermodynamic assessment of the Fe-Ni-Cr-C system. *Metallurgical Transactions* 22A: 2,187–2,198.

Macdonald, D.D., and M. Urquidi-Macdonald. 1990. Thin-layer mixed-potential model for corrosion of high-level nuclear waste canisters. *Corrosion* 46(5): 380–390.

Mulford, R.A., E.L. Hall, and C.L. Briant. 1983. Sensitization of austenitic stainless steels II. Commercial purity alloys. *Corrosion* 39(4): 132–1, and R.T. Pabalan. 1994. *Geochemical Investigations Related to the Yucca Mountain Environment and Potential Nuclear Waste Repository.* CNWRA 94-006. San Antonio, TX: Center for Nuclear Waste Regulatory Analyses.

Nuclear Regulatory Commission. 1994. *License Application Review Plan for a Geologic Repository for Spent Nuclear Fuel and High-Level Radioactive Waste, Draft Review Plan.* NUREG-1323 Rev 0. Washington, DC: Nuclear Regulatory Commission.

Okayama, S., Y. Uesugi, and S. Tsujikawa. 1987. The effect of alloying elements on the repassivation potential for crevice corrosion of stainless steels in 3% NaCl solution. *Corrosion Engineering* 36: 157–168.

Patrick, W.C. 1986. *Spent Fuel Test—Climax: An Evaluation of the Technical Feasibility of Geologic Storage of Spent Nuclear Fuel in Granite.* Final Report. UCRL-53702. Livermore, CA: Lawrence Livermore National Laboratory.

Ramirez, A.L., ed. 1991. *Prototype Engineered Barrier System Field Test (PEBSFT).* Final Report UCRL-ID-106159. Livermore, CA: Lawrence Livermore National Laboratory.

Raymond, E.L. 1968. Mechanism of sensitization and stabilization of Incoloy nickel-iron-chromium alloy 825. *Corrosion* 24(6): 180–188.

Ruffner, D.J., G.L. Johnson, E.A. Platt, J.A. Blink, and T.W. Doering. 1993. Drift emplaced waste package thermal response. *Proceedings of the Fourth Annual International High-Level Radioactive Waste Management Conference.* La Grange Park, IL: American Nuclear Society: 538–543.

Shaikh, M.A., M. Iqbal, M. Ahmad, J.I. Akhtar, and K.A. Shoaib. 1992. Precipitation study of heat-treated Incoloy 825 by scanning electron microscopy. *Journal of Materials Science Letters* 11: 1,009–1,011.

Smith, G.D.W., A.J. Garratt-Reed, and J.B. Vander Sande. 1981. Comparison between atom probe and STEM microanalysis. *Quantitative Microanalysis with High Spatial Resolution.* G.W. Lorimer et al., eds. London, U.K.: The Metals Society: 238–249.

Sridhar, N., and G.A. Cragnolino. 1992a. Long-term life prediction of localized corrosion of Fe-Ni-Cr-Mo high-level nuclear waste container materials. *Corrosion '93,* Paper No. 93197. Houston, TX: National Association of Corrosion Engineers.

Sridhar, N., and G.A. Cragnolino. 1992b. Integrated waste package experiments. *NRC High-Level Radioactive Waste Research at CNWRA July–December 1992.* B. Sagar, ed. NUREG/CR-5817, CNWRA 92-02S. Washington, DC: Nuclear Regulatory Commission.

Sridhar, N., and G.A. Cragnolino. 1993. Applicability of repassivation potential for long-term prediction of localized corrosion of alloy 825 and type 316L stainless steel. *Corrosion* 49(11): 885–894.

Sridhar, N., G.A. Cragnolino, and D. Dunn. 1993a. *Experimental Investigations of Localized Corrosion of High-Level Waste Container Materials.* CNWRA 93-004. San Antonio, TX: Center for Nuclear Waste Regulatory Analyses.

Sridhar, N., J.C. Walton, G.A. Cragnolino, and P.K. Nair. 1993b. *Engineered Barrier System Performance Assessment Codes (EBSPAC) Progress Report—October 1, 1992, through September 25, 1993.* CNWRA 93-021. San

Antonio, TX: Center for Nuclear Waste Regulatory Analyses.

Sridhar, N., G.A. Cragnolino, and D. Dunn. 1993c. Integrated waste package experiments. *NRC High-Level Radioactive Waste Research at CNWRA January–June 1993*. B. Sagar, ed. CNWRA 93-01S. San Antonio, TX: Center for Nuclear Waste Regulatory Analyses.

Sridhar, N., G.A. Cragnolino, D.S. Dunn, and H.K. Manaktala. 1994a. *Review of Degradation Modes of Alternate Container Designs and Materials*. CNWRA 94-010. San Antonio, TX: Center for Nuclear Waste Regulatory Analyses.

Sridhar, N., G.A. Cragnolino, and D. Dunn. 1994b. Integrated waste package experiments. *NRC High-Level Radioactive Waste Research at CNWRA July–December 1993*. B. Sagar, ed. CNWRA 93-02S. San Antonio, TX: Center for Nuclear Waste Regulatory Analyses.

Sridhar, N., G.A. Cragnolino, J.C. Walton, and D. Dunn. 1994c. Prediction of crevice corrosion using modeling and experimental techniques. *Application of Accelerated Corrosion Tests to Service Life Prediction of Materials*. G.A. Cragnolino and N. Sridhar, eds. ASTM Special Technical Publication 1194. Philadelphia, PA: American Society for Testing and Materials.

Strehblow, H.H. 1984. Breakdown of passivity and localized corrosion: Theoretical concepts and fundamental experimental results. *Werkstoffe und Korrosion* 35: 437–448.

Streicher, M.A. 1978. Theory and application of evaluation tests for detecting susceptibility to intergranular attack in stainless steels and related alloys–problems and opportunities. *Intergranular Corrosion of Stainless Alloys*. R.F. Steigerwald, ed. ASTM Special Technical Publication 656. Philadelphia, PA: American Society for Testing and Materials.

Szklarska-Smialowska, Z. 1986. *Pitting Corrosion of Metals*. Houston, TX: National Association of Corrosion Engineers: 201–236.

Thompson, N.G., and B.C. Syrett. 1992. Relationship between conventional pitting and protection potentials and a new, unique pitting potential. *Corrosion* 48(8): 649–659.

Thorvaldsson, T., H. Rubinsztein-Dunlop, H-O. Andren, and G.L. Dunlop. 1981. Analytical electron microscopy of carbide precipitates in a stabilized austenitic stainless steel. *Quantitative Microanalysis with High Spatial Resolution*. G.W. Lorimer et al., eds. London, U.K.: The Metals Society: 250–255.

Tsujikawa, S., Y. Soné, and Y. Hisamatsu. 1987. Analysis of mass transfer in a crevice region for a concept of the repassivation potential as a crevice corrosion characteristic. *Corrosion Chemistry Within Pits, Crevices, and Cracks*. A. Turnbull, ed. London, U.K.: Her Majesty's Stationery Office: 171–186.

Voice, W.E., and R.G. Faulkner. 1985. Carbide stability in NIMONIC 80A alloy. *Metallurgical Transactions* 16A: 511–520.

Walton, J.C. 1993. Effects of evaporation and solute concentration on presence and composition of water in and around the waste package at Yucca Mountain. *Waste Management* 13: 293–301.

Was, G.S., and R.M. Kruger. 1985. A thermodynamic and kinetic basis for understanding Cr depletion in Ni-Cr-Fe alloys. *Acta Metallurgica* 33(5): 841–854.

Zimmerman, R.M., R.L. Schuch, D.S. Mason, M.L. Wilson, M.E. Hall, M.P. Board, R.P. Bellman, and M.P. Blanford. 1986. *Final Report: G-Tunnel Heated Block Experiment*. SAND84-2620. Albuquerque, NM: Sandia National Laboratories.

THIS PAGE INTENTIONALLY LEFT BLANK

4 GEOCHEMICAL NATURAL ANALOG RESEARCH

by William M. Murphy, English C. Pearcy, Sitakanta Mohanty, and James D. Prikryl

Investigators: *William M. Murphy, English C. Pearcy, Ronald T. Green, James D. Prikryl, Sitakanta Mohanty, Kristi A. Meyer, and Gregory D. James*

NRC Project Officer: *Linda A. Kovach*

4.1 TECHNICAL OBJECTIVES

The technical objective of the Geochemical Natural Analog Research Project is to develop an understanding of the utility and limitations of natural analog studies in support of a license application for a high-level waste (HLW) repository and to provide fundamental data on the long-term behavior of an HLW repository. This objective is pursued through field, laboratory, theoretical, and interpretive analyses of natural systems that are analogous to aspects of the proposed HLW repository at Yucca Mountain (YM), Nevada. Many factors affecting the long-term behavior of waste forms, the engineered barrier system (EBS), and radionuclides in the environment of the proposed repository are poorly known. The absence of this basic information limits the confidence with which repository performance may be evaluated. Natural systems that have evolved for periods of time comparable to that required for HLW disposal (i.e., 10^3–10^4 yr and greater) (U.S. Environmental Protection Agency, 1989) provide unique opportunities to obtain observational knowledge of the behavior of HLW repository components. Such information provides important support to long-term predictive models of repository performance (Nuclear Regulatory Commission, 1987).

The Geochemical Natural Analog Research Project addresses uncertainties raised in several Compliance Determination Strategies (CDSs). Specific Key Technical Uncertainties (KTUs) that may be supported include those in CDSs for groundwater travel time (3.3), hydrogeologic processes (3.2.2.1), hydrologic conditions (3.2.2.9), perched water (3.2.2.12), mineral assemblages (3.2.3.3), geochemical processes (3.2.2.5), EBSs (3.2.3.5.4), cumulative release (6.1), and individual protection (6.2). Data and interpretations developed within the Geochemical Natural Analog Research Project will assist resolution of KTU topics including: (i) equal or increased capacity of alteration mineral assemblages to inhibit radionuclide migration; (ii) uncertainty in identifying geochemical processes that reduce radionuclide "retardation;" (iii) uncertainty in determining the magnitude of the effect of the geochemical processes that reduce radionuclide "retardation;" (iv) conceptual model representations of the natural and engineered systems; (v) uncertainty in extrapolation of short-term laboratory test results to predict long-term performance of waste packages and EBSs; (vi) uncertainty in modeling groundwater flow through unsaturated fractured rock caused by the lack of codes tested against field and laboratory data; (vii) conceptual model representations of the natural and engineered systems; (viii) appropriateness of assumptions and simplification in mathematical models; and (ix) validation of mathematical models. Information presented in this chapter relates primarily to KTU topics (iv), (v), (vii), (viii), and (ix).

The Geochemical Natural Analog Research Project is an integrated effort combining expertise in geochemistry, hydrology, geology, and transport modeling, among others. The need for interdisciplinary input is reflected in a number of technical interfaces with other Nuclear Regulatory Commission (NRC) Office of Nuclear Regulatory Research projects. An active connection has been established with the Performance Assessment (PA) Research Project (Chapter 6 of this document). Within the Geochemical Natural Analog Research Project, the hydrologic properties of welded silicic tuff from the Nopal I analog site are being measured; these data are being analyzed within the PA Research Project to allow more complete interpretation of long-term transport of uranium through tuff at the site. Observations and measurements from the Geochemical Natural Analog Research Project are also being used within the Sorption Research Project (Chapter 5 of this document) as a comparison to laboratory studies. Additionally, results from the Geochemical Natural Analog Research Project are being used to guide the anticipated Near-Field Processes and Variations Research Project. Specifically, at the Nopal I site, it has been observed that alteration phases formed after uraninite (a spent fuel analog material) are

dominated by the minerals uranophane, soddyite, and weeksite. The Nopal I analog suggests that these phases are likely to be important to radionuclide release and transport in a YM repository. The Near-Field Processes and Variations Research Project plan has been written to include experiments to determine thermodynamic properties of uranyl minerals so that their behavior and impact on repository performance may be evaluated.

The Geochemical Natural Analog Research Project addresses needs identified by the Office of Nuclear Material Safety & Safeguards concerning assessment of the degree to which data from analogous sites may be extrapolated to support modeling for a repository site. It also addresses the need for an evaluation of the extent to which repository modeling can be validated using data from natural analogs. Specific NRC research needs that may be met through this project include: (i) comparison of laboratory sorption, mineral stability, leaching, and kinetic data with observations from natural systems; (ii) evaluation of radionuclide transport in unsaturated tuff; (iii) assessment of the effects of oxidation state on leaching and radionuclide release; and (iv) investigation of coupled interactions affecting radionuclide release and transport.

Research in the Geochemical Natural Analog Research Project includes work at two sites: the Nopal I uranium deposit in the Peña Blanca district, Chihuahua, Mexico, and the Akrotiri archaeologic site on Santorini, Greece. Earlier reports in this series documenting progress to date include Pearcy (1994); Pearcy et al. (1994); Leslie et al. (1993); Pearcy and Leslie (1993); Pearcy et al. (1993a, b); and Pearcy and Murphy (1990, 1991a-c).

4.2 SIGNIFICANT TECHNICAL ACCOMPLISHMENTS

This report presents an initial summary of an effort to evaluate the use of natural analog data to support modeling of repository performance over long time periods. Qualitative and quantitative comparisons are made between field data for contaminant transport at Delta 3 in the Akrotiri, Santorini natural analog site and a corresponding numerical flow and transport model. The archaeologic site has many features that are analogous to the proposed repository at YM: silicic volcanic rocks, chemically oxidizing environment, partially saturated hydrology, semiarid climate, well constrained source of contaminant material, and a time scale of burial (approximately 3,620 yr) comparable to the regulatory period (Murphy et al., 1991). Field samples have been collected and analyzed to detect and document the contaminant plume that emanated from bronze Minoan artifacts buried for approximately 3,620 yr in silicic volcanic materials. Other meteorologic, hydrologic, geologic, and geochemical data have been collected to characterize the site to support unsaturated flow and transport modeling.

The flow and transport model was developed using data collected at the site, laboratory data on site materials, and literature data. Although site characterization data from Akrotiri are subject to considerable practical limitations, both the data and the limitations reflect fundamental facets of the development of PAs for the YM repository. Similarly, modeling presented in this report was conducted without knowledge of the character and extent of the contaminant plume at Akrotiri. The objective of the comparison of natural analog data to results of blind modeling is to discover how the natural analog data may be useful in supporting repository modeling.

Research to date leads to the conclusion that although some results from the field are generally consistent with model results, important discrepancies result from poor representation of heterogeneity in the model and poorly constrained model parameters. System components that appear to have had major impacts on distribution of contaminants (i.e., Mn minerals in packed earth and the fracture adjacent to Hole VII) were neglected in the model. Identification of such components in relevant systems is confirmed as a major contribution that analog studies can make in support of repository modeling.

4.2.1 Field Data for the Contaminant Plume

Bronze artifacts within the Akrotiri excavation consist predominantly of Cu, Sn, and Pb, with minor Zn and Fe (Slater, 1980). Semi-quantitative electron microanalyses of bronze corrosion products from Delta 3 show them to be composed of Cu, Cl, and Fe, with trace amounts of Co, Mn, and Ag in some samples (Pearcy et al., 1994). X-ray diffraction analyses of corrosion products associated with a bronze saw blade collected in 1994 from Delta 8A, which is adjacent to Delta 3, indicate that the predominant Cu-bearing

phases are cuprite (CuO_2) and paratacamite [$Cu_2(OH)_3Cl$], consistent with corrosion products from elsewhere in the excavations (Pearcy et al., 1994). Optical observations suggest the presence of azurite [$Cu_3(CO_3)_2(OH)_2$] and malachite [$Cu_2CO_3(OH)_2$]. Corrosion crusts and coatings commonly show an intergrowth or layering of copper phases. Cuprite is the only Cu phase identified by XRD in another sample of tuff contaminated with corrosion products taken adjacent to a bronze tong, which was also collected in 1994 from near Delta 3. Archaeologic field notes from the time of excavation also describe a lead balance weight among the artifacts found in Delta 3.

The buried locations of bronze artifacts prior to excavation from Delta 3 in 1970 were constrained using archival photographs from the Greek archaeologists and the National Geographic Society (Pearcy et al., 1994). Samples of packed earth of the Minoan floor of Delta 3 and the underlying rock (Cape Riva Formation) were taken from the area immediately below the location where the artifacts were found (Figure 4-1). Samples were excavated by hammer and chisel from "holes" and by manual percussion coring from "boreholes." The samples cover an array over a volume approximately 1 m^2 by 0.5 m deep. Rock and packed earth samples were powdered using a SPEX Mixer/Mill with a tungsten carbide vial. Powdered samples were dried in a forced air oven at 105 °C, cooled, and stored in a desiccator. Evidence for a plume of contaminants from the buried artifacts was investigated by extraction of trace elements from the powders in a succession of aqueous solutions that select for different components of the solid material (Tessier et al., 1979). Sequential extractions focused on three fractions: (i) trace metals in cation-exchangeable sites, (ii) trace metals bound to carbonates, and (iii) trace metals bound to reducible Fe and Mn oxides. Trace metals analyzed in the leachates were Cu, Co, Ag, Pb, Zn, Mn, and Fe.

The following chemical extraction sequence was run on four separate 1-g samples of each rock powder in polypropylene centrifuge tubes. (i) *Exchangeable.* The powder was leached at room temperature for 1 hr with 8 mL of magnesium chloride solution (1 M $MgCl_2$, pH 7.0) with continuous agitation provided by a wrist shaker. (ii) *Bound to Carbonates.* The solid residue from (i) was leached at room temperature for 5 hr with 8 mL of sodium acetate solution (1 M CH_3COONa) adjusted to a pH of 5.0 with acetic acid (CH_3COOH) with continuous agitation. (iii) *Bound to Fe-Mn Oxides.* The residue from (ii) was leached for 5 hr in 10 mL of acid-reducing hydroxylamine-hydrochloride solution (0.04M NH_2OH•HCl) in 25 percent acetic acid at 96±3 °C with occasional agitation. Between successive extractions, separation was effected by centrifuging.The supernatant in the four centrifuge tubes for each sample was removed by pipet, combined, and analyzed for trace metals. Between successive extractions, the solid residue was washed with 8 mL of ultrapure water, centrifuged for 30 min, and the supernatant discarded.

Metal concentrations in the leachates were determined by atomic absorption spectrophotometry (AA). A standard addition method was used to measure trace metal concentrations because matrix effects would have contributed to additional errors up to 15 percent. Leachates from samples containing corrosion products were analyzed by AA using appropriate calibration curves. Leachate concentrations were converted to solid mass concentrations (prior to leaching) based on measured water-rock mass ratios. Analytical uncertainties are generally in the range of 5 to 15 percent.

Samples of corrosion products from the saw blade had high leachable amounts of Cu corresponding to 1.14×10^5 ppm or 0.114 percent of the solid mass. Ash contaminated with corrosion products from the tong released Cu equivalent to 9,170 ppm of the solid. In both cases the Cu was primarily released in the carbonate fraction and Fe-Mn oxide fraction leaches. In contrast, leachates from Delta 3 rock and packed earth samples had low concentrations of Cu (and other analyzed elements) with a few exceptions. The primary challenge in interpretation of the data from Delta 3 is to determine if a contaminant plume can be detected.

Solid concentrations of Cu removed in ion exchange selective and carbonate selective preparations for Delta 3 samples (Figures 4-2a and 4-2b, respectively) show a roughly normal distribution with little evidence of anomalous values and little or no distinction between bedrock and packed earth samples. One notable pattern is that both preparations yield high Cu values for samples from Hole VII, which is adjacent to a major fracture. Cu concentrations derived from Fe-Mn oxide-selective procedures (Figure 4-3) are anomalously high in several samples relative to a roughly normally distributed pattern of low concentrations for most samples. All anomalously high concentrations (i.e., >3 ppm) are for packed earth

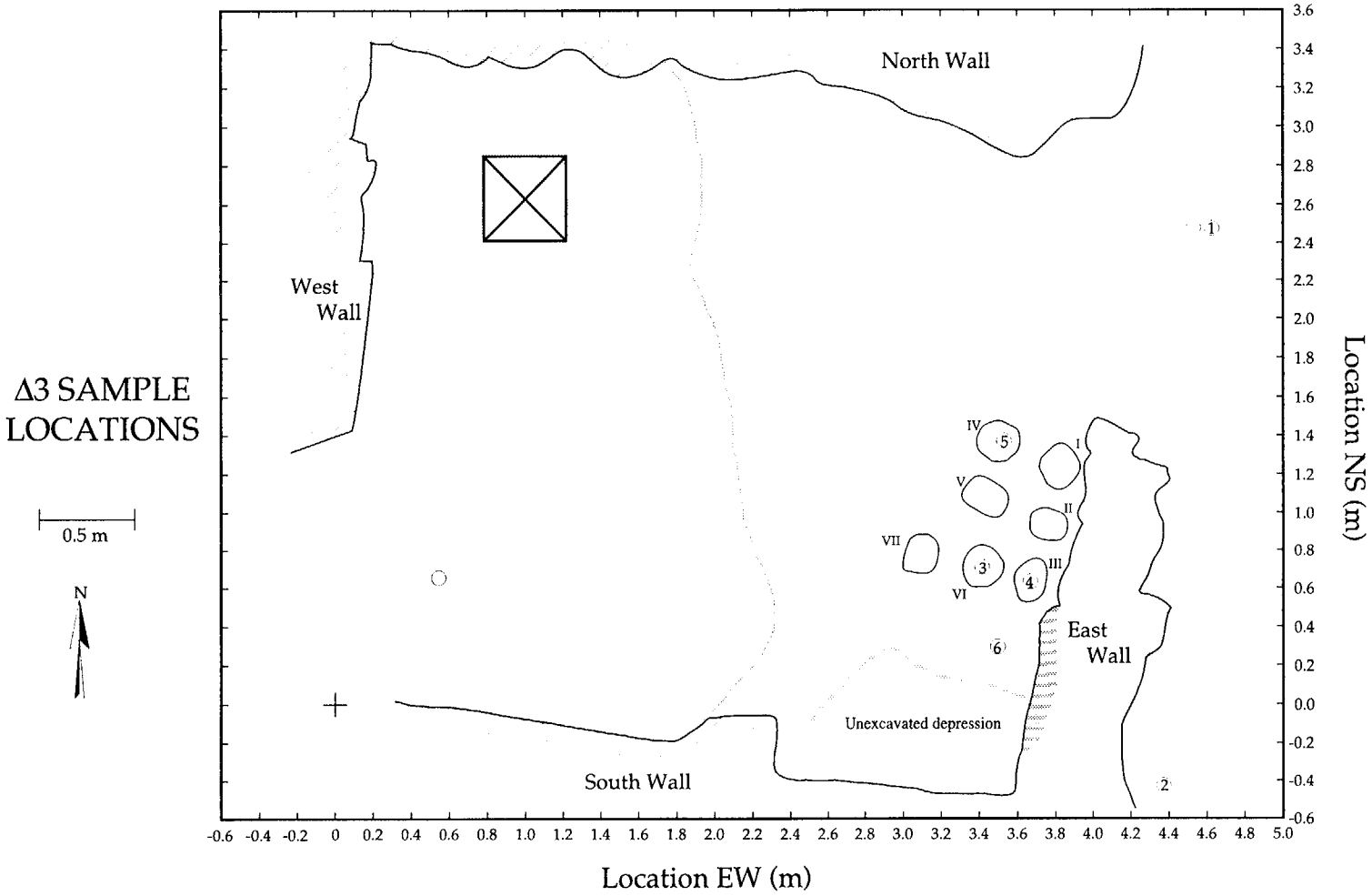

Figure 4-1. Map of the Delta 3 room at the Akrotiri site. Holes are marked by irregular outlines labeled by roman numerals. Boreholes are shown as small circles. Bronze artifacts were excavated from above the holes.

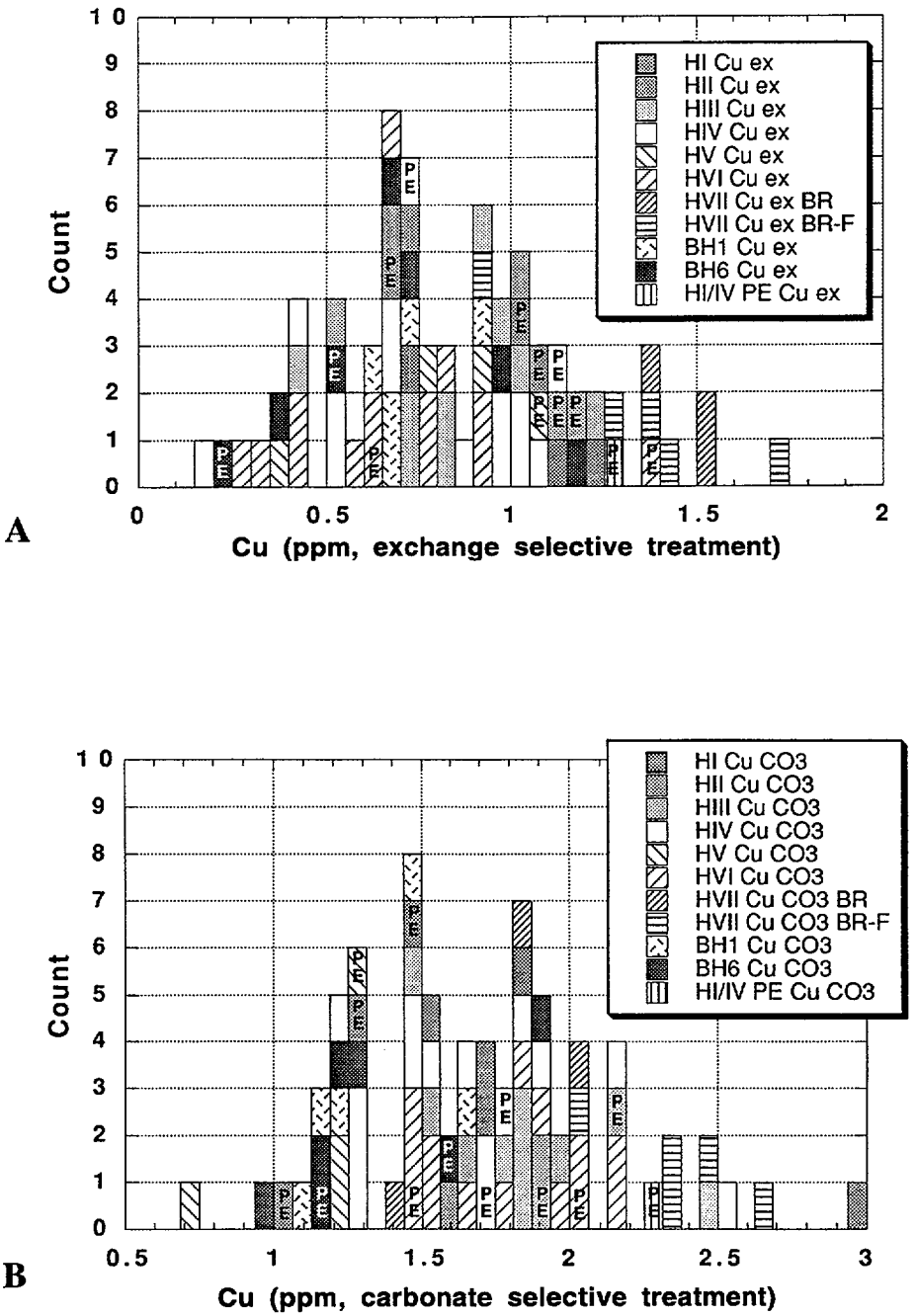

Figure 4-2. Histograms showing Cu concentrations in samples from Delta 3 extracted by (A) ion exchange selective leaching (ex), and (B) carbonate selective leaching (CO3). H refers to the hole number, BH refers to borehole numbers, BR stands for bedrock, F stands for fracture, PE stands for packed earth, and HI/IV PE denotes a PE sample from between HI and HIV. All samples other than PE samples are bedrock samples.

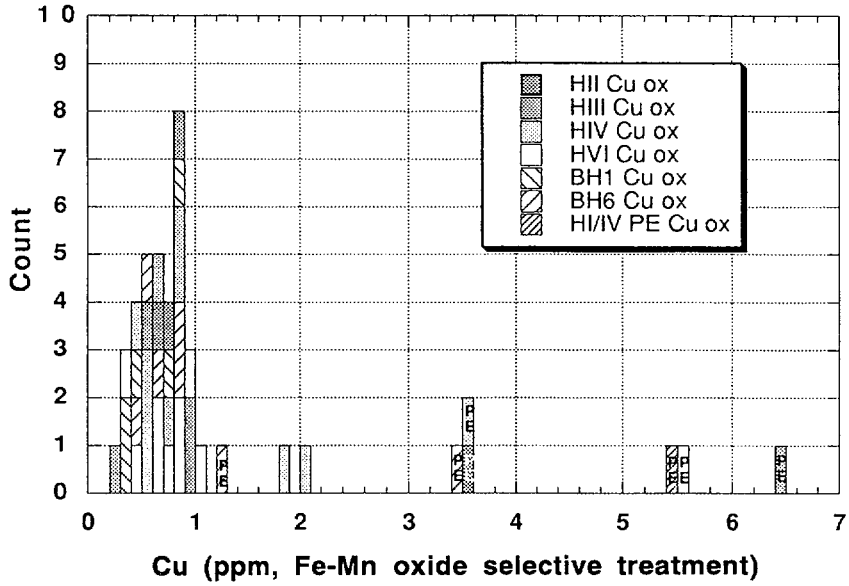

Figure 4-3. Histogram showing Cu concentrations in samples from Delta 3 extracted by Fe-Mn oxide selective leaching. Symbols as in Figure 4-2.

samples. Mn extracted using the Fe-Mn selective method is correlated with Cu concentrations (Figure 4-4), and Mn concentrations are also generally high in packed earth samples. Linear regression of Cu from the oxide selective extraction as a function of Mn in the same fraction yields a line that passes close to the origin. This relation indicates that Cu released in this process is related to Mn minerals. The line regressed through data for the total Cu removed in all three treatments has essentially the same slope, indicating generally that all anomalous high Cu is associated with Mn. It remains ambiguous whether the anomalous Cu has a mineralogical (e.g., natural Mn phases in the packed earth) or anthropological (e.g., contaminant) source.

Cu concentrations for three holes (plus boreholes) to a depth of 0.5 m (Figure 4-5) show anomalous values for packed earth (above the bedrock surface) and a roughly constant value with depth, with the exception of two marginal samples from the top and bottom of Hole IV (at 2 ppm). The pattern for Zn data resembles Cu data. It is especially concentrated in the oxide fraction of packed earth samples. Zn and Cu data from Hole IV show patterns resembling transient contaminant plumes (Figure 4-5). Anomalously high values of Zn and Cu at the greatest depth in Hole IV sampled also suggest heterogeneous transport.

Pb data provide moderately good evidence for a contaminant plume. It is mainly detected in the ion exchange and carbonate selective treatments, but quantities of Pb extracted by these two methods are poorly correlated. Amounts of Pb in the carbonate fraction (Figure 4-6) exhibit a fairly large range. For most holes, Pb concentrations are roughly distributed throughout the range from 0 to 5 ppm. However, the five highest values and eight of the nine highest values are from Hole VII, and all Pb concentrations from Hole VII associated with the carbonate leach are greater than 5 ppm. Results for the exchange fraction are similar, but not as exclusive. All samples from Hole VII were taken at depths below the bedrock surface of less than approximately 15 cm, with no definitive correlations of concentrations with depth. Pb in the carbonate fraction from three deeper holes (Figure 4-7) is at concentrations less than approximately 2 ppm below 20 cm, whereas most data from above approximately 15 cm are over 2 ppm. Data for each individual hole show a rough decrease with depth. In these holes, the Pb in excess of approximately 2 ppm appears to be a contaminant plume, which may have derived from either bronze or lead artifacts buried in Delta 3 for 3.6 millennia.

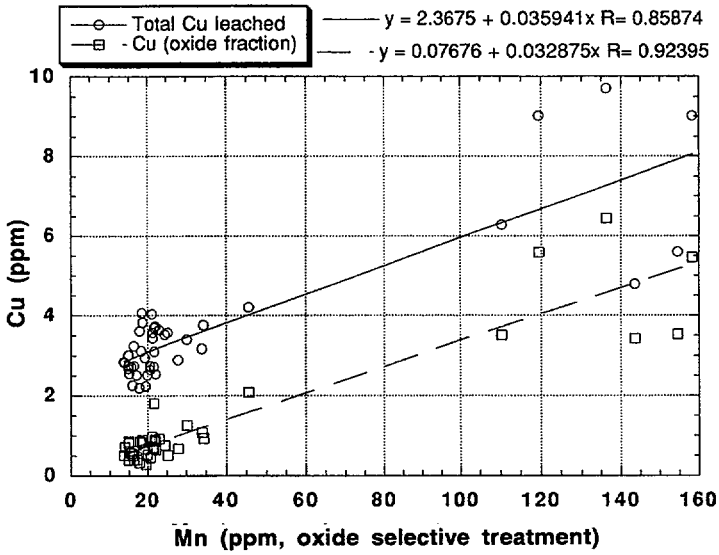

Figure 4-4. Cu in samples from Delta 3 as a function of Mn concentrations extracted by Fe-Mn selective leaching. Squares represent cumulative Cu concentrations leached by all three techniques. Circles represent Cu concentrations leached by the Fe-Mn selective treatments. Boxes give parameters for linear regressions.

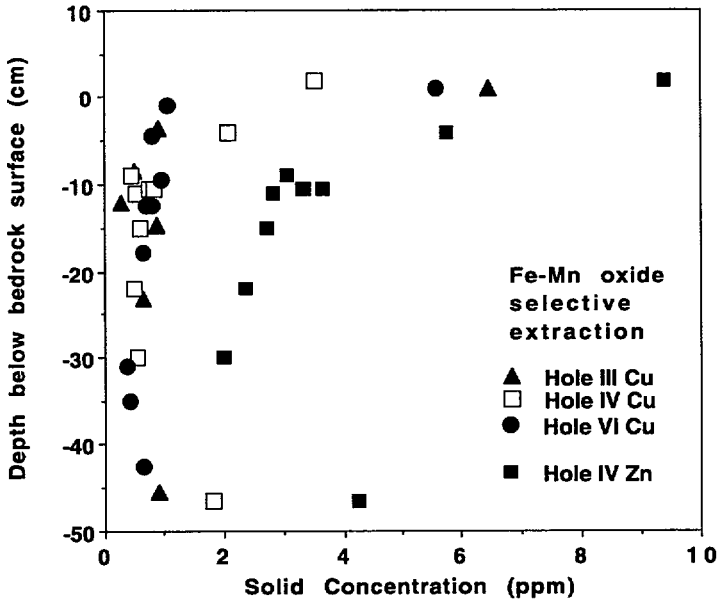

Figure 4-5. Cu concentrations extracted by Fe-Mn oxide selective leaching as a function of depth of sample for three holes at Delta 3 and Zn concentrations extracted by Fe-Mn oxide selective leaching as a function of depth in Hole IV

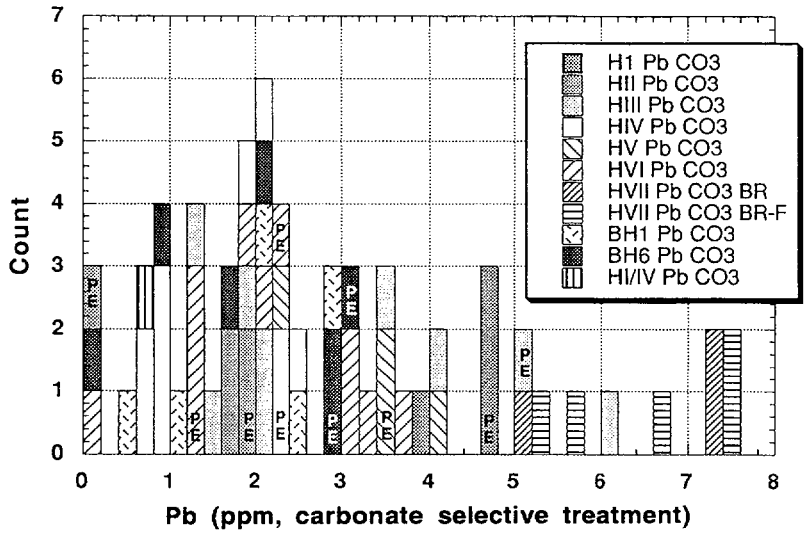

Figure 4-6. Histogram showing Pb concentrations in samples from Delta 3 extracted by carbonate selective leaching. Symbols as in Figure 4-2.

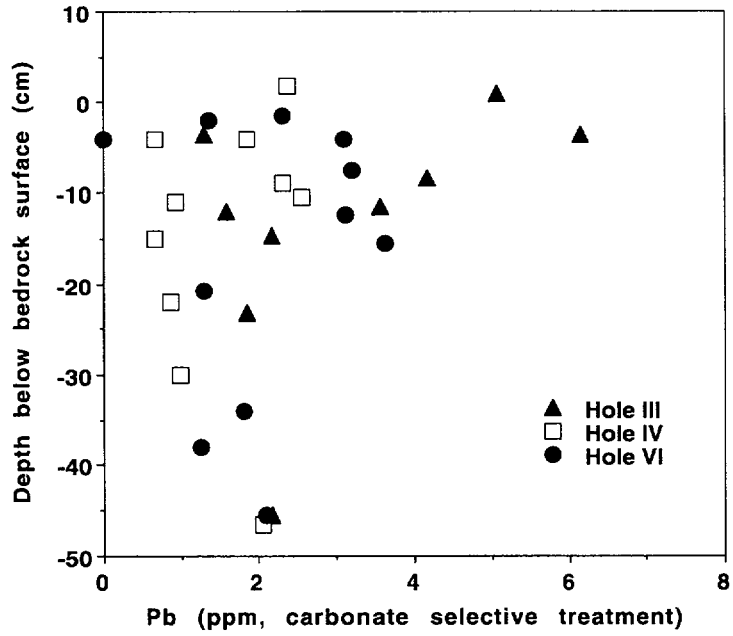

Figure 4-7. Pb concentrations extracted by carbonate selective leaching as a function of depth of sample for three holes at Delta 3.

However, modern lead pollution is also a possible source.

Data for Ag indicate mostly nonsystematic heterogeneity with concentrations ranging from below or near the detection limit to several times the limit. Ag data show no good evidence of a contaminant plume. Fe is extracted appreciably in the Fe-Mn oxide fraction leach (e.g., hundreds of ppm), but data indicate no clear systematic pattern of contamination. Neither are Co data particularly revealing, except for relatively high values for the carbonate fraction in the deepest sample of Hole IV and generally high values in Hole VII.

To summarize field evidence for a contaminant plume at Delta 3, Cu is a primary component of the bronze artifacts and occurs in large concentrations in visible corrosion products located only immediately adjacent to artifacts. Cu occurs at slightly elevated concentrations associated with Mn in packed earth material. Zn shows a pattern of decreasing concentration with depth, particularly in Hole IV. Focusing on the oxide fraction, Zn correlates well with Cu, which both suggest a heterogeneous path to the deepest sampled point. Pb associated with the carbonate fraction reveals considerable heterogeneity. Relatively high values for Pb commonly occur in the top 15 cm, but they have not been observed to occur below 20 cm. Pb is also significantly enriched in Hole VII, which is adjacent to a major fracture.

4.2.2 Model Development

A flow and transport model was assembled to simulate processes at the Delta 3 site. Although realism rather than conservatism was an objective of the modeling, practical computational constraints and data limitations mandated many approximations and simplifications. Model geometry is based on field observations (e.g., Pearcy et al., 1993a, 1994). The vertical, one-dimensional model system extends from the pre-excavation ground surface to the groundwater table at a depth of 24 m (Figure 4-8). At the top is a flux boundary with yearly sinusoidal infiltration reflecting the Mediterranean climate at the site. Total infiltration is poorly constrained at the site. Average annual rainfall of 32 cm (Hellenic National Meteorological Service) provides an upper limit. The observation of sustainable summer agriculture in the absence of summer rainfall indicates significant transpiration. Net infiltration was assumed in the base model to be 15 cm/yr. Infiltration is simulated by sinusoidal winter infiltration of 20 cm of water over a period of 240 d followed by summer exfiltration of 5 cm of water (to mimic evapotranspiration) over a period of 125 d. The bottom boundary condition is set at zero suction pressure. Initial conditions for water flow were set to equal the suction pressure for steady-state infiltration of 15 cm/yr. Based on field observations, four vertically disposed zones in the model correspond to the overlying Minoan tuff, the zone of Minoan deposits enclosing artifacts, a zone of packed earth floor material immediately beneath the zone of artifacts, and a zone of underlying Cape Riva tuff. No fractures or other heterogeneities are incorporated explicitly in the base model.

Porosity, hydraulic conductivity, retention curve parameters, and distribution coefficients assigned to the unsaturated matrix materials in the simulations are tabulated in Figure 4-8. These data were determined in part from property values measured in the field and in the laboratory on samples from the Akrotiri site (e.g., Pearcy et al., 1994). Where hydrologic data are incomplete (e.g., for packed earth), estimates were made using literature data for similar materials (Neuman et al., 1974; Case et al., 1983). Cu transport from the artifacts was modeled. The Cu source was fixed in the model by specifying a constant, solubility-limited concentration in the zone containing artifacts. Cu solubility of 10^{-5} molar was based on a simple model for the groundwater chemistry and published thermodynamic properties for the secondary Cu phase atacamite as simulated with EQ3 version 7.1 and its associated database DATA0.COM.R16 (Wolery and Daveler, 1992). Constant equilibrium distribution coefficients were invoked for all zones. These coefficients are also based on the simple water chemistry model and literature data for Cu sorption on quartz for the tuffaceous units (Schindler et al., 1987) and on kaolinite for the packed earth (Salomons, 1984). Refinement of parameter measurements and estimates is continuing, and details will be published at a later date. Future sensitivity analyses will also permit evaluations of the significance of the various parameters. PORFLOW (Runchal and Sagar, 1993) was used for numerical implementation of the model.

4.2.3 Model Results

Results for the base case simulation are presented to identify general features of the flow and transport model and to permit their comparison to field

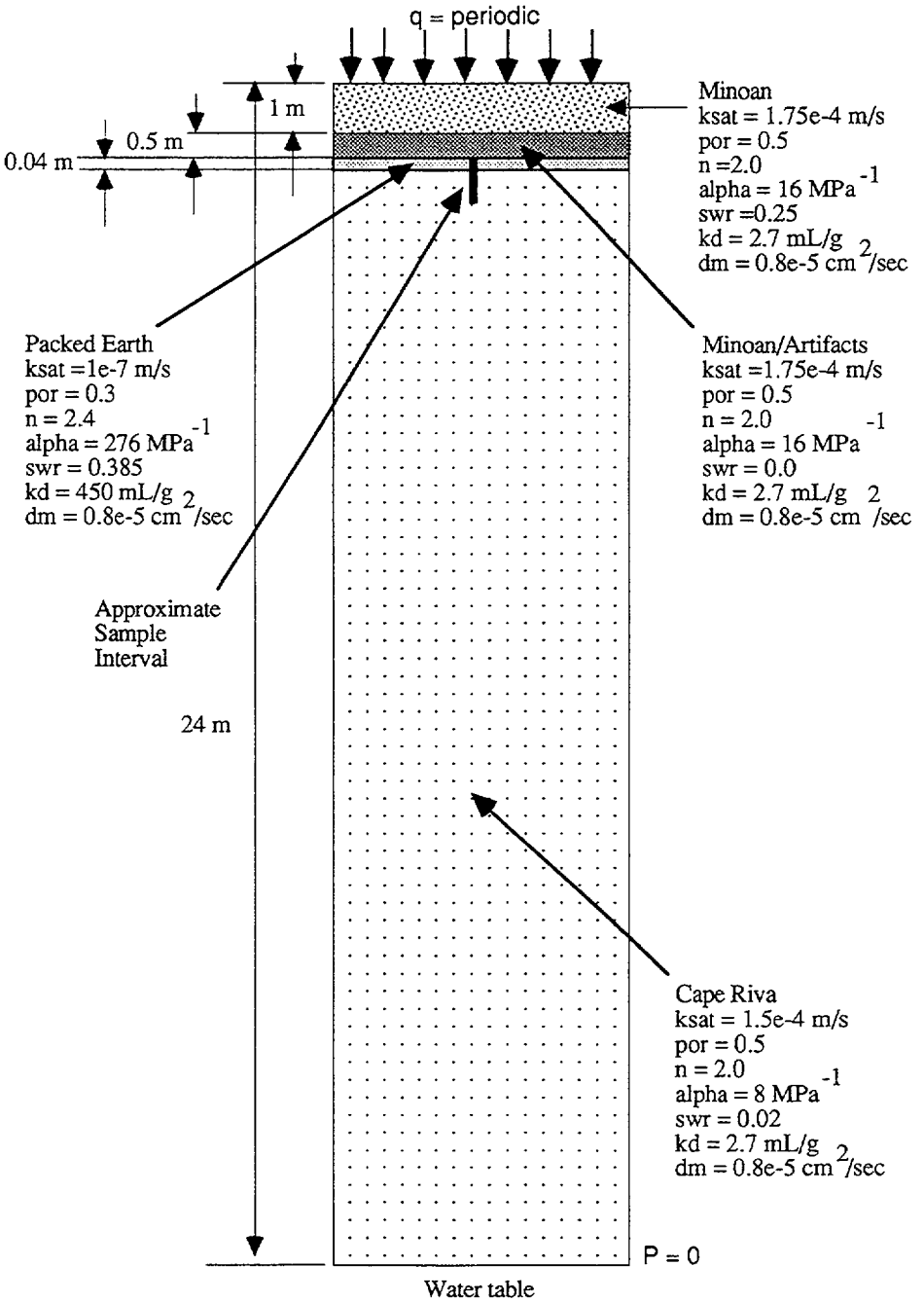

Figure 4-8. Schematic of 1D model geometry and model parameters. Symbolically, ksat represents the saturated hydraulic conductivity, por stands for porosity, n and alpha are Van Genuchten parameters, swr represents the residual water content, kd stands for the solid-liquid distribution coefficient for Cu (K_d), and dm stands for the molecular diffusivity of aqueous Cu. Figure is to scale except exaggeration of the packed earth level by 6.5×.

data. Steady state conditions are achieved rapidly in the model and correspond for most of the profile to initial conditions. The low permeability, highly sorptive packed earth layer has a dominant effect on modeled flow and transport. A discontinuity of 2 m in pressure head occurs at this horizon (Figure 4-9), with the system remaining wetter above the packed earth. Nevertheless, the modeled system remains fairly dry, with saturations increasing from 46 to 47 percent between the ground surface and the packed earth layer, remaining at 75 percent in the packed earth, and increasing smoothly from 50 percent to 100 percent between the base of the packed earth and the water table. Sinusoidal infiltration has a small effect on steady state hydraulic oscillations, which is detectable only above the packed earth. Differences between winter and summer pressure conditions in the model are insignificant on the scale of Figure 4-9.

Aqueous Cu concentrations computed in the model (Figure 4-10) show that, over the time scale of millennia, concentrations beneath the source zone equal the constant value of the source. The model predicts that effectively no gradient in aqueous Cu concentrations would be observed over the depth at which samples were collected at Akrotiri. Model use of constant distribution coefficients therefore indicates no gradient in sorbed Cu over the same distances, except as a consequence of distribution coefficient changes for different materials. Cu concentrations above the source zone remain low. Upward transport by diffusion and summer flow is erased by dominant downward winter flow in the model.

4.2.4 Comparison

Qualitatively, field data indicate that little of the bronze material has been transported away from its primary location. Original artistic textures and patterns and constructional detail have been preserved largely intact even on artifacts that were apparently crushed by falling or compacting debris. Massive dissolution and transport of primary components away from the site of burial would have obscured these details. Model results are generally supported by this observation. The total amount of Cu predicted to have been removed from the artifacts is given approximately by the product of the infiltration rate, the cross sectional area of the artifact deposit, the concentration of Cu in the solution flowing through the artifact horizon, and the time period. This value is given by (15 cm/yr) × (1 m^2) × (100^2 cm^2/m^2) × (10^{-5} moles/L) × (L/1,000 cm^3) × (63.546 g/mole) × (3,600 yr)×(cm^3/8.96 g)=38 cm^3, which is a reasonably small volume.

The bronze artifacts from Akrotiri have been visibly altered (oxidized) at least surficially. Also, large Cu concentrations have been observed only in contaminated materials taken from the immediate vicinity (e.g., within millimeters) of bronze artifacts at Akrotiri. These observations and the occurrence of secondary Cu minerals associated with the bronzes support the solubility-limited source term assumption in the model. Metal oxidation and secondary phase formation is rapid relative to the rate of transport of material out of the system. Transport rather than alteration rate is the rate-limiting process.

Field data indicate that minimal excess Cu remains in bedrock within 0.5 m of the location of the bronzes at Delta 3. This result generally supports model predictions. The low solubility predicted for the Cu source term, coupled with small sorption presumed for the tuffaceous rock, is compatible with minimal Cu deposition on the rock. The 10^{-5} molar solubility and a K_d of 2.7 mL/g derived from the simple water chemistry model and data for Cu sorption on quartz yield predictions of excess Cu concentrations in the rock of only 1.7 ppm. This value corresponds closely to the maximum leachable Cu concentrations observed in the tuff; the maximum observed excess Cu plus background Cu is 4 ppm.

At distances on the scale of a few centimeters from the artifacts, slight apparent excess Cu found at Delta 3 is associated with Mn minerals in packed earth. Although elevated sorption of Cu on packed earth was predicted in the model, the prediction was based on data for Cu sorption on kaolinite, the main component of the packed earth. Manganese mineral specific sorption was neglected in the base model. However, maximum excess Cu predicted in the model is 286 ppm, based on the Cu solubility estimate and the K_d applied for Cu sorption on kaolinite. This value contrasts the maximum leachable Cu observed in the packed earth, which is less than 10 ppm. Model results indicating strong sorption and significant excess Cu on kaolinite of the packed earth are not supported by field data.

Field data from Delta 3 indicate gradients in concentrations of Zn and Pb and possibly Cu deposited on the solid matrix on the scale of tens of centimeters from the artifact horizon (Figures 4-5 and 4-7). These results are consistent with a transport regime that

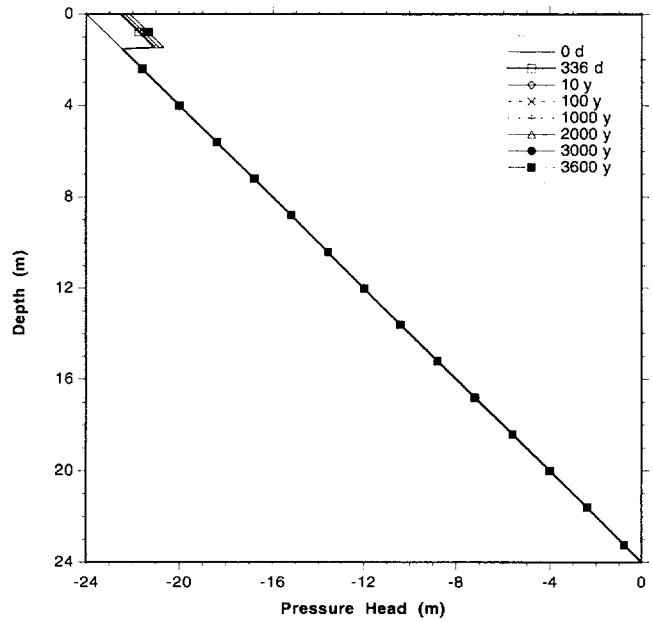

Figure 4-9. Modeled pressure head variation with time and depth from the ground surface to the water table.

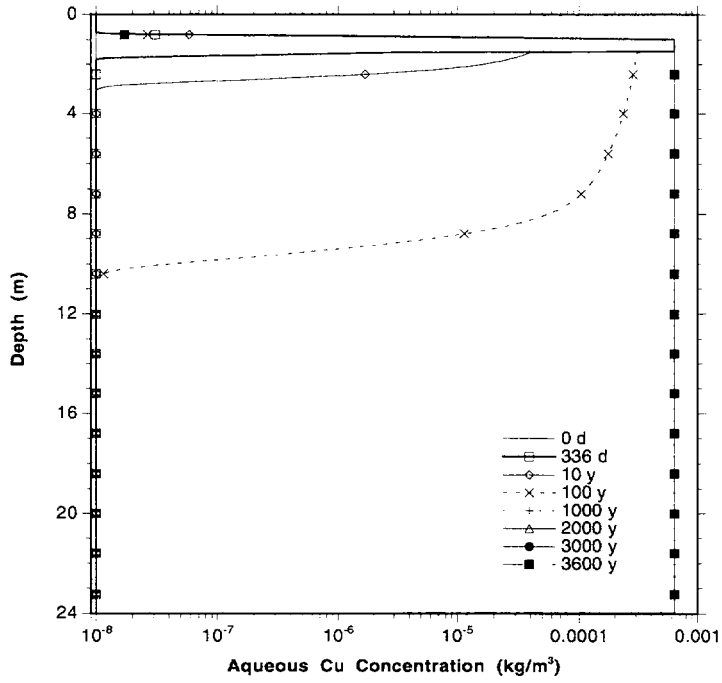

Figure 4-10. Modeled aqueous Cu concentration variations with time and depth from the ground surface to the water table.

remained transient. In contrast, the base model predicts that steady state, constant concentration profiles develop on this distance scale over a short time period relative to the 3,620 yr since burial of the artifacts. This major discrepancy suggests that transport may be dominated by diffusion in the real system, whereas advective transport dominates model results.

Field data indicate that system heterogeneity played an important role in the distribution of contaminants on solids at Delta 3. Heterogeneity in the model was represented by four hydrostratigraphic and geochemical horizons. Model results indicating greater Cu deposition in the packed earth horizon than in the underlying Cape Riva tuff horizon are qualitatively supported by the field data. However, dominant heterogeneous effects observed in the field are association of Cu with Mn minerals in the packed earth and preferential deposition of Pb in Hole VII adjacent to a major fracture. Neither of these important effects was represented in the model.

Temporal changes in pressure heads have been observed in the field between successive summers at depths up to 0.5 m using equilibrated gypsum block resistor devices. These measurements indicate pressure heads of approximately −10 m or less, whereas the maximum modeled steady state values are approximately −22 m. This discrepancy suggests that the modeled infiltration is too small or exfiltration is too large. Annual variations in the pressure head measured under the roofed and unvegetated archaeological site indicate significant gas phase moisture transport. Explicit gas phase moisture transport is absent in the model, but may be partially represented by negative infiltration in the summer. However, gas phase moisture transport could lead to the wetter conditions observed near the ground surface at the site. Future improvements to the model will take improved field hydrologic conditions as constraints.

In summary, although some results from the field are qualitatively consistent with model results, important discrepancies result from poor representation of heterogeneity in the model and poorly constrained model parameters. System components that appear to have had major impacts on distribution of contaminants (i.e., Mn minerals in packed earth and the fracture adjacent to Hole VII) were neglected in the model. Identification of such components in relevant systems is confirmed as a major contribution that analog studies can make in support of repository modeling. Major assumptions were required in the base model concerning infiltration and water chemistry and its control on the source term and retardation. Future data collection and interpretation will be used to refine these assumptions, and tests will be performed to examine the sensitivity of model results to such parameters. This process may resolve discrepancies such as the apparent remaining transient nature of the Zn plume and the over prediction of sorption on packed earth.

4.3 ASSESSMENT OF PROGRESS TOWARD MEETING PROJECT OBJECTIVES

The Geochemical Natural Analog Research Project is making good progress toward the objectives listed in Section 4.1. Research results presented in this report and elsewhere (e.g., Pearcy et al., 1994) have begun to provide a realistic understanding of the utility and limitations of natural analog studies when employed to support a license application for an HLW repository.

At Peña Blanca, fundamental data have been gathered and interpreted on U mineral characteristics, stabilities, and alteration sequences in a geologic environment comparable to that anticipated for the proposed YM repository. This information is required for development and evaluation of reasonable PA models for radionuclide transport. For example, data being gathered within the Analog Research Project on the matrix hydraulic properties of silicic tuff is being used within the PA Research Project to support modeling efforts. Additionally, progress has been made in evaluation of the roles of fracture and matrix transport of U in a YM-like environment. This information has been used in the development of CDS 3.2.3.3 (mineral assemblages), CDS 3.2.3.5 (geochemical processes), and CDS 5.4 (EBS).

Previous work at Akrotiri included definition of specific areas for analog study, completion of initial observations confirming similarities to YM, analyses of source term compositions, and constraints on models for hydraulic infiltration and runoff (e.g., Murphy et al., 1991; Murphy and Pearcy, 1994; Pearcy et al., 1993b; Pearcy et al., 1994). Generally, the long-term preservation of metallic artifacts at Akrotiri, and the stability of their oxidation products are at least qualitative indications of good material isolation

capacity in this climatically semiarid, hydrologically unsaturated, and chemically oxidizing environment.

Results in this report on Akrotiri constitute significant progress toward the objectives given in Section 4.1. An explicit role and objective of natural analog studies specified in 10 CFR Part 60 is to support models for repository performance. Models for repository performance range from conceptualizations of physical processes, to mechanistic models of specific processes, to probabilistic assessments designed to bound total-system performance and to evaluate uncertainty in the bound. Research reported here demonstrates that natural analog studies can support these models by identification of important components and processes in a contaminant transport system and by quantitative evaluations of the long term behavior of contaminants in a geologic environment. This understanding is anticipated to provide essential input to development of Compliance Determination Methods involving KTUs such as (i) conceptual model representations of the natural and engineered systems; (ii) uncertainty in extrapolation of short-term laboratory test results to predict long-term performance of waste packages and the EBS; and (iii) uncertainty in modeling groundwater flow through unsaturated fractured rock caused by the lack of codes tested against field and laboratory data.

The U.S. Department of Energy (DOE) has initiated analog research related to a YM repository. The DOE is studying water/rock interactions in hot springs in New Zealand in an attempt to validate the EQ3/6 computer code. In addition to these efforts, other DOE analog research is under consideration (e.g., Chapman et al., 1992). Center for Nuclear Waste Regulatory Analyses (CNWRA) work at Peña Blanca and at Akrotiri provides a strong base of experience from which to evaluate DOE analog studies. Results from CNWRA analog research allows informed comment on selection of sites, site characterization techniques, applications of the analog data, and use of the analog data for evaluation of models for the performance of a YM repository.

4.4 PLANS FOR NEXT REPORT PERIOD

Field research anticipated during the next report period (January 1, 1995 to June 30, 1995) will focus mainly on the Peña Blanca site. At Peña Blanca, observations will be made, and samples will be collected to further investigate the partitioning of U among secondary, fracture-filling minerals within and near the Nopal I deposit. Detailed observations and measurements will be made of fracture patterns and fracture geometries in selected areas to improve conceptual models of transport through the Nopal I fracture network. These observations and measurements will also support planning for proposed field infiltration tests at the Nopal I site.

Laboratory research during the next period is planned to include U content and rare earth content measurements on samples from Peña Blanca. Optical microscopy, scanning electron microscopy, energy dispersive x-ray analyses, and powder diffraction x-ray analyses are planned for both Peña Blanca samples and Akrotiri samples. Ion probe measurements are planned for Nopal I uraninite and secondary uranyl minerals to determine rare earth element contents and to make isotopic measurements to allow radiometric ages to be interpreted. Gamma spectrometry measurements will be used to measure U-series disequilibria within Nopal I samples. Measurement of the matrix hydraulic properties of the Cape Riva and Minoan tuffs is anticipated to be completed during the next reporting period.

Modeling and data interpretation activities planned for Peña Blanca during the next report period include attempts to extend infiltration calculations for the Peña Blanca site and numerical evaluation of the Nopal I fracture network properties. Conductivity data collected across the Nopal I cuesta will be interpreted to investigate the possibility of a perched water zone at the site.

Measurements and interpretations of hydrologic and geochemical data for the Akrotiri site will continue. Unsaturated hydraulic conductivity values for three of the four phases of the Minoan tuff will be determined using disk permeameter measurements made in the field. Moisture retention curves for the Cape Riva tuff and for undifferentiated Minoan tuff will be completed using core samples collected during the past field season. Transport modeling for the Akrotiri site described in this report will be extended by examination of a suite of variations on the base model to test sensitivity of model results to input parameters.

An expanded version of this report is scheduled to be submitted for publication in the next report period. The report will contain details of the geochemical model, descriptions of field and laboratory measurements of hydraulic parameters, and an expanded suite of model calculations. The paper will conclude with a discussion of applications of the natural analog study in support of repository modeling. Publication of this paper will effectively conclude research at the Delta 3 site. Additional research at Akrotiri will require coordination with the Greek archeological team to permit sampling of material immediately adjacent to newly excavated artifacts.

4.5 REFERENCES

Case, C., M. Kautsky, P. Kearl, R. Goldfarb, S. Leatham, and L. Metcalf. 1983. *Unsaturated Flow Properties Data Catalog.* DOE/NV/10162-12. Las Vegas, NV: Desert Research Institute.

Chapman, N., P.L. Cloke, J.-C. Petit, J.A.T. Smellie, and A.E.J. van Luik. 1992. *Applications of Natural Analogue Studies to Yucca Mountain as a Potential High Level Radioactive Waste Repository.* Las Vegas, NV: Office of Civilian Radioactive Waste Management, U.S. Department of Energy.

Leslie, B.W., E.C. Pearcy, and J.D. Prikryl. 1993. Geochemical natural analogs. *NRC High-Level Radioactive Waste Research at CNWRA January-June 1992.* W.C. Patrick, ed. NUREG/CR-5817, CNWRA 92-01S. Washington, DC: Nuclear Regulatory Commission: 3(1).

Murphy, W.M., and E.C. Pearcy. 1994. Performance assessment significance of natural analog studies at Peña Blanca, Mexico, and at Santorini, Greece. *Fifth Natural Analogue Working Group Meeting and Alligator Rivers Analogue Project (ARAP) Final Workshop.* H. von Maravic and J. Smellie, eds. Brussels: Commission of the European Communities: Final Report n° EUR 15178 EN: 219–224.

Murphy, W.M., E.C. Pearcy, and P.C. Goodell. 1991. Possible analog research sites for the proposed high-level nuclear waste repository in hydrologically unsaturated tuff at Yucca Mountain, Nevada. *Fourth Natural Analogue Working Group Meeting and Poços de Caldas Project Final Workshop.* B. Come and N.A. Chapman, eds. Brussels: Commission of the European Communities: Final Report n° EUR 13014 EN: 267–276.

Neuman, S.P., R.A. Feddes, and E. Bresler. 1974. Finite element simulation of flow in saturated-unsaturated soils considering water uptake by plants, development of methods, tools and solutions for unsaturated flow. *Third Annual Report (Part 1), Hydrodynamics and Hydraulic Engineering Laboratory.* Haifa, Israel: Israel Institute of Technology.

Nuclear Regulatory Commission. 1987. *Disposal of High-Level Radioactive Wastes in Geologic Repositories.* Title 10, Energy, Part 60. Washington, DC: U.S. Government Printing Office.

Pearcy, E.C. 1994. Geochemical natural analog research. *NRC High-Level Radioactive Waste Research at CNWRA January–June 1994.* B. Sagar, ed. CNWRA 94-01S. San Antonio, TX: Center for Nuclear Waste Regulatory Analyses: 57–76.

Pearcy, E.C., and W.M. Murphy. 1990. Geochemical natural analogs. *Report on Research Activities for Calendar Year 1990.* W.C. Patrick, ed. NUREG/CR-5817. Washington, DC: Nuclear Regulatory Commission: 7-1 to 7-7.

Pearcy, E.C., and W.M. Murphy. 1991a. Geochemical natural analogs. *Report on Research Activities for the Quarter July 1 through September 30, 1991.* W.C. Patrick, ed. CNWRA 91-03Q. San Antonio, TX: Center for Nuclear Waste Regulatory Analyses: 7-1 to 7-9.

Pearcy, E.C., and W.M. Murphy. 1991b. Geochemical natural analogs. *Report on Research Activities for the Quarter April 1 through June 30, 1991.* W.C. Patrick, ed. CNWRA 91-02Q. San Antonio, TX: Center for Nuclear Waste Regulatory Analyses: 7-1 to 7-7.

Pearcy, E.C., and W.M. Murphy. 1991c. Geochemical natural analogs. *Report on Research Activities for the Quarter January 1 through March 31, 1991*. W.C. Patrick, ed. CNWRA 91-01Q. San Antonio, TX: Center for Nuclear Waste Regulatory Analyses: 7-1 to 7-7.

Pearcy, E.C., and B.W. Leslie. 1993. Geochemical natural analogs. *NRC High-Level Radioactive Waste Research at CNWRA January–June 1993*. W.C. Patrick, ed. CNWRA 93-01S. San Antonio, TX: Center for Nuclear Waste Regulatory Analyses: 7-1 to 7-20.

Pearcy, E.C., B.W. Leslie, W.M. Murphy, and R.T. Green. 1993a. Geochemical natural analogs. *NRC High-Level Radioactive Waste Research at CNWRA July–December 1992*. W.C. Patrick, ed. CNWRA 92-02S. San Antonio, TX: Center for Nuclear Waste Regulatory Analyses: 7-1 to 7-27.

Pearcy, E.C., W.M. Murphy, R.T. Green, B.W. Leslie, and J.D. Prikryl. 1993b. Geochemical natural analogs. *NRC High-Level Radioactive Waste Research at CNWRA for Calendar Year 1991*. W.C. Patrick, ed. NUREG/CR-5817. Washington, DC: Nuclear Regulatory Commission: 7-1 to 7-32.

Pearcy, E.C., R.T. Green, and W.M. Murphy. 1994. Geochemical natural analogs. *NRC High-Level Radioactive Waste Research at CNWRA July–December 1993*. W.C. Patrick, ed. CNWRA 93-02S. San Antonio, TX: Center for Nuclear Waste Regulatory Analyses: 5-1 to 5-16.

Runchal, A.K., and B. Sagar. 1993. *PORFLOW: A Multifluid Multiphase Model for Simulating Flow, Heat Transfer, and Mass Transport in Fractured Porous Media*. NUREG/CR-5991. Washington, DC: Nuclear Regulatory Commission.

Salomons, W., and U. Förstner. 1984. *Metals in the Hydrocycle*. New York, NY: Springer-Verlag.

Schindler, P.W., P. Liechti, and J.C. Westall. 1987. Adsorption of copper, cadmium and lead from aqueous solution to the kaolinite/water interface. *Netherlands Journal of Agricultural Science* 35: 219–230.

Slater, E.A. 1980. Late bronze age Aegean metallurgy in the light of the Thera analyses. *Thera and the Aegean World*. C. Doumas, ed. London, England: Thera and the Aegean World, Inc.: 197–215.

Tessier, A., P.G.C. Campbell, and M. Bisson. 1979. Sequential extraction procedure for the speciation of particulate trace metals. *Analytical Chemistry* 51: 844–850

U.S. Environmental Protection Agency. 1989. *Environmental Radiation Protection Standards for Management and Disposal of Spent Nuclear Fuel, High-Level and Transuranic Radioactive Wastes*. Title 40, Protection of the Environment, Part 191. Washington, DC: U.S. Government Printing Office.

Wolery, T.J., and S.A. Daveler. 1992. EQ3/6, *A Software Package for Geochemical Modeling of Aqueous Systems*. UCRL-MA-110772, vols. PT I-IV. Livermore, CA: Lawrence Livermore National Laboratory.

5 SORPTION MODELING FOR HIGH-LEVEL WASTE PERFORMANCE ASSESSMENT

by F. Paul Bertetti, Roberto T. Pabalan, and David R. Turner (CNWRA)

Investigators: Roberto Pabalan, David Turner, F. Paul Bertetti, Michael Almendarez, Todd Dietrich, James Prikryl, and Paula Muller

NRC Project Officer: George F. Birchard

5.1 TECHNICAL OBJECTIVES

A fundamental concern in evaluating the suitability of Yucca Mountain (YM), Nevada, as a repository for high-level nuclear wastes (HLW) is the possibility of radionuclide migration from the repository to the accessible environment as dissolved constituents in groundwater. Sorption of radionuclides on minerals encountered along the flow paths could be an important mechanism for attenuating radionuclide migration. Sorption is specifically referred to in 10 CFR Part 60.122(b) as a favorable geochemical condition that could inhibit radionuclide migration and "favorably affect the ability of the geologic repository to isolate the waste." Conversely, geochemical processes that "would reduce sorption of radionuclides" are included [10 CFR Part 60.122(c)(8)] as potentially adverse conditions that could reduce the effectiveness of the natural barrier system.

To support the Nuclear Regulatory Commission (NRC) HLW program, the Center for Nuclear Waste Regulatory Analyses (CNWRA) is conducting research activities under the Sorption Modeling for HLW Performance Assessment (PA) Research Project. The broad objective of this project is to develop sufficient understanding of radionuclide transport issues so that timely prelicensing guidance can be provided to the U.S. Department of Energy (DOE) and a sound basis is available for evaluating the DOE license application. The results will be used to support the preparation of the NRC License Application Review Plan (LARP), particularly Sections 3.2.3.2, 3.2.3.3, and 3.2.3.5, pertaining to favorable and potentially adverse geochemical conditions and processes at a potential repository site, and Section 3.4, which addresses the effectiveness of natural barriers against the release of radioactive material to the environment. Laboratory (Task 3) and modeling (Task 2) studies of radionuclide sorption, retardation, and transport, which are central to the Sorption Research Project, will provide independent bases for addressing Key Technical Uncertainties (KTUs), particularly uncertainties in identifying geochemical processes and conditions that affect radionuclide retardation and determining and predicting the magnitude of the effects at YM. In addition, development of Compliance Determination Methods (CDMs) for determining compliance with the regulatory requirements will utilize data and models generated from this research project.

Results arising from this project will be integrated with those from other CNWRA activities. For example, data on U sorption will be used in interpreting data on U distribution and migration at the Peña Blanca field site of the Geochemical Natural Analog Research Project of this report. The data will also be used in developing conceptual models for radionuclide transport/retardation in near- and far-field environments related to the PA Research Project (Chapter 6) and the Iterative Performance Assessment (IPA) Phase 3. Results of activities undertaken during the second half of 1994 are discussed in the following sections.

5.2 SORPTION EXPERIMENTS

To develop an understanding of radionuclide sorption processes and the important physical and chemical parameters that affect sorption behavior in the YM environment, experiments are being conducted to investigate the sorption behavior of U and other actinides on geologic media. During the second half of 1994, experiments were completed to determine the effects of pH, solid-mass/solution-volume ratio, and U(6+) concentration on the sorption of U(6+) on quartz sand. Quartz is a widespread, major rock-forming mineral at YM, and makes up nearly one-third by mass of the geologic units surrounding the proposed repository horizon (e.g., Bish and Vaniman, 1985; Bish and Chipera, 1989). The experimental data were interpreted using a surface-complexation model (SCM),

which permitted predictions to be made regarding U(6+) sorption on quartz at other physicochemical conditions. Methods and results of experiments concerning U(6+) sorption on quartz are discussed in Section 5.2.1, and modeling results are given in Section 5.3.

5.2.1 Uranium Sorption on Quartz

5.2.1.1 Preparation of Quartz Sand

Foundry grade quartz sand (Wedron #510), quarried from the St. Peters Sandstone in Illinois, was obtained from Wedron Silica Co., Wedron, Illinois. The sand is comprised almost entirely (>99 percent) of quartz grains. Purity of the sand was checked by x-ray diffraction analysis using a Siemens D-500 diffractometer and Ni-filtered CuK_α radiation. As shown in Figure 5-1, the sand's x-ray powder diffraction pattern exhibits no nonquartz peaks. However, petrographic and chemical analyses of the sand revealed that some minor impurities were present. When viewed using transmitted and reflected light microscopy minor mineral impurities (<1 percent), predominantly Fe-oxide grain coatings or pyrite inclusions, were observed. Size separation using U.S. standard sieves indicated that nearly 94 percent by weight of the sand was coarser than 0.104 mm and that 48±0.5 percent of the sand consisted of grains between 0.250 and 0.149 mm. A larger percentage of the impurities were associated with the finer grain size fractions (<0.074 mm). Chemical analyses by atomic absorption or plasma emission spectrometry confirmed that Al and Fe impurities were present but decreased with increasing grain size. Other investigators have also reported that a significant portion of the nonquartz component of the sand is associated with the smallest size fractions (Siegel et al., 1993). Based on these analyses and the measured size distribution of Wedron #510 sand, the 0.149 to 0.250-mm size fraction was selected for use in the sorption experiments.

The selected quartz sand size fraction was chemically treated to remove soluble salts, carbonates and iron-(hydr)oxides. Soluble salts and carbonates were removed by washing the sand in deionized ultrapure water (17.8 MΩ) and processing it in buffered (pH 5.0) acetic acid solution (Morgan's solution) according to the method of Jackson (1956). Approximately 100 g of sand were washed in 300 mL of buffer for 30 min at 90 °C. The solution was then decanted, and the process repeated twice more. Following the removal of carbonates and soluble salts, the sand was rinsed repeatedly with deionized water, filtered, and dried at 80 °C. After drying, the sand was washed in sodium citrate-dithionate-bicarbonate (CDB) solution according to a method modified from Kuntze and Dixon (1986) to remove free iron-(hydr)oxides (e.g., hematite and goethite). About 50 g of sand were immersed in the CDB solution for 30 min at 80 °C. The procedure was repeated three times and was followed by rinsing, filtration, and drying as done previously. Chemical and petrographic analyses of the treated sand showed a virtual elimination of Fe-oxide coatings on the grains. Minerals and grains (i.e, those with pyrite inclusions) with density above that of quartz (2.65 g/cm^3) were then removed by density separation using heavy liquid (Na-polytungstate, Geoliquids). Following removal of nonquartz and "heavy" quartz grains, the sand was rinsed and cleaned using an ultrasonic bath and deionized water, then dried at 80 °C. Surface area measurement of the cleaned 0.149 to 0.250-mm sand size fraction using $N_2(g)$ adsorption (BET method) indicated a surface area of 0.03 m^2/g.

5.2.1.2 Uranium Solutions

U experimental solutions were prepared by dilution of a purchased ^{233}U standard solution (Isotope Products, Inc.) consisting of 99.5 percent by mass ^{233}U. Dilutions were made in a 0.1 molal $NaNO_3$ matrix. A 500 ppb U(6+) (μg/kg) stock solution was prepared initially, and experimental solutions of lower U(6+) concentration (5 and 50 ppb) were prepared by diluting the stock solution. Prior to addition of any quartz sand, the initial pH of each experimental solution was adjusted to a value in the range of 2.0 to 9.0 at approximately 0.25 pH intervals by addition of $NaHCO_3$ or HNO_3. The amount of reagent needed to achieve the desired initial pH of the U(6+) solutions was estimated using the EQ3NR geochemical code (version 3245.R124) with database Data0.com.R12 (Wolery, 1992). For U(6+) solutions with added $NaHCO_3$, equilibration with atmospheric $CO_2(g)$ as indicated by constant pH was reached in about 10 days. Measurements of pH were made using a Ross combination electrode and an Orion 920A pH meter.

U was analyzed by measurement of ^{233}U α-decay using liquid scintillation counting in a Packard 1900TR or 2505TR/AB liquid scintillation analyzer. Prior to counting, duplicate 0.5-mL aliquots were withdrawn from experimental solutions, combined with 0.5 mL of 0.02M HNO_3, and mixed with 5 mL of

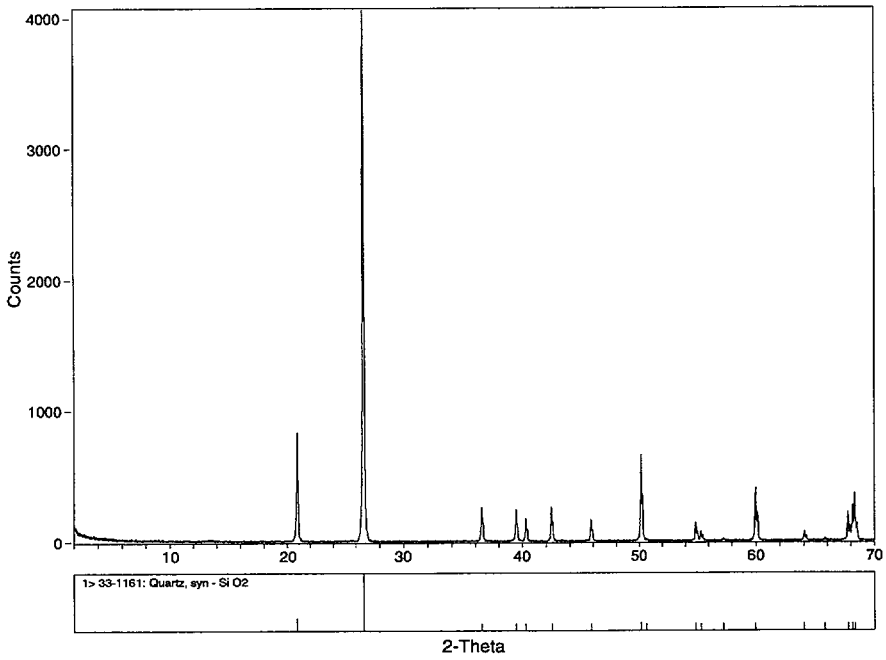

Figure 5-1. X-ray powder diffraction pattern of Wedron #510 silica sand, 0.149 to 0.250-mm size fraction, as compared to JCPDS-PDF card 33-1161, synthetic quartz. The diffraction pattern was collected using Ni-filtered CuK_α radiation (2 to 70 degrees 2-theta, 0.02 2-theta/sec).

Ultima-Gold (Packard) scintillation cocktail in a 7-mL glass vial. For the conditions specified, counting efficiency is at or very near to 100 percent for α-particles, although the counting region of interest is quenched to 100 to 350 keV. Because of the purity of the original standard solution and the relatively long half-life of ^{233}U, the contribution to the measured sample activity from other alpha- or beta-emitting U isotopes and decay daughters is less than 0.1 percent within the counting region of interest and, therefore, was not considered. Each sample was counted for a period of time such that the 2σ error of the reported sample activity in counts per minute (cpm), including background (~3 cpm), was 3 percent for experimental solutions with initial U(6+) concentrations of 500 or 50 ppb, or 5 percent for solutions that initially had 5 ppb U(6+).

5.2.1.3 Experimental Procedure

Experiments were conducted as batch experiments in 60-mL polycarbonate containers. The selection of container type is important because different container materials exhibit differing degrees of sorption affinity for U(6+) (Pabalan et al., 1994). CNWRA investigations showed that, under these experimental conditions, polycarbonate containers performed better (i.e., sorbed less U(6+) at a given pH) than containers made of Teflon-FEP or polypropylene. Even so, the polycarbonate containers adsorb a significant quantity of U(6+) over the pH range from 4 to 8. As a result, the effects of container sorption must be taken into account. Therefore, each experiment consisted of a sorption and desorption phase as described in the following text. The sorption and desorption steps provide information regarding the amount of U(6+) sorbed onto both the container and the substrate of interest, in this case, quartz sand. Experiments were designed such that initial U(6+) concentrations were 5, 50, or 500 ppb, whereas the solid-mass/solution-volume (M/V) ratio was fixed at 2, 20, or 50 g/L. The experimental mixtures were agitated using gyratory shakers (~120 rpm). Five sets of experiments were conducted; the initial conditions of each are summarized in Table 5-1.

The sorption phase of each experiment was started by adding approximately 50 g of ^{233}U solution to

Table 5-1. Summary of experiments

Experiment	[U] (ppb)	M/V (g/L)	Mass Quartz (g)	Average Mass Balance Error	2σ Counting Error
Q1	50	2	0.1	−1.42 ± 1.5%	3%
Q2	50	20	1.0	−0.49 ± 1.0%	3%
Q3	50	50	2.5	0.20 ± 1.3%	3%
Q4	5	20	1.0	−1.26 ± 1.9%	5%
Q5	500	50	2.5	−0.51 ± 1.6%	3%

each experimental container and adjusting the pH. The polycarbonate bottles were loosely capped to allow equilibration with atmospheric $CO_2(g)$ to be maintained throughout the sorption phase of the experiment. After equilibration with $CO_2(g)$, the pH of each solution was then measured, and sample aliquots were withdrawn from solution for U analysis. A predetermined mass of quartz sand was subsequently added to each container. After about 14 days, solution pH was again measured and sample aliquots withdrawn from solution for U analysis.

The desorption phase of the experiment was subsequently started by quantitatively removing the sand from each experimental container using Eppendorf micropipets and transferring the sand (along with some entrained U(6+) solution) to 50-mL polypropylene test tubes. The contents of each polypropylene test tube were acidified using small amounts (~3 mL) of 0.1 M HNO_3 to effect the desorption of U(6+) from the sand. The mass of U(6+) sorbed onto the quartz was determined by analyzing the U(6+) concentration of the solution in each tube after an additional 14 days and making corrections for the U(6+) solution entrained during the sand transfer. The percent of total U(6+) sorbed onto the quartz, percent U_{sorbed}, was calculated by dividing the mass of U(6+) desorbed from the sand, U_{qtz}, by the total mass of U(6+) available (corrected for losses due to sampling) as shown in the following equation:

$$\%U_{sorbed} = \frac{U_{qtz}}{U_{total} - U_{sample}} \times 100\% \qquad (5\text{-}1)$$

where U_{total} is the mass of U originally added to each experimental container and U_{sample} is the mass of U(6+) calculated to have been removed during sampling. It was assumed that the total mass of U(6+) initially added to the experimental containers, corrected for sampling losses, was available to the quartz. This assumption implies that all the U(6+) sorbed onto the container walls prior to addition of quartz can be desorbed and is available for sorption on the mineral; that is, the effect of sorption on the container is neglected, and the mass of U(6+) sorbed on the container is included as part of U_{total}.

By collecting container sorption data in addition to the data for U(6+) sorption on quartz, it may be possible to explicitly account for the effects of container sorption in the conceptual model. Though not included in this report, efforts to incorporate the partitioning of U(6+) onto the container are in progress, and results will be included in future reports. To determine the amount of U(6+) remaining in the original polycarbonate experimental containers U(6+) in the aqueous phase plus U(6+) sorbed on the container walls, the remaining solutions were also acidified with 0.1 M HNO_3 after withdrawal of the quartz sand. Figure 5-2 shows the percent of total U(6+) sorbed onto container walls before and after addition of quartz in the 50-ppb experiment at M/V= 20 g/L.

Mass balance was used to track the total mass of U(6+) in each experiment. The total mass of U(6+) at the end of the desorption phase of the experiment was compared to the mass of U(6+) at the start of the desorption phase. The percent mass error was calculated from the equation:

$$\%\ \text{mass error} = \frac{(U_{qtz} + U_{solution})}{(U_{total} - U_{sample})} \times 100\% \qquad (5\text{-}2)$$

where $U_{solution}$ is the mass of U(6+) remaining in the

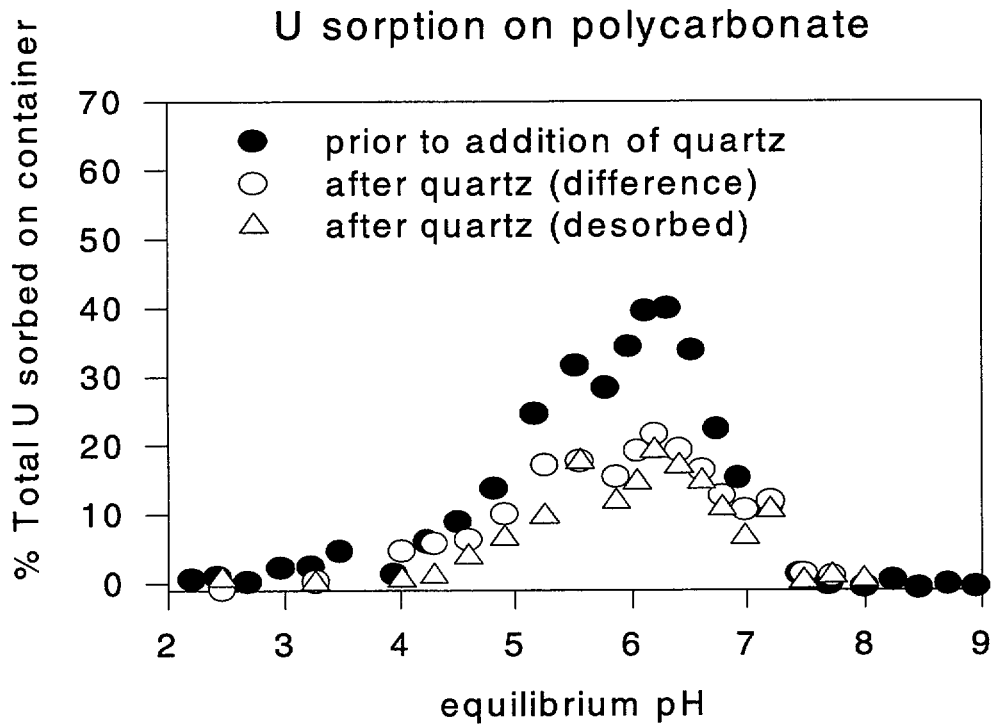

Figure 5-2. Plot of equilibrium U sorption, before (closed circles) and after addition of quartz sand (open circles and triangles), on polycarbonate containers as a function of pH. Container sorption after addition of quartz was determined by subtracting percent U sorbed on quartz from the total percent U sorbed on both quartz and polycarbonate at the end of the sorption phase (open circles) and by calculating the percent U sorbed on the containers from amount U desorbed from the containers in the desorption phase (open triangles).

experimental solution. Mass balance varied for each experiment due to differences in counting error but averaged 2 percent or better. Mass balance results are included in the summary of experimental data (Table 5-1).

5.2.1.4 Experimental Results and Discussion

Figures 5-3(a) and 5-3(b) show U(6+) sorption on quartz as functions of pH and initial U(6+) concentration at M/V ratios equal to 20 and 50 g/L, respectively. Figure 5-4 shows experimental data for initially 50 ppb U(6+) solutions as functions of pH and M/V ratio. The data in these figures demonstrate that U(6+) sorption on quartz is strongly affected by solution pH. U(6+) sorption reaches a maximum at near neutral pH (6.8) and steeply decreases toward acidic or alkaline conditions. This dependence of U(6+) sorption on solution pH has been observed in other studies of U(6+) sorption on quartz and other silicate minerals (e.g., Allard et al., 1980; Pabalan et al., 1993, Waite et al., 1994b), as well as in studies of U(6+) sorption on aluminum- and iron-(hydr)oxides (e.g., Hsi and Langmuir, 1985; Prikryl et al., 1994; Waite et al., 1994a; Zachara and McKinley, 1994).

Figure 5-4 compares the results of three experiments at an initial U(6+) concentration of 50 ppb and M/V ratios of 2, 20, and 50 g/L. The results show that U(6+) sorption increases with increasing M/V ratio. At lower M/V ratios (2 and 20 g/L), the change in sorption with a change in M/V is approximately linear; for example, the maximum sorption for the 2 g/L curve is about 4 to 5 percent, whereas with a tenfold increase in M/V (20 g/L), the maximum sorption is approximately 45 percent. The rise in percent U(6+) sorbed with an increase in M/V results from a corresponding increase in available sorption sites. However, as the M/V ratio continues to increase, the increase in U(6+) sorbed is not proportional (that is, it becomes nonlinear). Previous sorption studies have shown that eventually U(6+) sorption becomes

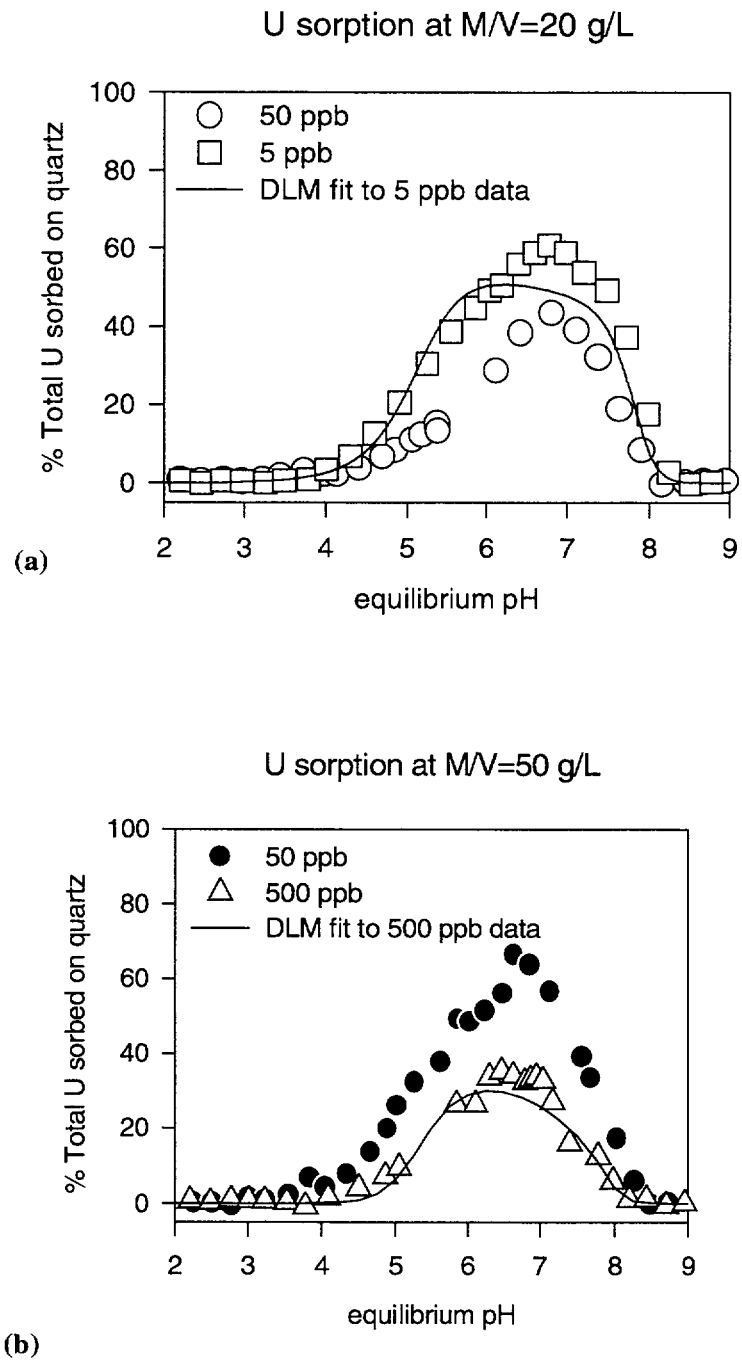

Figure 5-3. Sorption of U on quartz as a function of initial U concentration and pH. (a) U sorption at initial U concentrations of 5 and 50 ppb. Both experiments were conducted at an M/V ratio of 20 g/L. Diffuse-Layer Model (DLM) fit for the 5 ppb data was determined using a two species sorption model as discussed in the modeling section of the text. (b) U sorption at initial concentrations of 50 and 500 ppb. Both experiments were conducted at an M/V ratio of 50 g/L. DLM fit for the 500 ppb data was determined using a two species sorption model as discussed in the text.

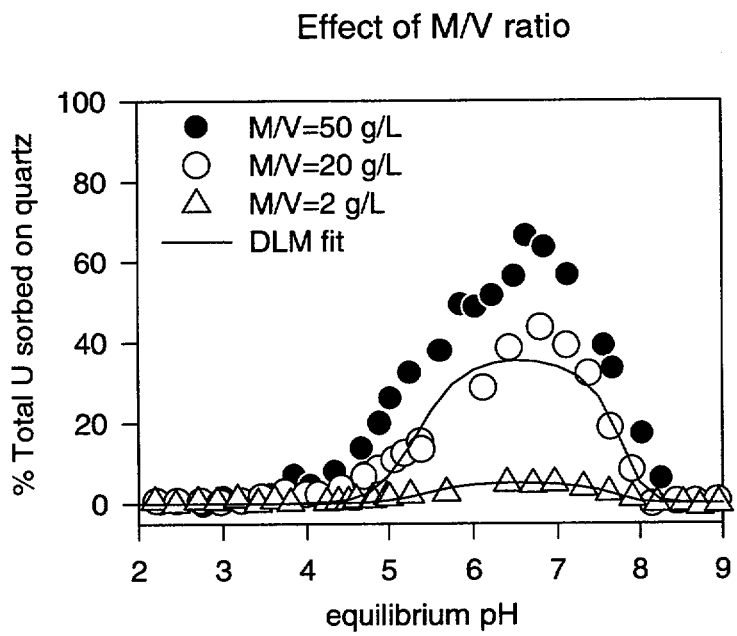

Figure 5-4. Sorption of U on quartz as a function of M/V ratio and pH. All experiments were conducted at an initial uranium concentration of 50 ppb. DLM curves represent best fit for the data at M/V=20 g/L and predicted fit (based on parameters from the fit at 20 g/L) for the data at M/V=2 g/L using a single species complexation model.

insensitive to continued increase in M/V ratio (e.g., Turner, 1995). Essentially, there is a limit to the effect of adding excess sorption sites.

The initial concentration of U(6+) in solution also influences U(6+) sorption on quartz. As shown in Figure 5-3, at a fixed M/V, the percent U(6+) sorbed increases as the initial U(6+) concentration decreases. Indeed, when sorption data at a given pH are plotted versus equilibrium concentration in solution, the data fit a nonlinear Freundlich isotherm (Figure 5-5) well. This fit indicates that sorption of U(6+) on quartz is not proportional to dissolved U(6+) concentration. The trend in adsorption with increasing U(6+) concentration is likely due to the formation of multinuclear aqueous complexes (O'Day, 1994) and is consistent with the postulation that mononuclear U(6+) surface complexes form during U(6+) adsorption (Waite et al., 1994a). The sorption behavior of U(6+) with increasing U(6+) concentration is also indicative of a decrease in the average free energy of adsorption (per mole) with increasing surface coverage (Waite et al., 1994a).

The reasons for the observed sorption behavior with change in M/V and U(6+) concentration are a consequence of the mass balance and equilibrium chemistry in the U(6+)-quartz system. An equilibrium sorption reaction in the form of Eq (5-7) can be combined with the fraction sorbed [(Eq. 5-1)] to give (neglecting activity coefficients, H^+ term, and mass loss due to sampling) an expression [Eq (5-3)] that can be used to describe the effects of changing M/V and initial U(6+) concentration on the percent U sorbed by quartz:

$$\%U_{sorbed} = \frac{(K)\ (>XOH^0)\ (U_{solution})}{U_{initial}}\left(\frac{M}{V}\right) \qquad (5\text{-}3)$$

where K is the equilibrium constant for the sorption reaction, $U_{initial}$ is the initial concentration of U(6+) in solution, and $>XOH^0$ represents available surface sites. As M/V increases, at a given initial U(6+) concentration, the number of available sites also increases. The concentration of U(6+) in solution decreases to compensate for the increase in surface sites, and the relative percent U(6+) sorbed increases. As the initial U(6+) concentration increases, at a given M/V ratio,

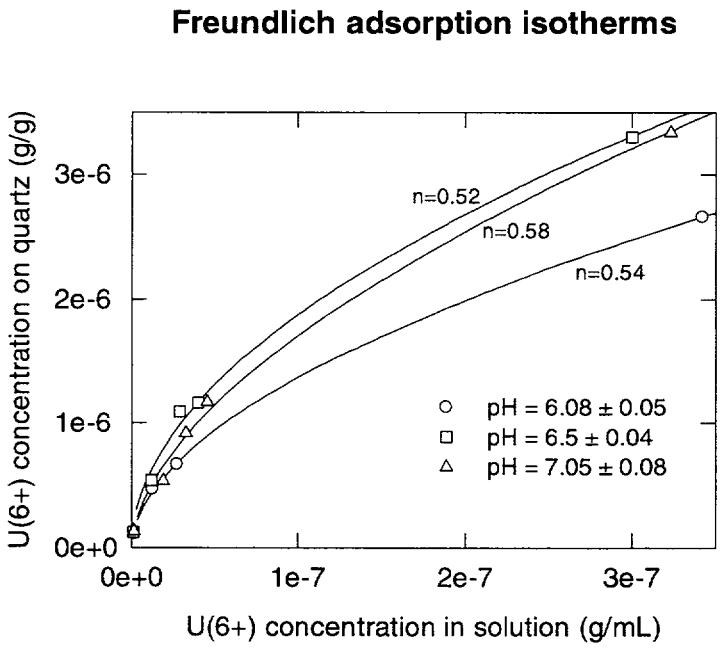

Figure 5-5. Freundlich isotherms of U(6+) sorption data at pH 6, 6.5, and 7. Data are fitted by nonlinear least squares regression using the equation $S=KC^n$, where S is the concentration of U(6+) on the quartz, C is the concentration of U(6+) in solution, and K and n are constants. Values of n below 1 indicate a nonlinear trend in the increase of sorption with increased solution equilibrium concentration of U(6+).

more surface sites are occupied, the equilibrium concentration of U(6+) must increase because less surface sites are available, and the relative percent U(6+) sorbed decreases.

Although it is convenient to represent adsorption data in terms of percent total U(6+) sorbed, plotting sorption results in terms of a distribution coefficient, or Kd, provides a means to normalize the data-to-sediment concentration (or M/V ratio) and to account for the change (decrease) in aqueous solution concentration during the sorption process. The Kd may be defined as:

$$\text{Kd (mL/g)} = \frac{U_{qtz}/\text{mass quartz (g)}}{U_{solution}/\text{volume solution (mL)}} \qquad (5\text{-}4)$$

A plot of log Kd versus equilibrium pH (Figure 5-6) shows the relative effects of changing M/V ratio and initial U(6+) concentration. Even at pH of maximum sorption, the Kd varies over only one order of magnitude for a change in equilibrium U(6+) concentration in solution of two orders of magnitude. Likewise, a change in M/V from 2 to 50 results in a change in log Kd of about 0.25. The results compare favorably to those of other studies of U(6+) sorption on quartz (Figure 5-6). Higher Kd values reported by Waite et al. (1994b) and Allard et al. (1984) are likely due to the combined effects of large substrate surface areas and low initial U(6+) concentrations in solution. Reported sorption values for quartz-rich tuffs from the YM region are somewhat lower (Thomas, 1987).

5.3 SORPTION MODELING

The experimental results presented here for U(6+) sorption on quartz agree with studies for other minerals that have demonstrated that a desorption edge develops at high pH in UO_2–H_2O–CO_2 systems for other minerals (Tripathi, 1984; Hsi and Langmuir, 1985; Pabalan et al., 1993; Prikryl et al., 1994; Waite et al., 1994a). As noted previously (van Geen et al., 1994; Pabalan et al., 1994), one possible explanation for this behavior is the competition for available surface sites by carbonate species such as CO_3^{2-} and HCO_3^-. Due to a lack of data on carbonate sorption on quartz, the conceptual model for U(6+) sorption on quartz developed in this study (discussion following) does not

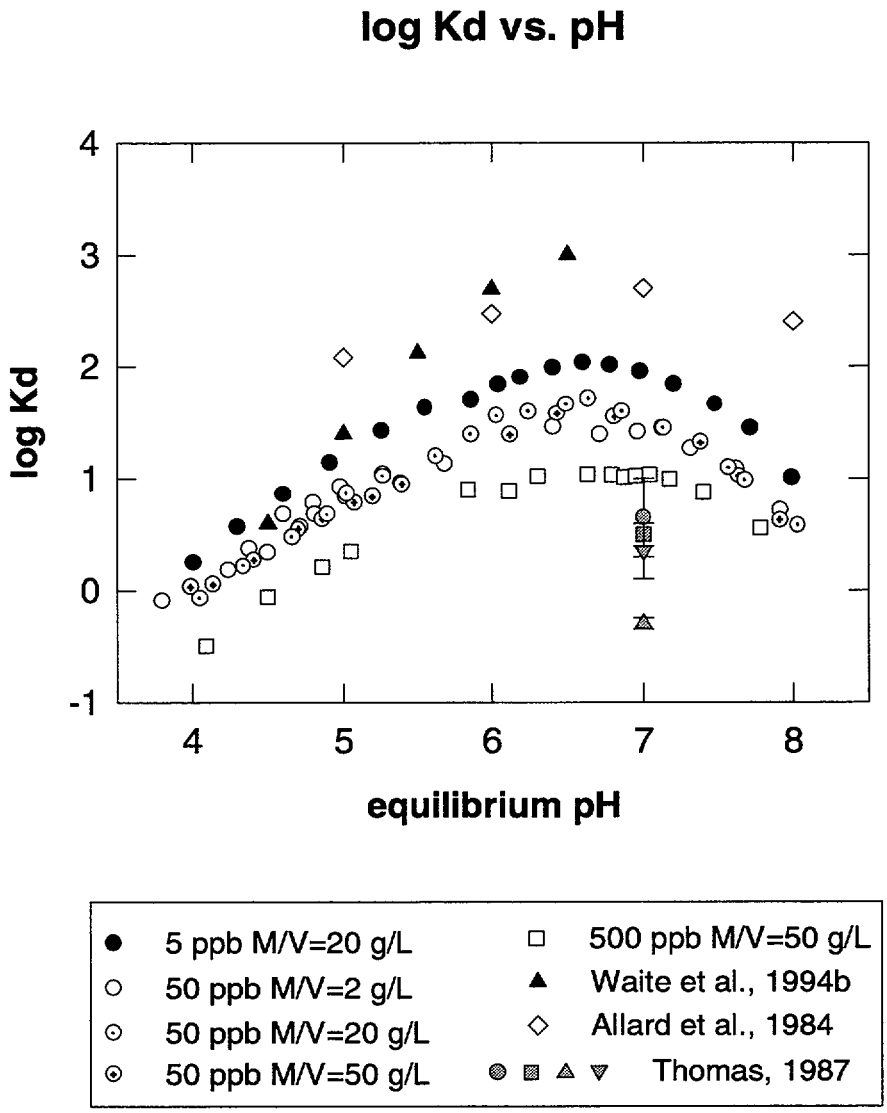

Figure 5-6. Comparison of data for U(6+) sorption on quartz. All data collected under atmospheric conditions and converted to Kd in g/mL. Data from this study are labeled with associated initial solution U(6+) concentration and M/V ratio. Data from Waite et al. (1994b) were determined at [U(6+)]= 1×10^{-6}M (~238 ppb) and M/V=100 g/L using a size fraction between 0.008 and 0.015 mm (equivalent surface area ~50 times that used in this study). Data from Allard et al. (1984) were collected using natural quartz and [U(6+)]=$1–5\times10^{-11}$M (~0.005 ppb) (surface area not available). Data from Thomas (1987) represent sorption experiments on devitrified tuff core samples with predominant quartz and feldspar mineralogy (cores: G1-1982, G1-2333, YM-22, and JA-32) with [U(6+)]=$2\times10^{-7}–5\times10^{-6}$M (~50 to 1000 ppb). Error bars give range of reported Kd values.

explicitly invoke the competition for surface sites by carbonate species (e.g., $>SiOH_2–CO_3^-$). At relatively low carbonate concentrations, this assumption should be reasonable. In the model developed here, the desorption edge at higher pH is assumed to be due to increased carbonate concentration and the stronger U(6+) affinity of the aqueous carbonate ligand relative to the sorption sites. Although this representation may not be accurate, in the absence of definitive data on the surface complexes being formed, it was decided to use the simplest model capable of reproducing the observed sorption behavior.

Surface complexation modeling provides a means to interpret the sorption behavior of actinides in a mechanistic fashion. SCMs are based on the assumption of analogous behavior between the complexation of radionuclides by aqueous ligands in the bulk solution and the formation of radionuclide complexes with functional binding sites at the mineral-water interface. Through the development of a set of surface reactions, the surface sites are treated effectively as another ligand competing for the radionuclide in SCMs. Additional terms account for the effects of electrostatic interactions at the mineral surface on the system chemistry.

Recent efforts in surface complexation theory have developed a uniform Diffuse-Layer Model (DLM) for applications to sorption of heavy metals (Dzombak and Morel, 1990). The model has also been applied with good success to simulate the sorption behavior of actinides such as U and Np (Bradbury and Baeyens, 1993; Turner, 1993; Pabalan and Turner, 1994). The DLM is perhaps the simplest of the SCMs and uses a one-layer representation of the mineral-water interface. Although ionic strength effects on the electrostatic interactions are included in the DLM, supporting electrolytes such as Na^+ and NO_3^- are not assumed to interact with the surface, and sorption reactions for these ions are not included explicitly in the geochemical model. Details of the DLM are presented elsewhere (Dzombak and Morel, 1990; Davis and Kent, 1990; Turner, 1993), and only a brief overview will be presented here.

Neutral amphoteric surface sites ($>XOH^0$) are assumed to develop charge through the addition (protonation) or removal (deprotonation) of a proton to form charged surface sites represented as $>XOH_2^+$ and $>XO^-$, respectively. These reactions are written in the form

$$>XOH^0 + H^+ \leftrightarrow >XOH_2^+ \text{ (Protonation, } K_+) \quad (5\text{-}5)$$

$$>XOH^0 \leftrightarrow >XO^- + H^+ \quad \text{(Deprotonation, } K_-) \quad (5\text{-}6)$$

where K_+ and K_- are referred to as the surface acidity constants. The acidity constants K_+ and K_- are determined by analysis of potentiometric titration data for the mineral of interest (Dzombak and Morel, 1990; Turner, 1993). The values for the acidity constants are model specific, but once they are defined, the acid-base behavior of the surface is characterized, and these values become fixed in the geochemical model. Sorption is represented by postulating the formation of one or more complexes at the mineral-water interface between these sites and the cations and anions in solution. For the DLM, sorption is assumed to take place directly on the mineral surface, forming what are called inner-sphere complexes. For example, for the cation C^{z+} the reaction may be represented as

$$>XOH^0 + C^{z+} \leftrightarrow >XO\text{-}C^{(z-1)+} + H^+ \quad \text{(Complexation, } K_c) \quad (5\text{-}7)$$

where the constant K_c is often referred to as the binding constant and is the remaining adjustable parameter for the DLM. In the absence of independent data, the exact form of the reaction is typically postulated by the modeler based on the aqueous speciation of the element of interest.

In this study the DLM model used was further simplified to maximize the ease of computation and limit the number of required entry parameters. A site density of 2.3 sites/nm^2 (Dzombak and Morel, 1990) was assumed and combined with the specific surface area to calculate the total number of available sites. The acidity constant for the $>SiOH^0$ site was derived based on interpreting potentiometric titration data for amorphous SiO_2 as described in Turner (1993). Due to a lack of data on site heterogeneity, only one type of silanol site was assumed, and consideration was limited to the formation of monodentate, mononuclear uranyl surface complexes. Model parameters are given in Table 5-2.

To determine the binding constants for the U(6+) sorption reactions, the nonlinear parameter optimization code FITEQL, Version 2.0 was used (Westall, 1982). FITEQL requires as input a chemical

Table 5-2. Summary of DLM parameters

Surface Reactions	Binding Constant (log K)
$>SiOH^0 \leftrightarrow >SiO^- + H^+$	$-7.2^{(a)}$
$>SiOH^0 + UO_2^{2+} \leftrightarrow >SiO{-}UO_2^+ + H^+$	−0.1 to 0.5
$>SiOH^0 + UO_2^{2+} + CO_3^{2-} \leftrightarrow >SiOH{-}UO_2CO_3^0$	16.4 to 17.0
Specific Surface Area (A_{SP}) = 0.03 m^2/g Site Density (N_S) = 2.3 sites/nm^2 M/V = 2, 20, and 50 g/L (a) From Turner (1993).	

equilibrium model for the system of interest that includes stoichiometries and mass action constants for aqueous speciation reactions, acidity constants for the protonation and deprotonation of the surface sites [Eqs. (5-5) and (5-6)], and assumes a surface complexation reaction of the general form used in Eq. (5-7). The input file also includes the empirical pH-dependent sorption data to be regressed. Using mass balance and mass action constraints, FITEQL iteratively adjusts the binding constant for the postulated sorption reaction until the difference between the calculated results and the experimental data is minimized.

In the current study, the FITEQL derived binding constants were used in the geochemical speciation code MINTEQA2 (Allison et al., 1991) to reproduce U(6+) sorption behavior on quartz. Equilibrium constants for aqueous speciation reactions in the UO_2–H_2O–CO_2 system were selected from the CNWRA MINTEQA2 database (Turner, 1993), which is based on the NEA Thermodynamic Database for U (Grenthe et al., 1992). With the purpose of maintaining a simple model, the following inner-sphere reaction proved to reasonably reproduce the observed data at [U(6+)]=50 ppb and M/V=20 g/L and predict observed data at [U(6+)]=50 ppb and M/V=2 g/L (Figure 5-4):

$$>SiOH^0 + UO_2^{2+} + CO_3^{2-} \leftrightarrow >SiOH\text{-}UO_2CO_3^0 \qquad (5\text{-}8)$$

The binding constants determined for this reaction are listed in Table 5-2. The range for the binding constants reflects the differences in the values determined for each data set.

In an effort to improve the model predictions for the observed 5 and 500 ppb data, a second inner-sphere reaction was added.

$$>SiOH^0 + UO_2^{2+} \leftrightarrow >SiO\text{-}UO_2^+ + H^+ \qquad (5\text{-}9)$$

The binding constant range determined for this reaction is also listed in Table 5-2. Model results for the 5 and 500 ppb data are shown in Figures 5-3(a) and 5-3(b), respectively.

Developing approaches that are based on geochemical principles, such as the DLM, allows quantitative examination of sorption under physicochemical conditions outside experimental values in a way that is beyond the capabilities of purely empirical approaches. SCMs such as the DLM are designed to reproduce macroscopic behavior in solid-gas-water systems. Constructing the conceptual model of the mineral-water interface using a set of reactions of the form given in Eqs. (5-5) through (5-9) allows the application of mass balance and mass action constraints to determine sorption as a function of system chemistry. For example, since H^+ is the potential determining ion, the protonation/deprotonation of the surface sites and the formation of surface complexes vary as a function of pH. This feature enables the DLM to simulate pH-dependent sorption behavior observed for the actinides. The model can also be adapted to predict the effects of changes in M/V ratio and total carbon. Although the models define one or more surface

reactions, there is typically a lack of independent analytical data supporting the formation of a particular surface complex. In the absence of these data, the exact form of the surface reaction is generally selected by the modeler based on the analogous reactions in aqueous speciation.

Review of the sorption model curves reveals a slight over prediction of sorption between pH 5.5 and 6 and a slight under prediction of sorption near pH 7. The calculated distribution of uranyl species on the quartz surface and in solution for a U(6+) concentration of 50 ppb and an M/V=20 g/L (Figure 5-7) shows that sorption over the pH range from 4 to 8 is dominated by neutral and univalent positively charged U(6+) species. Slight differences in published log K values versus the actual log K values for these species could result in the fit errors observed. Similarly, model overestimation of the influence of carbon species (e.g., $UO_2(CO_3)_2^{2-}$) could result in the underestimation of sorption near pH 7. Another aspect to consider is that the modeling approach does not allow for automatic iterative regression of all possible species at once. As such, the analogous aqueous species reactions may be inadequate or the proper combination of species may not have been selected. Nevertheless, the DLM reproduces sorption behavior of U(6+) effectively, especially considering the complexity of the uranyl species distribution exhibited in Figure 5-7.

5.4 ASSESSMENT OF PROGRESS TOWARD MEETING PROJECT OBJECTIVES

The broad objective of this project is to develop sufficient understanding of issues of radionuclide sorption relevant to radionuclide transport modeling. An important mechanism for attenuating radionuclide transport could be sorption of radionuclides on minerals encountered along the flow paths. Results of laboratory experiments on U(6+) sorption combined with modeling efforts using surface-complexation models are providing an understanding of the important parameters that control the sorption behavior of an actinide element. For example, the experimental results reported here and in previous CNWRA reports (e.g., Pabalan and Turner, 1994; Pabalan et al., 1994) demonstrate that U(6+) sorption on quartz, montmorillonite, clinoptilolite, and α-alumina are strongly dependent on pH. U(6+) sorption on these minerals, which are sorbents of distinct mineralogic and surface properties, reaches a maximum at near neutral pH (~6.3 to 6.8) and decreases steeply towards more acidic or alkaline conditions. The M/V ratio (or analogously, surface-area to solution-volume ratio) also influences sorption, that is, as the ratio increases, the relative amount of U(6+) sorbed on the solid also increases. In addition, the relative amount of U(6+) sorbed increases with decreasing initial U(6+) concentration. Because of the strong dependence on pH, M/V ratio, and U(6+) concentration, modeling of sorption processes will likely require that changes in groundwater chemistry and in rock/fluid ratio be properly accounted for in PA calculations if retardation by sorption processes is included. However, the success of the surface-complexation model in describing and predicting U(6+) sorption on quartz, montmorillonite, and other minerals suggests that SCMs offer a scientifically defensible approach that may be useful for PA calculations.

The similarity in the pH-dependence of U(6+) sorption on quartz, montmorillonite, clinoptilolite, and α-alumina is important. It may help identify simplified approaches to modeling sorption and thus help in the development of CDMs relevant to the KTUs identified in Section 5.1 and in developing conceptual models related to the PA Research Project and the IPA Phase 3. The information derived from the laboratory experiments may also help interpret data on U distribution and migration at the Peña Blanca field site of the Geochemical Analog of Contaminant Transportation in Geochemical Rock Research Project.

5.5 PLANS FOR NEXT REPORT PERIOD

Experiments to be conducted in the future will focus on ^{237}Np sorption on quartz, clinoptilolite and montmorillonite. These experiments will investigate the dependence of Np sorption on pH, M/V, and Np concentration. In addition, experiments studying the effect of pCO_2 on U(6+) sorption on clinoptilolite will be completed, and results will be presented in the next semi-annual report. Preliminary experiments will also be initiated using ^{239}Pu as the sorbate. The data generated from all these experiments will continue to be utilized in the modeling activities being conducted in this project and extended to radionuclide transport models used in IPA.

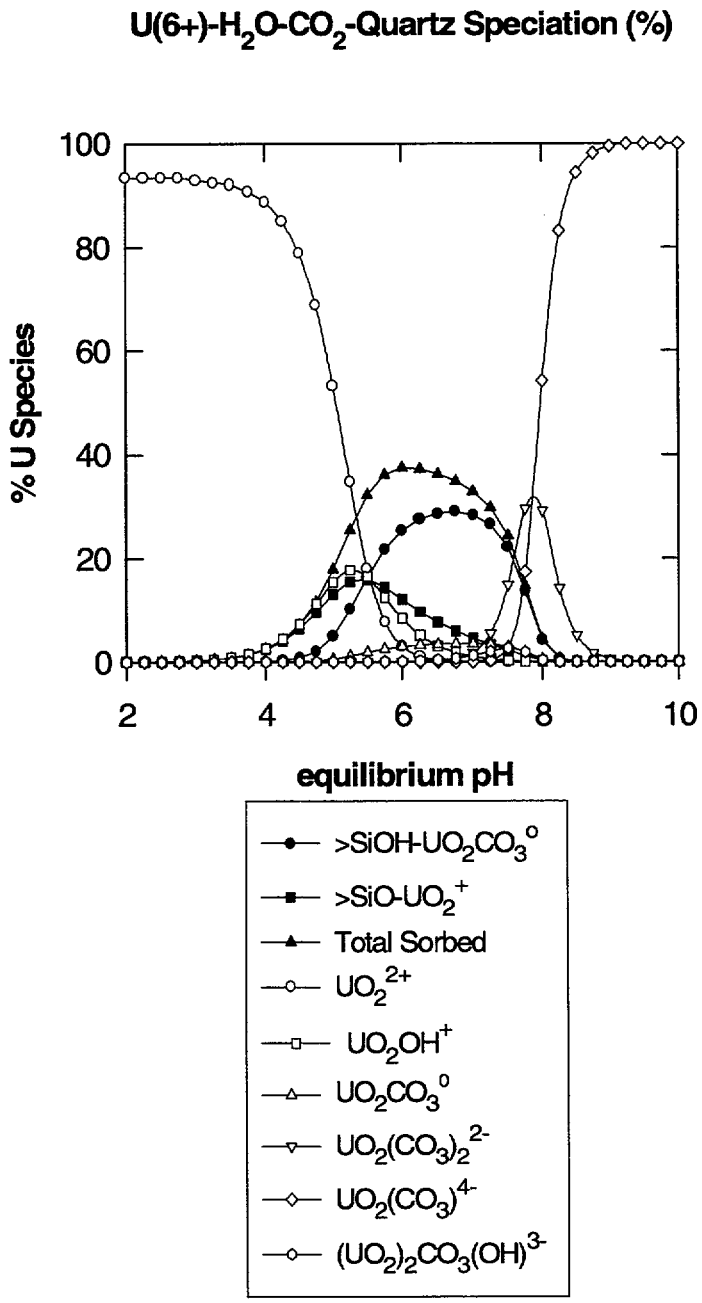

Figure 5-7. MINTEQA2 calculated distribution of uranyl species in solution (open symbols) and on the quartz surface (closed symbols) at [U(6+)]=50 ppb and M/V=20 g/L. Aqueous species contributing to less than 2 percent of the total distribution over the pH range of 2 to 9 are not plotted (nitrate species at low pH are also excluded).

5.6 REFERENCES

Allard, B., G.W. Beall, and T. Krajewski. 1980. The sorption of actinides in igneous rocks. *Nuclear Technology* 49: 474–480.

Allard, B., U. Olofsson, B. Torstenfelt. 1984. Environmental actinide chemistry. *Inorganica Chimica Acta* 94: 205–224.

Allison, J.D., D.S. Brown, and K.J. Novo-Gradac. 1991. *MINTEQA2/PRODEFA2, A Geochemical Assessment Model for Environmental Systems: Version 3.0 User's Manual.* EPA/600/3-91/021 Environmental Research Laboratory, Office of Research and Development. Athens, GA: U.S. Environmental Protection Agency.

Bish, D.L., and S.J. Chipera. 1989. *Revised Mineralogic Summary of Yucca Mountain, Nevada.* Report LA-11497-MS. Los Alamos, NM: Los Alamos National Laboratory.

Bish, D.L., and D.T. Vaniman. 1985. *Mineralogic Summary of Yucca Mountain, Nevada.* LA-10542-MS. Los Alamos, NM: Los Alamos National Laboratory.

Bradbury, M.H., and B. Baeyens. 1993. A general application of surface complexation to modeling radionuclide sorption in natural systems. *Journal of Colloid and Interface Science* 158: 364–371.

Davis, J.A., and D.B. Kent. 1990. Surface complexation modeling in aqueous geochemistry. *Reviews in Mineralogy: Volume 23. Mineral-Water Interface Geochemistry.* M.F. Hochella, Jr., and A.F. White, eds. Washington, DC: Mineralogical Society of America: 177–260.

Dzombak, D.A., and F.M.M. Morel. 1990. *Surface Complexation Modeling: Hydrous Ferric Oxide.* New York, NY: John Wiley and Sons.

Grenthe, I., J. Fuger, R. Konings, R. Lemire, A. Muller, C. Nguyen-Trung, and H. Wanner. 1992. *Chemical Thermodynamics of Uranium.* Amsterdam, North-Holland.

Hsi, C. D., and D. Langmuir. 1985. Adsorption of uranyl onto ferric oxyhydroxides: Application of the surface complexation site-binding model. *Geochimica et Cosmochimica Acta* 49: 1,931–1,941.

Jackson, M.L. 1956. *Soil Chemical Analyses—Advanced Course.* (Fourth Printing, 1968). Madison, WI: Published by the author, Department of Soil Science, University of Wisconsin.

Kuntze, G.W., and J.B. Dixon. 1986. Pretreatment for mineralogical analysis. *Methods of Soil Analysis, Part I. Physical and Mineralogical Methods. Agronomy Monograph No. 9* (2nd edition). Page et al., eds. Madison, WI: American Society of Agronomy—Soil Science Society of America: 91–100.

Nuclear Regulatory Commission. 1992. *Disposal of High-Level Radioactive Wastes in Geologic Repositories.* Title 10, Energy, Part 60 (10 CFR Part 60). Washington, DC: U.S. Government Printing Office.

O'Day, P.A. 1994. Free energies of adsorption of divalent metal ions on quartz. *Geological Society of America Abstracts with Program 1994 Annual Meeting.* Boulder, CO. Geological Society of America: 26(7): A-111.

Pabalan, R.T., J.D. Prikryl, P.M. Mueller, and T.B. Dietrich. 1993. Experimental study of U(+6) sorption on the zeolite mineral clinoptilolite. . *Scientific Basis for Nuclear Waste Management XVI.* MRS Symposium Proceedings 294. C.G. Interrante and R.T. Pabalan, eds. Pittsburgh, PA: Materials Research Society: 777–782.

Pabalan, R.T., and D.R. Turner. 1994. Sorption modeling for HLW performance assessment. *NRC High-Level Radioactive Waste Research at CNWRA July–December 1993.* B. Sagar, ed. CNWRA 93-02S. San Antonio, TX: Center for Nuclear Waste Regulatory Analyses: 8-1 to 8-23.

Pabalan, R.T., D.R. Turner, and F.P. Bertetti. 1994. Sorption modeling for HLW performance assessment. *NRC High-Level Radioactive Waste Research at CNWRA January–June 1994.* B. Sagar, ed. CNWRA 94-01S. San Antonio, TX: Center for Nuclear Waste Regulatory Analyses: 77–95.

Prikryl, J.D., R.T. Pabalan, D.R. Turner, and B.W. Leslie. 1994. Uranium sorption on α-alumina: Effects of pH and surface-area/solution-volume ratio. *Radiochimica Acta* (in press).

Siegel, M.D., D.B. Ward, W.C. Cheng, C. Bryant, C.S. Chaocas, and C.G. Reynolds. 1993. Preliminary characterization of materials for a reactive transport model validation experiment. *Proceedings of the Fourth Annual International High-Level Radioactive Waste Management Conference,* La Grange Park, IL: American Nuclear Society and American Society of Civil Engineers: 348–356.

Thomas, K.W. 1987. *Summary of Sorption Measurements Performed with Yucca Mountain, Nevada, Tuff Samples and Water from Well J-13.* Report LA-10960-MS. Los Alamos, NM: Los Alamos National Laboratory.

Tripathi, V.S. 1984. *U(VI) Transport Modeling: Geochemical Data and Submodels.* Unpub. Ph.D. Dissertation. Stanford, CA: Stanford University.

Turner, D.R. 1993. *Mechanistic Approaches to Radionuclide Sorption Modeling.* CNWRA 93-019. San Antonio, TX: Center for Nuclear Waste Regulatory Analyses.

Turner, D.R. 1995. *A Uniform Approach to Surface Complexation Modeling of Radionuclide Sorption.* CNWRA 95-001. San Antonio, TX: Center for Nuclear Waste Regulatory Analyses.

van Geen, A., A.P. Robertson, and J.O. Leckie. 1994. Complexation of carbonate species at the goethite surface: Implications for adsorption of metal ions in natural waters. *Geochimica et Cosmochimica Acta* 58: 2,073–2,086.

Waite, T.D., J.A. Davis, T.E. Payne, G.A. Waychunas, and N. Xu. 1994a. Uranium(VI) adsorption to ferrihydrite: Application of a surface complexation model. *Geochimica et Cosmochimica Acta* 58: 5,465–5,478.

Waite, T.D., T.E. Payne, J.A. Davis, and K. Sekine. 1994b. Uranium sorption modeling—A surface complexation approach. *Fifth Natural Analogue Working Group Meeting and Alligator Rivers Analogue Project (ARAP) Final Workshop.* Brussels: Commission of the European Communities: Final Report n° EUR EN: 95-100. H. von Maravic and J. Smellie, eds. EIR-15176: 95–100.

Westall, J.C. 1982. *FITEQL: A Computer Program for Determination of Chemical Equilibrium Constants from Experimental Data, Version 2.0.* Report 82-102. Corvallis, OR: Oregon State University, Department of Chemistry.

Wolery, T.J. 1992. *EQ3/6, A Software Package for Geochemical Modeling of Aqueous Systems: Package Overview 1 and Installation Guide (version 7.0).* UCRL-MA-110662 PT 1. Livermore, CA: Lawrence Livermore National Laboratory.

Zachara, J.M., and J.P. McKinley. 1994. Influence of hydrolysis on the sorption of metal cations by smectites: Importance of edge coordination reactions. *Aquatic Sciences* 55: 250–261.

THIS PAGE INTENTIONALLY LEFT BLANK

6 PERFORMANCE ASSESSMENT RESEARCH

by Robert G. Baca, Peter C. Lichtner, Gordon W. Wittmeyer, and Stuart A. Stothoff

Investigators: ***Robert G. Baca, Ronald T. Green, Peter C. Lichtner, Sitakanta Mohanty, Budhi Sagar, Stuart A. Stothoff, and Gordon W. Wittmeyer (CNWRA); Christopher J. Freitas (SwRI); Evaristo J. Bonano, Mohan Seth, and Michael Cruse (Consultants)***

NRC Project Officer: ***John D. Randall***

6.1 TECHNICAL OBJECTIVES

Performance Assessment (PA) is a scientific evaluation process that will be used to judge the acceptability of the proposed repository system at Yucca Mountain (YM). In conducting a PA, the Nuclear Regulatory Commission (NRC) will utilize a hierarchy of models and codes. The top level or total-system PA code, which is being developed under the NRC Division of Waste Management (DWM) Iterative Performance Assessment (IPA) activity, models a wide variety of processes, phenomenological interactions, and future system states, but in a necessarily simplified manner. In contrast, the lower-level codes in this hierarchy are very sophisticated, but model only a few processes in a very detailed manner. Quite interestingly, both types of codes typically exceed the computational limits of conventional computers and push the capability of the most advanced, high-performance supercomputers. The technical objectives of the PA Research Project are to develop PA modeling technology appropriate for NRC compliance determination in three specific areas: (i) alternate conceptual models of key phenomena and future system states (i.e., disruptive scenarios), (ii) efficient and robust computational and computer techniques for solving the model equations, and (iii) formalized approaches for evaluating (i.e., confidence building) mathematical models and testing computer codes.

One of the primary programmatic objectives of the PA Research Project is to provide modeling technology that will benefit the ongoing NRC IPAs. Another, and equally important, programmatic objective is to provide the knowledge base necessary for supporting: (i) revision of the postclosure PA Compliance Determination Strategies (CDSs) (i.e., CDS 6.1, 6.2, and 6.3), and (ii) development of postclosure performance Compliance Determination Methods (CDMs) that will be incorporated into appropriate sections of the License Application Review Plan (LARP) (Nuclear Regulatory Commission, 1994). Specifically, this research project is contributing to the knowledge base for addressing Key Technical Uncertainties (KTUs) associated with:

(i) Conceptual models

(ii) Mathematical models

(iii) Model parameters

(iv) Future system states

(v) Model validation

At present, the KTU related to the first three items resulted in the associated CDS being classified as Review Level 4, while the CDS associated with the fourth item is classified Review Level 5; these KTUs are broadly addressed in Tasks 1 and 2 of this research project. The last KTU requires a type Level 5 Review of CDS 6.1—Assessment of Compliance with the Requirement for Cumulative Releases of Radioactive Materials and is being addressed in a focused effort under Task 3 of this research project. In addition, the practical experience and expertise gained from this research project will place the NRC and the Center for Nuclear Waste Regulatory Analyses (CNWRA) in a position to thoroughly and independently evaluate the U.S. Department of Energy (DOE) PA models and codes.

Because of its multidisciplinary nature, the PA Research Project is an integrated programmatic effort drawing on expertise from many technical disciplines such as hydrology, geochemistry, structural geology, volcanology, seismology, climatology, computational fluid dynamics, and computer science. At present, the PA Research Project is closely integrated with the DWM IPA activity and three other Office of Nuclear Regulatory Research (RES) projects: (i) the Geochemical Analog of Contaminant Transport in Unsaturated Rock Research Project, (ii) the Sorption

Modeling for High-Level Waste Performance Assessment Research Project, and (iii) the Subregional Hydrogeologic Flow and Transport Research Processes. In conjunction with the Geochemical Analog of Contaminant Transport in Unsaturated Rock Research Project, data from rock cores obtained from the Peña Blanca field site are being analyzed to improve conceptual and mathematical models of: (i) variably saturated flow in the fractured porous tuff, and (ii) radionuclide transport in discrete fractures and diffusion into and out of the rock matrix. In addition, data on diffusion and sorption coefficients, compiled under the Sorption Modeling for High-Level Waste Performance Assessment Research Project, are contributing to conceptual/mathematical model development of radionuclide transport phenomena. Studies recently initiated under the Subregional Hydrogeologic Flow and Transport Research Project have identified a number of PA technology needs associated with: (i) computational aspects that currently limit the practical application of detailed hydrologic codes (e.g., BIGFLOW) to the YM site, and (ii) modeling variably saturated flow in tuff rocks with interconnected fracture systems. Work conducted under Task 2 of the PA Research Project is being focused to reduce or remove these modeling limitations.

The PA Research Project is designed to address a number of user needs identified by the DWM for post-closure PA. Specific research needs include: (i) the means to identify and screen scenarios, (ii) efficient integration of mathematical models into repository PA methodology, (iii) validation of mathematical models, (iv) evaluation of mathematical models, (v) evaluation of mathematical flow and transport models applicable to unsaturated fractured rock and application to a range of scales and heterogeneities, and (vi) appraisal of the applicability of existing mathematical models of hydrologically and chemically coupled flow and transport.

Research conducted under the PA Research Project is divided among three major tasks. The first task, Conceptual Model Development, focuses on developing conceptual/mathematical models in two areas: (i) the flow and transport phenomena, and (i) the computational Model Development. Research is directed toward the development of advanced numerical methods necessary to implement PA conceptual and mathematical models. Under the third task, Model Evaluation, model testing and confidence building techniques are being developed based on the experience gained from the INTRAVAL project test cases. Work completed on these tasks has been reported in previous semi-annual research reports. This section describes the results of the PA Research Project for the second half of 1994.

6.2 SIGNIFICANT TECHNICAL ACCOMPLISHMENTS

In this reporting period, research emphasis was focused on topics associated with Conceptual Model Development (Task 1) and Model Evaluation (Task 3). Under Task 1, a reconnaissance level study was performed to evaluate the possible effect of hydrochemical conditions on porosity and permeability of tuff. Simple models were developed for the chemical kinetics of mineral dissolution and its impact on the hydraulic properties of the tuff. The models were then applied to gain insight into possible permeability and porosity changes as a function of repository temperature. As part of Model Evaluation (Task 3), a detailed study was conducted to examine the relation of model predictive reliability to the level of complexity incorporated into the hydrogeologic conceptual model. The study was conducted using the extensive data set obtained from the Las Cruces trench experiment in New Mexico. Significant findings and results of these two activities are summarized in the following subsections. More detailed information can be found in Lichtner (1994a) and Wittmeyer et al. (1994).

A number of research activities, which are not summarized in this section, also produced substantive products. Those activities made direct contributions by addressing the five PA KTUs, providing models and codes for use in IPA, and establishing a technical knowledge base useful for reviewing the DOE PA activities. Further discussion of the benefits of these PA research activities is presented in Section 6.3.

6.2.1 Analysis of Hydrochemical Effects on Porosity and Permeability

During the postclosure phase, the repository system is expected to experience significant changes in its physical properties and chemical conditions. Thermal conditions produced by radiological-decay heating will be the primary factor inducing these changes. One important concern is the possibility that hydrochemical conditions created by the elevated rock temperatures may have an adverse effect on the hydraulic properties of the tuff rocks. A preliminary study was conducted to

estimate the maximum increase in porosity and permeability that might occur as a result of refluxing fluid into the tuff, which is well-undersaturated (chemically) with respect to the host rock minerals. This undersaturation could occur at the condensation region of a stationary heat-pipe. However, for these results to fully apply, the heat-pipe would have to remain stationary for time periods of hundreds to several thousands of years, which is unlikely. The calculations presented here do not take into account the possible formation of secondary mineral products that could reduce the porosity and permeability. Therefore, the calculations represent conservative bounds on adverse porosity and permeability changes.

To compute changes in porosity and permeability, it is necessary to calculate the rate at which minerals dissolve at the desired temperature. The maximum temperature that can occur in a partially saturated porous medium can be substantially above 100 °C due to vapor pressure lowering effects resulting from capillary forces. The mineral dissolution rate involves the kinetic rate constant, mineral surface area, and chemical saturation state of the mineral in the aqueous solution in which it is reacting. The kinetic rate constant $k(T)$ is given as a function of temperature T by the equation

$$k(T) = k_0 \frac{T}{T_0} \exp\left[-\frac{\Delta H}{R}\left(\frac{1}{T}-\frac{1}{T_0}\right)\right] \qquad (6\text{-}1)$$

where k_0 denotes the rate constant at temperature T_0, ΔH is the enthalpy of activation, and R denotes the gas constant. The rates of K-feldspar and cristobalite are plotted in Figure 6-1 as a function of temperature using activation enthalpies of 35.3 and 75.3 kJ mol^{-1} and rate constants of 3×10^{-16} and 1.58×10^{-18} mol cm^{-2} sec^{-1}, respectively. The rate constant for cristobalite is derived from data of Rimstidt and Barnes (1980), and the K-feldspar rate constant is derived from data of Helgeson et al. (1984). As can be seen from the figure, the K-feldspar rate constant increases by approximately 1.3 and cristobalite by 2.75 log units from 25 to 100 °C.

The maximum change in porosity and permeability can be calculated independent of the fluid flow velocity by allowing the minerals in the rock to dissolve at the far-from-equilibrium dissolution rate. It must be emphasized that this gives the maximum change possible for a given rate constant, and ignores effects of the chemical saturation state on the dissolution rate, which would act to reduce the rate or even change its sign. To calculate the dissolution rate, it is necessary to make some assumptions regarding the change in surface area with reaction progress. Fortunately, the final results should not differ greatly (less than an order of magnitude) for different assumptions made. Clearly, in the limit that a mineral grain completely dissolves, the surface area must vanish. One possible form for the variation of mineral surface area with dissolution is to assume a two-thirds dependence of the surface area on mineral volume fraction according to the expression:

$$s_m = s_m^0 \left(\frac{\phi_m}{\phi_m^0}\right)^{2/3} \qquad (6\text{-}2)$$

where s_m^0 and ϕ_m^0 denote the initial surface area per bulk volume of rock and initial volume fraction of the m^{th} mineral, respectively. The initial surface area, taken to be proportional to the amount of the m^{th} mineral present and inversely proportional to the mineral grain size taken as cubical grains with dimension b_m, is as follows

$$s_m^0 = \phi_m^0 \frac{6}{b_m} \qquad (6\text{-}3)$$

where the factor 6 arises from the 6 faces of a cube. For far-from-equilibrium conditions, the change in mineral volume fraction at a fixed point in space satisfies the differential equation

$$\frac{\partial \phi_m}{\partial t} = -\bar{V}_m k_m s_m^0 \left(\frac{\phi_m}{\phi_m^0}\right)^{2/3} \qquad (6\text{-}4)$$

where $\bar{V}_m$ denotes the mineral molar volume and k_m is the rate constant corresponding to the mth mineral as given by Eq. (6-1). This equation has the solution (Helgeson et al., 1984)

$$\phi_m(t) = \phi_m^0 \left(1 - \frac{1}{3}\frac{\bar{V}_m k_m s_m^0}{\phi_m^0}\right)^3 \qquad (6\text{-}5)$$

The mineral completely dissolves when

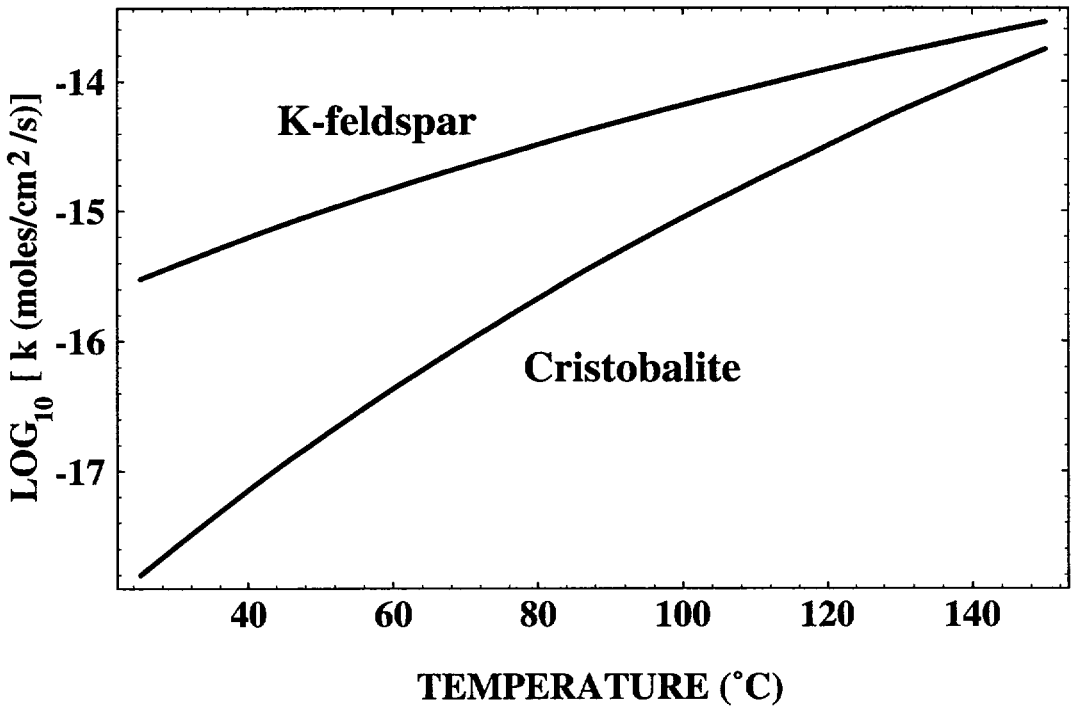

Figure 6-1. Rate constants (t_ε) for K-feldspar and cristobalite as a function of temperature

$$t = 3\frac{\phi_m^0}{\bar{V}_m k_m s_m^0} \qquad (6\text{-}6)$$

The time for the mineral volume fraction to change by a factor ε , denoted by t_ε , is given by

$$t_\varepsilon = \frac{3\phi_m^0}{\bar{V}_m k_m s_m^0}(1-\varepsilon^{1/3}) \qquad (6\text{-}7)$$

The quantity t_ε is plotted in Figure 6-2 as a function of temperature for K-feldspar and cristobalite for ε =0.9 (a 10-percent change in mineral volume fraction) using ϕ_{Kf}^0 =0.6, ϕ_{Cb}^0 =0.3, s_{Kf}^0=36,000 cm^{-1}, and s_{Cb}^0=18,000 cm^{-1}, that is, one-tenth of a millimeter-sized grain ($\bar{V}_{Cb}$=25.74, $\bar{V}_{Kf}$=108.9 cm^3 mol^{-1}). These values are representative of tuff at YM. With these values at 100 °C, cristobalite takes approximately 2,400 yr and K-feldspar only 75 yr for the volume fraction to change by 10 percent, both well within the time span that a temperature of this magnitude can be maintained in a high-level waste repository. Plotting the volume functions of K-feldspar and cristobalite as a function of temperature at an elapsed time of 1,000 yr, in Figure 6-3, it can be seen that K-feldspar is completely dissolved at a temperature of approximately 120 °C.

It should be kept in mind that the rate constants and surface areas may be uncertain by orders of magnitude. It has been observed, for example, that the rate of quartz dissolution can increase by orders of magnitude with the addition of alkali to the solution (Dove and Crerar, 1990). Therefore, the value used here for cristobalite may be too small and, hence, the time for a 10-percent change in volume fraction may be too long. However, the measured groundwaters at YM are supersaturated with respect to cristobalite, indicating the presence of a kinetic barrier at 25 °C. Furthermore, it has been tacitly assumed that water is able to come in contact with the entire surface of a mineral grain. This

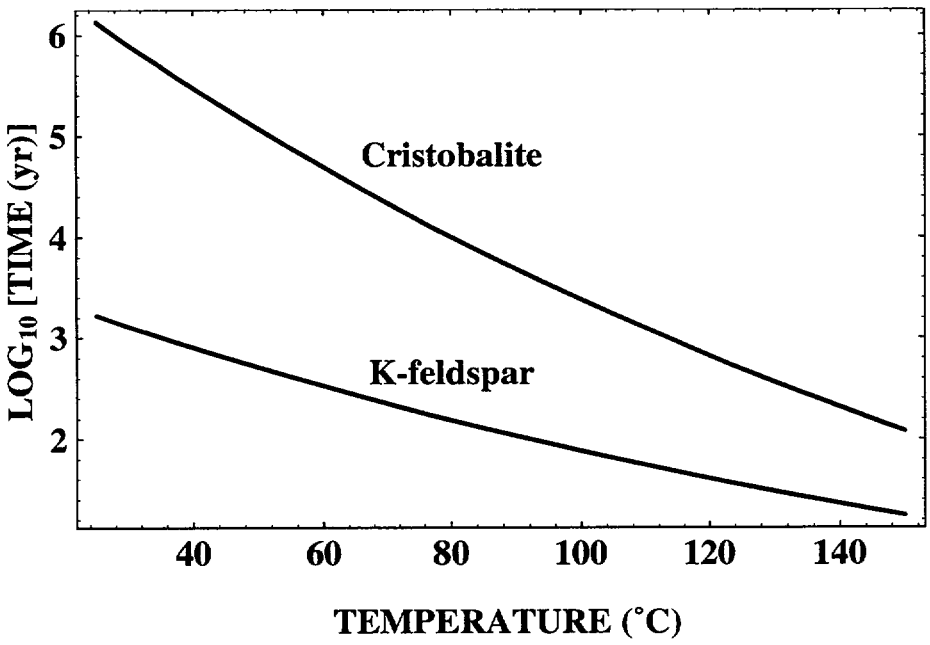

Figure 6-2. Time required for the volume fractions of K-feldspar and cristobalite to change by 10 percent as a function of temperature

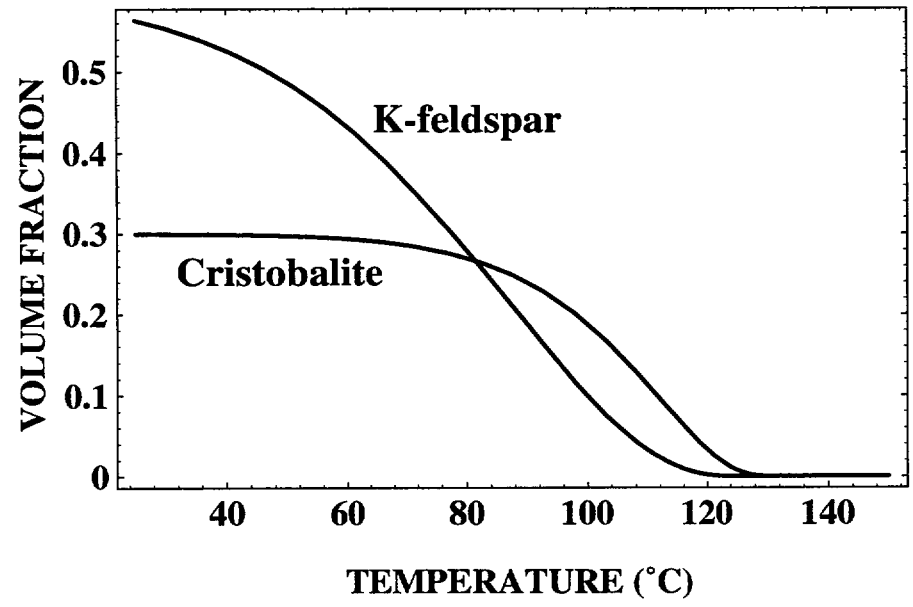

Figure 6-3. Volume fractions of K-feldspar and cristobalite as a function of temperature at an elapsed time of 1,000 yr

assumption may be unrealistic, and water may contact only a tiny fraction of any given grain.

The change in permeability can be estimated from a phenomenological equation of the form

$$\kappa = \kappa_0 \left(\frac{\phi}{\phi_0} \right)^{\sigma} \tag{6-8}$$

where κ_0 denotes the initial permeability of the porous medium. This equation represents the permeability as the porosity raised to some power σ. It gives the correct limiting value of zero for zero porosity, but it does not account for the change in permeability resulting from the change in mineral texture, for example. If the porosity is related to the mineral volume fractions by the usual equation

$$\phi = 1 - \Sigma_m \phi_m \tag{6-9}$$

representing the total porosity (which may not be identical with the flow or connected porosity), this leads to the expression

$$\kappa = \kappa_0 \left(\frac{1 - \Sigma_m \phi_m}{1 - \Sigma_m \phi_m^0} \right)^{\sigma} \tag{6-10}$$

The ratio κ / κ_0 is plotted as a function of temperature in Figure 6-4 for times of 100, 1,000, and 10,000 yr for a rock composed of 60 percent K-feldspar and 30 percent cristobalite with a porosity of 10 percent using the rates and surface areas given previously. The plateau in the permeability curves occurs when K-feldspar completely dissolves. Substantial changes in permeability are clearly possible according to the predictions of this simple conservative model.

6.2.2 Study of Predictive Reliability and Sampling Design

Total-system and subsystem PAs conducted by the NRC and DOE are expected to examine alternative conceptual models of the geologic setting at YM. The reliability of these PAs will greatly depend on how well the conceptual models capture important details that control movement of water through the subsurface. Thus, one of the key licensing concerns that the DOE and NRC must ultimately address is how well the site is characterized. A preliminary study was undertaken to examine how model predictive reliability depends on conceptual model complexity. As used here, model complexity is a function of three factors: (i) number of hydrostratigraphic units or parameter zones, (ii) number of measurements or samples, and (iii) sampling pattern used.

A hydrologic modeling study was conducted to examine the worth of additional data and the design of sampling patterns using data from a field experiment. The data used in the study are from the Las Cruces field experiment in New Mexico. This field experiment was originally conducted for the express purpose of "validating" mathematical models of flow and transport in partially saturated porous media (Wierenga et al., 1986, 1989; Nicholson, 1990). Because of the original objective of this field experiment, measurements of flow and transport properties were collected on a very dense sampling network. Such dense measurement networks are impractical at YM; nevertheless, this experiment presents an excellent data set to investigate the issue of data sufficiency since the ultimate "true" characteristics of the site are known *a priori*. A variety of data sampling patterns are employed to determine how the number and location of sample points affect the accuracy of predictions obtained from mathematical models.

6.2.2.1 Study Approach

This study examined the number and configuration of sample locations where the unsaturated soil hydraulic properties should be measured in order to minimize the error in predicting the propagation of a moisture plume. This problem, while similar to the network design problem of choosing the measurement locations for Y that minimize the prediction error in hydraulic head, is greatly complicated by the nonlinearity of the unsaturated flow equation and the large number of parameters needed to adequately describe the unsaturated hydraulic conductivity and soil moisture characteristic functions. At the time this study was performed, all site characterization activities and infiltration experiments had already been completed at the Las Cruces field experiment site. The strategy for this study was to use a limited amount of the available qualitative and quantitative data to construct the conceptual flow model, select soil hydraulic parameters

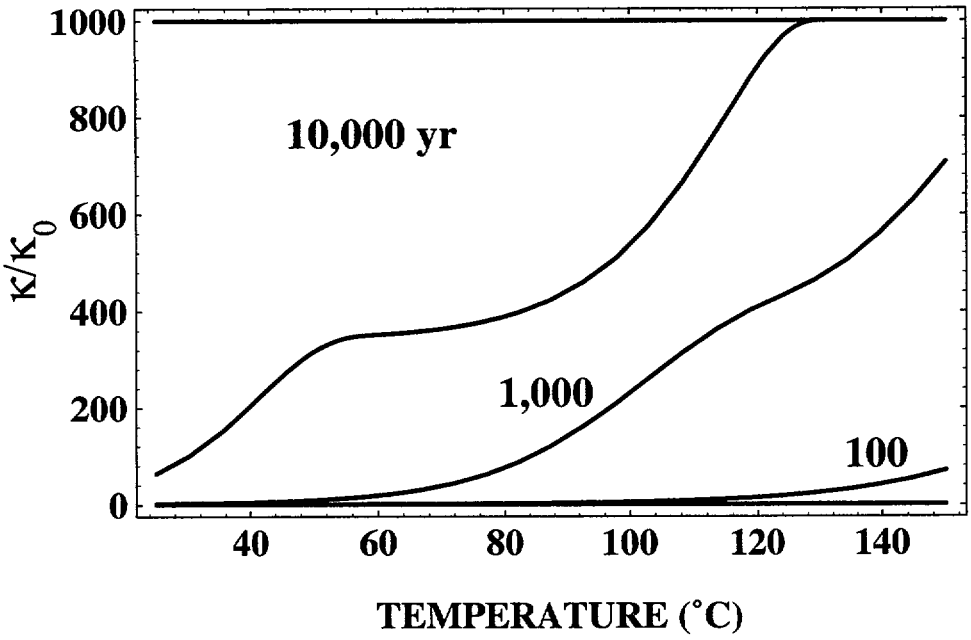

Figure 6-4. Changes in permeability κ/κ_0 for a rock composed of 60 percent K-feldspar and 30 percent cristobalite as a function of temperature for times of 100, 1,000, and 10,000 yr with a=3

from the existing database, and compare the predicted water contents to the measured water content values.

Soil hydraulic data may be used both to design the basic conceptual model and to assign parameter values to the distinct hydrostratigraphic units or zones. However, since the objective of this study is to estimate the impact of different sampling schemes on the accuracy of model predictions, a single conceptual model was chosen and the parameters of that model were varied based on the sampling scheme. For example, a conceptual model composed of two parameter zones, within each of which a single sample was collected to obtain parameter values, cannot be compared to a model composed of a single parameter zone, in which two samples were collected to assign effective, average properties to the zone. Clearly two soil samples were used in each case, but because the conceptual models employed are fundamentally different (one zone versus two), it would be difficult to draw conclusions about the superiority of one sampling pattern over the other. For this study, a single conceptual model was used, which assumes that moisture redistribution is two-dimensional in a vertical slice containing nine horizontal layers or parameter zones coincident with nine soil horizons identified on the north face of the trench identified in Figure 6-5. Each parameter zone is assumed to have uniform properties. By selecting a single conceptual model, the study could be focused on the experimental factors most relevant to site characterization: (i) how many samples should be taken, and (ii) what sampling pattern should be used.

The considered model domain extends 10 m laterally to the east from the northwest corner of the trench and 7 m vertically from the strip source to a location 1 m below the bottom of the trench. The computational mesh used consisted of 81 nodes in the horizontal and 97 nodes in the vertical direction, increasingly refined toward the center and top of the domain to accommodate the large pressure head gradients expected to occur at early time directly below the strip source. Boundary conditions were defined everywhere to be no-flow, except at the bottom of the model and at the 1.2-m horizontal portion at the top where the strip infiltration source is located. To simulate gravity drainage, a negative pressure head gradient of unit magnitude was specified at the bottom of the domain. At the strip source, the boundary condition was a prescribed flux of 1.82 cm/d during the first 70 days of simulation and zero thereafter. The redistribution of the moisture plume was monitored for 240 days after infiltration ceased.

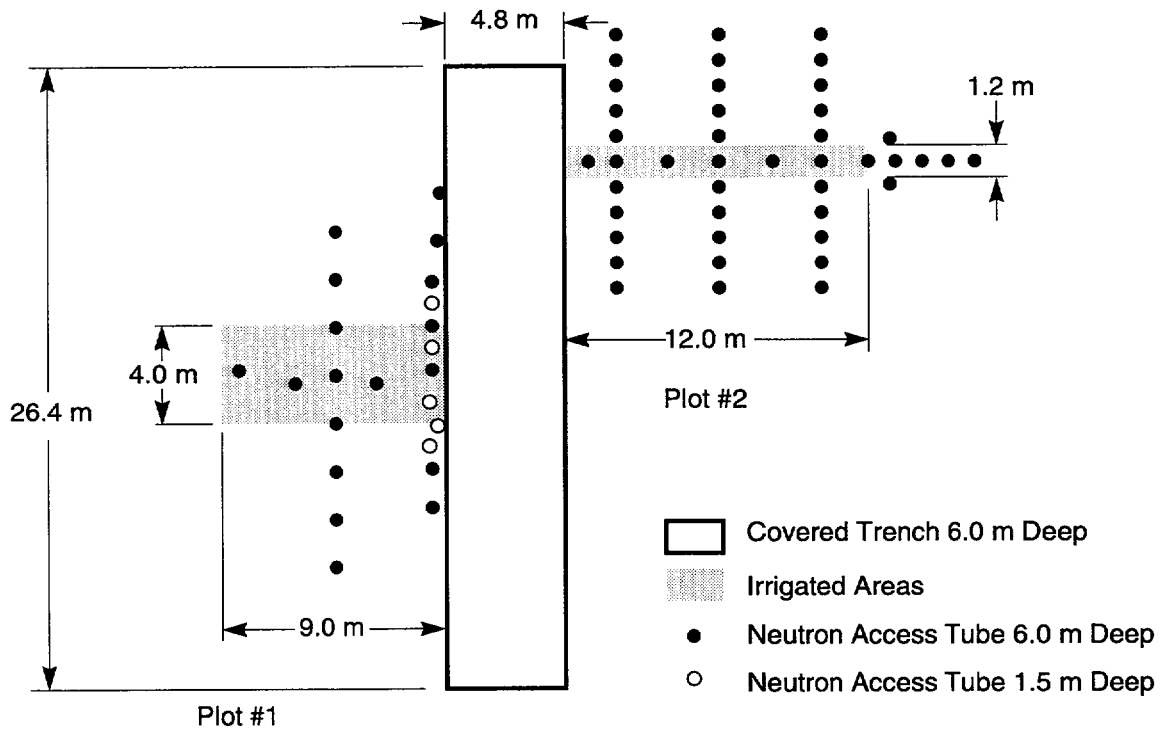

Figure 6-5. Plan view of the Las Cruces trench site

Two basic sampling patterns were employed in this study: (i) random sampling, and (ii) stratified sampling. For the purely random sampling plan, one or more soil samples were randomly selected from the existing sample locations in each of the nine parameter zones and the values of θ_s (saturated water content), θ_r (residual water content), K_s (saturated hydraulic conductivity), and α and n (van Genuchten fitting parameters) were obtained. When a single random sample was taken, the soil hydraulic properties corresponding to that sample were assigned to the entire zone. When two or more samples were taken, the arithmetic averages for θ_s, θ_r , and n, and the geometric averages for K_s and α , were assigned to the entire zone. Empirical data suggests that θ_s, θ_r , and n are normally distributed, and K_s and α are lognormally distributed. For the stratified sampling plan, each of the nine parameter zones was divided into two or more equally sized sampling strata. One or more soil samples were then randomly selected from each stratum, and all selected samples were again appropriately averaged to determine the effective model parameters.

Truly random sampling could not be performed given the constraint of having to choose from the existing sampling network, which provided between 13 and 20 available samples per horizontal layer. Spatial random sampling was approximated by: (i) mapping each sampling stratum to a unit square, (ii) generating a pair of uniformly distributed $[0, 1]$ random numbers corresponding to the Cartesian coordinates of a point in the unit square, and (iii) selecting the sample location within the stratum closest to the randomly generated point. Because the horizontal sampling transects were intentionally aligned with the nine soil horizons, sample location randomness was effectively constrained to the horizontal axis, except where a stratum intersected one of the vertical transects.

Two metrics were used to determine which sampling plan produced the most accurate estimates of the propagation of the moisture plume. The first metric was based on the direct point-to-point comparison of the measured and predicted water contents at the neutron probe measurement locations in the y=2m transect collected at 55 measurement times, where $t \in [0,310]$.

This measure, called the cumulative sum of squared errors, is given by

$$SSE = \sum_{j=1}^{N_T} \sum_{i=1}^{N_{OBS}} \left(\theta_{ij}^{*} - \hat{\theta}_{ij} \right)^2 \quad (6\text{-}11)$$

where N_{OBS} is the number of neutron probe measurement locations, N_T is the number of measurement times, θ^* are the measured water contents, and $\hat{\theta}$ are the predicted water contents. The second metric was based on the first and second moments of the water content difference plumes. The moment of order l in the x-direction and k in the z-direction for the observed water content difference plume is

$$M_{lk}^{*}(t) = \iint_{ZX} \left[\theta^{*}(x, z, t_0) - \theta^{*}(x, z, t) \right] x^l z^k dx dz \quad (6\text{-}12)$$

where $\theta^{*}(x, z, t_0)$ and $\theta^{*}(x, z, t)$ are the measured water contents for point (x, z) at times t_0 and t, respectively. Similarly, the moment of order l in the x-direction and k in the z-direction for the predicted water content difference plume is

$$\hat{M}_{lk}(t) = \iint_{ZX} \left[\hat{\theta}(x, z, t_0) - \hat{\theta}(x, z, t) \right] x^l z^k dx dz \quad (6\text{-}13)$$

The x and z coordinates of the plume centroid for either the measured or predicted water content differences are given for the general case

$$X_c(t) = M_{10}(t) / M_{00}(t) \quad (6\text{-}14)$$

$$Z_c(t) = M_{01}(t) / M_{00}(t) \quad (6\text{-}15)$$

The centroid is used to represent the mean position of the plume, while the second moment about the centroid is used to represent the extent of the spread of the plume about its center. Equations for the second moments are given in the general case by

$$S_{xx}(t) = M_{20}(t) / M_{00}(t) - X_c^2(t) \quad (6\text{-}16)$$

$$S_{zz}(t) = M_{02}(t) / M_{00}(t) - Z_c^2(t) \quad (6\text{-}17)$$

The square roots of the second moments have units of length and are interpreted as measures of plume spread.

Because each simulation took between 1.5 and 5 CPU hours on a Sun SPARCstation 10/40, the total number of sampling patterns that could be investigated was restricted to a small number. In addition, the maximum number of sample strata per zone was limited to six by the horizontal spacing of the existing sample locations. Compact nomenclature is used to designate the sampling pattern, namely *m-n-l*, where *m* is the number of parameter zones, *n* is the number of sample strata per zone, and *l* is the number of samples per stratum. Five stratified sampling patterns in which one measurement was randomly selected from each stratum (9-2-1, 9-3-1, 9-4-1, 9-5-1, 9-6-1), three purely random sampling patterns in which one, two, and four measurements were selected (9-1-1, 9-1-2, 9-1-4), and two sampling patterns in which each model zone was divided into two strata with two and four measurements randomly selected from each stratum (9-2-2, 9-2-4) were tested.

6.2.2.2 Discussion of Results

Plots of the mean SSE versus time for sample patterns 9-1-1, 9-2-1, 9-3-1, 9-4-1, 9-5-1, and 9-6-1 are shown in Figure 6-6. During the wetting portion of the infiltration experiment, which extends from day 0 to day 70, sampling configuration 9-1-1 produces a somewhat smaller mean and median SSE than do the other sampling configurations. However, once the moisture redistribution period begins after day 70, sample patterns 9-4-1, 9-5-1, and 9-6-1 produce the smallest mean SSE. Figure 6-7 shows the mean and median SSE at day 310 for these six stratified sampling patterns. It is clear that dividing each model zone into two strata leads to a significant reduction in the mean SSE. Further increases in the number of sampling strata per zone lead to a general decrease in the mean SSE, although it is also apparent that the percentage decrease is not as great as that from 9-1-1 to 9-2-1. Because the median is less affected by outliers than the mean, the results are somewhat smoother and better depict the general decrease in the marginal value of adding another stratum and sample in each model zone.

The median SSE at day 310 is also plotted in Figure 6-7 for sample patterns 9-1-1, 9-1-2, and 9-1-4. These sampling configurations correspond to using a single stratum per model zone, with one, two, and four

random samples selected per stratum. There is a marked decrease in the median SSE as the number of random samples increases from one to four. The decrease in the marginal value of additional samples is similar to that observed for the stratified sampling patterns, although more benefit is derived from additional samples.

Analyses of the means of the first [Eqs. (6-13) and (6-14)] and second [Eqs. (6-15) and (6-16)] moments lead to somewhat different, and somewhat equivocal, sets of observations about the marginal value of additional measurements. Figures 6-8a through 6-8c show the evolution of the mean vertical coordinate of the centroid of the water content difference plume, the mean horizontal spread of the plume, and the mean vertical spread of the plume, respectively, for sample patterns 9-1-1, 9-2-1, 9-3-1, 9-4-1, 9-5-1, and 9-6-1. From Figure 6-8a, it may be concluded that increasing the number of sampling strata leads to a general improvement in the ability of the model to predict the depth of penetration of the water content difference plume. It is also apparent from Figure 6-8a that improvement in predicting the Z-coordinate of the centroid of the plume is far greater during the moisture redistribution period. Figure 6-8b indicates that using fewer strata improves the mean accuracy of predicting the horizontal spreading of the plume during the infiltration phase, while using more strata increases the mean prediction accuracy during the redistribution phase. Conversely, from Figure 6-8c, it appears that using fewer strata decreases the mean accuracy of predicting the vertical spread of the water content difference plume during infiltration, while using more strata decreases the mean prediction accuracy during redistribution.

While it is disconcerting to discover that in some cases, the moment-based measure of model performance suggests that using more samples may lead to poorer predictions, the root cause of these inconsistent results is most likely the selection of an incorrect conceptual model. In previous work, the authors noted that their models were unable to replicate a distinct vertical bifurcation in the water content distribution that was observed at a depth of 3-m (Wittmeyer and Sagar, 1993). Spatial analyses of the grain-size distribution data indicated that there was a thin, but distinct, coarse sandy layer at 3 m depth. Soil samples collected from this horizon for determination of the soil hydraulic properties clearly failed to capture the capability of this sandy layer to transmit relatively large water fluxes without a measurable increase in the water content (Wittmeyer and Sagar, 1993). While the models all generally predict the rate of vertical movement of the water content difference plume, none of the models adequately capture the rate of the horizontal and vertical spread. In this study, limited to using the original soil moisture characteristic data, the model should be expected to produce biased predictions. For this reason, one must not conclude from the moment comparisons that using additional samples necessarily reduces the accuracy of model predictions.

If the correlation lengths for the soil hydraulic model parameters are much greater than the largest dimension of the model zone, one soil sample per zone is sufficient for characterization. If the model parameters exhibit little spatial correlation, a number of purely random samples should be taken within a model zone to obtain the effective parameter value used for that zone. Finally, if the correlation length for a particular parameter is comparable to model zone dimensions, stratified sampling should be used to obtain an effective parameter value. In both instances in which the purely random and the stratified sampling schemes use the same number of samples, the purely random pattern produces more accurate model predictions than does the stratified sampling pattern, suggesting that the soil hydraulic parameters to which the flow model is most sensitive are spatially uncorrelated. We may reject the possibility that each zone is homogeneous, both on the basis of visual inspection of the trench face, and because using two random samples per stratum instead of one produces more accurate predictions in terms of the SSE measure.

The results indicate that the marginal value of additional samples decreases rapidly as the sample size increases. Thus, the greatest improvement in model predictions was obtained when the sample size was increased from one sample per material zone to two samples per material zone. Thereafter, the rate of improvement decreased significantly. Of the two measures of "goodness" employed–the median cumulative squared error and the moment-based measures of the centroid and spread of the moisture plume–the first measure appeared to provide more consistent results.

It appears that the sufficiency of data can only be determined in terms of the modeling results and the measures selected for determining the value of data. In addition, whether additional data will modify a decision can only be judged after the additional data are

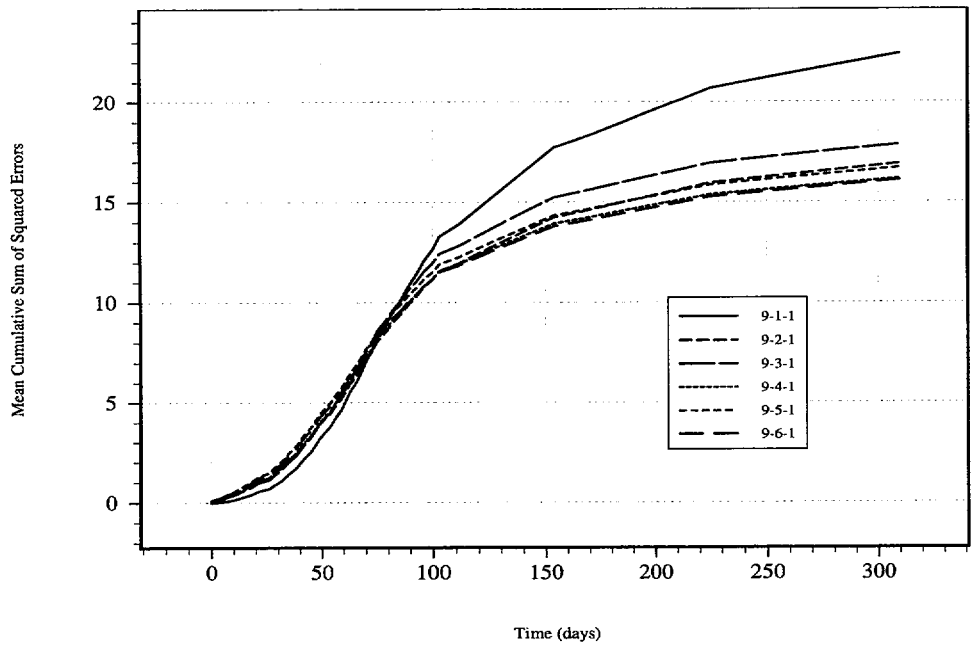

Figure 6-6. Mean cumulative sum of squared errors as a function of time for the six stratified sampling configurations

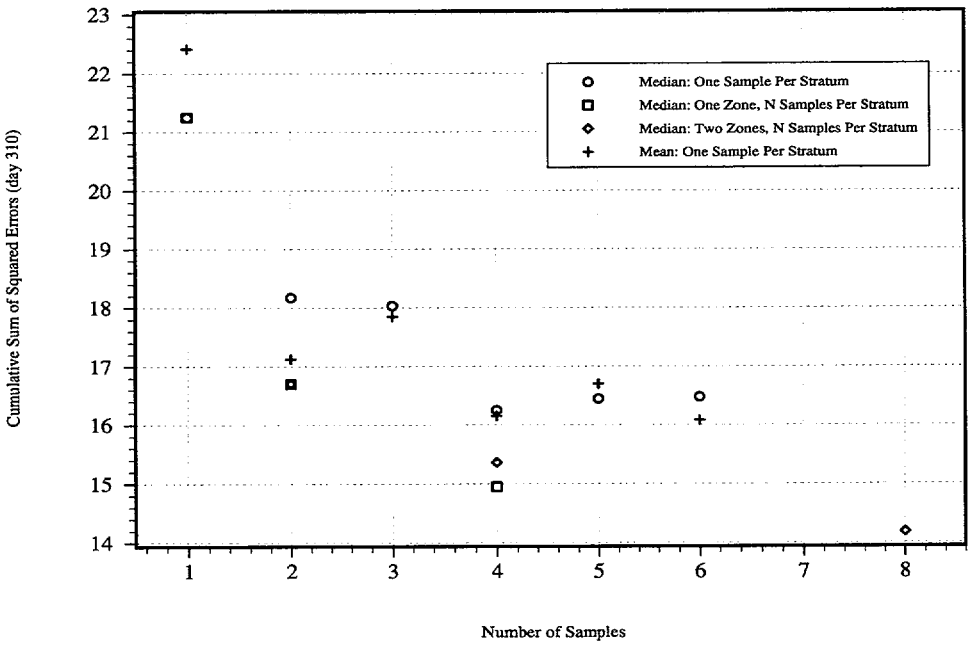

Figure 6-7. Cumulative sum of squared errors at day 310 for the various sampling configurations

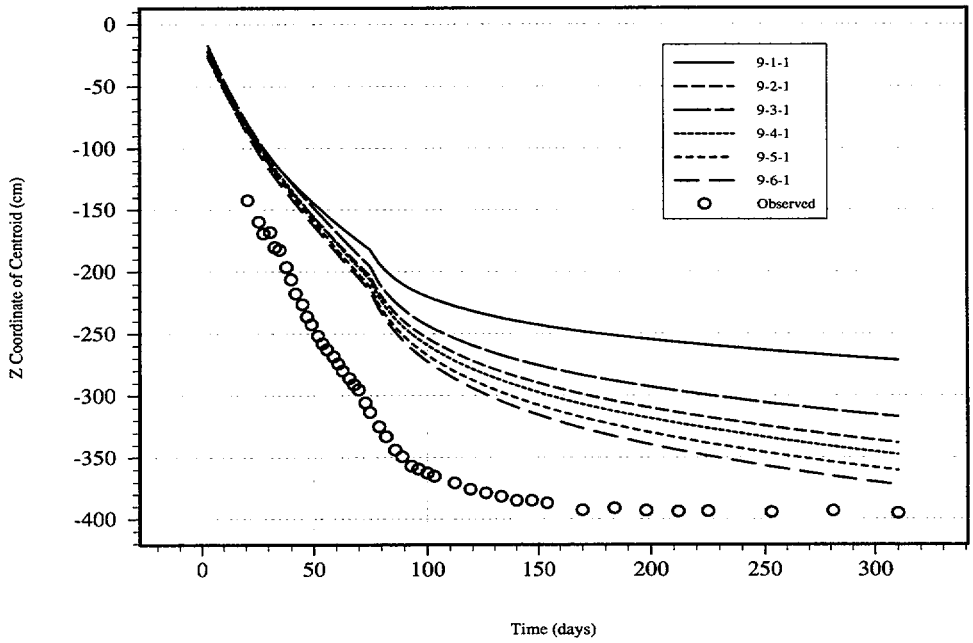

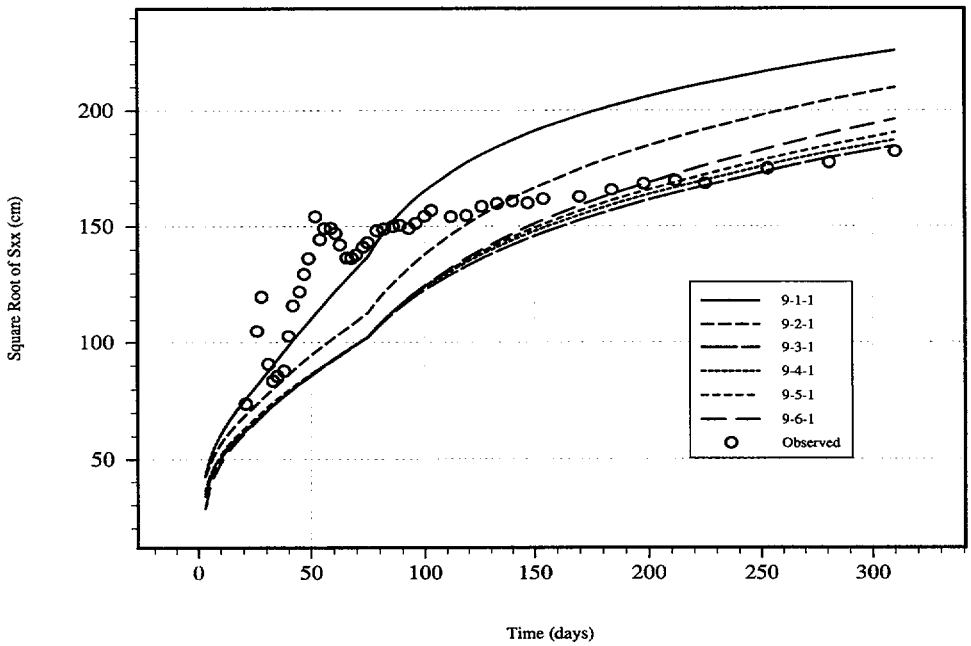

Figure 6-8. Water content difference plume as a function of time for six stratified sampling patterns: (a) Mean vertical position, (b) Mean horizontal spread

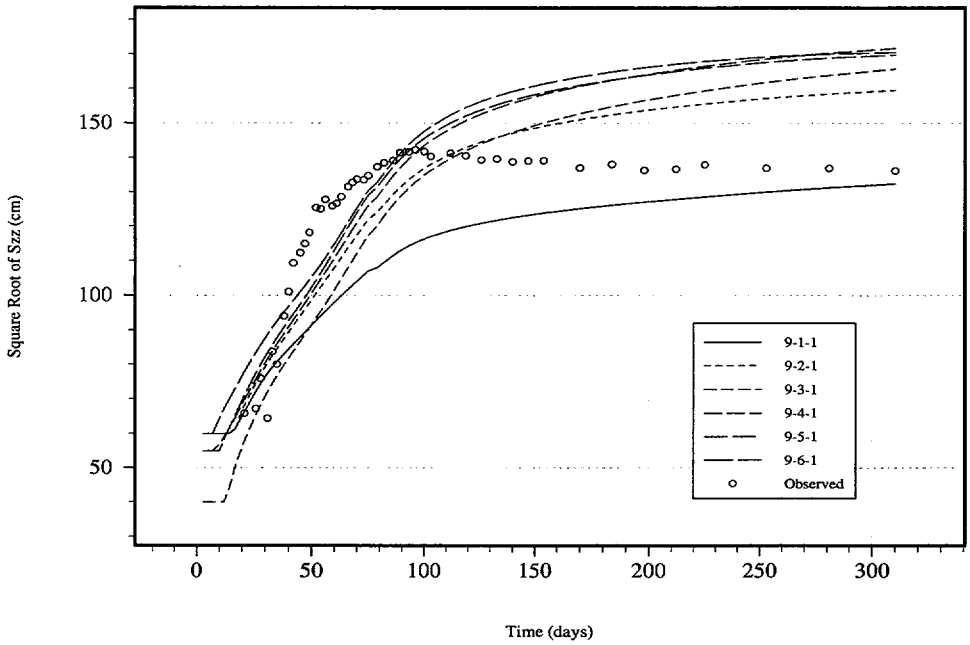

Figure 6-8 (Cont'd). Water content difference plume as a function of time for six stratified sampling patterns: (c) Mean vertical spread

collected. All existing procedures for judging the value of data before then collection are based on assumptions that imply statistical extrapolation of prior data. The numerical experiment described above indicates that an iterative coupling between data collection and modeling will be advantageous for deciding data sufficiency.

6.3 ASSESSMENT OF PROGRESS

In accordance with NRC technical direction, research emphasis during this period was placed on the technical scope of Task 1—Conceptual Model Development, which includes studies of hydrologic conceptual models and disruptive event scenarios, and Task 3—Model Evaluation, which focuses on model confidence building and code testing. Limited research effort was devoted to the scope of Task 2—Computational Model Development. Research activities conducted under Task 1 made noteworthy progress on topics associated with fracture flow under both isothermal and nonisothermal flow. Similarly, numerical modeling studies conducted as part of Task 3 addressed aspects of model confidence building and included benchmark testing of DOE thermohydrologic codes. In addition, work conducted for Task 2 focused on preparations for evaluation of Parallel Virtual Machine (PVM) computing technology and documentation of the infiltration model developed in the previous period.

A detailed review and critique of the conceptual and mathematical models used in the existing thermohydrologic models was completed. This technical review, which was documented in a CNWRA report (Lichtner, 1994a), was beneficial in identifying the limitations and ranges of applicability of DOE thermohydrologic models and codes currently being applied to YM. One of the very important conclusions of this review and related studies (Lichtner, 1994b) was that current thermohydrologic codes using the Equivalent Continuum Media (ECM) concept are likely to produce nonconservative predictions for fracture flow. This conclusion has a direct bearing on the effectiveness of the DOE "extended dry concept" and estimation of time-to-wetting for the waste packages. The findings and conclusions drawn from this study are directly beneficial to: (i) addressing aspects of the Conceptual and Mathematical KTUs, (ii) providing a strong technical background necessary for CDM development and useful for future prelicensing reviews of DOE studies associated with their proposed extended dry concept, and (iii) assessing predictions of repository performance conducted as part of NRC IPA activity. In addition, the approach used in this detailed review of

thermohydrologic models may be followed in future reviews of DOE topical reports.

As part of an integrated effort between the PA Research Project and the Geochemical Natural Analog Project, a study was conducted of the hydraulic characteristics of tuff samples from the Peña Blanca site (Green et al., 1994). One of the main objectives of this study was to examine the possible importance of hydrothermal alteration on the unsaturated hydraulic properties of the tuff. Data collected as part of the Geochemical Natural Analog Project were analyzed to identify trends and relationships. In turn, the measured hydraulic properties were used in fracture flow simulations using the VTOUGH code to model a proposed infiltration experiment at the Peña Blanca field site. These simulations provided insight into the possible impact of hydrothermally altered rock properties on the nature of fracture flow in tuff. The knowledge gained from this work is relevant to the Conceptual, Mathematical, and Model Parameter KTUs. In addition, the study gives good evidence of the specific use of data from natural analog studies.

Two studies were conducted to address the Model Validation KTU. The first study examined the relationship between model predictive reliability and conceptual model complexity. Results of that study are highlighted in Section 6.2.2 of this chapter and presented in more detail in the paper by Wittmeyer et al. (1994), which was recently submitted for journal publication. The second study consisted of benchmark testing of available DOE thermohydrologic codes against comparable CNWRA/NRC codes. The TOUGH2, VTOUGH, and FEHMN codes were acquired from DOE contractors, and testing was initiated on a series of computational problems of progressive complexity. This code benchmark testing, which will be documented in the next semi-annual report, is expected to benefit the NRC review of the forthcoming DOE Topical Report on Process Models. In addition, the conduct of this type of activity positions the CNWRA and NRC to perform thorough prelicensing review of DOE design analyses and subsystem PAs.

Research conducted under the scope of the Computational Model Development task was limited to: (i) continued work on evaluating the PVM computing technology for possible application to the Total-System Performance Assessment (TPA) code used in the IPA activity, and (ii) documentation of the previously developed infiltration model. Progress on the evaluation of PVM was not noteworthy at this time, but greater emphasis on this activity is planned in the next reporting period. With regards to the infiltration model, a CNWRA report (Stothoff, 1994) was prepared and issued. This document provided a description of the mathematical theory and user guide for the use of the code. This code is being used in IPA Phase 3 and in the Subregional Hydrology Research Project to address the very important issue of understanding infiltration processes occurring at YM and estimating the percolation rates.

6.4 PLANS FOR NEXT REPORTING PERIOD

In the next reporting period, a number of new and challenging research topics will be pursued for the purpose of meeting the priority modeling needs of IPA and subsystem PA. In addition, the research will be conducted in an integrated manner with collaborative interactions with the Subregional Hydrogeology, Volcanic Systems, and Geochemical Analogs Research Projects. New PA technology developed under this project will be documented in CNWRA reports, NUREG/CR reports, conference proceedings, and journal publications.

Under the scope of Task 1, activities will concentrate on two major research areas–analyses of site- and repository-induced disruptive scenarios relevant to YM and studies of conceptual models for flow in fractured porous media with emphasis on fracture-matrix interactions. In the first area, a probabilistic climatic model will be developed for use in IPA Phase 3. In addition, certain aspects of both these areas will be studied by application of CNWRA PA models. It is expected that these analyses and investigations will be conducted as parametric and sensitivity studies. The research activities will be coordinated with the NRC IPA Phase 3 exercise and aimed at providing information that can be used in prelicensing reviews of DOE activities.

As part of Task 2, research effort will continue on: (i) evaluation of the PVM technology, (ii) testing and evaluation of DOE thermohydrologic codes, and (iii) development and documentation of advanced computational techniques. Application of PVM to the IPA TPA code, which was initiated this period, will be evaluated by making runs on a network of workstations. The PVM technology has the potential to reduce the computing time from 160 hr on a Cray X/MP to possibly 10 hr on a network of Sun workstations. Achieve-

ment of this computing efficiency will greatly benefit the IPA activity. Benchmark testing of three of the DOE thermohydrologic codes (i.e., TOUGH2, VTOUGH, and FEHMN) will continue. These codes will be rigorously tested against the CNWRA codes (i.e., CTOUGH and PORFLOW). The results will be beneficial to the NRC/CNWRA review of future DOE thermohydrologic studies. In addition, new and advanced computational methods have been developed that can greatly improve the simulation capability of existing CDM tools such as CTOUGH. These computational methods will be documented in reports and journal publications.

Within Task 3, studies of model evaluation methodologies will be directed at a detailed examination of the recently developed NRC/SKI model validation strategy. In addition, a broad-based literature review on model evaluation and confidence-building approaches will be conducted and documented. This work will be closely coordinated with the continuing effort of the DWM activity on the NRC/SKI strategy. The aim of this activity will be to provide the technical basis for a future NRC technical position and guidance on model validation.

6.5 REFERENCES

Dove, P.M., and D.A. Crerar. 1990. Kinetics of quartz dissolution in electrolyte solutions using a hydrothermal mixed flow reactor. *Geochimica et Cosmochimica Acta* 54: 955–969.

Green, R.T., K. Meyer, and G. Rice. 1994. *Hydraulic Characterization of Hydrothermally Altered Nopal Tuff.* CNWRA 94-027. San Antonio, TX: Center for Nuclear Waste Regulatory Analyses.

Helgeson, H.C., W.M. Murphy, and P. Aagaard. 1984. Thermodynamic and kinetic constraints on reaction rates among minerals and aqueous solutions. II. Rate constants, effective surface area, and the hydrolysis of feldspar. *Geochemica Cosmochemica Acta* 48: 2,405–2,432.

Lichtner, P. 1994a. *Multi-Phase Reactive Transport Theory.* CNWRA 94-018. San Antonio, TX: Center for Nuclear Waste Regulatory Analyses.

Lichtner, P. 1994b. *Near-Field Liquid-Vapor Transport in a Partially Saturated High-Level Nuclear Waste Repository.* CNWRA 94-022. San Antonio, TX: Center for Nuclear Waste Regulatory Analyses.

Nicholson, T.J. 1990. Recent accomplishments in the INTRAVAL project—A status report on validation efforts. *Proceedings of Geoval 90 Symposium on Validation of Geosphere Flow and Transport Models.* Stockholm, Sweden: INTRAVAL: 1: 81–92.

Nuclear Regulatory Commission. 1994. *License Application Review Plan for a Geologic Repository for Spent Nuclear Fuel and High-Level Radioactive Waste, Draft Review Plan.* NUREG-1323, Rev. 0. Washington, DC: Nuclear Regulatory Commission.

Rimstidt, J.D., and H.L. Barnes. 1980. The kinetics of silica-water reactions. *Geochimica et Cosmochimica Acta* 44: 1,683–1,699.

Stothoff, S. 1994. *BREATH Version 1.0—Coupled Flow and Energy Transport in Porous Media Simulator Description and User Guide.* CNWRA 94-020. San Antonio, TX: Center for Nuclear Waste Regulatory Analyses.

Wierenga, P.J., L.W. Gelhar, C.S. Simmons, G.W. Gee, and T.J. Nicholson. 1986. *Validation of Stochastic Flow and Transport Models for Unsaturated Soils: A Comprehensive Field Study.* NUREG/CR-4622. Washington, DC: Nuclear Regulatory Commission.

Wierenga, P.J., D. Hudson, J. Vinson, M. Nash and A. Toorman. 1989. *Soil Physical Properties at the Las Cruces Trench Site.* Soil and Water Science Report No. 89-002. Tucson, AZ: University of Arizona.

Wittmeyer, G., and B. Sagar. 1993. Model complexity and model validity: Application to the Las Cruces trench experiment, INTRAVAL Test Case 10. *Proceedings Site Characterization and Model Validation, Focus '93.* La Grange Park, IL: American Nuclear Society: 209-216.

Wittmeyer, G., B. Sagar, and M. Cruse. 1994. Network design and accurate prediction of infiltration at the las cruces trench site. Submitted to the *Journal of Groundwater.*

THIS PAGE INTENTIONALLY LEFT BLANK

7 VOLCANIC SYSTEMS OF THE BASIN AND RANGE

by Charles B. Connor and Brittain E. Hill

Investigators: ***Charles B. Connor, Brittain E. Hill, and Gerry L. Stirewalt***

NRC Project Officer: ***Linda A. Kovach***

7.1 OVERALL TECHNICAL OBJECTIVES

Characterization of the frequency and nature of past volcanic events in the Yucca Mountain region (YMR) and assessment of the probability and consequences of future volcanism are critical aspects of prelicensing scientific investigation. The technical objectives of the Volcanic Systems of the Basin and Range Research Project are to (i) assess the probability of continued magmatic activity in the YMR, (ii) develop models that better predict the interaction between structure and volcanism in this tectonic setting, and (iii) develop scenarios for the impact of volcanism on the proposed Yucca Mountain repository. Effective review of the U.S. Department of Energy (DOE) license application will require insight into volcanic processes operating in the YMR on several scales. These scales include assessment of: western Great Basin tectonic and structural controls on volcanism on local scales (10^2 to 10^3 km^2), the longevity of cinder cone clusters and individual volcanoes in the western Great Basin, and the relationship between specific, mappable fractures (e.g., faults and joint trends), and volcanic conduits, such as dikes and dike swarms. The western Great Basin has been the site of recurring small volume basaltic volcanism throughout the Quaternary Period. Modern analogs and theoretical studies have demonstrated convincingly that this activity encompasses a variety of eruption styles. The Volcanic Systems of the Basin and Range Research Project has been designed to assess the probability of future volcanism in the YMR, taking into account the range of activity and structural controls on activity that are an inherent part of western Great Basin volcanism.

Insight gained through the Volcanic Systems of the Basin and Range Research Project will be used to support specific sections of the License Application Review Plan (LARP). Research on Basin and Range volcanism will form an integral part of the description of the site and site characterization activities (evidence of igneous activity as a potentially adverse condition, Section 3.2.1.9, and impact of volcanism on groundwater movement, Section 3.2.2.7) and the description of overall system performance (assessment of compliance with the requirement for cumulative releases of radioactive materials, Section 6.1). Compliance Determination Strategies (CDSs) for these LARP sections have recently been developed or are currently under development. However, the CDS associated with evidence of Quaternary volcanism is of Type 5, indicating that independent research must be conducted to evaluate Key Technical Uncertainties (KTUs) associated with volcanism, and that volcanism poses a high risk of noncompliance with 40 CFR Part 191 as set forth by the U.S. Environmental Protection Agency, and Parts 10 CFR 60.122(c)(15) and 10 CFR 60.122(c)(3) as determined by the Nuclear Regulatory Commission (NRC). Consequently, volcanism research at the Center for Nuclear Waste Regulatory Analyses (CNWRA) will assist in the resolution of specific KTU topics, including: (i) prediction of future system states (disruptive scenarios), (ii) prediction of future changes in the hydrologic system (due to tectonism), (iii) development and use of conceptual tectonic models as related to igneous activity, (iv) low resolution of exploration techniques to detect and evaluate igneous features, and (v) inability to sample igneous features. Of these KTUs, (i) and (iii) are focused upon most strongly in the Volcanic Systems of the Basin and Range Research Project.

Research efforts in the Volcanic Systems of the Basin and Range Research project are primarily directed toward the development of probability models of potential volcanic events in the YMR, based as far as possible on geologic insight into tectonic processes operating in the western Great Basin and geologic controls on areal cinder cone volcanism in general. Key elements of the research design include the development of robust probability models for cinder cone volcanism and creation of a comprehensive database on cinder cone volcanism in the southwestern United States.

Review of the regional tectonic setting of cinder cone volcanism in the Great Basin, Task 1 of this project, is provided by Stirewalt et al. (1992). Connor and Hill (1993) discuss initial work on probability model development and the nature of cinder cone volcanism in the YMR. This report describes research activities since July 1994.

7.2 SIGNIFICANT TECHNICAL ACCOMPLISHMENTS

Research during the last 6 mo focused on:

- Critical review of the Volcanism Geographic Information System (GIS) database
- Peer review of the volcanism research projects
- Development of two new nonparametric models for the probability of volcanic disruption of the proposed repository

Critical review of the GIS database was the topic of a major milestone (MM) delivered in January 1995. The purpose of this review is to summarize the utility of data contained in the volcanism GIS as a research tool, primarily for the development and testing of probability, geochemical, and neotectonic models. As this MM was received by the NRC in January 1995, it is not discussed further in this semi-annual report.

Both the Volcanic Systems of the Basin and Range and the Field Volcanism Research Projects were reviewed by a panel of five world-renowned volcanologists in October and November of 1994. The results of this review are discussed in detail in Chapter 9 on the Field Volcanism Project.

Two new probability models developed and applied to probability of volcanic disruption of the proposed repository are the kernel and nearest-neighbor kernel methods. Together with the spatio-temporal nearest-neighbor model (Connor and Hill, 1993), these models represent the first application of nonparametric, nonhomogeneous Poisson models to the probability of disruption of the proposed repository by volcanism. These models are discussed in a paper currently submitted to the *Journal of Geophysical Research*. In order to present these models to NRC staff in a timely and convenient manner, much of this paper is presented in the following sections. These sections will comprise part of a MM on probability of volcanic eruptions to be delivered to the NRC in June 1995.

7.2.1 Patterns in Cinder Cone Volcanism

Patterns in the distribution and timing of cinder cone volcanism in the YMR are similar to patterns identified in other, often more voluminous volcanic fields. For example, abrupt shifts or migration in the location of volcanism over periods of millions of years have been documented in many basaltic volcanic fields. In the Coso Volcanic Field, California, Duffield et al. (1980) found that basaltic volcanism has taken place in essentially two stages. Eruption of basalts took place over a broad area in what is now the northern and western portions of the Coso Volcanic Field from approximately 4 to 2.5 Ma. In the Quaternary, the locus of volcanism shifted; the youngest basalts erupted in the southern portion of the Coso field. Condit et al. (1989) noted the tendency for basaltic volcanism to gradually migrate from west to east in the Springerville Volcanic Field between 2.5 to 0.3 Ma. Other examples of volcanic fields in which the location of cinder cone volcanism has migrated include the San Francisco Volcanic Field, Arizona (Tanaka et al., 1986), the Lunar Crater Volcanic Field, Nevada (Foland and Bergman, 1992), the Michoacán-Guanajuato Volcanic Field, Mexico (Hasenaka and Carmichael, 1985), and the Cima Volcanic Field, California (Dohrenwend et al., 1984; Turrin et al., 1985). In some instances, migration is readily explained by plate movement, as is the case in the San Francisco and Springerville Volcanic Fields (Tanaka et al., 1986; Condit et al., 1989; Connor et al., 1992). In other areas, the direction of migration or shifts in the locus of volcanism does not correlate with the direction of plate movement. In any case, models developed to describe the recurrence rate of volcanism, or to predict locations of future eruptions in volcanic fields, need to be sensitive to these shifts in the location of volcanic activity.

On a slightly finer scale, cinder cones are known to cluster within many volcanic fields (Heming, 1980; Hasenaka and Carmichael, 1985; Tanaka et al., 1986). Spatial clustering can be recognized through field observation, or through the use of exploratory data analysis or cluster analysis techniques (Connor, 1990). Clusters identified using the latter approach in the Michoacán-Guanajuato and the Springerville Volcanic Fields were found to consist of 10 to 100 individual cinder cones. Clusters in these fields are roughly

circular to elongate in shape with diameters of 10 to 50 km. The simplest explanation for the occurrence, size, and geochemical differences between many clusters is that these areas have higher magma supply resulting from persistent partial melting or higher rates of partial melting. Factors affecting magma pathways through the upper crust, such as fault distribution, appear to have little influence on cluster formation (Connor, 1990; Connor and Condit, 1994). In some volcanic fields, the presence of silicate melts in the crust may influence cinder cone distribution by impeding the rise of basaltic magma (Eichelberger and Gooley, 1977; Bacon, 1982) and result in the formation of clusters.

Tectonic setting, strain-rate, and fault distribution may all influence the distribution of basaltic vents within clusters, and sometimes across whole volcanic fields (Nakamura, 1977; Smith et al., 1990; Parsons and Thompson, 1992; Takada, 1994). Kear (1964) discussed local vent alignments, in which vents are of the same age and easily explained by a single episode of dike injection, and regional alignments, in which vents of varying age and composition are aligned over distances of 20 to 50 km or more. Numerous mathematical techniques have been developed to identify and map vent alignments on different scales, including the Hough transform (Wadge and Cross, 1988), two-point azimuth analysis (Lutz, 1986), and frequency-domain map filtering techniques (Connor, 1990). Regional alignments identified using these techniques are commonly colinear or parallel to mapped regional structures. For example, Draper et al. (1994) mapped vent alignments in the San Francisco Volcanic Field that are parallel to, or colinear with, segments of major fault systems in the area. About 30 percent of the cinder cones and maars in the San Francisco Volcanic Field are located along these regional alignments (Draper et al., 1994). Lutz and Gutmann (1994) identified similar patterns in the Pinacate Volcanic Field, Mexico. Although alignments can clearly form due to episodes of dike injection (Nakamura, 1977) and therefore are sensitive to stress orientation (Zoback, 1989), there are also examples of injection along pre-existing faults (e.g., Kear, 1964; Draper et al., 1994) oblique to maximum horizontal compressional stress.

Cumulatively, these studies indicate that models describing the recurrence rate, or probability, of basaltic volcanism should reflect the clustered nature of basaltic volcanism and shifts in the locus of basaltic volcanism through time. Models should also be amenable to comparison with basic geological data, such as fault patterns and neotectonic stress information, which may impact vent distributions on a comparatively more detailed scale. In addition, probability models should incorporate uncertainties in the distribution and timing of volcanism. Uncertainty in the distribution of volcanoes is particularly important for pre-Quaternary volcanoes. These volcanoes may be buried as a result of subsequent volcanic activity (e.g., Condit et al., 1989) or sedimentation (e.g., Langenheim et al., 1993), or have been so deeply eroded that vent locations cannot be recognized. Uncertainty in the ages of volcanoes is the result of variations in the precision and accuracy of different techniques used to date the volcanoes and open-system behavior.

Finally, it is possible to define a volcanic event in various ways. A simple definition that can be applied to young cinder cones, spatter mounds, and maars is based on morphology: an individual edifice represents an individual volcanic event. In the literature, volcanic events used in distribution analyses are defined as mapped vents (Condit et al., 1989; Connor et al., 1992, Lutz and Gutmann, 1994; Wadge et al., 1994), or volcanic edifices of a minimum size (Hasenaka and Carmichael, 1985; Connor, 1990; Bemis and Smith, 1993). In older, eroded systems, evidence of the occurrence of vents, such as near-vent breccias or radial dikes, is required. However, several edifices can form in single, essentially continuous, eruptive episodes. For example, three closely spaced cinder cones formed during the 1975 Tolbachik fissure eruption (Tokarev, 1983; Magus'kin et al., 1983). In this case, the three cinder cones represent a single eruptive event that is distributed over a larger area than is represented by a single cinder cone. The three 1975 Tolbachik cinder cones have very different morphologies, and erupted adjacent to three older (late? Holocene) cinder cones (Braytseva et al., 1983). Together this group forms a 5-km long N-trending alignment. Without observing the formation of this alignment, it would likely be difficult to resolve the number of volcanic events represented by these six cones. This type of eruptive activity results in uncertainty in the number of volcanic events represented by individual cones, even where these are well preserved.

These uncertainties represent a serious problem in most, if not all, volcanic fields because often there is no clear way to resolve them. An alternative approach is to ascertain the impact of this uncertainty on the

probability model. We adopt this approach here by developing several data sets for basaltic volcanism in the YMR that likely bound the uncertainties associated with the age, distribution, and number of volcanic events in the area.

7.2.2 Probability Model Development

7.2.2.1 Kernel Estimates

Lutz and Gutmann (1994) applied a kernel method (Silverman, 1986) for estimation of the spatial recurrence rate of volcanism in their study of vent alignment distribution in the Pinacate Volcanic Field, Sonora, Mexico. In the kernel estimation technique, spatial variation in estimated recurrence rate is a function of distance to nearby volcanoes and a smoothing constant, h. The kernel function is a probability density function that is symmetric about the locations of individual volcanoes. Following the example of Lutz and Gutmann (1994), an Epanechnikov kernel is used (Cressie, 1991). For a purely spatial, bivariate distribution:

$$\kappa(u) = \begin{cases} \frac{2}{\pi}\left(1-\left(\frac{\overline{pv}_i}{h}\right)^2\right), & \text{if } \left(\frac{\overline{pv}_i}{h}\right)^2 < 1 \\ 0, & \text{otherwise} \end{cases} \quad (7\text{-}1)$$

where h is the smoothing constant, used to normalize the distance between point p, the location for which recurrence rate is estimated, and volcano v_i. The spatial recurrence rate at point p is then:

$$\lambda_h(p) = \frac{1}{e_h(p)} \sum_{i=1}^{n} h^{-2} \kappa(u) \quad (7\text{-}2)$$

where n volcanoes are used in the analysis and $e_h(p)$ is an edge correction (Diggle, 1985; Cressie, 1991), or normalization factor (Silverman, 1986). In the case of a volcanic field, integrating $\lambda_h(p)$ over some large area, A, relative to the size of the field and the smoothing constant, h, should yield n. Therefore, $eh(p)=n$ and $\int_A \lambda_h(p)\,dp = 1$, where the units of $\lambda_h(p)$ are volcanoes/km^2. Using this value for $e_h(p)$, $\lambda_h(p)$ can be multiplied by an estimate of the temporal recurrence rate, λ_t, to calculate the expected number of volcanoes per unit area per time. The value of $\lambda_h(p)$ at a given point p depends on the number of volcanoes found within a distance h of p. If no volcanoes are located within h of a point p, then $\lambda_h(p)=0$.

Eruptions will have a high probability close to existing volcanoes if h is chosen to be small. Conversely, a large value of h will result in a more uniform probability distribution. Clearly, utility of the kernel model depends on the assumption that the smoothing constant can be estimated in a geologically meaningful way. Silverman (1986) recommends using a wide range of smoothing constants in density calculations, an approach adopted by Lutz and Gutmann (1994). We use an identical approach here. However, we further constrain the range of reasonable smoothing constants by using a spatial cluster analysis. The shape of the kernel function is an additional assumption in the model. Alternative kernel functions include uniform random and normal density distributions. Although Cressie (1991) and Lutz and Gutmann (1994) indicate that the choice of the kernel function is not as important as the choice of an appropriate smoothing constant, we used several different kernels in our analysis of volcano distribution in the YMR. Even with this limited number of volcanic events, we also found that the kernel function has a trivial impact on probability calculations compared with the choice of a smoothing constant.

7.2.2.2 Nearest-Neighbor Kernel Estimate

In the nearest-neighbor kernel method, a value $r_m(p)$ is substituted for the smoothing constant, h, in Eq. (7-2), where $r_m(p)$ is the distance between point p and the m^{th} nearest-neighbor volcano (Silverman, 1986). For $m>1$, $\lambda_r(p)>0$ everywhere. In this case $e_h(p)$ is determined for each value of m. Thus, this nearest-neighbor kernel method produces smoother variation in the probability surface far from the mapped cones than is calculated for all but the largest values of a smoothing constant in the kernel method. Nonetheless, the estimated recurrence rate will be higher near the center of clusters than is estimated using the large values for the smoothing constant in the kernel method. As in spatio-temporal nearest-neighbor methods (Connor and Hill, 1993), the number of near neighbors used to estimate $\lambda_r(p)$ will strongly impact the results, and experimentation using a range of near-neighbors is necessary to identify the resulting variation in $\lambda_r(p)$.

7.2.3 Application to the Yucca Mountain Region

7.2.3.1 Distribution and Age of Yucca Mountain Region Basaltic Volcanoes

The YMR contains more than 30 Miocene-Quaternary basaltic volcanoes distributed over approximately 2,500 km^2. The region has been the site of recurring basaltic volcanism since the cessation of Miocene caldera-forming activity in the Southwestern Nevada Volcanic Field (e.g., Sawyer et al., 1994). Basalts younger than about 9 Ma are petrogenetically distinct from older basalts and better represent the mafic system that produced Quaternary eruptions in the YMR (Crowe et al., 1983; 1986). Figure 7-1 illustrates the location of mapped and inferred basaltic vents younger than about 9 Ma. Several subdivisions have been proposed for YMR post-caldera basaltic volcanism. The Crater Flat Volcanic Zone (CFVZ) of Crowe and Perry (1989) is a NNW-trending zone that includes all YMR Quaternary volcanoes, most Pliocene volcanoes, and the Amargosa Valley aeromagnetic anomalies. The Area of Most Recent Volcanism (AMRV) of Smith et al. (1990) includes all Pliocene and younger YMR volcanoes. Both the CFVZ and AMRV are expanded from their original boundaries to include all the aeromagnetic anomalies of Amargosa Valley (Figure 7-1).

The recognition of vent locations is particularly difficult for many Pliocene and older volcanic centers. Vent locations used were generally reported as such on geologic maps and in reports (Byers et al., 1966; Ekren et al., 1966; Carr and Quinlivan, 1966; Byers and Barnes, 1967; Byers and Cummings, 1967; Hinrichs et al., 1967; Noble et al., 1967; Tschanz and Pampeyan, 1970; Cornwall, 1972; Crowe and Perry, 1991; Crowe et al., 1983, 1986, 1988; Carr, 1984; Swadley and Carr, 1987; Faulds et al., 1994), or interpreted in the field from the presence of feeder dikes, vent agglutinate, or cinder cone remnants. Some of the Miocene volcanic centers have been eroded to hundreds of meters below the paleosurface, removing most of the evidence of vent locations. The number of vents reported for Pliocene and older volcanic centers should be regarded as a minimum estimate. This estimate of the number of vents may affect estimated cluster size, shape, and longevity, but has little impact on the spatial of spatio-temporal recurrence rate when data are weighted by age.

Over 200 isotopic age determinations have been published for YMR basaltic rocks younger than about 9 Ma. Many of the older analyses have relatively low degrees of precision and are occasionally inaccurate. For example, dates as old as 10.4±0.4 Ma are reported for the basalt of Pahute Mesa (Crowe et al., 1983), which overlies the 9.40±0.03 Ma Rocket Wash Tuff (Sawyer et al., 1994). Following the example of Crowe (1994), we selected age estimates from more recent analyses, which are generally regarded as more precise and accurate than older analyses (Sinnock and Easterling, 1983; Vaniman and Crowe, 1981; Vaniman et al., 1982). For units with multiple analyses, the age estimates represent the mean and one standard deviation of the data set and in cases where there is apparent discrepancy between two recent dates, both are incorporated in the analyses by use of alternative data sets, as discussed in Section 7.2.3.2.

Several of the age estimates used require further explanation. The dipolar aeromagnetic anomalies in Amargosa Valley (Kane and Bracken, 1983; Langenheim et al., 1993) have both normal (Figure 7-1, sites B and C) or reversed (Figure 7-1, sites D and E) magnetic polarities. Anomaly B has been drilled, and samples of this basalt unit dated at 4.3±0.1 (Turrin, 1992) and 3.8±0.1 Ma (Perry, 1994). Magnetic polarities are used to constrain the ages of the other anomalies, which have not been drilled but are interpreted to be caused by buried basaltic centers (Langenheim et al., 1993). The aeromagnetic anomaly in southern Crater Flat likely represents a buried basaltic unit with normal magnetic orientation (Kane and Bracken, 1983; Crowe et al., 1986). The age of this unit is problematic, as all of the other basalts in Crater Flat have reversed magnetic orientations (Crowe et al., 1986). This possible volcanic center is not included in our current analysis. Over 100 age determinations are published for the Lathrop Wells volcano, which range from about 0.4 Ma to younger than 0.01 Ma and represent numerous analytical methods such as $^{40}Ar/^{39}Ar$ (Turrin et al., 1991), U-series disequilibrium (Crowe et al., 1992b), and cosmogenic isotopes (Poths and Crowe, 1992; Zreda et al., 1993; Poths et al., 1994). Some of the variation in the Lathrop Wells dates may represent polycyclic activity (e.g., Crowe et al., 1992b), the evaluation of which is beyond the scope of this paper. In an attempt to encompass many of the higher-precision age determinations for Lathrop Wells, we use an estimated age of 0.1±0.05 Ma for this volcano. *A posteriori* experimentation indicates that the age of Lathrop Wells may be varied from 0.01 to 0.4 Ma

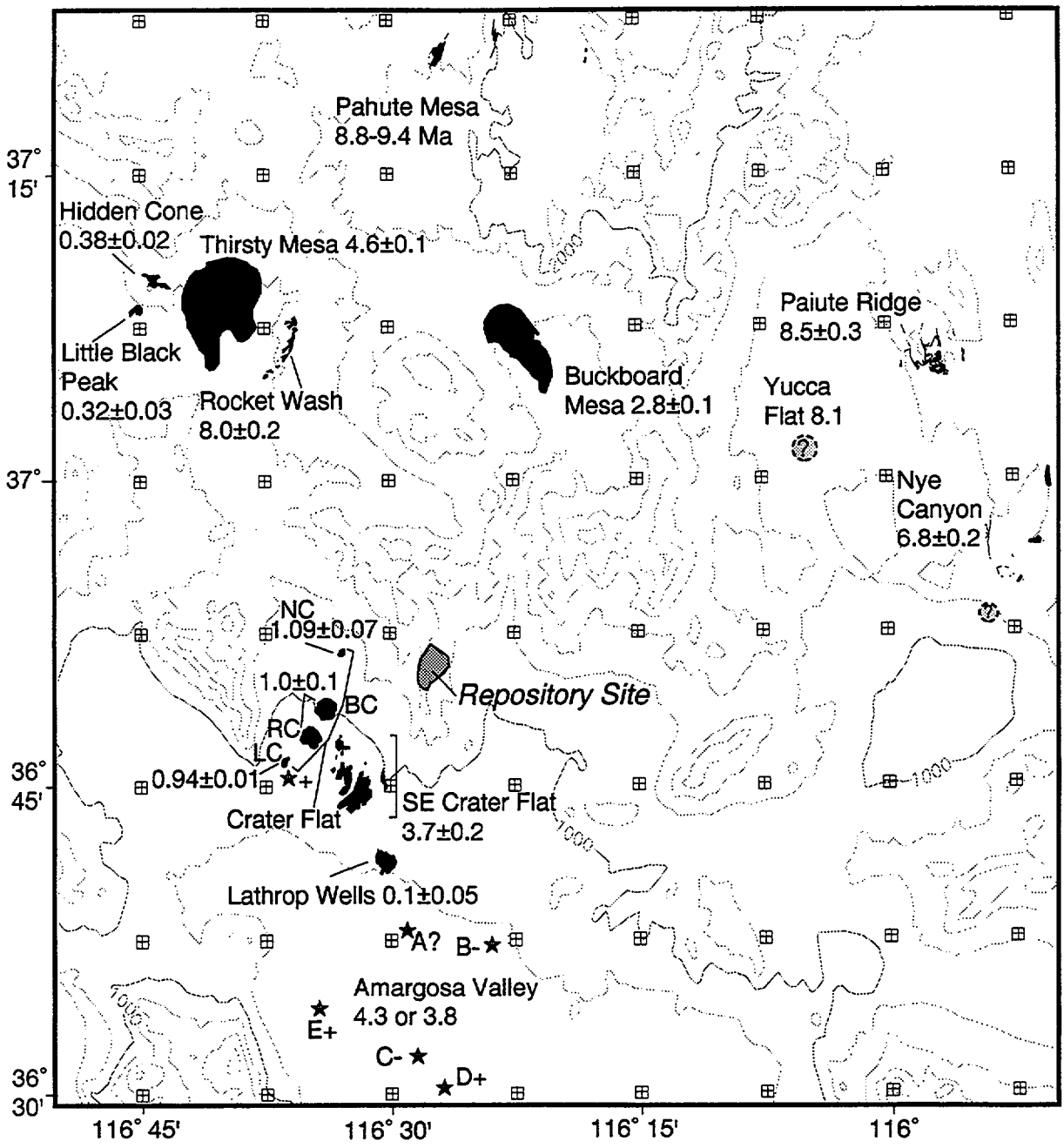

Figure 7-1. Basaltic vents, lavas, and intrusions of the YMR younger than about 9 Ma are illustrated as solid black areas on a map of the YMR. Geology compiled from Byers et al. (1966); Ekren et al. (1966); Carr and Quinlivan (1966); Byers and Barnes (1967); Byers and Cummings (1967); Hinrichs et al. (1967); Noble et al. (1967); Tschanz and Pampeyan (1970); Cornwall (1972); Crowe et al. (1983, 1986); Carr (1984); Swadley and Carr (1987); and Faulds et al. (1994). Locations of aeromagnetic anomalies (stars) from Kane and Bracken (1983) and Langenheim et al. (1993). Contours generated from regional 3-arc-second Digital Elevation Model by B. Henderson, Southwest Research Institute, 200-m contour interval.

with little impact on probability of volcanic eruptions at the location of the repository.

7.2.3.2 Data Used in Models

Based on the abundant geological and geochronological data available for the YMR, we use two data sets throughout the following analyses. These two data sets are meant to encompass most of the uncertainty of the number and timing of volcanoes formed in the YMR. Data set 1 maximizes the number and minimizes the ages of events in the YMR. For example, closely spaced cinder cones, like Little Cone NE and Little Cone SW are treated as distinct events in data set 1. Minimum ages are defined by one-sigma uncertainty reported for age determinations. In cases where there is no overlap between two recent age determinations, such as is the case for Black Cone, we use the younger of the dates in data set 1. Data set 2 excludes several mapped vents from the analysis because these vents are closely spaced with others, and therefore may represent a single eruptive event. For example, Little Cone NE is not included in data set 2 because of its proximity to Little Cone SW. Also, several undrilled aeromagnetic anomalies are not included in data set 2. Older volcano ages are used in data set 2. We believe that these two data sets bound current estimates of the timing and distribution of post-caldera basaltic volcanic events in the YMR, noting that alternative data sets may certainly be developed and ages may be revised as additional geochronological analyses are reported.

In addition, these two data sets are further subdivided throughout the analyses that follow by volcano age. Each analysis is made for all volcanoes in the data set (i.e., all mapped post-caldera basalts), volcanoes less than 5 Ma, and volcanoes less than 2 Ma. This is done in recognition of the nonstationary character of cinder cone volcanism. Inspection of Figure 7-1, for example, reveals that Miocene clusters have little spatial relationship to Pliocene and Quaternary cluster distribution. However, Pliocene clusters have certainly reactivated in the Quaternary. Thus, further division of the two data sets preferentially weights the distribution of younger volcanoes.

Estimate of the regional recurrence rate, λ_t, of volcanism for the YMR during the Quaternary has received a great deal of study. These estimates range from about 1 volcano per million years (v/my) to 8 v/my (e.g., Ho, 1991; Ho et al., 1991; Crowe et al., 1992a). This range of estimates is based on the application of various averaging techniques and statistical estimators. For example, one approach has been to consider the number of volcanoes that have been formed in the last 1.8 m.y. (Crowe et al., 1982). A total of eight volcanoes formed during that time interval and $\lambda_t \approx 4$ v/my (Crowe et al., 1982). However, the YMR Quaternary volcanoes are all less than approximately 1 Ma, so, averaging over the last 1 m.y., $\lambda_t \approx 7$ to 8 v/my. For all post-caldera basalts, $\lambda_t \approx 3$ v/my. Using a maximum likelihood estimator, Ho et al. (1991) calculated $\lambda_t \approx 5$ to 6 v/my. Finally, based on a Poisson-Weibull model, Ho (1992) calculated that $\lambda_t \approx 2$ to 13 v/my with 90 percent confidence. We do not attempt to refine these estimates here. Rather, our probability estimates assume $\lambda_t = 5$ to 10 v/my in order to encompass most previous estimates.

7.2.3.3 Probability Models

Connor and Hill (1993) reported several statistical tests for clustering in the YMR. A weighted-centroid cluster analysis (Späth, 1980) of vent distribution in the YMR helps illustrate vent clustering and provides additional insight into vent distribution. The results of the cluster analysis are shown by a dendrogram (Figure 7-2), which plots the distance at which individual cones and clusters link, where the linkage distance is the distance between the centers of clusters (Späth, 1980). The dendrogram shown was calculated using data set 1 and volcanoes formed less than 5 Ma. The cluster analysis was repeated using both data sets, subdivided by age, and a variety of clustering algorithms with very similar results to those plotted (Figure 7-2). The weighted centroid cluster analysis shows that four clusters of volcanoes less than 5 Ma exist in the YMR. These clusters consist of (i) the Amargosa Valley Cluster, including Lathop Wells, (ii) the Crater Flat Cluster, (iii) the Sleeping Butte Cluster, including Hidden Cone, Little Black Peak, and Thirsty Mesa (Figure 7-1), and (iv) the Buckboard Mesa Cluster, which consists of only two closely spaced vents. These four clusters are complete and self-contained at linkage distances of 15 km or less. The four clusters begin forming groups at 23 km, when the Amargosa Valley and Crater Flat Valley Clusters form a single group (Figure 7-2). Together these volcanoes are isolated from the Sleeping Buttes and Buckboard Mesa Clusters. The Amagosa Valley and Crater Flat Clusters are less distinct using a single linkage clustering algorithm because of the comparatively intermediate position of Lathrop Wells (Figure 7-1). Vent pairs,

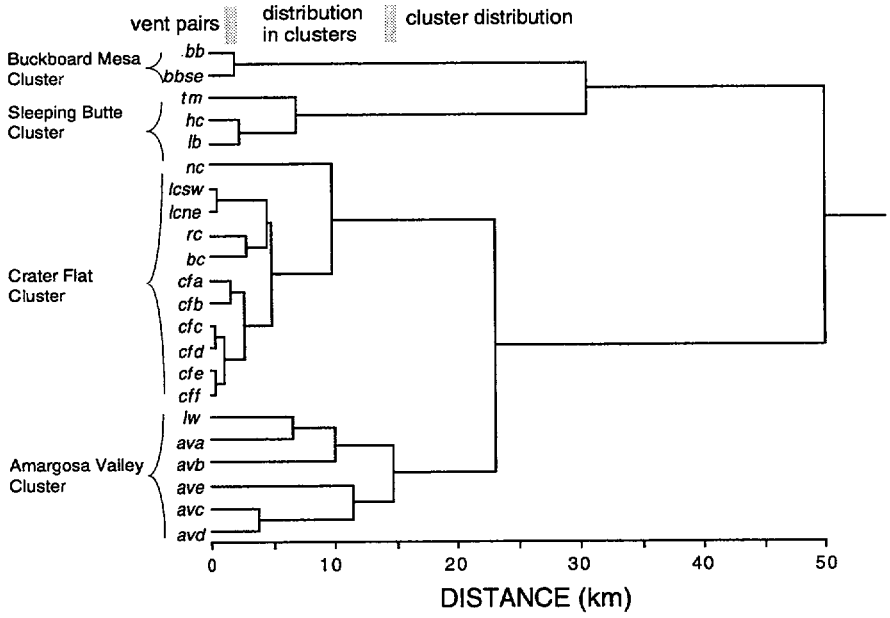

Figure 7-2. Weighted centroid cluster analysis of volcano distribution in the YMR, calculated for volcanoes formed <5 Ma. Volcano abbreviations are bb—Buckboard Mesa, bbse—Buckboard Mesa SE, tm—Thirsty Mesa, hc—Hidden Cone, lb—Little Black Peak, nc—Northern Cone, rc—Red Cone, bc—Black Cone, lcsw and lcne—Little Cones SW and NE, lw—Lathrop Wells, cf(a-f)—Pliocene Crater Flat vents, av(a-e)—Amargosa Valley aeromagnetic anomalies.

which are grouped as single events in data set 2, such as the Little Cones, link at distances of less than 2 km. The absence of these vent pairs in the Amargosa Valley Cluster is evident in comparing linkage distances in this cluster with Crater Flat. Absence of vent pairs may indicate the comparatively low resolution of aeromagnetic methods for the delineation of buried vent pairs, or reflect a difference in the style of volcanism between the two clusters. Adding a hypothetical volcanic event at the location of the candidate repository (Figure 7-1) alters the cluster analysis very little. The hypothetical repository event links with Northern Cone at a distance of 8.2 km; this group then links with the rest of the Crater Flat Cluster at a distance of approximately 11 km.

In summary, the analysis of volcano distribution yields several observations that are useful for interpretation of the near-neighbor analyses. First, vents form statistically significant clusters in the YMR. Volcanoes less than 5 Ma form four clusters, the Crater Flat and Amargosa Valley Clusters overlapping somewhat due to the position of the Lathrop Wells cone. Second, a volcanic event located at the repository would be part of, albeit near the edge of, the Crater Flat Cluster, rather than forming between or far from clusters in the YMR. Third, three of the four clusters contain Quaternary basalts, indicating that these clusters are long-lived and provide some indication of the likely areas of future volcanism. Finally, the cluster analysis provides one mean of estimating the smoothing constant, h, used in method 2. If h is chosen to be less than 15 km, then significant, perhaps unwarranted, variation in recurrence rate will be predicted within clusters. If h is chosen to be greater than 25 to 30 km, recurrence rate will be comparatively high between

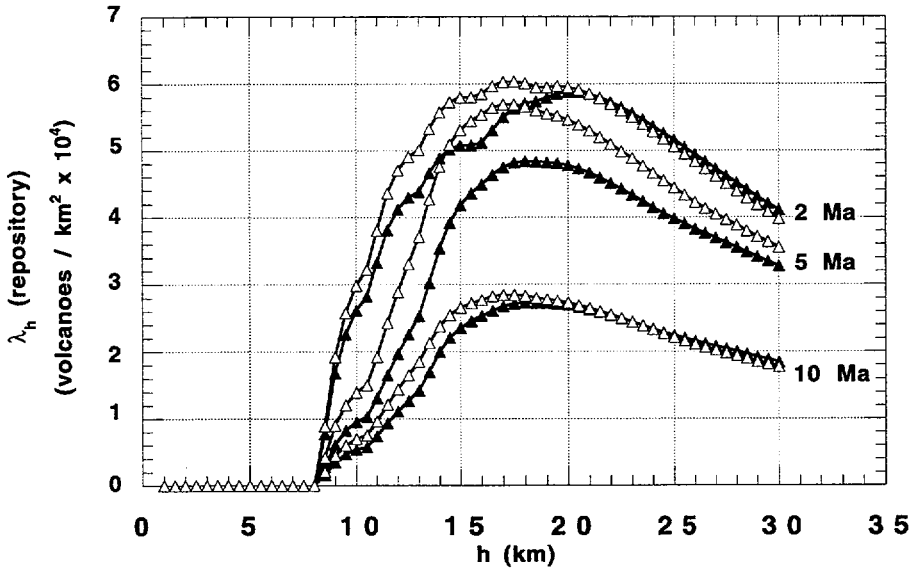

Figure 7-2. Spatial recurrence rate of basaltic volcanism estimated for the location of the proposed repository using the kernel method, where *h* is the smoothing constant. Solid triangles—data set 1, open triangles—data set 2. These data are further subdivided and calculations repeated for all volcanoes (<10 Ma), volcanoes formed less than 5 Ma, and less than 2 Ma.

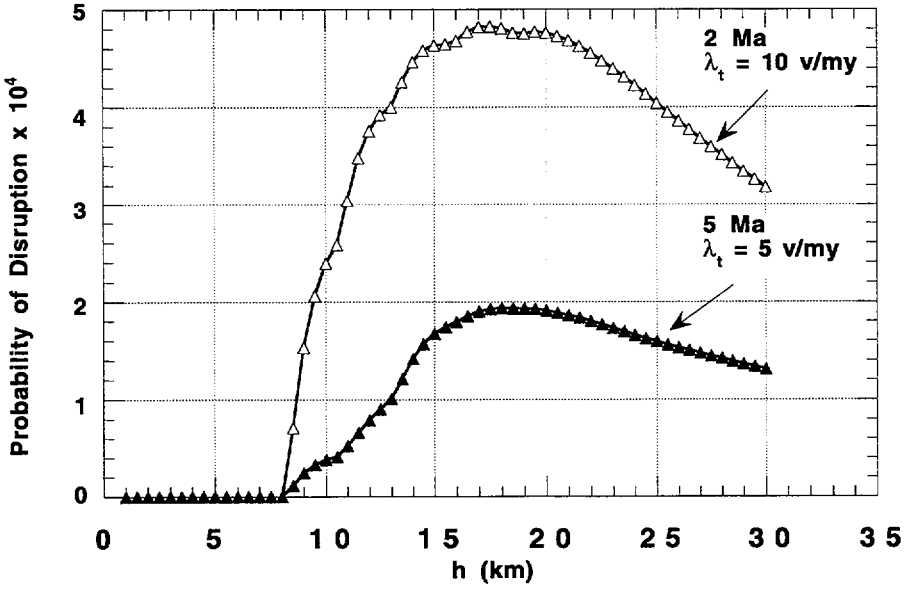

Figure 7-3. Probability of volcanic disruption of the proposed repository, estimated using the kernel method, is bounded by two curves, calculated assuming a=8 km^2 and t=10,000 yr. Open triangles—data set 2, including volcanoes formed less than 2 Ma and λ_t=10 v/my. Solid triangles—data set 1, including volcanoes formed less than 5 Ma and λ_t=5 v/my.

clusters. Choosing h between 15 and 25 km, therefore, will best capture the clustered nature of volcano distribution in the YMR.

Application of the Kernel Method

Spatial recurrence rate $\lambda_h(p)$ [Eq. (7-1)] is calculated for the repository using the same data sets for a range of smoothing constants (Figure 7-3). For h=5 to 30 km, $\lambda_h(p)$=1.3×10^{-4} to 6.0×10^{-4} v/km^2 at the repository with a maximum at h=20 km for most data sets. At h<15 km, the recurrence rate drops with decreasing h to 0 at h=8 km, the approximate distance between Northern cone and the repository site. Letting λ_t=5 to 10 v/my, the probability of volcanic disruption of the repository (a=8 km^2 and t=10,000 yr) is calculated for data set 1 (volcanoes formed <5 Ma) and data set 2 (volcanoes formed <2 Ma), other calculations falling at intermediate values between the two curves (Figure 7-4). Taking 15 km<h<25 km, based on interpretation of the cluster analysis, the probability of volcanic disruption of the repository in 10,000 yr is between 1×10^{-4} and 5×10^{-4}. Maps of the probability of volcanic eruptions throughout the region are plotted in Figure 7-5a and b. The clustered nature of volcanism in the YMR is clearly illustrated on these maps, as is the overall NNW-trend in vent distribution. The probability of volcanic eruptions drops to zero very close to the log $P[N \geq 1, a=8 \text{ km}^2, t=10{,}000 \text{ yr}] = -4.5$ contour, for h= 0 km.

Application of the Nearest-Neighbor Kernel Method

Spatial recurrence rate, $\lambda_k(p)$, is calculated at the repository site using Eq. (7-2) where the smoothing constant h is replaced by the distance to the m^{th} nearest-neighbor volcano. The maximum value of $\lambda_k(p)$ at the repository is estimated to be 4.0×10^{-4} v/km^2, for data set 2 (Figure 7-6), volcanoes less than 2 Ma and the fifth nearest-neighbor. Each of the data sets goes through a maximum, the value of $\lambda_k(p)$ at the maximum depending on the number of volcanoes included in the analysis. Data sets of volcanoes less than 5 Ma and all volcanoes have maxima at the same number of nearest-neighbors because the nearest-neighbors to the repository are all less than 5 Ma. Nearly all estimates of $\lambda_k(p)$>1×10^{-4} v/km^2. The probability of volcanic disruption of the repository site largely varies from $P[N=1, a=8 \text{ km}^2, t=10{,}000 \text{ yr}]$=5×10^{-5} to 1.5×10^{-4}, with a maximum probability of 3.4×10^{-4} (Figure 7-7), based on the distribution of Quaternary volcanoes and λ_t=10 v/my. Maps showing the variation in probability of volcanic eruptions across the YMR calculated using $\lambda_k(p)$ are plotted in Figure 7-8a and b.

7.2.4 Discussion

The three nonparametric methods—spatio-temporal nearest-neighbor (Connor and Hill, 1993), kernel, and nearest-neighbor kernel—are sensitive to basic patterns in cinder cone distribution to varying degrees. These patterns include shifts in the location of cinder cone volcanism in time, cinder cone clustering, and the presence of vent and regional volcano alignments. These features of areal volcanic fields make nonhomogeneous models useful for modeling volcano distributions and calculating the probability of future volcanic eruptions within these areas.

7.2.4.1 Comparison of the Three Methods

The spatio-temporal nearest-neighbor method is most sensitive to shifts in the locus of cinder cone volcanism through time because it incorporates time since volcano formation directly into the recurrence rate estimate. Thus, using all post-caldera basalts in the calculation of probability of future volcanic eruptions in the YMR, the method produces a small mode in probability at Miocene clusters, but this mode is distinctly smaller than the Crater Flat mode. Using kernel and nearest-neighbor kernel methods and the same data, modes at Crater Flat and in Miocene clusters are of nearly equal amplitude. However, application of the spatio-temporal nearest-neighbor method requires a high degree of precision in age determinations to be applied with confidence. In areas where shifts in the locus of volcanism are as temporally distinct as they are in the YMR, the two kernel methods are easily adapted by subdividing the volcano data set on the basis of age, as we have done for the YMR. The kernel method is least sensitive to shifts in the location of volcanism because the probability of volcanic eruptions is zero at distances greater than the smoothing constant if the Epanechnikov kernel is used [Eq. (7-1)].

The occurrence of cinder cone clusters is commonplace and well documented in basaltic volcanic fields (e.g., Heming, 1980; Connor, 1990). This clustering may be the result of various geologic controls on cinder cone emplacement, including the size, distribution, and longevity of partial melt zones, or possibly the heterogeneity of extension rates within the crust (Heming, 1980; Connor, 1990). Geological factors such as these suggest a mechanistic basis for application

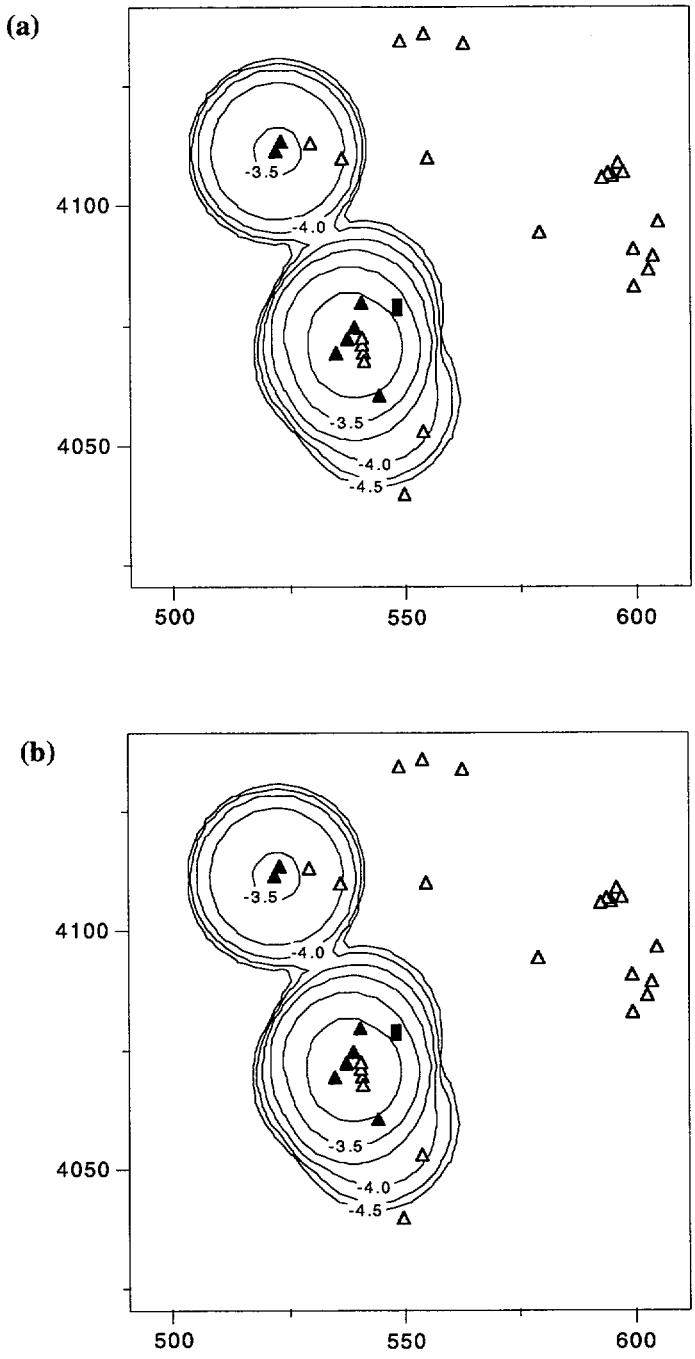

Figure 7-5. Maps showing the variation in probability of volcanic eruptions across the YMR calculated using the kernel method, contoured using h=20 km and (a) all volcanoes in data set 1 formed <5 Ma, and (b) all volcanoes in data set 2 formed <2 Ma. The contour interval is 0.25 log [P(N≥1, a=8 km^2, t =10,000 yr)]. Solid triangles show vent locations used in probability models. Open triangles show vents not used. Black rectangle represents proposed repository. Map coordinates are in UTM, zone 11.

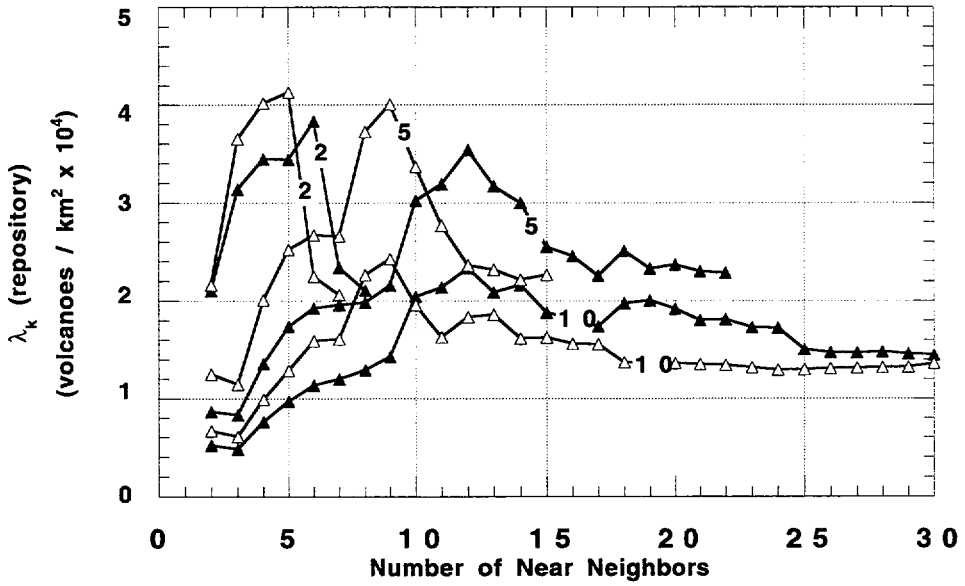

Figure 7-6. Spatial recurrence rate of volcanism at the location of the proposed repository, estimated using the nearest-neighbor kernel method. Symbols and line labels are as in Figure 7-3; curves labeled in millions of years.

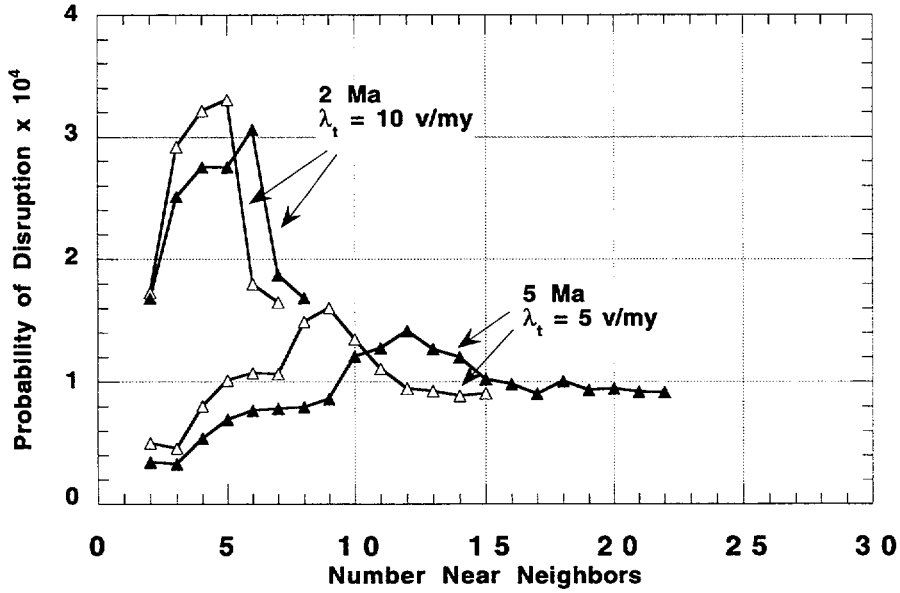

Figure 7-7. The probability of disruption of the proposed repository, estimated using the nearest-neighbor kernel method, is shown for four curves, each calculated using a=8 km^2 and t=10,000 yr. Open triangles — data set 2; solid triangles — data set 1. Calculations using volcanoes formed <2 Ma, labeled 2 Ma, are calculated using λ_t=10 v/my; calculations using volcanoes formed <5 Ma, labeled 5 Ma, are calculated using λ_t=5 v/my.

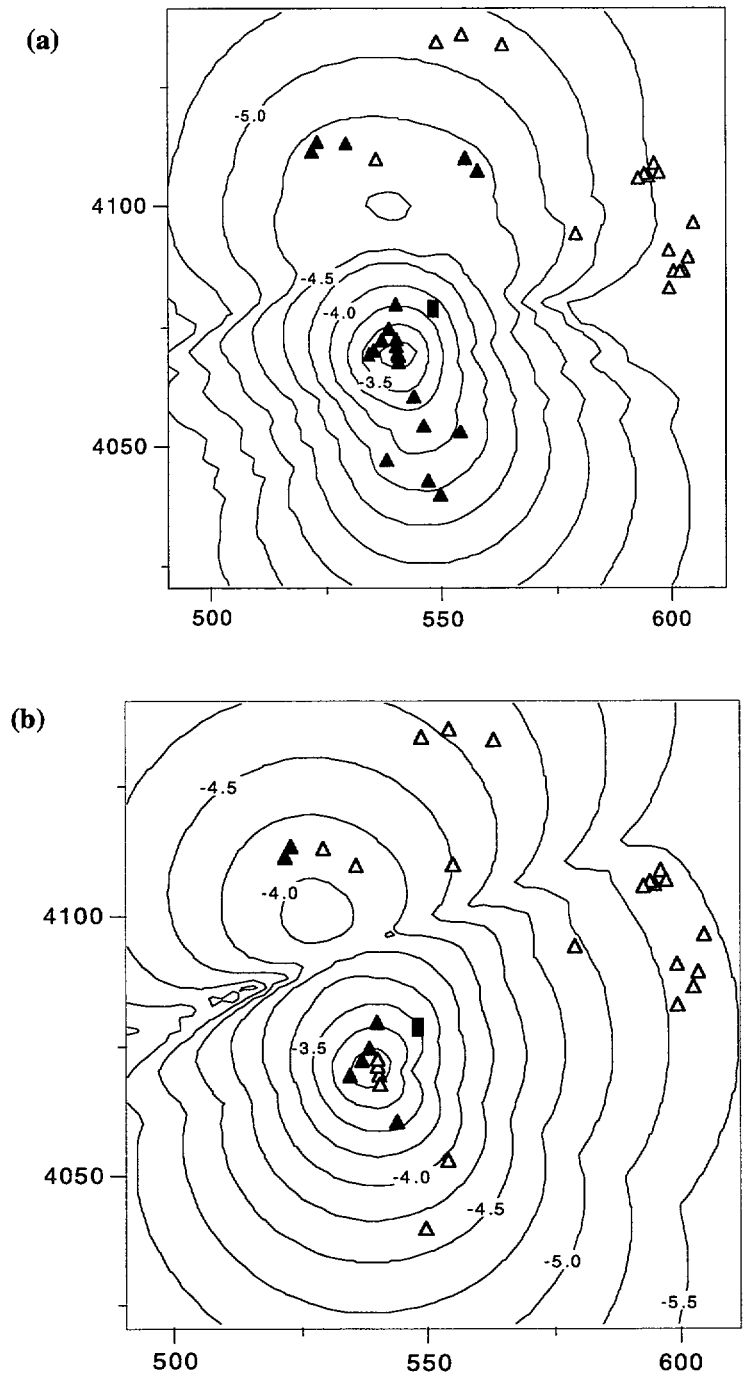

Figure 7-8. Maps showing the variation in probability of volcanic eruptions across the YMR calculated using the nearest-neighbor kernel method, contoured using (a) m=12 nearest-neighbors and all volcanoes in data set 1 formed < 5 Ma, and (b) m=5 nearest-neighbors and all volcanoes in data set 2 formed < 2 Ma. The contour interval is 0.25 log(P[N≥1, a=8 km^2, t =10,000 yr]). Symbols are as in Figure 7-5. Map coordinates are in UTM, zone 11.

of temporally and spatially nonhomogeneous Poisson probability models. The three methods treat clusters using different criteria, with varying results. The kernel method presupposes that volcano density and distance between volcanoes best defines clustering. As a result, for example, the kernel method effectively identifies the Sleeping Butte area as a cluster of three volcanoes (Hidden Cone, Little Black Peak, and Thirsty Mesa), in a manner quite consistent with the cluster analysis (Figure 7-5). The nearest-neighbor kernel method presupposes that the number of volcanoes, or volcanic events, is the predominant characteristic defining clusters. Therefore, these methods weight rates of volcanic activity between clusters much more heavily than does the kernel method. For example, the nearest-neighbor kernel method does not identify a separate cluster in the Sleeping Butte area, because only three volcanoes define the cluster (e.g., Figure 7-8). Rather, contour lines tend to elongate between the Sleeping Butte Cluster and the Crater Flat Cluster when recurrence rate is determined using either spatio-temporal nearest-neighbor or nearest-neighbor kernel methods, and probability of volcanic eruptions in the center of the Crater Flat Cluster is calculated to be comparatively high.

All three methods respond to the presence of regional volcano alignments. In the YMR, the NNW trend of the Crater Flat Volcanic Zone (CFVZ) is reflected in the overall shape of the probability surfaces calculated using the three methods. It is possible to model existing local vent alignments, such as the vent alignments within the Crater Flat Cluster, by decreasing the smoothing constant, h, in the kernel method (Lutz and Gutmann, 1994) or decreasing the number of nearest-neighbors used in the other two methods. In the case of the YMR, alignments are modeled by choosing h <5 km or m≤ 3 nearest-neighbor volcanoes.

7.2.4.2 Probability of Volcanic Disruption of the Proposed Yucca Mountain Repository

Volcano clustering in the YMR is statistically significant at the 95-percent confidence level. Probability models based on a homogeneous Poisson density distribution will overestimate the likelihood of future igneous activity in parts of the YMR far from Quaternary centers and underestimate the likelihood of future igneous activity within and close to Quaternary volcano clusters.

The probability of volcanic disruption of the proposed High-Level Waste (HLW) repository site calculated using the three methods is consistently between 1×10^{-4} and 5.0×10^{-4}, in 10,000 yr for an 8-km^2 area. This range is close to, or slightly higher than, ranges indicated by most calculations based on homogeneous Poisson models. For example, Crowe et al. (1982) propose a range of probability of disruption between 3.3×10^{-6} and 4.7×10^{-4} in 10,000 yr, noting that only a "worst case" model leads to probabilities in excess of 1×10^{-4}. Other reported ranges of between 1×10^{-6} and 1×10^{-4} in 10,000 yr (Crowe et al., 1992a) are close to the probabilities calculated using near-neighbor nonhomogeneous models. Differences, especially at the lower bound, arise because the candidate repository site is relatively close to the youngest large volcano cluster in the YMR. More recently, Crowe et al. (1993) proposed a range of models and calculated a range of probabilities of disruption between 9×10^{-5} and 2.6×10^{-4} in 10,000 yr using various area terms. "Worst case" models of repository disruption in which structural controls, such as those that may have resulted in the alignment of cinder cones in Crater Flat, are assumed to focus magmatism (Smith et al., 1990; Ho, 1992) and include probabilities as high as 1×10^{-3} in 10,000 yr. The nonhomogeneous models developed here do not support such high probabilities because they do not include this kind of mechanistic control. The model of Smith et al. (1990) precludes volcanism anywhere else in the YMR, and therefore appears to be overly conservative. However, it is noted that the nonhomogeneous methods do give probabilities as high as 1×10^{-3} near the center of the Crater Flat Cluster. Thus, specific areas in the YMR have experienced volcanism on the scale Smith et al. (1990) suggest for the repository block.

The basic agreement between many of these estimates of the probability of volcanic disruption of the proposed repository must be tempered, however, by a fundamental result of the spatial and spatio-temporal nonhomogeneous techniques developed here. All three nonhomogeneous methods indicate that the proposed repository is positioned on a probability gradient due to its proximity to Crater Flat. Immediately west of the proposed site, the probability of volcanism within the next 10,000 yr increases by about one order of magnitude due to the presence of Quaternary volcanoes in Crater Flat Valley. The probability of volcanism within the next 10,000 yr decreases east of the proposed repository site; 20 km east of the site, the probability of

a new volcano forming within an 8-km^2 area is on the order of 1×10^{-5} in 10,000 yr or less. This rapid change in probability, resulting from clustering in volcano distribution, has important implications for the uncertainty associated with the use of probability models. Within 20 km of the proposed site, the probability of volcanism during the next 10,000 yr and within a given 8-km^2 area varies by more than two orders of magnitude. Given the change in probability across the area, it seems likely that additional geologic information, such as the role of pre-existing structure (Smith et al., 1990; McDuffie et al., 1994), orientation of pre-existing faults in a three-dimensional stress field (Ferrill et al., 1995), or strain rate (Parsons and Thompson, 1991), may alter estimates of the probability of future volcanic activity at the proposed repository site.

7.2.4.3 Conclusions

Near-neighbor estimates of spatial and spatio-temporal variation in recurrence rate of basaltic volcanism can account, to varying degrees, for several basic features of volcano distribution in areal basaltic fields. These features include spatial shifts in the locus of volcanism, clustering of volcanoes within the field, and the occurrence of volcano alignments. A strength of near-neighbor methods is that uncertainty can be estimated, both by mapping variation in the probability surface across the region of interest and through experimentation encompassing the precision and accuracy of geochronological information.

Application of the Hopkins F-test and related methods shows with some other recent estimates that cinder cones cluster in the YMR with greater than 95-percent confidence. Assuming a regional Quaternary recurrence rate of 5 to 10 v/my, these models estimate probabilities of disruption of between 1×10^{-4} and 5×10^{-4} in 10,000 yr, and are in close agreement. However, spatial variation in estimated recurrence rate is substantial across the YMR, with the probability of volcanic eruptions varying by more than two orders of magnitude within 20 km of the proposed repository site. This variation indicates that refinement of models, primarily through the incorporation of additional geological information, may alter these probability estimates.

7.3 ASSESSMENT OF PROGRESS

The Volcanic Systems of the Basin and Range Research Project was initiated more than 2 yr ago and will be completed in less than 12 mo. Progress at this late stage in the project must be assessed in terms of how helpful this research has been in clarifying and reducing KTUs associated with volcanism. In particular

- Prediction of future system states (disruptive scenarios)
- Development and use of conceptual tectonic models as related to igneous activity

KTUs, which were developed, in part, because of early research on this project, need to be examined in view of the results of research to date. Much of the following discussion is preliminary and may be revised with submission of MMs on probability of volcanism and tectonic models for the setting of volcanism.

7.3.1 Prediction of Future System States

Research at the CNWRA into the probability of volcanic disruption of the proposed repository has led to recognition of several scales of spatial and temporal patterns in cinder cone volcanism that must be incorporated into any viable probability model. The patterns include: (i) shifts in the location of volcanism, either by migration or more abrupt changes in the locus of volcanism; (ii) development of clusters, and (iii) development of regional alignments and local vent alignments. Research in this project has documented and quantified these aspects of vent distribution in a comprehensive fashion for the first time. Recognition of these aspects of basaltic volcano distribution provides the NRC with a direct means of assessing the utility and applicability of any volcanism probability model, and determining if this model is conservative.

Planned research is now essentially complete on the development and implementation of nonparametric, nonhomogeneous probability models, which includes spatio-temporal nearest-neighbor, kernel, and nearest-neighbor kernel models. This research represents the first application of nonparametric and nonhomogeneous probability models to volcanism in the YMR, and the first time these models have been developed for use in volcanic fields in

general. Development of these models has provided insight into the spatial scale of probability variation in the YMR that was not otherwise available. Although probability estimates of volcanic disruption of the proposed repository based on nonparametric, nonhomogeneous models are broadly similar to those based on simpler techniques, such as homogeneous models, they also indicate that probability varies by more than two orders of magnitude within 20 km of the center of the repository block, due to the position of the repository at the edge of the Crater Flat Cluster. Thus, these models show that much of the uncertainty in prediction of the probability of disruptive scenarios lies in the constraints that can be placed on this spatial scale of variation. If a proposed model for disruptive scenarios does not address the occurrence of this variation, as brought out by the nonparametric models, then it may not be conservative. Development is continuing on other probability models, including spatio-temporal Markov models. This continued development is very important, because Markov models may provide a link between probability models and deterministic models, related to tectonism.

7.3.2 Development and Use of Conceptual Tectonic Models Related to Igneous Activity

Research on the development and use of conceptual tectonic models as related to igneous activity within the Volcanic Systems of the Basin and Range Research Project has been limited to literature review and the compilation of the volcanism and tectonics GIS databases. These activities have not resulted in development of new models. Rather, these activities have enabled investigators on the project to evaluate the level of complexity of application of tectonic models to volcanism issues warranted by current developments in the field. Three broad and preliminary statements can be made regarding the utility of structural models in igneous disruptive scenario modeling.

(1) Correlation between regional rates of extension and volcanism is clear, yet, given available data, this correlation does not in itself provide insight into the likelihood of continuing volcanism in the YMR on the spatial and temporal scales of most concern. Rates of deformation are poorly known compared with geochronological data available for most volcanic fields. Episodes of volcanism may occur synchronously with episodes of extension, but this possibility has not been demonstrated conclusively in any western Great Basin volcanic field. Future work may resolve this by using specific field examples where timing of volcanism and deformation (magnitude and rate) can be determined.

(2) On a regional scale, volcanism in the western Great Basin is, in some cases, localized in pull-apart zones (e.g., the Coso Volcanic Field) and similar structures. Broad, regional fault patterns in the YMR may be consistent with this relationship. However, the scale of this correlation is regional and may not impact probability calculations given the proximity of the repository to Crater Flat.

(3) Fault and dike interaction is a viable means of focusing magmatism, particularly in areas like the YMR, where regional fault patterns and principal stress orientations are sympathetic. Therefore, fault pattern should be considered in formulating probabilistic models on a detailed, local scale, such as in Iterative Performance Assessment. Yet little data are available related to the extent to which this interaction controls the ascent and localization of basaltic magmas. Continued field work in tectonics and volcanism research must focus on these relationships at map scales of 10 km or less.

One conclusion from these observations is that current probability models based on structural control are tentative at best. Nonetheless, incorporation of structural and tectonic data does remain as one of the most likely avenues for introducing a mechanistic basis for probability models development and evaluation. Future CNWRA research in tectonics and volcanism will investigate testable hypotheses that can help alleviate difficulties with the direct incorporation of structural and tectonic information into volcanism probability models.

7.4 PLANNED PROGRESS IN THE NEXT SIX MONTHS

The critical review of the GIS database (MM for Task 3) was delivered in January 1995; an intermediate milestone was delivered in January 1995, summarizing the results and recommendations of the peer review panel; a MM on probability model development is scheduled to be delivered in June 1995. The June 1995 MM will summarize the probability model development that has resulted from research in the Volcanic Systems of the Basin and Range research project.

7.5 REFERENCES

Bacon, C.R. 1982. Time-predictable bimodal volcanism in the Coso Range, California. *Geology* 10: 65–69.

Bemis, K.G., and D.K. Smith. 1993. Production of small volcanoes in the Superswell region of the South Pacific. *Earth and Planetary Science Letters* 118: 251–262.

Braytseva, O.A., I.V. Melekestev, and V.V. Ponomareva. 1983. Age divisions of the Holocene volcanic formations of the Tolbachik Valley. *The Great Tolbachik Fissure Eruption, Geological and Geophysical Data, 1975–1976.* S.A. Fedotov and Ye. K. Markhinin, eds. New York City, NY: Cambridge University Press: 83–95.

Byers, F.M., and H. Barnes. 1967. *Geologic Map of the Paiute Ridge Quadrangle, Nye County, Nevada.* U.S. Geological Survey Geological Quadrangle Map GQ-577. Reston, VA: U.S. Geological Survey.

Byers, F.M., and D. Cummings. 1967. *Geologic Map of the Scrugham Peak Quadrangle, Nye County, Nevada.* U.S. Geological Survey Geological Quadrangle Map GQ-695. Reston, VA: U.S. Geological Survey.

Byers, F.M., C.L. Rogers, W.J. Carr, and S.J. Luft. 1966. *Geologic Map of the Buckboard Mesa Quadrangle, Nye County, Nevada.* U.S. Geological Survey Geological Quadrangle Map GQ-552. Reston, VA: U.S. Geological Survey.

Carr, W.J. 1984. *Regional and Structural Setting of Yucca Mountain, Southwestern Nevada, and Late Cenozoic Rates of Tectonic Activity in Part of the Southwestern Great Basin, Nevada and California.* U.S. Geological Survey Open-File Report 84-854. Reston, VA: U.S. Geological Survey.

Carr, W.J., and W.D. Quinlivan. 1966. *Geologic Map of the Timber Mountain Quadrangle, Nye County, Nevada.* U.S. Geological Survey Geological Quadrangle Map GQ-503. Reston, VA: U.S. Geological Survey.

Condit, C.D., L.S. Crumpler, J.C. Aubele, and W.E. Elston. 1989. Patterns of volcanism along the southern margin of the Colorado Plateau: The Springerville Field. *Journal of Geophysical Research* 94: 7,975–7,986.

Connor, C.B. 1990. Cinder cone clustering in the Trans-Mexican volcanic belt: Structural and petrologic implications. *Journal of Geophysical Research* 95: 19,395–19,405.

Connor, C.B., and C.D. Condit. 1994. Estimating recurrence rate of volcanism in the Springerville volcanic field, Arizona. *Geological Society of America Abstracts with Programs—1994 Annual Meeting.* Boulder, CO: Geological Society of America: 26(7):A-115.

Connor, C.B., and B.E. Hill. 1993. Estimating the probability of volcanic disruption of the candidate Yucca Mountain repository using spatially and temporally nonhomogeneous Poisson models. *Proceedings—Site Characterization and Model Validation, Focus '93.* La Grange Park, IL: American Nuclear Society: 174–181.

Connor, C.B., C.D. Condit, L.S. Crumpler, and J.C. Aubele. 1992. Evidence of regional structural controls on vent distribution: Springerville Volcanic Field, Arizona. *Journal of Geophysical Research* 97: 12,349–12,359.

Cornwall, H.R. 1972. *Geology and Mineral Deposits of Southern Nye County, Nevada.* Nevada Bureau of Mines and Geology Bulletin 77. Reno, NV: Nevada Bureau of Mines and Geology.

Cressie, N.A.C. 1991. *Statistics for Spatial Data,* New York City, NY: John Wiley and Sons.

Crowe, B.M. 1990. Basaltic volcanic episodes of the Yucca Mountain region. *Proceedings of the International Conference on High-Level Radioactive Waste Management.* La Grange Park, IL: American Nuclear Society: 1: 65–73.

Crowe, B.M. 1994. Probabilistic volcanic risk assessment. *Presentation to the Advisory Committee on Nuclear Waste.* Washington, DC: Advisory Committee on Nuclear Waste.

Crowe, B.M., and F.V. Perry. 1989. Volcanic probability calculations for the Yucca Mountain site: estimation of volcanic rates. *Proceedings–Nuclear Waste Isolation in the Unsaturated Zone, Focus '89*, La Grange Park, IL: American Nuclear Society: 326–334.

Crowe, B., and F. Perry. 1991. *Preliminary Geologic Map of the Sleeping Butte Volcanic Centers.* Los Alamos National Laboratory Report LA-12101-MS. Los Alamos, NM: Los Alamos National Laboratory.

Crowe, B.M., M.E. Johnson, and R.J. Beckman. 1982. Calculation of the probability of volcanic disruption of a high-level nuclear waste repository within southern Nevada, USA. *Radioactive Waste Management and the Nuclear Fuel Cycle* 3: 167–190.

Crowe, B.M., D.T. Vaniman, and W.J. Carr. 1983. *Status of Volcanic Hazard Studies for the Nevada Nuclear Waste Storage Investigations.* Los Alamos National Laboratory Report LA-9325-MS. Los Alamos, NM: Los Alamos National Laboratory.

Crowe, B.M., K.H. Wohletz, D.T. Vaniman, E. Gladney, and N. Bower. 1986. *Status of Volcanic Hazard Studies for the Nevada Nuclear Waste Storage Investigations.* Los Alamos National Laboratory Report LA-9325-MS, Vol. II. Los Alamos, NM: Los Alamos National Laboratory.

Crowe, B.M., C. Harrington, L. McFadden, F. Perry, S. Wells, B. Turrin, and D. Champion. 1988. *Preliminary Geologic Map of the Lathrop Wells Volcanic Center.* Los Alamos National Laboratory Report LA-UR-88-4155. Los Alamos, NM: Los Alamos National Laboratory.

Crowe, B.M., R. Picard, G. Valentine, and F.V. Perry. 1992a. Recurrence models for volcanic events: Applications to volcanic risk assessment. *Proceedings of the Third Annual International High-Level Radioactive Waste Management Conference.* La Grange Park, IL: American Nuclear Society: 2: 2,344–2,355.

Crowe, B., R. Morley, S. Wells, J. Geissman, E. McDonald, L. McFadden, F. Perry, M. Murrell, J. Poths, and S. Forman. 1992b. The Lathrop Wells volcanic center: Status of field and geochronology studies. *Proceedings of the Third Annual International High-Level Radioactive Waste Management Conference.* La Grange Park, IL: American Nuclear Society: 2: 1,997–2,013.

Crowe, B.M., F.V. Perry, G.A. Valentine, P.C. Wallmann, and R. Kossik. 1993. Simulation modeling of the probability of magmatic disruption of the potential Yucca Mountain site. *Proceedings–Site Characterization and Model Validation, Focus '93.* La Grange Park, IL: American Nuclear Society: 182–191.

Diggle, P.J. 1985. A kernel method for smoothing point process data. *Applied Statistics* 34: 138–147.

Dohrenwend, J.C., L.D. MacFadden, B.D. Turrin, and S.G. Wells. 1984. K-Ar dating of the Cima volcanic field, eastern Mojave Desert, California: Late Cenozoic volcanic history and landscape evolution. *Geology* 12: 163–167.

Draper, G., Z. Chen, M. Conway, C.B. Connor, and C.D. Condit. 1994. Structural control on magma pathways in the upper crust: Insights from the San Francisco volcanic field, Arizona. *Geological Society of America Abstracts with Programs—1994 Annual Meeting*: Boulder, CO: Geological Society of America: 26(7): A-115.

Duffield, W.A., C.R. Bacon, and G.B. Dalrymple. 1980. Late Cenozoic volcanism, geochronology, and structure of the Coso Range, Inyo County, California. *Journal of Geophysical Research* 85: 2,381–2,404.

Eichelberger, J.C., and R. Gooley. 1977. Evolution of silicic magma chambers and their relationship to basaltic volcanism. The Earth's Crust, J.G. Heacock, ed. *American Geophysical Union Monograph* 20: 57–77.

Ekren, E.B., R.E. Anderson, P.P. Orkild, and E.N. Hinrichs. 1966. *Geologic Map of the Silent Butte Quadrangle, Nye County, Nevada.* U.S. Geological Survey Geological Quadrangle Map GQ-493. Reston, VA: U.S. Geological Survey.

Faulds, J.E., J.W. Bell, D.L. Feuerbach, and A.R. Ramelli. 1994. *Geologic Map of the Crater Flat Area, Nevada.* Nevada Bureau of Mines and Geology Map 101. Reno, NV: Nevada Bureau of Mines and Geology.

Ferrill, D.A., A.P. Morris, D.B. Henderson, and R.H. Martin. 1995. *Tectonics Research NRC High-Level Radioactive Waste Research at CNWRA July–December 1994.* B. Sagar, ed. CNWRA 94-02S. San Antonio, TX: Center for Nuclear Waste Regulatory Analyses.

Foland, K.A., and S.C. Bergman. 1992. Temporal and spatial distribution of basaltic volcanism in the Pancake and Reveille ranges north of Yucca Mountain. *Proceedings of the Third Annual International High-Level Radioactive Waste Management Conference.* La Grange Park, IL: American Nuclear Society and American Society of Civil Engineers: 2,366–2,371.

Hasenaka, T., and I.S.E. Carmichael. 1985. The cinder cones of Michoacán-Guanajuato, central Mexico, their age, volume, distribution, and recharge rate. *Journal of Volcanology and Geothermal Research* 25: 195–204.

Heming, R.F. 1980. Patterns of Quaternary basaltic volcanism in the northern North Island, New Zealand. *New Zealand Journal of Geology and Geophysics* 23: 335–344.

Hinrichs, E.N., R.D. Krushensky, and S.J. Luft. 1967. *Geologic Map of the Ammonia Tanks Quadrangle, Nye County, Nevada.* U.S. Geological Survey Geological Quadrangle Map GQ-638. Reston, VA: U.S. Geological Survey.

Ho, C.-H. 1992. Risk assessment for the Yucca Mountain high-level nuclear waste repository site: Estimation of volcanic disruption. *Mathematical Geology* 24: 347–364.

Ho, C.-H. 1991. Time trend analysis of basaltic volcanism at the Yucca Mountain site. *Journal of Volcanology and Geothermal Research* 46: 61–72.

Ho, C.-H., E.I. Smith, D.L. Feurbach, and T.R. Naumann. 1991. Eruptive probability calculation for the Yucca Mountain site, USA: Statistical estimation of recurrence rates. *Bulletin of Volcanology* 54: 50–56.

Kane, M.F., and R.E. Bracken. 1983. *Aeromagnetic Map of Yucca Mountain and Surrounding Regions, Southwest Nevada.* U.S. Geological Survey Open-File Report 83-616, Reston, VA: U.S. Geological Survey.

Kear, D. 1964. Volcanic alignments north and west of New Zealand's central volcanic region. *New Zealand Journal of Geology and Geophysics* 7: 24–44.

Langenheim, V.E., K.S. Kirchoff-Stein, and H.W. Oliver. 1993. Geophysical investigations of buried volcanic centers near Yucca Mountain, southwestern Nevada. *Proceedings of Fourth Annual International Conference on High-Level Radioactive Waste Management.* La Grange Park, IL: American Nuclear Society: 1,840–1,846.

Lutz, T.M. 1986. An analysis of the orientations of large scale crustal structures: A statistical approach based on areal distributions of pointlike features. *Journal of Geophysical Research* 91: 421–434.

Lutz, T.M., and J.T. Gutmann. 1994. An improved method of determining alignments of point-like features and its implications for the Pinacate volcanic field, Mexico. *Journal of Geophysical Research,* in press.

Magus'kin, V.B. Enman, and V.S. Tselishchev. 1983. Changes in the height, volume, and shape of the New Tolbachik volcanoes of the Northern Breakthrough, *The Great Tolbachik Fissure Eruption, Geological and Geophysical Data, 1975–1976.* S.A. Fedotov and Ye. K. Markhnin, eds. New York City, NY: Cambridge University Press: 307–315.

McDuffie, S., Connor, C.B., and Mahrer, K.D., 1994. A simple model of fault-dike interaction. *EOS, Transactions of the American Geophysical Union 75: 384.*

Nakamura, K. 1977. Volcanoes as possible indicators of tectonic stress orientation–Principles and proposal. *Journal of Volcanology and Geothermal Research* 2: 1–16.

Noble, D.C., R.D. Krushensky, E.J. McKay, and J.R. Ege. 1967. *Geologic Map of the Dead Horse Flat Quadrangle, Nye County, Nevada.* U.S. Geological Survey Geological Quadrangle Map GQ-614. Reston, VA: U.S. Geological Survey.

Parsons, T., and G.A. Thompson. 1992. The role of magma overpressure in suppressing earthquakes and topography: Worldwide examples. *Science* 253: 1,399–1,402.

Perry, F.M. 1994. Update on characterization of volcanic features. *Presentation to the Advisory Committee on Nuclear Waste.* Washington, DC: Advisory Committee on Nuclear Waste.

Poths, J., and B.M. Crowe. 1992. Surface exposure ages and noble gas components of volcanic units at the Lathrop Wells volcanic center, Nevada. *EOS, Transactions of the American Geophysical Union* 73: 610.

Poths, J., F. Perry, and B.M. Crowe. 1994. *3He Surface Exposure Ages at the Lathrop Wells, NV, Volcanic Center.* U.S. Geological Survey Circular 1107. Reston, VA: U.S. Geological Survey: 255.

Ripley, B.D. 1981. Spatial statistics. *Wiley Series in Probability and Mathematics.* New York City, NY: John Wiley and Sons: 252.

Sawyer, D.R., R.J. Fleck, M.A. Lanphere, R.G. Warren, D.E. Broxton, and M.R. Hudson. 1994. Episodic caldera volcanism in the Miocene southwestern Nevada volcanic field: Revised stratigraphic framework, $^{40}Ar/^{39}Ar$ geochronology, and implications for magmatism and extension. *Geological Society of America Bulletin* 106: 1,304–1,318.

Silverman, B.W. 1986. *Density Estimation for Statistics and Data Analysis.* London, England: Chapman and Hall.

Sinnock, S., and R.G. Easterling. 1983. *Empirically Determined Uncertainty in Potassium-Argon Ages for Plio-Pleistocene Basalts from Crater Flat, Nye County, Nevada.* Sandia National Laboratories Report SAND 82-2441. Albuquerque, NM: Sandia National Laboratories.

Smith, E.I., T.R. Feuerbach, and J.E. Faulds. 1990. The area of most recent volcanism near Yucca Mountain, Nevada: Implications for volcanic risk assessment. *Proceedings of the International Topical Meeting on High-level Radioactive Waste.* La Grange Park, IL: American Nuclear Society: 1: 81–90.

Späth, H. 1980. *Clustering Algorithms.* New York City, NY: John Wiley and Sons.

Stirewalt, G.L., S.R. Young, and K.D. Mahrer. 1992. *A Review of Pertinent Literature on Volcanic-Magmatic and Tectonic History of the Basin and Range.* CNWRA 92-025. San Antonio, TX: Center for Nuclear Waste Regulatory Analyses.

Swadley, W.C, and W.J. Carr. 1987. *Geologic Map of the Quaternary and Tertiary Deposits of the Big Dune Quadrangle, Nye County, Nevada, and Inyo County, California.* U.S. Geological Survey Miscellaneous Investigations Series Map I-1767. Reston, VA: U.S. Geological Survey.

Takada, A. 1994. The influence of regional stress and magmatic input on styles of monogenetic and polygenetic volcanism. *Journal of Geophysical Research* 99: 13,563–13,574.

Tanaka, K.L., E.M. Shoemaker, G.E. Ulrich. and E.W. Wolfe. 1986. Migration of volcanism in the San Francisco volcanic field, Arizona. *Geological Society of America Bulletin*: 97: 129–141.

Tokarev, P.I. 1983. Calculation of the magma discharge, growth in the height of the cone and dimensions of the feeder channel of Crater I in the Great Tolbachik Fissure Eruption, July 1975. *The Great Tolbachik Fissure Eruption, Geological and Geophysical Data, 1975–1976.* S.A. Fedotov and Ye. K. Markhinin, eds. New York City, NY: Cambridge University Press: 27–35.

Tschanz, C.M, and E.H. Pampeyan. 1970. Geology and mineral deposits of Lincoln County, Nevada. *Nevada Bureau of Mines and Geology Bulletin*: Reno, NV: Nevada Bureau of Mines and Geology: 73.

Turrin, B. 1992. New high-precision $^{40}Ar/^{39}Ar$ step heating results from basalts near Yucca Mountain. *U.S. Nuclear Waste Technical Review Board, Panel on Structural Geology and Engineering Meeting on Volcanism.* Washington, DC: Nuclear Waste Technical Review Board.

Turrin, B.D., J.C. Dohrenwend, R.E. Drake, and G.H. Curtis. 1985. K-Ar ages from the Cima volcanic field, eastern Mojave Desert, California. *Isochron West* 44: 9–16.

Turrin, B.D., D. Champion, and R.J. Fleck. 1991. $^{40}Ar/^{39}Ar$ age of the Lathrop Wells volcanic center, Yucca Mountain, Nevada. *Science* 253: 654–657.

Vaniman, D.T., and B.M. Crowe. 1981. *Geology and Petrology of the Basalts of Crater Flat: Applications to Volcanic Risk Assessment for the Nuclear Waste Storage Investigations.* Los Alamos National Laboratory Report LA-8845-MS. Los Alamos, NM: Los Alamos National Laboratory.

Vaniman, D.T., B.M. Crowe, and E.S. Gladney. 1982. Petrology and geochemistry of Hawaiite lavas from Crater Flat, Nevada. *Contributions in Mineralogy and Petrology* 80: 341–357.

Wadge, G., and A. Cross. 1988. Quantitative methods for detecting aligned points: An application to the vents of the Michoacán-Guanajuato volcanic field, Mexico. *Geology* 16: 815–818.

Wadge, G., P.A.V. Young, and I.J. McKendrick. 1994. Mapping lava flow hazards using computer simulation. *Journal of Geophysical Research* 99: 489–504.

Zoback, M.L. 1989. State of stress in the northern Basin and Range Province. *Journal of Geophysical Research* 94: 7,105–7,128.

Zreda, M.G., F.M. Phillips, P.W. Kubik, P. Sharma, and D. Elmore. 1993. Cosmogenic ^{36}Cl dating of a young basaltic eruption complex, Lathrop Wells, Nevada. *Geology* 21: 57–60.

THIS PAGE INTENTIONALLY LEFT BLANK

8 TECTONIC PROCESSES IN THE CENTRAL BASIN AND RANGE REGION

by David A. Ferrill, Alan P. Morris, D. Brent Henderson, and Ronald H. Martin

Investigators: ***David A. Ferrill, Richard V. Klar, Ronald H. Martin, Alan P. Morris, Kathy H. Spivey, Gerry L. Stirewalt, Scott G. Walnum, and Stephen R. Young (CNWRA); and D. Brent Henderson (SwRI)***

NRC Project Officer: ***George F. Birchard***

8.1 TECHNICAL OBJECTIVES

The principal technical objectives of the Tectonics Research Project are to: (i) compile and integrate tectonic data for the central Basin and Range and Yucca Mountain (YM) regions, and (ii) develop and assess models of tectonic processes in those regions. Of particular concern is the adequacy of existing and anticipated data for evaluating compliance with quantitative waste-isolation performance objectives.

Geologic structure and tectonic processes are important to long-term repository performance and to preclosure operational safety. Structural deformation and tectonic processes are critical to long-term performance objectives because tectonic processes present potentially adverse conditions if they are characteristic of the controlled area or may affect isolation within the controlled area [10 CFR 60.122(c)]. Furthermore, design criteria for the geologic repository operations area require design of structures, systems, and components such that natural phenomena (e.g., earthquakes and ground rupture associated with fault slip) anticipated at the geologic repository operations area will not interfere with the necessary safety functions [10 CFR 60.131(b)(1)].

Information concerning models of tectonic processes (e.g., patterns and rates of historic and prehistoric faulting and seismicity) and structural features will be necessary to assess compliance with specific regulatory requirements as documented in License Application Review Plan (LARP) Sections 3.2.1.5 through 3.2.1.9 and 3.2.2.8. Key Technical Uncertainties (KTUs) that have been or will be addressed by the Tectonics Research project include:

- Poor resolution of exploration techniques to detect and evaluate structural features (see LARP Section 3.2.1.5)
- Evaluation of faulting mechanisms in alluvium (see LARP Section 3.2.1.5)
- Development and use of conceptual tectonic models as related to structural deformation (see LARP Section 3.2.1.5)
- Inability to predict the likelihood of earthquake occurrence during the next 10,000 yr (see LARP Sections 3.2.1.7 and 3.2.1.8)
- Correlation of earthquakes with tectonic features (see LARP Sections 3.2.1.7 and 3.2.1.8),
- Migrating seismicity between fault systems in the Basin and Range province (see LARP Section 3.2.1.8)
- Uncertainty in fault plane solutions (see LARP Section 3.2.1.8)
- Low resolution of exploration techniques to detect and evaluate igneous features (see LARP Section 3.2.1.9)
- Understanding the cause of the large hydraulic gradient located north of YM and the potential for tectonic disruption of fault-related barriers (see LARP Section 3.2.2.8)

The Tectonics Research staff is currently in the process of re-evaluating these KTUs to improve focus, eliminate redundancy, and identify additional sources of uncertainty.

Important goals of the Tectonics Research Project include development and analyses of alternate tectonic models, evaluation of potential hazards due to fault displacement and seismic shaking, and initiation of field studies to address tectonic issues. Field studies will focus on the following topics: (i) identification and analysis of structural/tectonic analogs for YM, (ii) development and assessment of alternative

structural/tectonic models for the central Basin and Range and YM regions, (iii) interaction of faulting and igneous activity (collaboration with Volcanology Research), and (iv) determination and analysis of structural/tectonic controls on regional groundwater flow (collaboration with Regional Hydrology Research). Descriptions of key tasks of the Tectonic Processes of the Central Basin and Range Research Project are available in the project plan (Young et al., 1994b).

The material presented in this chapter addresses the following KTUs: (i) Development and use of conceptual tectonic models as related to structural deformation, (ii) Correlation of earthquakes with tectonic features, (iii) Uncertainty in fault-plane solutions, and (iv) Low resolution of exploration techniques to detect and evaluate igneous features.

8.2 SIGNIFICANT TECHNICAL ACCOMPLISHMENTS

Significant technical accomplishments by the Tectonics Research Project prior to the present reporting period include: (i) development of digital terrain models of the YM and central Basin and Range regions; (ii) production of integrated maps of Quaternary faults, Quaternary basaltic volcanic fields, historic earthquake seismicity, and *in situ* stress data for the central Basin and Range region using the Tectonics Geographic Information System; (iii) compilation of an initial database of geodetically measured regional strain and geologically determined slip rates for individual fault systems in the central Basin and Range region; (iv) evaluation of historic earthquakes in southern California and Nevada with emphasis on the relationships between earthquakes and mapped faults, temporal and spatial clustering of earthquakes, and the 1992 Landers earthquake sequence in the southern Mojave desert; (v) sampling at Bare Mountain, Nevada, for fission track analyses; (vi) reconnaissance field work in the Black Mountains, California; (vii) participation in the Nuclear Regulatory Commission (NRC)/CalTech YM/Death Valley Global Positioning System (GPS) Survey; and (viii) collaborative research, with the Regional Hydrology Research, on the effects of *in situ* stress on transmissivity and regional groundwater flow in the Death Valley region.

Significant accomplishments during this reporting period include: (i) development of an interactive computer program to analyze slip tendency and dilation tendency for mapped faults and fractures; (ii) slip-tendency analyses of existing fault sets (including YM faults) to evaluate risk of slip in a contemporary stress state; (iii) analyses of dilation tendency for faults and fractures, to investigate potential for magma channeling by faults and extension fractures and to evaluate potential effects of *in situ* stress on transmissivity and regional groundwater flow; (iv) continued field research on fault and dike interaction along the Mesa Butte Fault in the San Francisco Volcanic Field, Arizona; (v) sampling at Bare Mountain, Nevada, for paleomagnetic and microstructural analyses; (vi) continued participation in the 1994 campaign of the NRC/CalTech YM/Death Valley GPS Survey; and (vii) continued collaborative research, with the Regional Hydrology Research program, on the effects of *in situ* stress on transmissivity and regional groundwater flow. The first four items in the above list are the primary focus of this chapter.

8.2.1 Slip-Tendency Analysis

A new technique referred to as slip-tendency analysis has been developed to assess the risk of fault slip and associated earthquakes on existing faults (Ferrill et al., 1994bc; Morris et al., 1994). The technique also provides a basis for selection of slip planes from focal mechanism solutions. Slip-tendency analysis is summarized and then applied to practical problems, such as assessing patterns of slip in normal-faulting regimes including the southern Great Basin, assessing potential slip patterns in the YM region, analyzing the pattern of aftershocks associated with the 1992 Little Skull Mountain earthquake sequence, and evaluating published chosen slip surfaces from focal mechanism solutions.

Slip is likely to occur on a surface when the resolved shear stress, τ, on that surface equals or exceeds the frictional resistance to sliding, which is proportional to the normal stress acting across that surface, σ_n (Figure 8-1; e.g., Jaeger and Cook, 1979). Whether or not a surface will actually slip depends upon this constant of proportionality, which describes the frictional characteristics of the surface, that is, the rock's coefficient of static friction, μ. At the instant of sliding, then:

$$\tau = \mu\sigma_n \qquad (8\text{-}1)$$

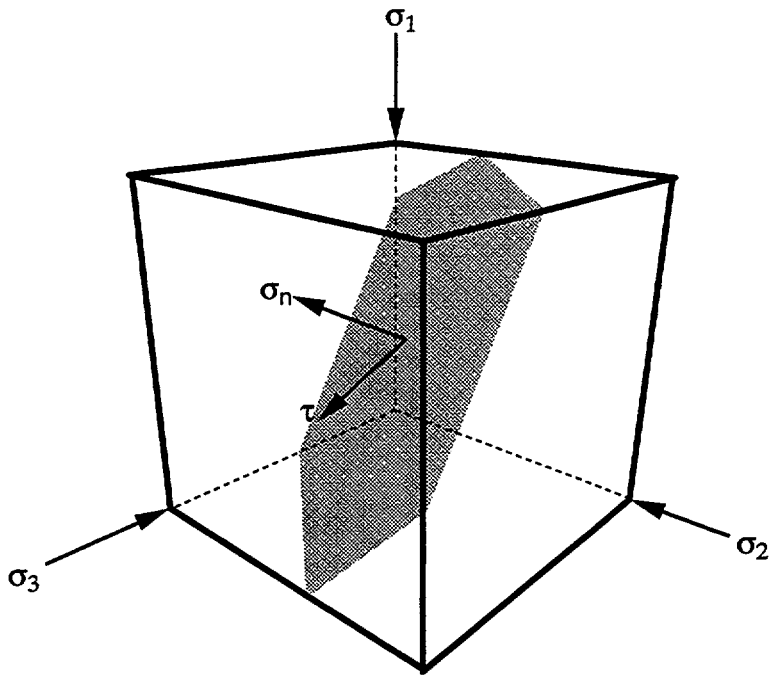

Figure 8-1. Illustration of resolved shear stress (τ) and resolved normal stress (σ_n) for a surface within a 3D stress state.

The slip tendency (T_s) of a surface can be defined as the ratio of shear stress to normal stress acting on that surface:

$$T_s = \tau/\sigma_n \qquad (8\text{-}2)$$

Thus, when T_s equals or exceeds the coefficient of static friction, μ, for a given surface, slip will occur on that surface. The coefficient of static friction is often referred to as the "strength" of a fault in earthquake focal mechanism analysis.

In a state of homogeneous stress, there is usually a pair of surfaces for which slip tendency is maximized, and this forms the basis of "Andersonian" fault analysis (Jaeger and Cook, 1979). The maximum developable slip tendency, T_{SMAX}, is determined by the differential stress, σ_1–σ_3. However, there are many other surfaces that have slip tendencies close to the maximum value. The distribution of these surfaces with respect to orientation depends upon the relative values of all three principal stresses (Wallace, 1951; Bott, 1959) and is very sensitive to the axial symmetry of the stress tensor. Natural fault systems, and those developed in analog model materials, tend to be anastomosing networks of slip surfaces with variable orientations. Some slip-surface orientations that are close to the theoretical maxima will tend to dominate, but many surfaces contribute to the overall deformation.

If the orientations and magnitudes of the principal stresses are known or assumed, it is possible to determine the state of stress on any surface within that overall stress state (e.g., Ramsay, 1967). Three parameters of special interest to structural geologists are: (i) the normal stress, σ_n; (ii) the shear stress, τ; and (iii) the direction of the resolved shear stress vector, $\vec{\tau}$, in the surface. The normal and shear stresses together give the slip tendency (τ/σ_n), and the shear stress vector indicates the type of motion that is likely to occur, for example, dipslip (normal or reverse), obliqueslip, or strikeslip (Figure 8-2). This property of the stress tensor has been most commonly exploited in inverse form to determine stress states from earthquake data (McKenzie, 1969; Gephart, 1990) and paleoslip data (Angelier, 1979). More recently, paired fault systems in the southern Great Basin have been examined for their

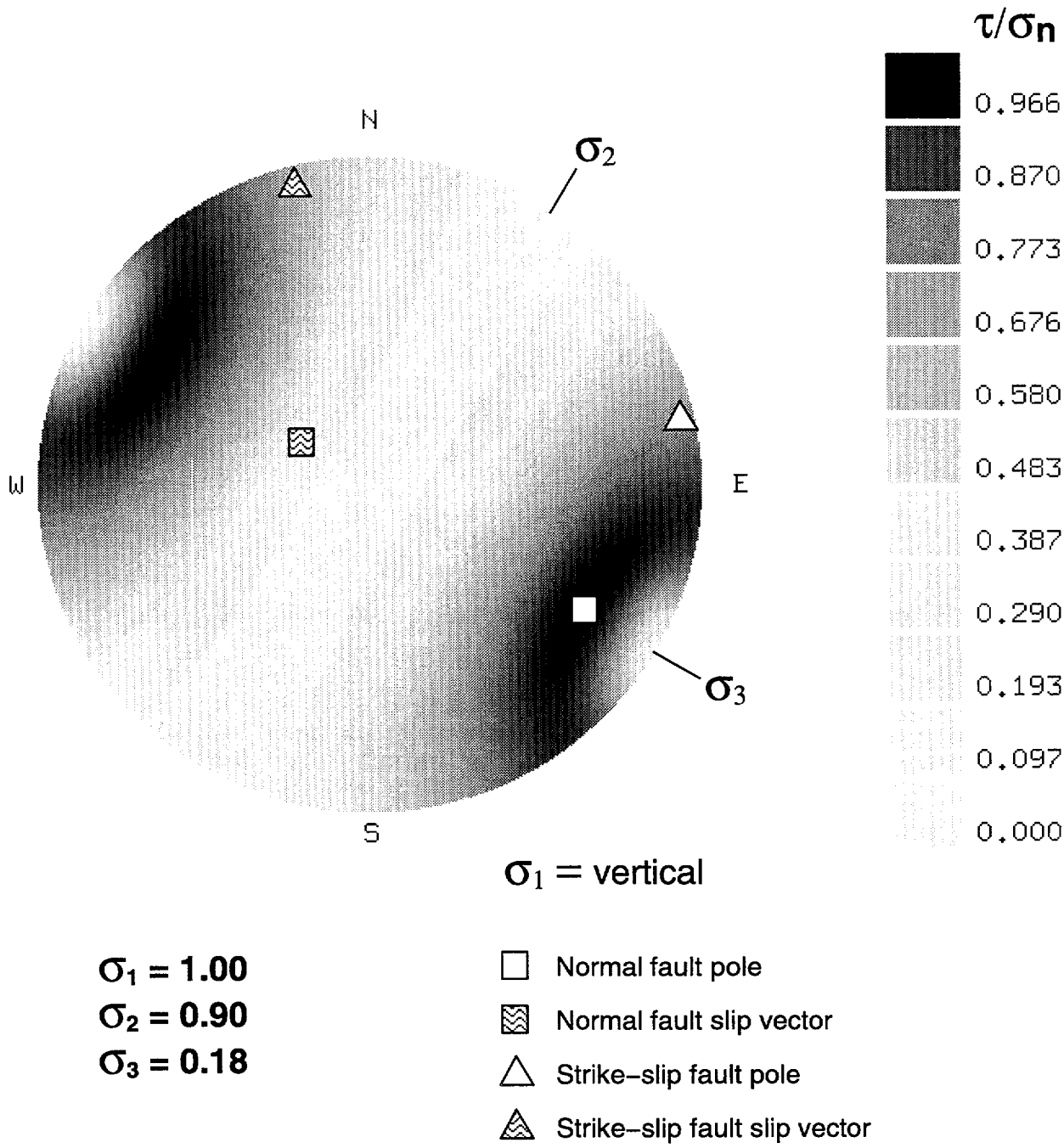

Figure 8-2. Lower hemisphere equal angle plot of poles to surfaces in a 3D stress state shaded with respect to slip tendency. Superimposed on this plot are poles to two potential slip surfaces with their resolved slip vector ($\tau^{\rightarrow}$) orientations to illustrate the coexistence of strike slip and normal faults in a single stress state

synergistic qualities by computing σ_n, τ, and $\vec{\tau}$ (Wesnousky and Jones, 1994).

It is also interesting to consider the reverse perspective. The Center for Nuclear Waste Regulatory Analyses (CNWRA) has developed an interactive computer tool that enables the stress tensor to be specified by choosing values and orientations for the principal stresses, and the slip-tendency data for surfaces of all orientations are then calculated and displayed. This slip-tendency display can then be modified by changing the magnitude or orientations of the three principal stresses and "browsed" to investigate the slip tendency and slip vector on any individual surface. The slip-tendency data are also linked to fault map traces, enabling the user to investigate various stress scenarios and their effects on known or suspected fault geometries.

Many general states of stress result in resolved stresses on faults such that there is a relatively high potential for slip on surfaces throughout a wide range of orientation. This phenomenon is especially important to an understanding of inversion methods that determine unique stress states from either paleotectonic or neotectonic slip data. The stress state inferred by current inversion techniques optimizes the slip-direction data. An alternative inversion method utilizing slip tendency data could potentially infer a different stress state. Viewing the data from the perspective of slip tendency and slip direction places the results of the inversion process in a broader context and permits stress states that are different from the computed "optimal" stress state to be considered. Most regions of the crust contain faults of many generations. Slip-tendency analysis provides a means of rapidly assessing which faults are best explained by any given stress state and which are likely to have continued accumulating slip during changing stress conditions. For example, in a complexly deformed area, slip-tendency analysis might reveal that existing faults could not have formed in a single-stress state. With a knowledge of both the *in situ* stress state and the distribution of existing faults in an area, it is possible to assess relative earthquake hazard. Whether a fault will actually slip depends upon the absolute magnitudes of the principal stresses and the coefficient of static friction, μ. In order to determine the likelihood that a fault will slip, slip tendency must be calibrated using known active faults and 3D stress tensors. Slip-tendency analysis can be used to assess the potential for and direction of slip on existing faults and to provide a basis for earthquake hazard assessment.

8.2.2 Stress States in "Normal Faulting Regimes"

In order to assign a probability that a fault will slip, slip tendency must be calibrated using known active faults, three-dimensional (3D) stress tensors, rock-strength data, and friction data. Normal faults predominate where the maximum principal compressive stress, σ_1, is vertical, and the intermediate and minimum principal compressive stresses, σ_2 and σ_3, are horizontal. However, the population of surfaces that experience high slip tendencies (e.g., $T_s \geq 0.8\ T_{sMAX}$) is variable and only approaches a bimodal distribution for a limited range of stress configurations (Figure 8-3a). Stress regimes can be defined in terms of K, where:

$$K = (\sigma_1/\sigma_2) / (\sigma_2/\sigma_3) \quad (8\text{-}3)$$

or,

$$K = (\sigma_1\sigma_3)/\sigma_2^2 \quad (8\text{-}4)$$

Stress states with $K \approx 1$ have strongly bimodal distributions of surfaces with high slip tendencies, which fall along the diagonal line (marked K=1) in Figure 8-3. This bimodal distribution of normal faults is typical of areas of relatively simple normal faulting, such as the central part of the Basin and Range province. Where K<1, for example 0.25, the distribution of high slip-tendency surfaces tends toward a girdle about the σ_3 axis including both strike-slip and dip-slip surfaces, which is more typical of transtensional regions such as the eastern California shear zone and Walker Lane region (Figure 8-3a). Conical distributions of dip-slip surfaces are unusual but characteristic of stress regimes where K>1, such as ring faults associated with collapse of a caldera (Figure 8-3a).

8.2.3 Southern Great Basin Stress State

Numerous authors have noted the apparent synchroneity of both normal and strike-slip faulting in the southern Great Basin (e.g., Wernicke et al., 1988). Some workers have suggested that this synchroneity may be a function of σ_1 and σ_2 "flip-flopping" between vertical and horizontal, NNE. There is no necessity to invoke this flip-flop if the stress state is broadly uniaxial and radially symmetrical about a horizontal σ_3 axis. The

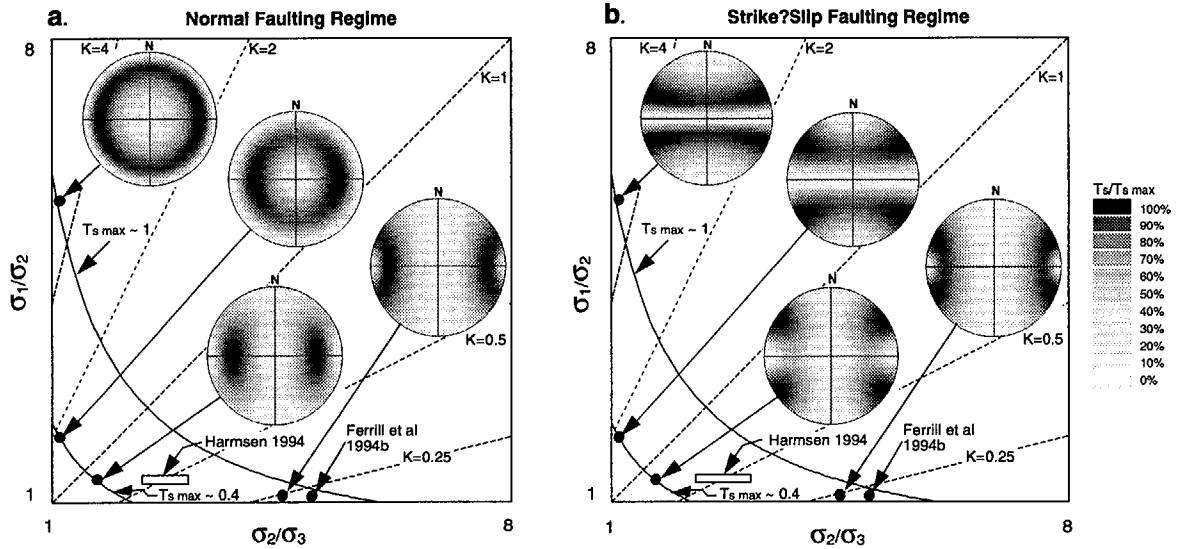

Figure 8-3. (a) σ_1/σ_2 versus σ_2/σ_3 plot for normal faulting regime (σ_1, vertical, σ_2 north-south, σ_3 east-west). Four stress states are illustrated with lower hemispheres, equal angle plots of poles to all surfaces, shaded with respect to slip tendency. Also shown are selected lines of equal K values, and curves of equal TsMAX. The Harmsen (1994) Focal Mechanism Stress Inversion (FMSI) result $[(\sigma_1-\sigma_2)/(\sigma_2-\sigma_3)=0.35]$ for the Little Skull Mountain earthquake sequence is indicated, as is the Ferrill et al. (1994b) stress state, which uses an approximate minimum case value for σ_2 of 18 percent of σ_1.

condition where σ_3 is significantly different in magnitude from σ_1 and σ_2 ($\sigma_3 << \sigma_2 \cong \sigma_1$) causes the pattern of surfaces experiencing high slip tendencies to be insensitive to changes in σ_1 and σ_2. Consequently, σ_1 and σ_2 are relatively unimportant in determining the active slip systems. Because of similarity in magnitude of σ_1 and σ_2, there is likely to be considerable uncertainty in their orientations, and less uncertainty in the orientations for σ_3. Such stress states are represented on Figure 8-3a in the bottom right of the plot ($K \approx 0.25$, $T_{sMAX} \approx 1$). There is no change in the distribution of surfaces with high T_s for stress states representative of the southern Great Basin when the stress state is instead modeled with σ_2 vertical. This phenomenon is to be expected because the axis of rotation to accomplish the flip-flop of σ_1 and σ_2 is the same as the axis of radial symmetry of the stress field (in this case, the σ_3 axis). Thus, a flip-flopping stress field is unnecessary to explain the pattern of active faulting in the southern Great Basin. Dip-slip and strike-slip faults can coexist (e.g., Figure 8-3b) within the stress states that are likely to occur in the region, those with $K < \sim 0.5$. The only noticeable change when σ_1 and σ_2 are exchanged is that normal faulting is slightly favored over strike-slip faulting when σ_1 is vertical; when σ_2 is vertical, T_s values are slightly higher for strike-slip faults.

8.2.4 Slip Tendency of Yucca Mountain Faults

Only rarely is it possible to obtain full 3D data for the surface of a fault. It is more common to have map traces. Slip-tendency computations can be linked with fault-trace maps such that the stress state can be varied, and the effects of the change in stress state on the slip tendencies of known faults can be viewed. This technique provides a means for rapidly assessing if certain sets of faults can operate simultaneously or are mutually exclusive for various stress states. A consequence of this viewing technique is that faults can be semiquantitatively assessed for their slip potential in any chosen stress state, a first step in determining seismic hazard on known or suspected faults.

Applying this technique to the faults of the YM area suggests that moderately to steeply dipping faults with north-south to northeast-southwest strikes tend to have high slip tendency (Figure 8-4). Both strike-slip and normal faults are expected to coexist in the modeled stress state (stress state after Stock et al., 1985; Zoback, 1992; Zoback et al., 1992; Ferrill et al.,1994b).

This conclusion is in excellent agreement with that of Stock et al. (1985), who infer a stress state of σ_1=20 MPa (vertical), σ_2=17 MPa (N25E), and σ_3=12 MPa (N65W) for the uppermost 1.5 km of crust at YM. The Ferrill et al. (1994b) stress state represents an extreme lower bound for the magnitude of σ_3 (=18% of σ_1) and is likely more representative of depths of about 5 km, as differential stress increases with depth (Vetter and Ryall, 1983). Harmsen (1994) infers a stress state based on the 1992 Little Skull Mountain earthquake sequence that occurred at depths of between 6 and 12 km, in which the ratios of the principal stresses (σ_1:σ_2:σ_3) are 100:74:27. All three of these stress states have qualitatively similar patterns of slip tendencies, K values of less than 1, and stress-difference ratios $[(\sigma_1-\sigma_2)/\sigma_1-\sigma_3)]$ of less than 0.4, yielding patterns of high slip tendency that are strongly radially symmetric about the σ_3 axis.

8.2.5 Slip-Tendency-Based Selection of Little Skull Mountain Nodal Planes

Earthquake data can be analyzed using slip-tendency analysis as a basis for selection of nodal planes from focal mechanism solutions. The Ms 5.4 Little Skull Mountain (LSM) earthquake occurred about 15 km southeast of YM on June 29, 1992, the day after the Ms 7.6 Landers earthquake. The Landers earthquake is thought to have triggered the LSM earthquake (Hill et al., 1993; Anderson et al., 1994; Bodin and Gomberg, 1994; Gomberg and Bodin, 1994; Ferrill et al., 1994c). Harmsen (1994) determined the tectonic stress field responsible for the LSM mainshock and aftershock sequence using Gephart's (1990) Focal Mechanism Stress Inversion (FMSI) model. In order to obtain a "best-fit" stress tensor, the inversion technique used in FMSI matches the resolved shear stress vector ($\vec{\tau}$) field of the stress tensor against the slip directions determined from focal mechanism studies. No use is made of frictional criteria, although Gephart suggests that the frictional criteria can be superimposed as an additional constraint. Slip-tendency analysis yields both frictional (T_s), and slip direction ($\vec{\tau}$) information about the stress tensor and provides a semiquantitative means of assessing earthquake data. The FMSI solution for the LSM 1992 earthquake sequence gives orientations (bearing/plunge) and relative magnitudes for principal stresses as follows: σ_1–219/69; σ_2–024/21; σ_3–116/05; and $(\sigma_1-\sigma_2)/(\sigma_1-\sigma_3)$=0.35 (Harmsen, 1994).

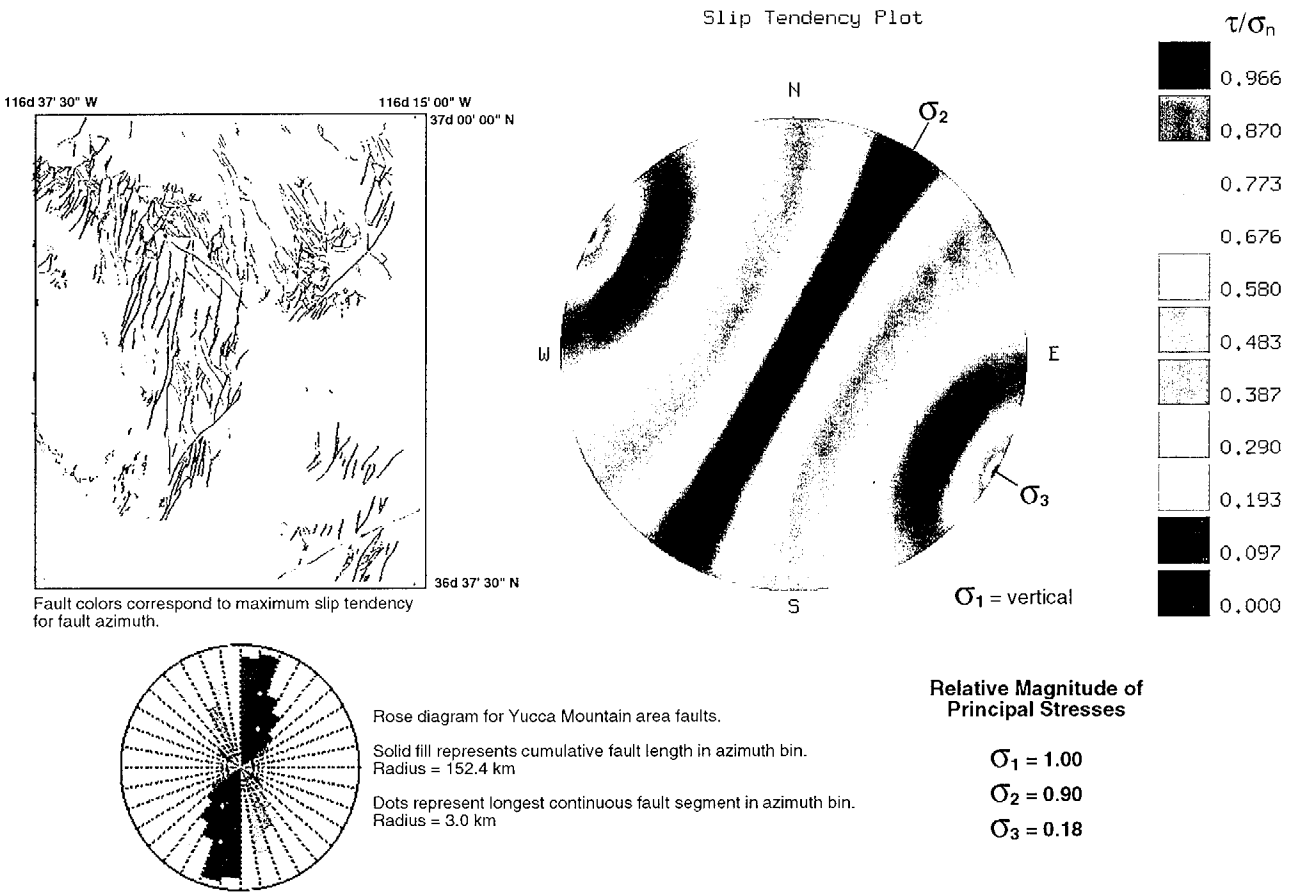

Figure 8-4. Slip-tendency analysis for YM area faults (from map by Frizzel and Shulters, 1990) suggests that moderately to steeply dipping faults with northeast-southwest strikes have high slip tendency. Both strike-slip and normal faults are expected to coexist in the modeled stress state as illustrated in Figure 8-3. Orientations of principal stresses are after Stock et al. (1985) and Zoback et al. (1992). Magnitude of σ_3 is a minimum case (18 percent of σ_1) from Ferrill et al. (1994b). When a larger σ_3 value is used, the magnitudes of the slip tendency are smaller, but the pattern of slip tendency remains virtually unchanged.

Alternatively, Harmsen and Rogers (1986) favor an axisymmetric stress field for the southern Great Basin where σ_1 is vertical and $\sigma_1 \equiv \sigma_2$. Harmsen's (1994) Figure 4 indicates that σ_3 is horizontal with an azimuth of 295°. Applying the stress field that CNWRA has used in a preliminary investigation of the YM area: σ_1=vertical; σ_2= 30° horizontal; σ_3= 00° horizontal; and $\sigma_1:\sigma_2:\sigma_3$=10:9:1.8 (Ferrill et al., 1994b) to the LSM sequence, both of the mainshock solutions given by Harmsen (1994) coincide with high (83 percent of T_{sMAX}) slip-tendency orientations and have angular misfits, β (between $\vec{\tau}$ and focal-mechanism-determined slip) of 18° [Southern Great Basin Seismic Net (SGBSN)] and 4° (Walter, 1993) respectively; whereas the FMSI-derived stress state gives slip tendencies and angular misfits of 53 percent and 4° (SGBSN) and 67 percent and 2° (Walter, 1993), respectively.

When slip tendency (T_s) is used as a criterion to pick preferred nodal planes from focal mechanism data, the slip-tendency choice disagrees with the $\vec{\tau}$-based nodal plane choice for 42 percent of the LSM events determined using the FMSI stress state and 47 percent of the LSM events using the Ferrill et al. (1994b) stress state. However, using the T_s criterion to pick the preferred nodal planes for both stress states yields the result that in the FMSI case, only 31 percent of events occurred on faults with high T_s (>80 percent of T_{sMAX}) compared with 67 percent in the Ferrill et al. (1994b) case. Although the Ferrill et al. (1994b) case does not fit the entirety of the slip-direction data as well as the FMSI stress state, it matches the slip-tendency data better.

The FMSI model specifically optimizes the focal mechanism data with the shear-stress-vector component of the stress tensor, and thus relies solely on the slip direction criteria to obtain a best-fit stress tensor. Although we do not question the validity of this approach, it does produce some anomalous results in the form of assumed slip on misoriented surfaces. Slip-tendency analysis provides a tool for the rapid assessment of such anomalies, and could be incorporated into a model such as FMSI as an additional constraint in the optimization process.

8.2.6 Dilation-Tendency Analysis

Fractures within a 3D stress state will experience a normal stress that is determined by the magnitudes and directions of the principal stresses. The ability of any fracture to open (dilate) and transmit fluid is directly related to the normal stress acting across the fracture as well as the fluid pressure. The magnitude of the normal stress can be computed for surfaces of all possible orientations within a known or hypothesized stress state that can be normalized by comparison with the differential stress. We define the dilation tendency (T_d) for a surface as follows:

$$T_d = (\sigma_1 - \sigma_n)/(\sigma_1 - \sigma_3) \qquad (8\text{-}5)$$

A composite of nine dilation-tendency plots in σ_1/σ_2, σ_2/σ_3 space (Figure 8-5) illustrates that patterns of dilation tendency are relatively simple when compared with slip-tendency patterns for identical stress states (compare with slip-tendency plots of Figure 8-6 in Ferrill et al., 1994c). A relatively simple bimodal pattern of high-dilation tendencies is expected for stress states where σ_1/σ_2 is small (Figure 8-5). Where σ_1/σ_2 is relatively large, σ_1 dominates and a conical pattern of high-dilation tendency orientations is predicted. Analysis of dilation tendency can be used to evaluate a population of existing faults and fractures to interpret the potential for fractures to act as pathways for fluid flow. Additionally, dilation-tendency analysis can be used to assess the relative risk for magma injection of existing faults and extension fractures. Two examples of applications of the dilation-tendency analysis technique are presented.

8.2.7 Dilation-Tendency Analysis of Natural Fractures and Groundwater Flow

Two factors, with respect to *in situ* stress and fractures, may contribute significantly to anisotropy of transmissivity in fractured rock (Ferrill et al., 1994c). First, existing fractures that are at a high angle to the maximum horizontal stress may preferentially be closed by the maximum horizontal stress, thereby reducing transmissivity parallel to the minimum *in situ* stress (Ferrill et al., 1994c; Wittmeyer et al., 1994; Wittmeyer and Ferrill, 1994). Secondly, new fractures tend to form in orientations that are parallel (mode 1 tensile fractures) or at a relatively low oblique angle (<45° mode 2 shear fractures) to the maximum horizontal stress. In either case, the *in situ* stress directly affects the bulk transmissivity of the rock. Transmissivity will tend to be relatively higher parallel to the maximum horizontal stress or relatively lower parallel to the

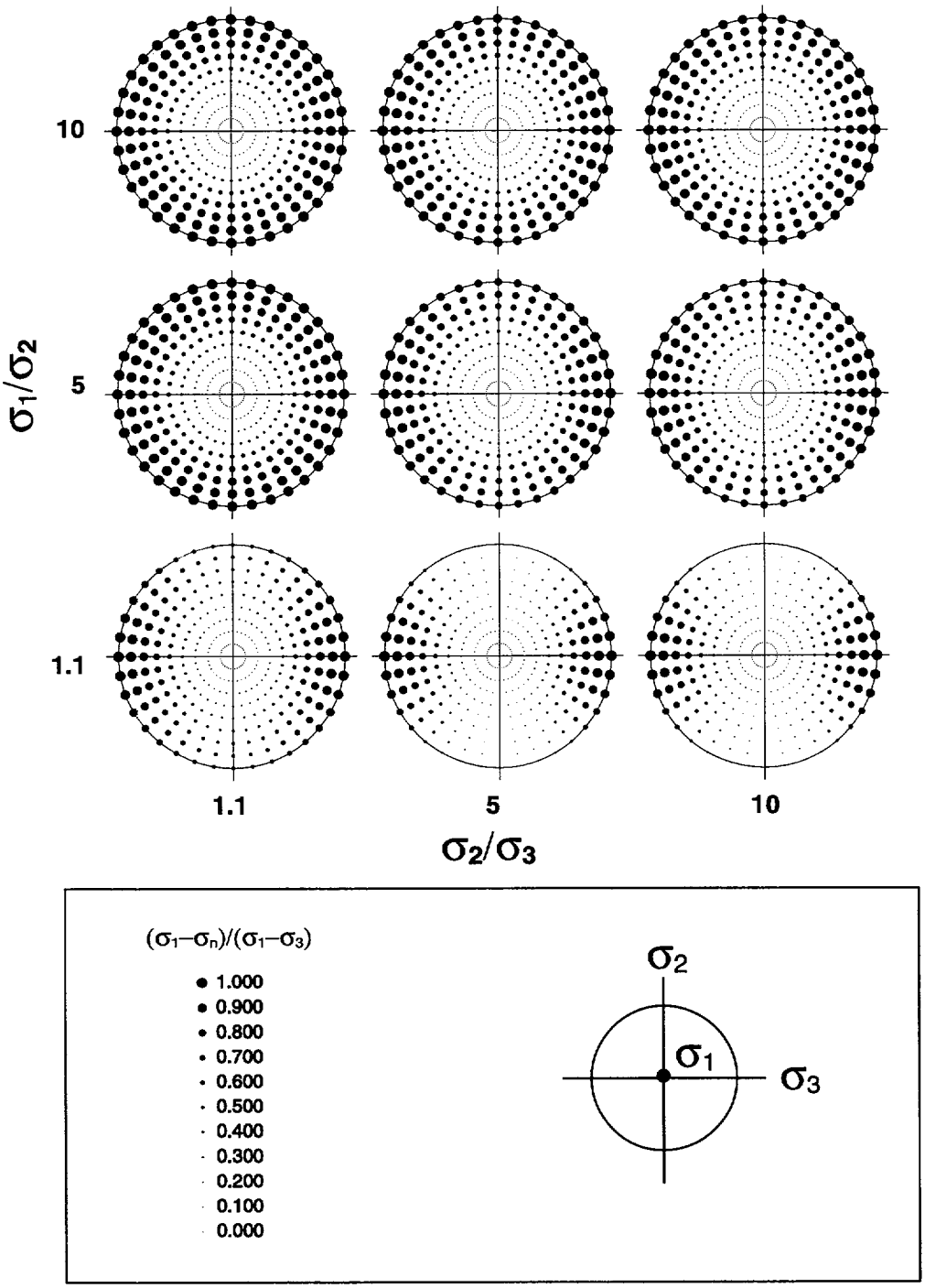

Figure 8-5. Lower hemisphere equal angle projections of poles to potential fracture surfaces. Dots that represent poles are scaled according to dilation tendency. Nine stress states are represented in $\sigma 1/s_2$, σ_2/σ_3 space.

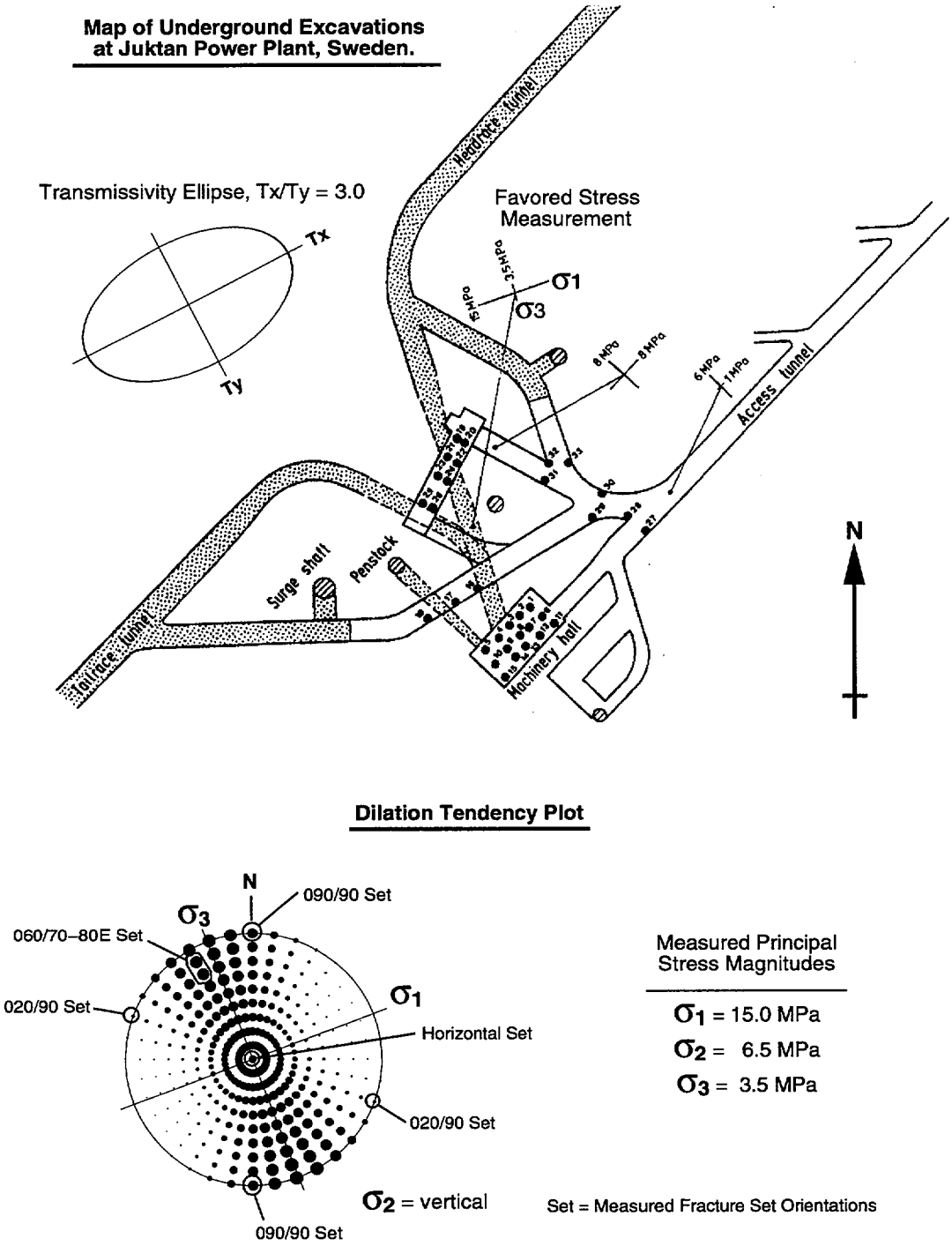

Figure 8-6. Dilation-tendency analysis for fractures and stress state at the site of the underground hydroelectric power plant, Juktan, Sweden (after Carlsson and Olsson, 1979).

minimum horizontal stress. As a test of the first model for effect of stress on transmissivity, dilation-tendency analysis was performed using *in situ* stress, transmissivity, and fracture measurements from the Juktan hydroelectric power plant.

For the Juktan underground hydroelectric power plant in northern Sweden (Carlsson and Olsson, 1979), underground tunnels were mined into fractured homogeneous Precambrian Revsund granite as deep as 400 m below the surface. A hydrologic study revealed that transmissivity is anisotropic (transmissivity anisotropy ratio = 1:3; Figure 8-6; Carlsson and Olsson, 1979) at the Juktan site. Four joint sets were identified that have the following orientations: one set that is nearly horizontal, and three vertical or subvertical sets that strike 020, 060, and 090. The 060/70-80E set was noted to be of primary importance for water inflow into the tunnels (Carlsson and Olsson, 1979). Three rock stress measurements were made using overcoring (Figure 8-6; Hiltscher et al., 1979; Leeman and Hayes, 1966). Carlsson and Olsson (1979) state that, of the three stress measurements, the following stress measurement "seems to be the most representative": 15 MPa (horizontal), 6.5 MPa (vertical), and 3.5 MPa (horizontal). There is strong agreement (approximately 5° difference) between the orientations of maximum horizontal stress and the maximum principal transmissivity (Figure 8-6; Carlsson and Olsson, 1979).

The dilation-tendency technique was applied to evaluate the dilation tendency for measured fracture orientations and observations of groundwater flow discussed by Carlsson and Olsson (1979) (Figure 8-6). The result illustrates that measured joint sets have the following dilation tendencies: 0.95–0.97 (060/70-80E set), 0.87 (090/90 set), 0.74 (horizontal set), and 0.43 (020/90 set). The 060/70-80E joint set has the highest calculated dilation tendency and was also observed to be the set of primary importance for water inflow into tunnels. Fractures of the east-west striking set also have very high dilation tendency and would, based on this analysis, also likely be significant groundwater conduits. The horizontal fracture set and the set that strikes 020 are both oriented such that normal stresses across the surfaces are relatively large. Therefore, these fractures are more likely to have small apertures than the fractures that are more nearly normal to the minimum principal compressive stress. Dilation-tendency analysis of existing joints can explain the pattern of anisotropic transmissivity in the context of the contemporary stress field. Thus, there is very strong agreement in this example between fracture-set dilation tendency and measurements and observations of groundwater flow.

8.2.8 Dilation-Tendency Analysis of Mesa Butte Fault System

Dikes typically form parallel to the maximum and intermediate principal compressive stresses and perpendicular to the minimum principal compressive stress. In situations where a fault pre-exists in an orientation that is relatively near to the optimal orientation for dike formation in the existing stress field (i.e., nearly normal to σ_3), the fault may be intruded by magma. The fault may partially or completely capture the ascending magma and serve as a feeder system for surface eruption. The potential for a fault to capture a dike is directly dependent on the 3D stress field and the orientation of the fault within the stress field. Faults that have large resolved normal stresses have very low potential for magma intrusion. Faults that are in orientations such that they have relatively low resolved normal stress have relatively high potential for magma intrusion. Dilation-tendency analysis provides an intuitive technique to study the relative potential for dilation of faults based on the resolved normal stress. Dilation-tendency analysis is applied to a natural example of fault and dike interaction along the Mesa Butte Fault (MBF) in the San Francisco Volcanic Field, Arizona, to illustrate the technique and to study the sensitivity of dilation tendency to fault orientation.

The MBF is the main fault in a ~150 km long system of northeast-trending faults that extends through the San Francisco Volcanic Field. The MBF is approximately 35 km southeast of the Grand Canyon at its northeastern end (Figure 8-7; Ulrich et al., 1984). The MBF trends northeast-southwest but has an unknown dip (direction and inclination). The Cedar Ranch Fault (CRF) parallels the MBF, near the southern end of the northeastern outcrop of the MBF, and is offset 2 to 3 km to the southeast (Ulrich and Bailey, 1987; Wolfe et al., 1987). The trend of the CRF changes by about 80° at its northeastern end where it trends northwestward and approaches intersection with the MBF (Figure 8-7). The actual intersection between the CRF and MBF is obscured by the Mesa Butte cinder cone (Ulrich and Bailey, 1987, Wolfe et al., 1987). The Mesa Butte cinder cone is at the southwestern end of an alignment of eruptive vents along the MBF that extends

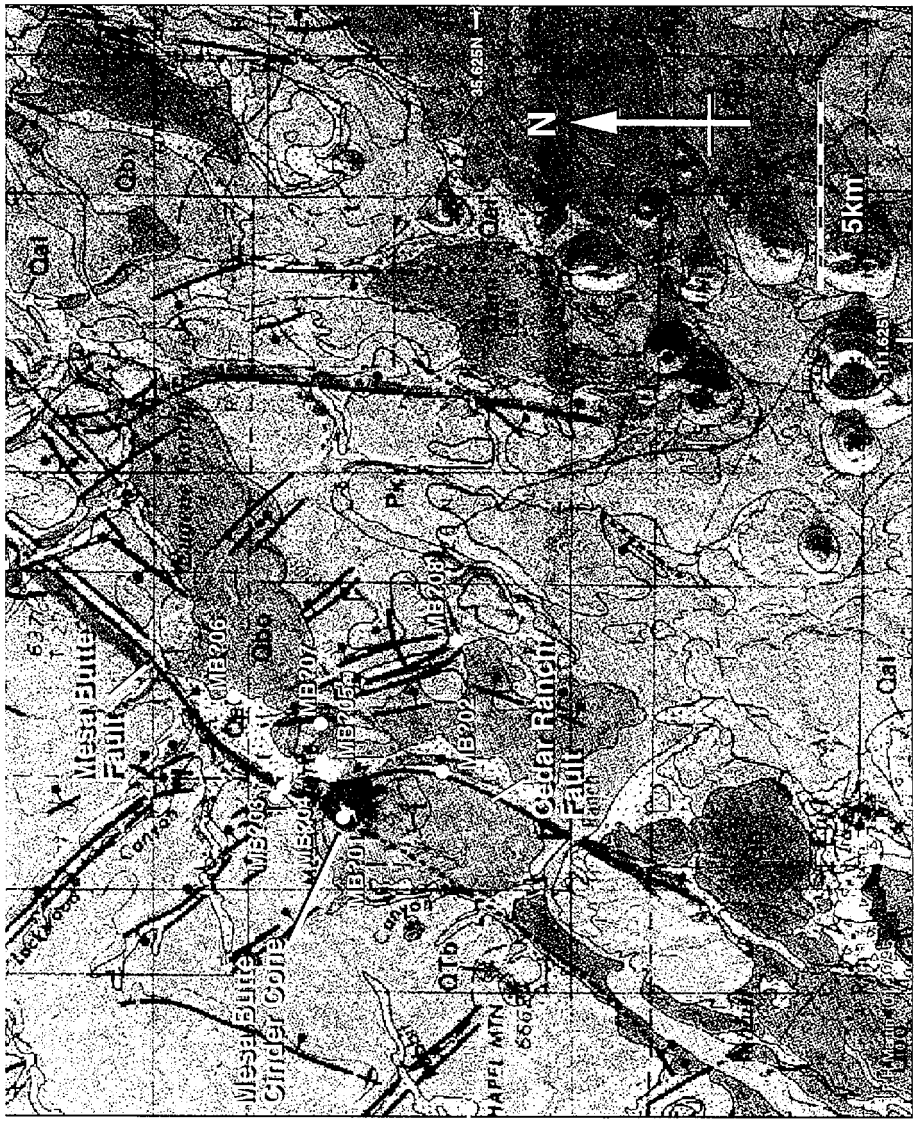

Figure 8-7. Geology of vicinity of Mesa Butte cinder cone from Ulrich et al. (1984) is superposed on Side-Looking Airborne Radar (SLAR) data. Geology and SLAR images are combined using ARCINFO and 50 percent intensity contributed from each of the two images. Labeled dots (MB-01) through MB-08) mark locations of samples of basaltic eruptive units collected for geochemical analyses and other studies designed to establish and test ages and correlation of eruptive units.

for at least 5 km (Figures 8-7 and 8-8). Published K/Ar ages for basaltic eruptive units that apparently originated along the MBF are: 0.83±0.04, 1.04±0.04, and 1.38±0.16 Ma (Ulrich and Bailey, 1987, Wolfe et al., 1987). The state of stress at 1 Ma is not known, however measurements of orientations of contemporary stresses have been made in the area and are used as the basis for this analysis. Contemporary maximum horizontal stress orientations measured in the vicinity of the Mesa Butte cinder cone (Zoback, 1992; Zoback et al., 1992) are of two orientations: parallel to the MBF (σ_1 vertical) and perpendicular to the MBF (σ_1 vertical). Maximum horizontal stress normal to the MBF produces extremely low dilation tendencies for the MBF and cannot explain eruptive vents along the MBF trace. Maximum horizontal stress oriented parallel to the MBF trace is used to model the sensitivity of dilation tendency to fault dip (Figure 8-9). For the modeled stress state, dilation tendency is 89–100 percent of the maximum possible for a range of dips for the MBF from 60° northwestward to 60° southeastward. Dilation tendency is significantly lower for dips that are shallower than 60° and strikes that are more than 20° from parallelism with the maximum horizontal stress, due to relatively large normal stress resolved on the surfaces by the maximum and intermediate principal stresses. Based on the near linearity of the MBF trace, a high-angle dip is most likely. Future work will further investigate the actual dip angle and direction of the MBF

8.3 ASSESSMENT OF PROGRESS TOWARD MEETING PROJECT OBJECTIVES

Compilation of data on tectonics, faulting, and seismicity into the Tectonics Geographic Information System (GIS), and critical review of the compiled tectonic data are proceeding on schedule. Regional data sets that have been compiled into the GIS to date include: digital terrain elevation, Quaternary faults, *in situ* stress, historic earthquakes, conodont color alteration indices, and volcanic fields. Compilation of data on fault activity (e.g., fault orientation, total displacement, slip direction, slip rate, recurrence interval, date of last major earthquake, associated earthquake magnitudes, length of surface rupture, etc.) into the GIS is in progress and will be reported in an upcoming Major Milestone (20-5704-167-008) report. The Tectonics GIS will provide the basis for assessing adequacy of existing and anticipated data for evaluating compliance with quantitative waste isolation performance objectives.

Slip- and dilation-tendency analysis techniques have recently been developed at the Center for CNWRA, which provide an interactive means for evaluating the relative risk of slip on existing faults, relative risk of magma injection along faults or extension fractures, and the potential effect of existing fractures on groundwater flow patterns. The slip-tendency technique also provides an independent means for critically evaluating fault-plane orientations inferred from earthquake focal–mechanism solutions and nodal plane selections made on the basis of existing stress inversion techniques. The slip- and dilation-tendency analysis techniques provide new tools for assessing compliance with performance objectives and for reducing KTUs that address aspects of tectonic modeling, earthquake hazard assessment, fault-plane solution interpretation, relationships between tectonic processes and groundwater, and affects of tectonics on igneous activity.

Data and references compiled by the Tectonics Research Project staff have been used to develop Compliance Determination Strategies on Structural Deformation (LARP 3.2.1.5), Evidence of Igneous Activity (LARP 3.2.1.9), and Structural Deformation and Groundwater (LARP 3.2.2.8). Digital terrain models, boundary data, Quaternary fault coverage, and *in situ* stress data compiled by Tectonics Research Project staff, along with visualization methods developed for tectonics research, are being used in a collaborative effort with the Regional Hydrology Research Project to study regional groundwater flow in the regional carbonate aquifer. Five major national conference presentations were made during the reporting period (Ferrill et al., 1994a,b; Morris et al., 1994; Wittmeyer and Ferrill, 1994; Young et al., 1994a).

8.4 PLANS FOR NEXT REPORTING PERIOD

Continued development and documentation of the slip- and dilation-tendency analysis techniques are planned for the next reporting period. The structural analog modeling laboratory will be established, and modeling activities will begin with sandbox modeling of strike-slip releasing bends similar to models for the central Death Valley pull apart and Crater Flat Valley.

Figure 8-8. Oblique aerial photograph looking southwest along the Mesa Butte Fault. Three basaltic vents along the fault include: (i) a fissure vent (bottom center), (ii) a small cinder cone including a spatter carapace that coated the Mesa Butte Fault escarpment, and (iii) the Mesa Butte cone (top center).

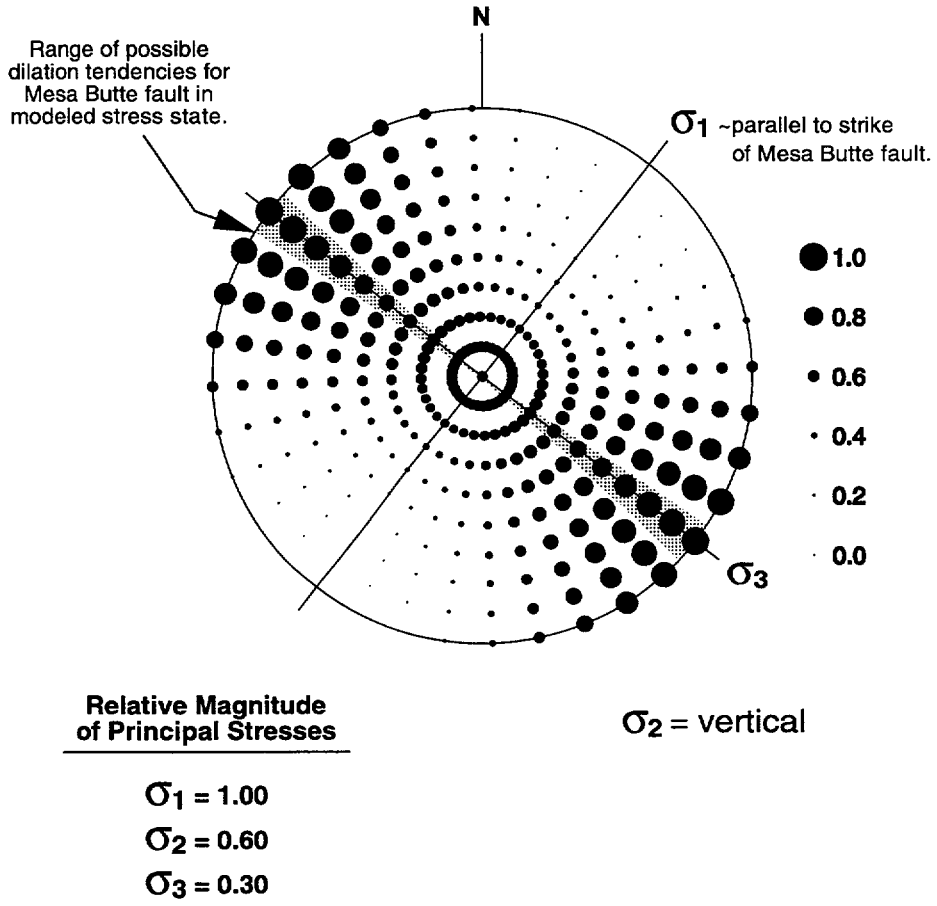

Figure 8-9. Dilation-tendency plot for MBF system illustrates that the maximum dilation tendency for the Mesa Butte Fault in the modeled stress state would be for a vertical fault plane. However, dilation tendencies nearly as large are calculated for dips in the range from 60° northwestward through vertical to 60° southeastward.

Compilation and analysis of the fault-slip database will continue during the next reporting period. Tectonogeomorphologic analyses of digital elevation data for the Death Valley region will continue, and results will be presented at the 1995 meeting of the Association of American Geographers. Field work will be conducted at Bare Mountain, Nevada, to evaluate in further detail the pattern of faulting within Bare Mountain, and at the northern end of Bare Mountain where the Tertiary volcanic sequence is separated from the Paleozoic strata of Bare Mountain by a low-angle extensional detachment.

Efforts of the Regional Tectonics Research Project during the next reporting period will focus on Task 3 – Critical Review Of Compiled Tectonic Data, Task 4 – Field Investigations and Task 6 – Regional Tectonic Modeling. Task 3 is planned to culminate in a NUREG report scheduled for an August 28, 1995 delivery to NRC-Research. Regional tectonic modeling activity will be increased during the next reporting period with planned emphasis on the 3D structural geometry and tectonic history of the Death Valley and YM regions, including the possible subsurface linkage of the Bare Mountain and YM faults (Scott, 1990;

Young et al., 1992). Specific activities that are planned to address these issues include (i) use of geometric modeling techniques to interpret deep structural geometry; (ii) use of structural analog modeling to produce 3D fault geometries that can be compared with structures in the Bare Mountain/Crater Flat/YM and greater Death Valley regions; and (iii) continued fission track, microstructural, and paleomagnetic analyses of Bare Mountain in an attempt to constrain the 3D displacement paths of Bare Mountain.

Collaboration between Tectonics Research and Volcanism Research is expected to increase during FY95. The initial focus of this collaborative research will be fault and dike interaction. Collaborative projects are planned to analyze dikes and basaltic eruptive units in Crater Flat Valley, to assess the patterns of dike intrusion in Crater Flat, and to assess the potential for fault and dike interaction in the YM area.

Integrated work between the Regional Tectonics Research and Regional Hydrology Research Projects will continue during the next reporting period. The potential effects of *in situ* stress on transmissivity and regional groundwater flow will continue to be investigated in the current collaborative effort. Also, efforts towards building a 3D model of the regional carbonate aquifer system in the greater Death Valley region will continue.

8.5 REFERENCES

Anderson, J.G., J.N. Brune, J.N. Louie, Y. Zeng, M. Savage, G. Yu, Q. Chen, and D. dePolo. 1994. Seismicity in the western Great Basin apparently triggered by the Landers, California, earthquake, 28 June 1992. *Bulletin of the Seismological Society of America* 84(3): 863–891.

Angelier, J. 1979. Determination of the mean principal directions of stresses for a given fault population. *Tectonophysics* 56: T17–T26.

Bodin, P., and J. Gomberg, 1994. Triggered seismicity and deformation between the Landers, California, and Little Skull Mountain, Nevada, earthquakes. *Bulletin of the Seismological Society of America* 84(3): 835–843.

Bott, M.H.P. 1959. The mechanics of oblique slip faulting. *Geological Magazine* 96: 109–117.

Carlsson, A., and T. Olsson. 1979. Hydraulic conductivity and its stress dependence. *Proceedings of the 1979 Workshop: Low-Flow, Low-Permeability Measurements in Largely Impermeable Rocks*, Paris, France: 249–259.

Ferrill, D.A., S.R. Young, and D.B. Henderson. 1994a. Geometry and kinematics of coseismic faulting along the Landers rupture zone using time and space patterns of seismicity. *EOS, Transactions of the American Geophysical Union* 75(44): 437.

Ferrill, D.A., S.R. Young, A.P. Morris, D.B. Henderson, and R.H. Martin. 1994b. 3-dimensional stress domains interpreted from fault slip patterns in southern California and Nevada. *Geological Society of America Abstracts with Program–1994 Annual Meeting.* Boulder, CO: Geological Society of America: 26(7): 185.

Ferrill, D.A., S.R. Young, G.L. Stirewalt, A.P. Morris, and D.B. Henderson. 1994c. Tectonic processes in the central Basin and Range region. *NRC High-Level Radioactive Waste Research at CNWRA, January–June 1994.* CNWRA 94-01S. B. Sagar, ed. San Antonio, TX: Center for Nuclear Waste Regulatory Analyses: 139–160.

Frizzel, V.A., Jr. and J. Shulters. 1990. *Geologic map of the Nevada Test Site, Southern Nevada.* 1: 100,000. U.S. Geological Survey Miscellaneous Investigations Series Map I-2046. Reston, VA: U.S. Geological Survey.

Gephart, J.W. 1990. Stress and the direction of slip on fault planes. *Tectonics* 9: 845–858.

Gomberg, J. and P. Bodin. 1994. Triggering of the Ms = 5.4 Little Skull Mountain, Nevada, earthquake with dynamic strains. *Bulletin of the Seismological Society of America* 84(3): 844–853.

Harmsen, S.C. 1994. The Little Skull Mountain, Nevada, earthquake of 29 June 1992: Aftershock focal mechanisms and tectonic stress field implications. *Bulletin of the Seismological Society of America* 84: 1,484–1,505.

Harmsen, S.C. and A.M. Rogers. 1986. Inferences about the local stress field from focal mechanisms: Applications to earthquakes in the southern

Great Basin of Nevada. *Bulletin of the Seismological Society of America* 76: 1,560–1,572.

Hill, D.P., P.A. Reasenberg, A. Michael, W.J. Arabaz, G. Beroza, D. Brumbaugh, J.N. Brune, R. Castro, S, Davis, D. dePolo, W.L. Ellsworth, J. Gomberg, S. Harmsen, L. House, S.M. Jackson, M.J.S. Johnston, L. Jones, R. Keller, S. Malone, L. Munguia, S. Nava, J.C. Pechmann, A. Sanford, R.W. Simpson, R.B. Smith, M. Stark, M. Stickney, A. Vidal, S. Walter, V. Wong, and J. Zollweg. 1993. Seismicity remotely triggered by the magnitude 7.3 Landers, California, earthquake. *Science* 260: 1,617–1,623.

Hiltscher, R., J. Martna, and L. Strindell. 1979. The measurement of triaxial rock stresses in deep boreholes and the use of rocks stress measurement in the design and construction of rock openings. *Proceedings of 4th International Congress on Rock Mechanics*. Montreux.

Jaeger, J.C., and N.G.W. Cook. 1979. *Fundamentals of Rock Mechanics*. 3rd ed. London, England: Chapman and Hall.

Leeman, E.R., and D.J. Hayes. 1966. A technique for determining the complete state of stress in rock using a single borehole. *Proceedings of the First Congress of the International Society of Rock Mechanics*, Lisbon.

McKenzie, D.P. 1969. The relation between fault plane solutions for earthquakes and the directions of the principal stresses. *Bulletin of the Seismological Society of America* 59: 591–601.

Morris, A.P., D.A. Ferrill, and D.B. Henderson. 1994. Slip tendency analysis and fault reactivation. *EOS, Transactions of the American Geophysical Union* 75(44): 591.

Ramsay, J.G. 1967. *Folding and Fracturing of Rocks*. New York City, NY: McGraw-Hill.

Scott, R.B. 1990. Tectonic setting of Yucca Mountain, southwest Nevada. Basin and Range Extensional Tectonics near the Latitude of Las Vegas, Nevada. B.P. Wernicke, ed. *Geological Society of America Memoir:* 176: 251–282.

Stock, J.M., J.H. Healy, S.H. Hickman, and M.D. Zoback. 1985. Hydraulic fracturing stress measurements at Yucca Mountain, Nevada, and relationship to regional stress field. *Journal of Geophysical Research* 90 (B10): 8,691–8,706

Ulrich, G.E., and N.G. Bailey, 1987. *Geologic Map of the SP Mountain part of the San Francisco Volcanic Field, north-central Arizona*. U.S. Geological Survey Miscellaneous Field Studies Map MF-1956. Reston, VA: U.S. Geological Survey.

Ulrich, G.E., G.H. Billingsley, R. Hereford, E.W. Wolfe, L.D. Nealey, and R.L. Sutton. 1984. *Map showing geology, structure, and uranium deposits of the Flagstaff 1°x2° Quadrangle, Arizona*. U.S. Geological Survey Miscellaneous Investigations Series Map I-1446. Reston, VA: U.S. Geological Survey.

Vetter, U.R., and A.S. Ryal. 1983. Systematic change of focal mechanism with depth in the western Great Basin. *Journal of Geophysical Research* 88: 8,237–8,250.

Wallace, R.E. 1951. Geometry of shearing stress and relationship to faulting. *Journal of Geology* 59: 118–130.

Walter, W. 1993. Source parameters of the June 29, 1992 Little Skull Mountain earthquake from complete regional waveforms at a single station. *Geophysical Research Letters* 20: 403–406.

Wernicke, B., G.J. Axen, J.K. Snow. 1988. Basin and range extensional tectonics at the latitude of Las Vegas, Nevada. *Bulletin of the Geological Society of America* 100: 1,738–1,757.

Wesnousky, S.G., and C.H. Jones. 1994. Oblique slip, slip partitioning, spatial and temporal changes in the regional stress field, and the relative strength of active faults in the Basin and Range, western United States. *Geology* 22: 1,031–1,034.

Wittmeyer, G.W., and D.A. Ferrill. 1994. Effect of contemporary regional stress on the anisotropy of transmissivity in fractured rock aquifers. *EOS, Transactions of the American Geophysical Union* 75(44): 258.

Wittmeyer, G.W., W.M. Murphy, and D.A. Ferrill. 1994. Regional hydrogeologic processes of the Death Valley region. *NRC High-Level Radioactive Waste Research at CNWRA January–June 1994*. CNWRA 94-01S. B. Sagar, ed. San Antonio,

TX: Center for Nuclear Waste Regulatory Analyses: 189–212.

Wolfe, E.W., G.E. Ulrich, and C.G. Newhall, 1987. *Geologic map of the northwest part of the San Francisco Volcanic Field, north-central Arizona.* U.S Geological Survey Miscellaneous Field Studies Map MF-1957. Reston, VA: U.S. Geological Survey.

Young, S.R., D.A. Ferrill, R.H. Martin, D.B. Henderson, R. Klar, and K. Spivey. 1994a. Tectonics GIS for the central Basin and Range and Yucca Mountain, Nevada, region. *Geological Society of America Abstracts with Program–1994 Annual Meeting.* Boulder, CO: Geological Society of America 26(7): 190.

Young, S.R., G.L. Stirewalt, and D.A. Ferrill. 1994b. *Project plan for research on tectonic processes in the central Basin and Range region.* CNWRA Project Plan, Rev 0, Change 6. San Antonio, TX: Center for Nuclear Waste Regulatory Analyses.

Young, S.R., G.L. Stirewalt, and A.P. Morris. 1992. *Geometric models of faulting at Yucca Mountain.* CNWRA 92-008. San Antonio, TX: Center for Nuclear Waste Regulatory Analyses.

Zoback, M.L. 1992. First- and second-order patterns of stress in the lithosphere: The World Stress Map Project. *Journal of Geophysical Research* 97 (B8): 11,703–11728.

Zoback, M.L. and 36 Project participants. 1992. World Stress map–maximum horizontal stress orientations. *Journal of Geophysical Research* 97(B8).

THIS PAGE INTENTIONALLY LEFT BLANK

9 FIELD VOLCANISM

by Brittain E. Hill and Charles B. Connor

Investigators: Brittain E. Hill and Charles B. Connor

NRC Project Officer: Linda A. Kovach

9.1 OVERALL TECHNICAL OBJECTIVES

The Yucca Mountain region (YMR) has been the site of recurring basaltic eruptions during the last 8 million yr (Vaniman et al., 1982; Smith et al., 1990). This volcanic activity has led to the formation of numerous cinder cones, six of which are less than about 1 million yr old and located within 20 km of the candidate repository site. Because of this igneous activity, it is necessary to evaluate the potential for volcanic disruption of the candidate high-level radioactive waste repository at Yucca Mountain (i.e., 10 CFR 60.122, Nuclear Regulatory Commission, 1991).

The probabilities of igneous activity and potential consequences on repository performance are the subject of considerable debate. Current research shows, however, that the probability of igneous activity at the candidate repository site is greater than 1×10^{-4} in 10^4 yr (e.g., Connor and Hill, 1993; Crowe, 1994). Ongoing research by the Center for Nuclear Waste Regulatory Analyses (CNWRA), Los Alamos National Laboratory, and the State of Nevada also demonstrates that basaltic volcanoes in the YMR likely represent a range of eruptive activity, which can produce different effects on repository performance. Highly explosive eruptions can fragment and entrain significant amounts of wall rock and transport that material tens to hundreds of kilometers away from the vent (e.g., Amos et al., 1983; Fedotov, 1983). Conversely, relatively gentle effusions of magma from fissure-fed eruptions may produce very limited disruption and dispersal of subsurface material (e.g., Vaniman and Crowe, 1981; Barr et al., 1993). These probability and consequence models will need to be evaluated in detail as part of prelicensing and licensing activities.

The Field Volcanism Research Project is designed to better characterize the effects of basaltic igneous activity on repository performance. This characterization will be possible through investigations of the: (i) mechanics of basaltic eruptions, (ii) extent and characteristics of shallow hydrothermal systems and diffuse degassing associated with basaltic volcanoes, and (iii) nature of basaltic intrusive geometries in the shallow subsurface. Successful completion of the Field Volcanism Research Project, which began in April 1993, will require study of Plio-Quaternary basaltic volcanoes in the western Great Basin (WGB) and comparison with historically active basaltic volcanoes located elsewhere.

Volcanism research independent of U.S. Department of Energy (DOE) activities is necessary to support specific sections of the Nuclear Regulatory Commission (NRC) License Application Review Plan (LARP) (NRC, 1994). Insight into the frequency, distribution, and volume of basaltic magmatism in the YMR, volcanism effects at the repository and regional scales, and the relationship between volcanism and regional tectonic and structural settings, forms an integral part of site characterization activities (Potentially adverse conditions: evidence of igneous activity, LARP Section 3.2.1.9) and the description of total system performance (Assessment of compliance with the requirement for cumulative releases of radioactive materials, LARP Section 6.1) (Nuclear Regulatory Commission, 1994). CNWRA Field Volcanism research also indirectly supports other site characterization activities that do not require directed research (Potentially adverse conditions: natural phenomena and groundwater, LARP Section 3.2.2.7). The Compliance Determination Strategy (CDS) associated with evidence of Quaternary volcanism concludes that independent research must be conducted to evaluate Key Technical Uncertainties (KTUs) associated with volcanism and that volcanism poses a high risk to the NRC of reaching unwarranted conclusions regarding compliance with 40 CFR Part 191 (U.S. Environmental Protection Agency, 1991) and 10 CFR Part 60.122(c)(15) (Nuclear Regulatory Commission, 1991).

Four KTUs related to igneous activity, identified as part of the CDS concerned with evidence of Quaternary igneous activity, are identified in the LARP (Nuclear Regulatory Commission, 1994):

- Low resolution of exploration techniques to detect and evaluate igneous features
- Inability to sample igneous features
- Development and use of conceptual tectonic models as related to igneous activity
- Prediction of future system states (disruptive scenarios)

These KTUs currently are being re-evaluated and new KTUs may be written or current KTUs may be combined. Evaluation of these KTUs requires detailed safety review supported by analyses. Several of these KTUs also require independent tests, analyses, or other investigations for evaluation, along with detailed safety reviews. In addition to KTU evaluation, independent research in volcanism provides a basis to question how DOE research will address the probabilities and potential consequences of igneous activity on repository performance and to evaluate the DOE responses to these questions.

9.2 SIGNIFICANT TECHNICAL ACCOMPLISHMENTS

Activities designed to address issues related to the probability and consequence of igneous activity in the YMR that have been initiated or completed during the last 6 mo include:

- An independent expert-panel review of the CNWRA volcanism research projects
- Extensive field work at Tolbachik volcano, Kamchatka
- Initial comparisons of YMR and Tolbachik eruption products
- Continued modeling of temperature and soil-gas data from Parícutin volcano, Mexico
- Continued modeling of fault-dike interactions

The details of the expert-panel review are reported in an Intermediate Milestone, Expert-Panel Review of CNWRA Volcanism Research Programs (Hill, 1995), which was completed during this reporting period. In addition, some results of fault-dike modeling studies (Draper et al., 1994) and degassing studies at Cerro Negro, Nicaragua (Conway et al., 1994), were presented in poster sessions at the annual meeting of the Geological Society of America. CNWRA contributions to melt-inclusion research at Cerro Negro, Nicaragua, were presented at the Fall Meeting of the America Geophysical Union (Roggensack et al., 1994). A paper on the significance of amphibole crystals in Quaternary YMR basalts, which was reported in Connor and Hill (1994), was accepted for presentation at the 1995 International High-Level Radioactive Waste Management Conference.

9.2.1 Expert-Panel Review of CNWRA Volcanism Research Projects

An independent panel of five experts in basaltic volcanology reviewed ongoing volcanism research programs at the CNWRA in October 1994. Drs. Paul Delaney (U.S. Geological Survey, Flagstaff), Peter Lipman (U.S. Geological Survey, Menlo Park), Alexander McBirney (University of Oregon), Stephen Self (University of Hawaii), and George Walker (University of Hawaii) were elected to the review panel using formal elicitation procedures. The goals of this review were to: (i) critically review the objectives and approaches of CNWRA volcanism research and their application to licensing issues at the proposed Yucca Mountain high-level waste repository site, (ii) recommend improvements to the research scope and methodologies, (iii) investigate new issues that may not be part of the original research plans, and (iv) evaluate interpretations of the available data and explore alternate hypotheses to these data. The panel members reviewed all CNWRA volcanism documents and numerous relevant publications by other YMR researchers, attended a 2-day meeting in San Antonio, and examined YMR basaltic volcanoes in the field for 2 days.

The main conclusions of the review are (i) CNWRA volcanism research projects are scientifically defendable, relevant to addressing important geological problems at the YMR, and are being undertaken by well-qualified personnel; (ii) studies of basaltic volcanism in the YMR should be increased, including Miocene basaltic activity associated with waning stages of caldera magmatism; (iii) independent physical volcanological studies of Quaternary YMR basaltic

volcanoes should be conducted and these studies supplemented with data from other appropriate Basin and Range and modern analog volcanoes; (iv) evaluation of the relationships between YMR and modern analog volcanoes should be continued as data from planned CNWRA studies become available; (v) project goals should be prioritized to focus on the most urgent tasks; and (vi) more time should be allocated for in-depth studies that result in peer-reviewed journal publications by decreasing the number of administrative reports.

9.2.1.1 Recommendations Specific to the Field Volcanism Project

Individual panel-member reports are presented in Hill (1995). Recommendations that are specific to the Field Volcanism research project are summarized in this section, along with planned actions for the recommendations pending NRC approval.

- Eruptions at modern analog volcanoes (Tolbachik, Cerro Negro, and Parícutin) need to be evaluated for rheological differences with YMR volcanoes.

Action: Data in the published literature show these modern volcanoes are comparable with the YMR volcanoes (Connor, 1993). However, the reviewers believed that unpublished data, especially on the microcrystallinity of the erupting magmas, may show that the analog volcano eruptions were more explosive than YMR volcanic eruptions. Petrologic studies at YMR and analog volcanoes are designed to constrain the extensive and intensive variables that control eruption explosivity in these magmatic systems. These variables are composition (including magmatic water content), temperature, crystallinity, vesicularity, and magma ascent and eruption rates. As work continues on the analog volcanoes, data on these variables will be used to evaluate similarities and differences between the analog and YMR volcanoes.

Models that interpret YMR eruption dynamics must account for the wide variety of deposits associated with these volcanoes. The goal of CNWRA volcanism analogs research is to better understand basaltic eruption processes utilizing well-constrained data from historical eruptions. Models for basaltic magmatism should be tested with data from field observations and measurements before these models can be applied to magma-repository interactions at Yucca Mountain. Data collected at well-observed historical eruptions provide the best possible test for model evaluations.

- Other potential differences between the geologic setting of modern analog and YMR volcanoes should be rigorously evaluated:
  - Arc-volcanic versus transtensional tectonic setting
  - Presence of possible upper-crustal magma reservoirs
  - Role of possible shallow groundwater on eruptions

Action: Arc volcanoes represent the best possible modern analogs with YMR basaltic volcanism, although obvious differences exist between these geological settings. Ongoing but undocumented work by CNWRA researchers at Tolbachik volcano has addressed the significance of some of these differences. For example, temperature measurements at the cooling cinder cones and dikes are not affected by regional heat flow or local thermal anomalies induced by upper-crustal magma reservoirs. The depth to the water table at Tolbachik is about 500 m, similar to the depth at Yucca Mountain. Work at any analog to the YMR, either historical or ancient, must document how potentially important differences in the geologic setting may affect the processes under investigation. This work is an ongoing part of CNWRA volcanism analog studies.

- Volcanic analog studies should consider the 1973 eruption of Heimay, Iceland, which may represent more typical Strombolian eruption processes than present analogs.

Action: Data on this eruption will be compiled from the available literature for use in CNWRA volcanism analog studies. Critical data, such as the microcrystallinity of the magma or pre-eruption volatile contents, may need to be obtained. These data likely can be acquired from samples provided by researchers studying this volcano.

- Continue characterization of subvolcanic structures for appropriate Basin and Range systems. Consider expanding work on subvolcanic structures to include anisotropy of magnetic susceptibility (AMS) studies, which can determine magma flow directions.

Action: The physical dimensions of subvolcanic structures, such as dikes, necks, and plugs, are entered into coverages in the CNWRA Volcanism Geographic Infor-

mation System when such data are available. There are few directed studies of these features for volcanic systems in the WGB, and geological mapping of these fields is usually at too coarse a scale to accurately measure these features from maps. However, work will continue in compiling this information where available. In addition, ongoing field research in the Reveille Range, Nevada, by E.I. Smith and coworkers at the University of Nevada, Las Vegas, likely will provide a large amount of information on these structures for a geological environment very similar to the YMR.

AMS studies of magma flow directions in dikes are potentially useful for fault-dike interaction models. This research task is ongoing with the CNWRA Tectonic Processes in the Central Basin and Range Region Research Project. As these studies progress, the possibility of involving additional researchers with AMS experience will be explored.

- Viscous-fluid experiments simulating the injection of magma into the repository may provide useful constraints on potential magma-repository interactions.

Action: One of the potentially most difficult problems to address during licensing will be the effects of basaltic magma upon repository performance. There are no naturally occurring analogs for ascending basaltic magma encountering a repository-sized void at 300-m depths. Evaluating these effects will involve a combination of modeling the decompression and fragmentation of rapidly depressurized magma and data from near-surface subvolcanic processes. Unquestionably, tank experiments scaled to simulate magma-repository interactions would provide useful information. These experiments are, however, well beyond the scope of the current CNWRA volcanism research programs. As additional CNWRA research programs are developed, the possibility of conducting tank experiments with outside consultants will be explored.

- Consider that future climates may be wetter and increase the possibility for magma-water interactions during eruptions.

Action: Crowe et al. (1986) evaluated the potential for hydromagmatic eruptions at the candidate YMR repository using current hydrologic and climatic conditions. However, a large amount of research on future climatic and hydrologic conditions has been conducted since that time. The results of this research should be applied to the problem of possible future hydromagmatic eruptions in the YMR. In addition, the importance of fracture-dominated flow in the Yucca Mountain system should be evaluated with regard to hydromagmatic eruption potential. Future work on eruption dynamics in the Field Volcanism Research Project will investigate this potential further.

- Evaluate possibility that cooling dikes can create a negative pressure gradient in the saturated zone and induce upward water flow and low-temperature hydrothermal alteration within the dike.

Action: Dikes at Fortification Hill, Arizona, and elsewhere commonly contain zeolite and carbonate alteration minerals whereas the surrounding wall rock is relatively fresh. A cooling, permeable dike below the water table may create a negative pressure gradient in the saturated zone and induce upward water flow. This influx of water into the dike may control the development of alteration minerals within the dike and inhibit alteration of the wall rock. Current studies will be expanded to accurately characterize the alteration mineralogy of the Fortification Hill dikes. These data can then be used to evaluate the proposed cooling model.

9.2.2 Field Work at Tolbachik Volcano, Russia

The Field Volcanism Research Project utilizes a dual approach to evaluate the consequences of potential volcanic activity in the YMR. This dual approach involves studies of extinct WGB cinder cones and of historically active analog volcanoes located outside the WGB. Clearly, the range of volcanic activity in the WGB, the duration of this activity, petrogenesis of magmas, and geology of near-surface structures must be evaluated using detailed field studies in the region. However, much about the dynamic nature of volcanism (e.g., eruption mechanics, extent and longevity of degassing, and perturbation of groundwater flow) also must be determined from the study of historically active cinder cones that have had well documented and monitored eruptions. No cinder cone eruptions have occurred in the western United States in the last 100 yr. In addition, many features necessary to evaluate dynamic volcanic processes are not present or preserved at WGB volcanoes. The 1975 eruption of the basaltic Tolbachik volcano was well documented by Russian scientists and provides important information on the

dynamic nature of YMR volcanism (e.g., Connor, 1993).

The 1975 eruption of Tolbachik was one of the most powerful, yet well-monitored eruptions to have occurred at a small-volume basaltic cinder cone. Eruption of about 0.5 km^3 of basaltic magma created an alignment of cinder cones and fissure-fed lava flows, and dispersed cinders and ash hundreds of kilometers downwind (Gusev et al., 1979). Eruption energetics ranged from periods of fire-fountaining during opening phases of boccas to days of plinian activity with sustained convective ash-columns (e.g., Budinkov et al., 1983). Additional details of the eruption are summarized in Connor (1993).

Field work conducted at the Tolbachik volcano during July 1994 consisted of:

- Continuous temperature monitoring of high-temperature fractures along the rims of Cones I and II over periods of several days each
- Measurements of shallow temperature gradients at the cinder cones, on proximal fall deposits, on lava flows, and above shallow dikes
- Sampling of fumarolic gases and condensates for geochemical analyses
- Detailed descriptions and sampling of proximal to medial cinder-fall and cone deposits
- Sampling of early-, middle-, and late-stage eruption products for petrographic and geochemical analyses
- Detailed sampling and measurements of shallow crustal xenoliths on the main cinder cones
- Radon surveys at the cones and on the proximal fall deposits
- Soil-mercury sampling surveys

The temperature surveys provide valuable information on the effects of cooling and degassing at cinder cones of comparable size to those in the YMR. In addition, these data provide a robust test for numerical models that simulate cinder cone cooling and degassing. The fumarole and soil-gas surveys also constrain the areal extent and magnitude of elevated gas-flux from cooling basaltic volcanoes. Studies of the fall deposits will be used to develop models of eruption energetics and will serve as a basis for comparison with poorly preserved deposits at YMR and elsewhere in the WGB. Finally, geochemical analyses of the eruption products will document the amount of chemical zonation possible in a single basaltic eruption and provide critical data for developing and testing physical process models.

9.2.2.1 Tolbachik Fall Deposits

Basaltic eruptions commonly are of low energy and can disperse tephra only kilometers away from the vent (e.g., Walker and Croasdale, 1972; Walker, 1973). However, tephra from some basaltic eruptions has been dispersed tens to hundreds of kilometers away from the vent (e.g., Amos et al., 1983; Williams, 1983). Determining the amount and extent of material dispersed from a basaltic eruption is a critical parameter for performance assessment models of the potential impact of basaltic volcanism on repository performance (e.g., Barr et al., 1993). These parameters cannot be measured directly for YMR volcanoes because most, and perhaps all, of the dispersed tephra has been eroded or buried. Thus, a range of credible dispersal parameters must be determined for these volcanoes, extrapolated from very limited amounts of data. Examination of well-preserved deposits from historical basaltic eruptions thus provides realistic constraints on past YMR eruptive activity (Connor, 1993).

The tephra-fall deposits from the 1975 Tolbachik eruption are particularly instructive, as eruption energies ranged from typical low-energy strombolian to plinian (e.g., Budinkov et al., 1983). As part of the July 1994 field work, ten complete sections of the Tolbachik fall deposits were described and sampled in detail. These sample locations ranged from 3 to 7 km away from the main vents and covered the primary dispersal axes for the eruption (Figure 9-1). Two additional sites with only partial sampling are located within 1 km of the vents (sites 22, 24; Figure 9-1).

The Tolbachik fall deposits consist of multiple complex beds of normal- and reverse-graded lapilli-fall, with subordinate amounts of ash-fall (Figure 9-2). Beds range in thickness from 0.5 to 50 cm, although most of the graded beds are less than about 10 cm thick. Xenoliths occur only in trace amounts (<0.1 weight percent) in the fall deposits. Observed xenoliths primarily are fragments of older basalt and basaltic

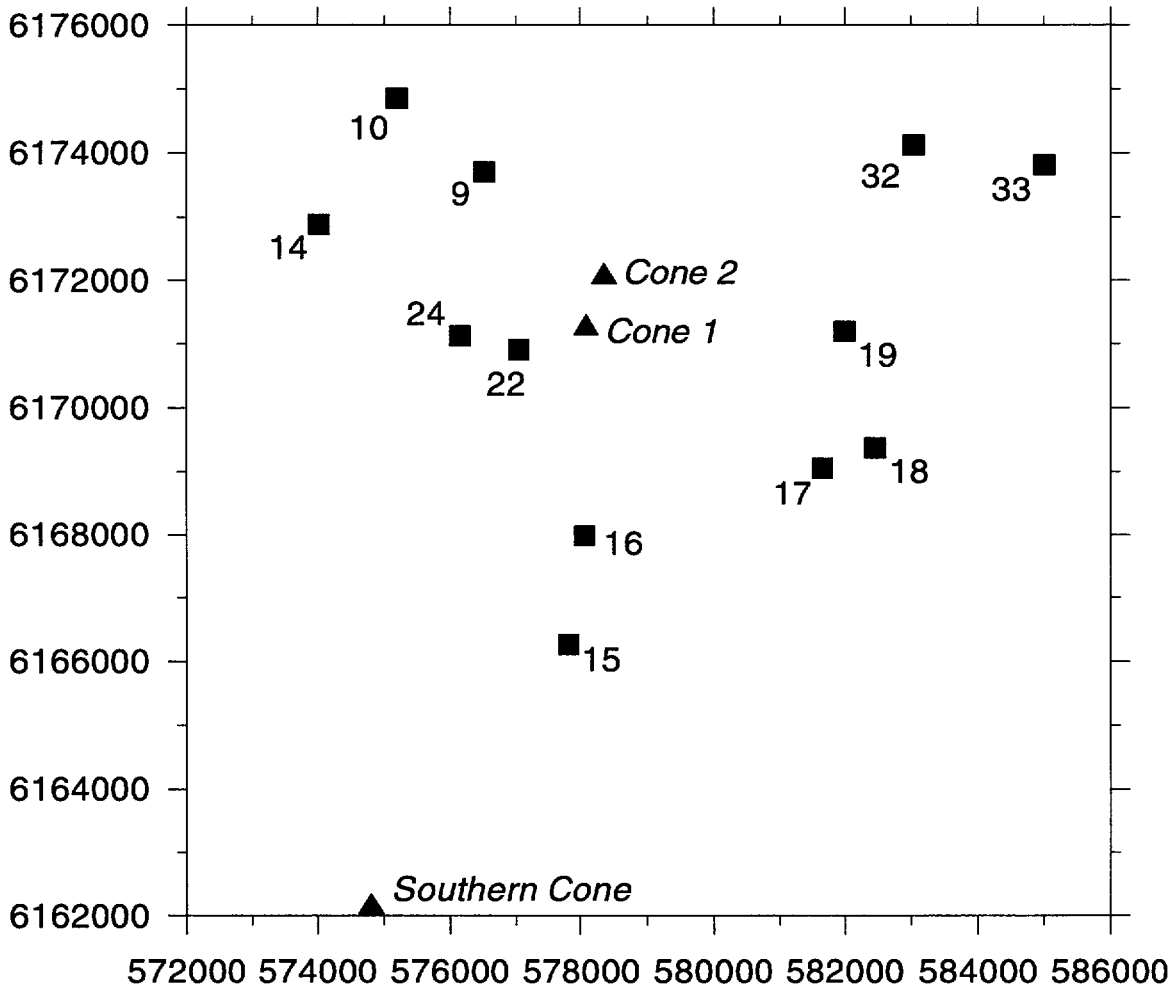

Figure 9-1. Sample locations for 1994 field work at the Tolbachik fall deposits, Russia. Coordinates are Universal Transverse Mercator, zone 57. Main cones of the 1975-76 eruption are shown by triangles, sample sites by squares.

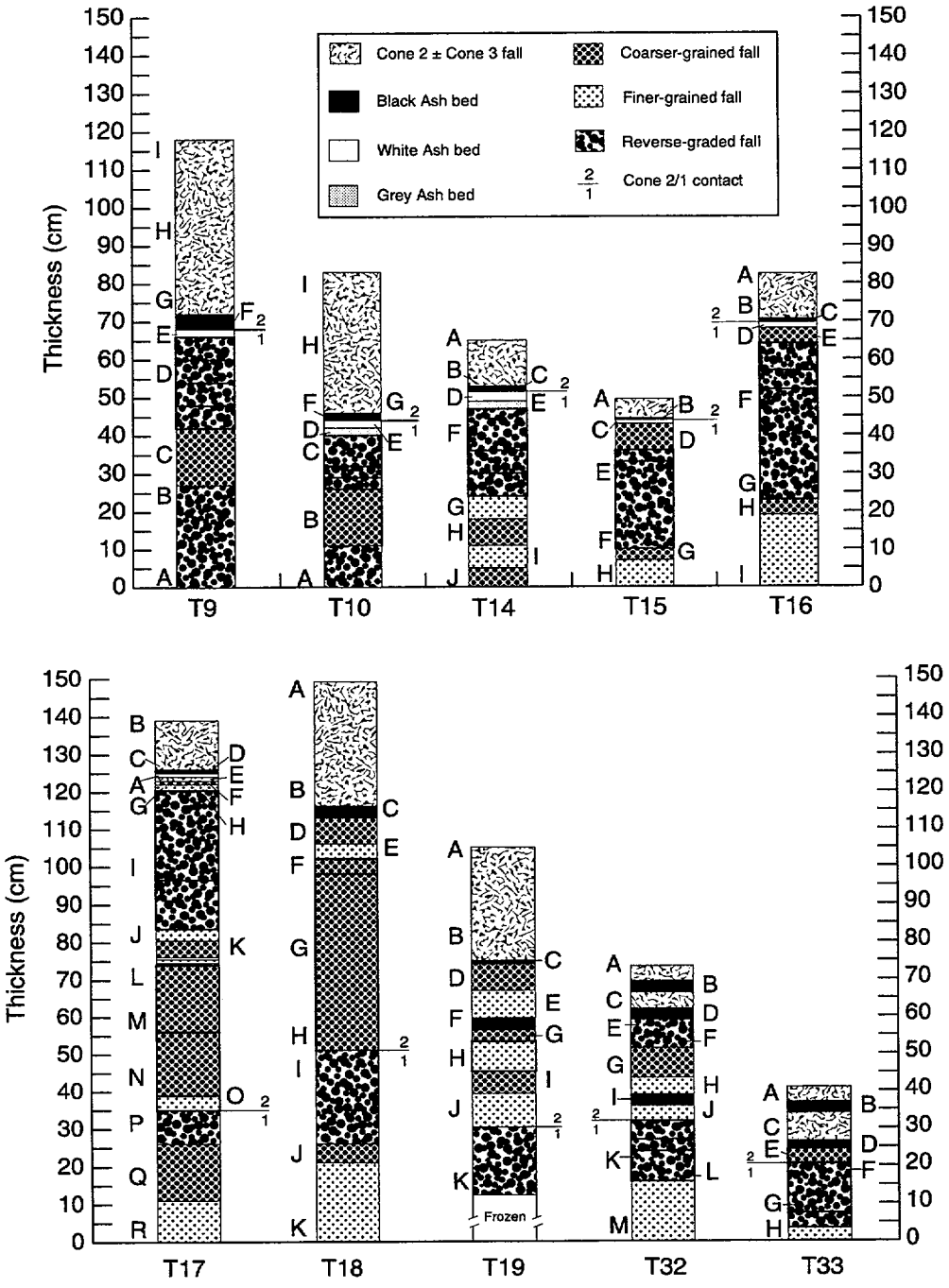

Figure 9-2. Detailed stratigraphy of 1975-76 Tolbachik fall deposits sampled during 1994 field work. Sample locations shown on Figure 9-1, letters refer to sampled units in each section

lithic wackes, with subordinate amounts of arkosic wacke and argillite. These xenoliths likely were derived from the upper 1 km of the crust (Flyorov, 1979).

Tolbachik fall-deposit samples were sieved manually with standard diameter 40, 20, 10, 5, 2.5, 1, 0.5, 0.25, and <0.25-mm sieves. Sieved fractions were weighed with a calibrated triple-beam balance, with total sample weights of about 2 kg. Size fractions were converted to phi units (i.e., $-\log_2$ scaling) and plotted as cumulative percentages. Representative cumulative-percent curves for two fall deposits are shown in Figure 9-3. The Tolbachik fall deposits strongly resemble cumulative percent curves from typical strombolian eruptions (e.g., Walker and Croasdale, 1972), in spite of the eruption being demonstrably more energetic than strombolian. Most noticeably, the fine-ash fraction (>0 phi) is <16 percent of the deposit for many samples, although some finer-grained samples occur (Figure 9-3). However, most of the finer-grained samples occur late in the eruption sequence during periods of strombolian activity. Plinian eruption energetics were characteristic of the earliest phases of the Tolbachik eruption.

Walker and Croasdale (1972) used simple granulometric parameters to outline characteristic fields of normal strombolian fall-deposits. The median diameter is the grain-size at the 50th percentile; the graphical standard deviation (sorting) is the difference between the grain-size at the 84th and 16th percentile, divided by two. Surprisingly, the Tolbachik fall-deposits all plot within the field of normal strombolian eruptions, in spite of the highly dispersive character of this eruption (Figure 9-4). The range in median diameter and sorting is typical for strombolian eruptions and, in part, represents variations in distance to the vent (Walker and Croasdale, 1972). In contrast, fall deposits from the historical eruption of the Parícutin volcano, Mexico, are significantly finer-grained than typical strombolian eruptions (Walker, 1993); Parícutin represents a basaltic eruption that is significantly more energetic than strombolian.

As part of the expert-panel review field trip, Dr. George Walker collected and sieved two fall-deposit samples from the base and about 400 m southeast of the base of the Lathrop Wells volcano. Significantly, these samples plot within the lower range of the 1975 Tolbachik fall deposits (Figure 9-4). The Lathrop Wells fall-deposits contain multiple graded beds and grain-size variations that are discernible in the field. Detailed sampling of these deposits, in addition to thorough exploration for medial to distal fall-deposits, is necessary before any firm conclusions can be reached about the dispersive characteristic of the Lathrop Wells eruption. However, the presence of late(?) Pleistocene basaltic ash in trenches at least 10 km from Lathrop Wells volcano (e.g., Menges et al., 1994) and the grain-size characteristics of the extremely proximal deposits do not preclude eruptions more energetic than typical strombolian (e.g., Crowe et al., 1983) from this volcano.

9.2.3 Yucca Mountain Region and Analog Volcano Eruption Dynamics

The explosivity of a basaltic eruption is controlled by many magma properties, including volatile content, composition, ascent and eruption rate, and crystallinity (e.g., Wilson and Head, 1981; Williams and McBirney, 1979). Published information shows that analog volcanoes (i.e., Tolbachik, Cerro Negro, Parícutin) have magma rheological properties that are similar to YMR volcanoes (Connor, 1993). However, concerns were raised during the recent expert-panel review that the analog volcanoes likely were more explosive than YMR volcanoes based on larger degrees of crystallinity and microcrystallinity in the analog magmas. Although data are available for the crystallinity of the analog basalts, little information has been published on microcrystallinity of these basalts. Ongoing CNWRA research at the analog and YMR volcanoes includes detailed petrographic studies to determine the crystallinities of pre-eruptive melts, which will strongly affect the viscosity and therefore explosivity of basaltic eruptions. Initial results of these studies show that YMR and Tolbachik basalt have comparable degrees of crystallinity and thus remain analogous.

Early phases of the 1975 Tolbachik eruption sustained convective eruption columns at least 10 km high, with over 500 km downrange transport of ash (e.g., Budnikov et al., 1983). Petrographic examination of several samples from the early stages of the eruption shows about 5 percent phenocrysts of olivine and clinopyroxene. Groundmass crystallinities are about 30 percent and consist primarily of equant olivine and clinopyroxene crystals with subordinate amounts of elongated orthopyroxene and plagioclase crystals (Figure 9-5A). Samples from the later stages of the eruption have similar phenocryst abundances, but have

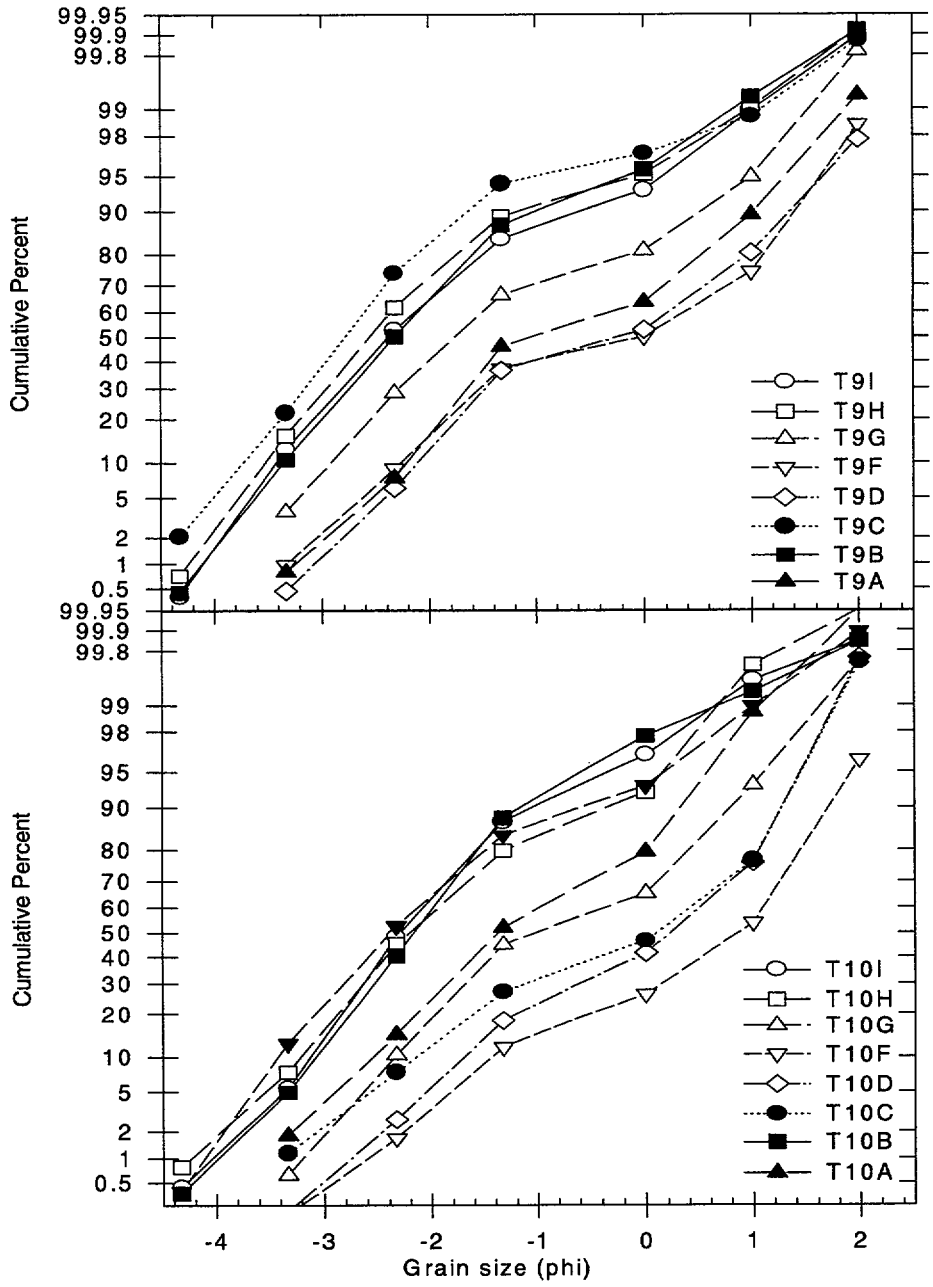

Figure 9-3. Representative cumulative weight-percent curves for fall deposits from the 1975 eruption of Tolbachik volcano, Russia. Grain size units (phi) represent $-\log_2$ of clast size (mm). Sample locations are shown in Figures 9-1 and 9-2.

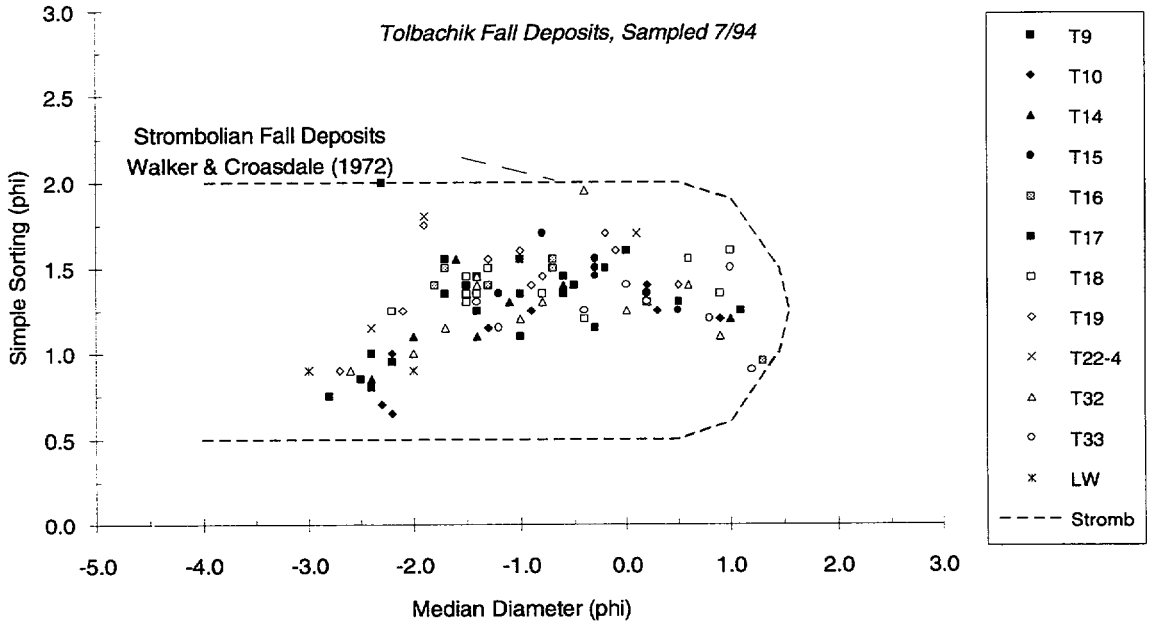

Figure 9-4. Graphically determined median diameter and simple sorting parameters for sampled Tolbachik fall deposits. Two samples from Lathrop Wells Volcano, Nevada (LW) also are shown. The dashed line outlines the field of normal strombolian eruption deposits (Walker and Croasdale, 1972). Tolbachik sample locations are shown in Figure 9-1.

groundmass crystallinities of only around 20 percent. Basaltic lapilli from the uppermost part of the Lathrop Wells proximal fall-deposit contains about 3 percent phenocrysts of olivine (Vaniman and Crowe, 1981). Groundmass crystallinities are about 40 percent and consist primarily of elongate crystals of plagioclase with subordinate amounts of equant olivine and clinopyroxene (Figure 9-5B). All the Quaternary Crater Flat basalts contain about 2 percent olivine and occasionally trace amounts of amphibole as the only phenocrysts (Vaniman and Crowe, 1981). Basaltic lapilli from the flanks of southwest Little Cone also have groundmass crystallinities of about 40 percent, which consists primarily of elongated plagioclase crystals (Figure 9-5C). In contrast, lapilli from the flanks of Black Cone have groundmass crystallinities of around 30 percent (Figure 9-5D).

Detailed petrographic studies are ongoing for these and other samples from Tolbachik and the YMR volcanoes. Besides quantifying mineral abundances, vesicle and mineral size-distributions and shape characteristics will be measured in detail using point-counting and computer-assisted image analysis. Visual examination of these samples clearly demonstrates, however, that Quaternary YMR basalts are as crystal-rich as basalts from the early, highly explosive stages of the 1975 Tolbachik eruption. In addition, the YMR basalt groundmass crystals are elongated to tabular plagioclase, whereas the Tolbachik groundmass crystals are more equant olivine and pyroxene. Relative to more equant crystals, elongated crystals such as plagioclase should increase the effective viscosity of the melt (Marsh, 1981). Thus, the predominance of groundmass plagioclase in the YMR basalts indicates that these magmas may have been more viscous than the 1975 Tolbachik magmas of comparable crystallinity.

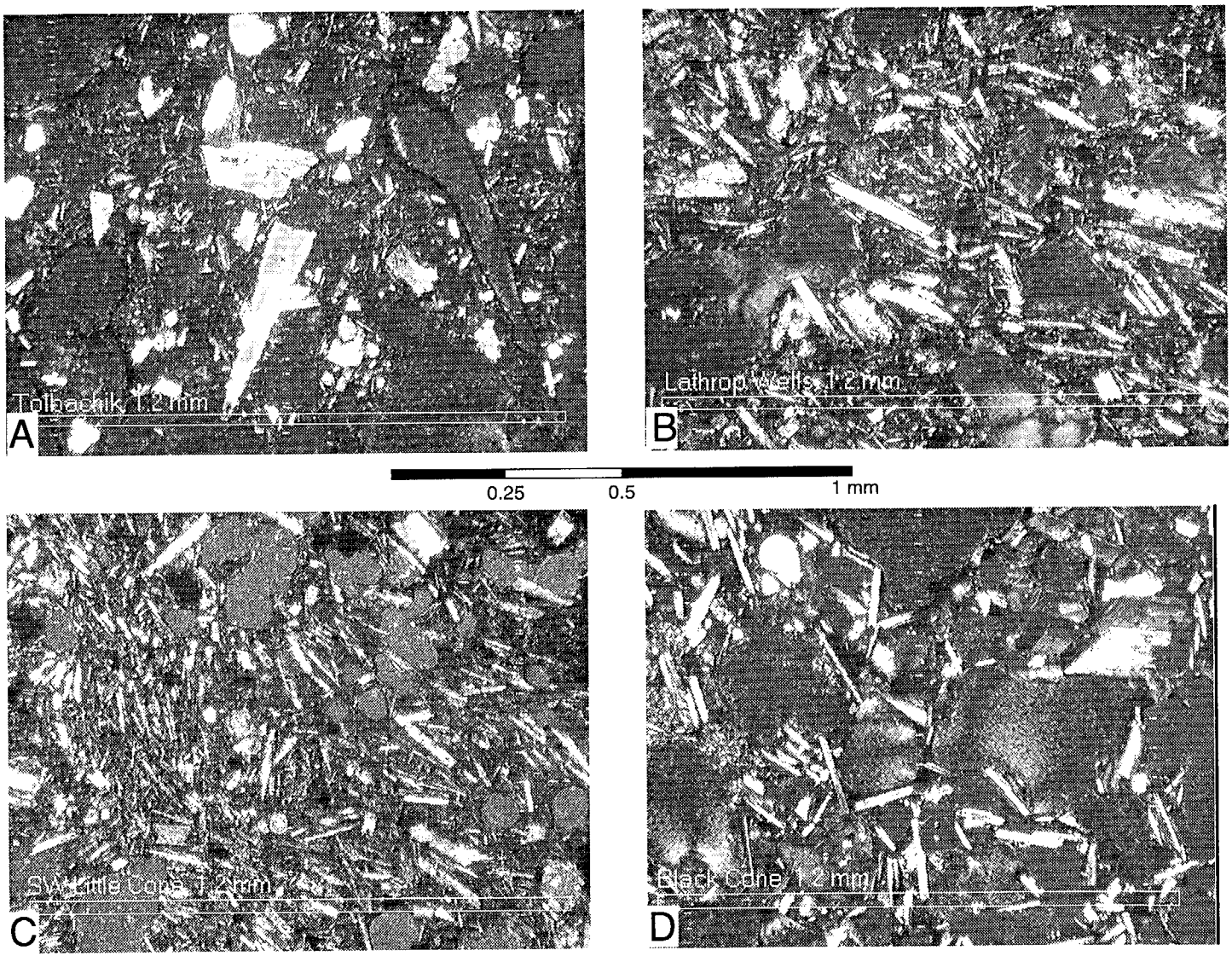

Figure 9-5. Plane-polarized photomicrographs of scoria from: (A) early explosive phases of the 1975 Tolbachik eruption, (B) Lathrop Wells, Nevada, uppermost fall deposits, (C) southwest Little Cone, Nevada, upper cone deposit, and (D) Black Cone, Nevada, upper cone deposit. Light crystals are primarily olivine and clinopyroxene (A) or plagioclase (B-D), larger crystal-free regions are vesicles.

9.3 ASSESSMENT OF PROGRESS

Research in the Field Volcanism project during the last 6 mo continues to provide critical data for assessing the potential consequences of basaltic magmatic activity on repository performance. Most importantly, the expert-panel review of CNWRA volcanism research has validated the approaches and goals of the Field Volcanism Research Project. Planned and completed research on historically active analog volcanoes was recognized as an appropriate approach towards understanding basaltic eruption dynamics and heat and mass transfer processes at YMR and other WGB volcanoes. Although there are important differences between YMR and the analog volcanoes, the processes that control these differences can be investigated and their effects accommodated in resulting models.

Degassing and thermal studies conducted at the Tolbachik volcano support initial work at the Parícutin volcano, which was reported in Connor and Hill (1994). These studies show that degassing occurs over a broad area at cooling cinder cones, for at least decades after cessation of the eruption. In addition, the detailed thermal studies at Tolbachik and Parícutin are being used to evaluate the Sandia Total-System Performance Assessment (TSPA) models that simulate cooling of igneous features (Wilson et al., 1994). Initial results of this analysis are that the numerical models used in the Sandia TSPA analysis do not accurately represent temperatures measured directly above cooling igneous features at Tolbachik volcano.

An inherent problem with investigation of the older volcanoes of the YMR is that many of the deposits necessary to determine eruption dynamics are not preserved. These deposits are, however, well preserved at the analog volcanoes. Models proposed for YMR basaltic magmatic processes (e.g., Crowe et al., 1983; Valentine et al., 1992) can be assessed using high-quality data from the analog volcanoes. In addition, recent work shows that the highly explosive eruptions at Tolbachik volcano have petrographic and granulometric characteristics similar to some Quaternary YMR volcanoes. Although these investigations are at an initial stage, they clearly demonstrate that information critical to directly evaluating the consequences of basaltic magmatism on repository performance can be readily obtained through field investigations at historically active basaltic volcanoes.

Research conducted in the Field Volcanism Research Project directly supports evaluation of KTUs on the inability to sample many features of igneous activity and the prediction of future system states. This research also is an integral part of the independent tests and analyses required for preparation of LARP Sections 3.2.1.9 and 6.1. There are relatively few volcanoes in the YMR, and many features of these volcanoes are poorly preserved. Research conducted as part of the Field Volcanism Research Project will provide scientifically defendable boundaries on the range of magmatic processes that may be possible during future basaltic eruptions. In addition, the study of historically active and WGB analog volcanoes and application of that knowledge to YMR volcanoes provide a comprehensive and defensible basis for evaluation of compliance with 40 CFR Part 191, 10 CFR 60.112, and 10 CFR 60.122.

9.4 PLANS FOR NEXT REPORTING PERIOD

Data collected during 1994 field work will continue to be analyzed and modeled. These investigations include detailed petrographic and granulometric analyses of tephra; analyses of fumarole, soil gas, and rock samples; and detailed modeling of temperature data from Tolbachik. A search of literature on the 1973 eruption of Heimay, Iceland, will be conducted to assess its analogy with YMR volcanism. In conjunction with the Volcanic Systems of the Basin and Range research project, field investigations on pyroclastic deposits from Quaternary YMR and other WGB volcanoes will be conducted.

9.5 REFERENCES

Amos, R.C., S. Self, and B. Crowe. 1983. Pyroclastic activity at Sunset Crater: Evidence of a large magnitude, high dispersal strombolian eruption. *EOS, Transactions of the American Geophysical Union* 62: 1,085.

Barr, G.E., E. Dunn, H. Dockery, R. Barnard, G. Valentine, and B. Crowe. 1993. *Scenarios Constructed for Basaltic Igneous Activity at Yucca Mountain and Vicinity*. Sandia National

Laboratories Report SAND91-1653. Albuquerque, NM: Sandia National Laboratories.

Budinkov, V.A., Y.K. Markhinin, and A.A. Ovsyannikov. 1983. The quantity, distribution and petrochemical features of pyroclastics of the great Tolbachik fissure eruption. *The Great Tolbachik Fissure Eruption Geological and Geophysical Data, 1975–1976*. S.A. Fedotov and Y.K. Markhinin, eds. New York, NY: Cambridge University Press: 41–56.

Connor, C.B. 1993. *Technical and Regulatory Basis for the Study of Recently Active Cinder Cones*. IM-20-5704-141-001. San Antonio, TX: Center for Nuclear Waste Regulatory Analyses.

Connor, C.B., and B.E. Hill. 1993. Estimating the probability of volcanic disruption of the candidate Yucca Mountain repository using spatially and temporally nonhomogeneous Poisson models. *Proceedings, American Nuclear Society Focus 93 Meeting*. La Grange Park, IL: American Nuclear Society: 174–181.

Connor, C.B., and B.E. Hill. 1994. Field volcanism research. *NRC High-Level Radioactive Waste Research at CNWRA, January–June 1994*. B. Sagar, ed. CNWRA 94-01S. San Antonio, TX: Center for Nuclear Waste Regulatory Analyses: 161–187.

Conway, F.M., A.W. Macfarlane, C.B. Connor, P.C. Lafemina, and M. Reimer. 1994. Degassing at a young cinder cone: Volcan Cerro Negro. *Geological Society of America Abstracts with Program—1994 Annual Meeting*. Boulder, CO: Geological Society of America: 26(7): 435.

Crowe, B.M. 1994. Probabilistic volcanic risk assessment. *Presentation to the Advisory Committee on Nuclear Waste, April 20, 1994, Bethesda, MD*. Washington, DC: Advisory Committee on Nuclear Waste.

Crowe, B., S. Self, D. Vaniman, R. Amos, and F. Perry. 1983. Aspects of potential magmatic disruption of a high-level radioactive waste repository in southern Nevada. *Journal of Geology* 91: 259–276.

Crowe, B.M., K.H. Wohletz, D.T. Vaniman, E. Gladney, and N. Bower. 1986. *Status of Volcanic Hazard Studies for the Nevada Nuclear Waste Storage Investigations*. Los Alamos National Laboratory Report LA-9325-MS, Vol. II. Los Alamos, NM: Los Alamos National Laboratory.

Draper, G., Z. Chen, M. Conway, C.B. Connor, and C. Condit. 1994. Structural controls of magma pathways in the upper crust: Insights from the San Francisco Volcanic Field, Arizona. *Geological Society of America Abstracts with Program—1994 Annual Meeting*. Boulder, CO: Geological Society of America: 26(7): 115.

Fedotov, S.A., 1983. Chronology and features of the southern breakout of the Great Tolbachik fissure eruption, 1975–1976. *The Great Tolbachik Fissure Eruption, Geological and Geophysical Data, 1975-1976*. S.A. Fedotov, and Ye. K. Markhinin, eds. New York, NY: Cambridge University Press: 11–26.

Flyorov, G.B. 1979. Crustal xenoliths in products of the large 1975–1976 fissure Tolbachik eruption. *Academy of Sciences of the USSR: Volcanology and Seismology* 2: 43–54.

Gusev, N.A., V.I. Dvigalo, and A.A. Razina. 1979. Remote sensing in studies of the Tolbachik eruption. *Academy of Sciences of the USSR: Volcanology and Seismology* 2: 27–42.

Hill, B.E. 1995. *Expert-Panel Review of CNWRA Volcanism Research Programs*. CNWRA 95-002. San Antonio, TX: Center for Nuclear Waste Regulatory Analyses.

Marsh, B.D. 1981. On the crystallinity, probability of occurrence, and rheology of lava and magma. *Contributions to Mineralogy and Petrology* 78: 85–98.

Menges, C.M., J.W. Whitney, J.A. Coe, J.A. Oswald, J.R. Wesling, F.H. Swan, A.P. Thomas, J.B. Paces, and S. Mahan. 1994. Preliminary results of paleoseismic investigations of Quaternary faults on eastern Yucca Mountain, Nye County, Nevada. *EOS, Transactions of the American Geophysical Union* 75(44): 452.

THIS PAGE INTENTIONALLY LEFT BLANK

Nuclear Regulatory Commission. 1991. *Disposal of High-Level Radioactive Wastes in Geologic Repositories.* Title 10, Energy, Part 60 (10 CFR Part 60). Washington, DC: U.S. Government Printing Office.

Nuclear Regulatory Commission. 1994. *License Application Review Plan for a Geologic Repository for Spent Nuclear Fuel and High-Level Radioactive Waste.* NUREG-1323. Washington, DC: U.S. Government Printing Office.

Roggensack, K., S.N. Williams, R.L. Hervig, S.B. McKight, C.B. Connor, and M. Navarro. 1994. Evidence of polybaric fractionation: Melt inclusions in 1992 eruption of Cerro Negro volcano, Nicaragua. *EOS, Transactions of the American Geophysical Union* 75(44): 747.

Smith, E.I., T.R. Feuerbach, and J.E. Faulds. 1990. The area of most recent volcanism near Yucca Mountain, Nevada: Implications for volcanic risk assessment. *Proceedings of the First International High-Level Radioactive Waste Management Conference.* La Grange Park, IL: American Nuclear Society: 81-90.

U.S. Environmental Protection Agency. 1991. *Environmental Radiation Protection Standards for Management and Disposal of Spent Nuclear Fuel, High-Level and Transuranic Radioactive Wastes.* Title 40, Protection of Environment, Part 191 (40 CFR Part 191). Washington, DC: U.S. Government Printing Office.

Valentine, G.A., B.M. Crowe, and F.V. Perry. 1992. Physical processes and effects of magmatism in the Yucca Mountain region. *Proceedings of Third International High-Level Radioactive Waste Management Conference.* La Grange Park, IL: American Nuclear Society: 2,014-2,024.

Vaniman, D., and B. Crowe. 1981. *Geology and Petrology of the Basalts of Crater Flat: Applications to Volcanic Risk Assessment for the Nevada Nuclear Waste Storage Investigations.* Los Alamos National Laboratory Report LA-8845-MS. Los Alamos, NM: Los Alamos National Laboratory.

Vaniman, D.T., B.M. Crowe, and E.S. Gladney. 1982. Petrology and geochemistry of Hawaiite lavas from Crater Flat, Nevada. *Contributions to Mineralogy and Petrology* 80: 341-357.

Walker, G.P.L. 1973. Explosive volcanic eruptions—a new classification scheme. Geologische Rundsche 62: 431-446.

Walker, G.P.L. 1993. The pyroclastic deposits of El Parícutin. *50 Años Del Volcán Parícutin, Reunion Internacional Conmemorative, Programa y Resumenes.* Urapan, Michoacán: Mexico City: Instituto de Geofisica.

Walker, G.P.L., and R. Croasdale. 1972. Characteristics of some basaltic pyroclastics. *Bulletin of Volcanology* 35: 303-317.

Williams, H., and A.R. McBirney. 1979. *Volcanology.* San Francisco, CA: Freeman, Copper and Company.

Williams, S.N. 1983. Plinian airfall deposits of basaltic composition. *Geology* 11: 211-214.

Wilson, L., and J.W. Head, III. 1981. Ascent and eruption of basaltic magma on the Earth and Moon. *Journal of Geophysical Research* 86(B4): 2,971-3,001.

Wilson, M.L., J.H. Gauthier, R.W. Barnard, G.E. Barr, H.A. Dockery, E. Dunn, R.R. Eaton, D.C. Guerin, N. Lu, M.J. Martinez, R. Nilson, C.A. Rautman, T.H. Robey, B. Ross, E.E. Ryder, A.R. Schenker, S.A. Shannon, L.H. Skinner, W.G. Halsey, J.D. Gansemer, L.C. Lewis, A.D. Lamont, I.R. Triay, A. Meijer, and D.E. Morris. 1994. Total-System Performance Assessment for Yucca Mountain – SNL Second Iteration (TSPA-1993). Sandia National Laboratories Report SAND93-2675. Albuquerque, NM: Sandia National Laboratories.

10 REGIONAL HYDROGEOLOGIC PROCESSES OF THE DEATH VALLEY REGION

by Gordon W. Wittmeyer and Richard V. Klar

Investigators: David A. Ferrill, Richard V. Klar, H. Lawrence McKague, William M. Murphy, David A. Pickett, and Gordon W. Wittmeyer (CNWRA); George Rice (Consultant)

NRC Project Officer: Thomas J. Nicholson

10.1 TECHNICAL OBJECTIVES

Yucca Mountain (YM) has been proposed as a potential site for a high-level nuclear waste repository, in part, because of the favorable geochemical and hydrologic environment provided by its 700-m thick unsaturated zone. Siting the repository in the unsaturated zone may significantly reduce the potential for waste canister corrosion and subsequent dissolution of the waste form. Moreover, the low water flux rates that are presumed to exist in the unsaturated zone reduce the likelihood that any radionuclides reaching the water table would be rapidly transported to the accessible environment. Mechanisms that may saturate the repository horizon, and thus compromise favorable conditions provided by the YM site, include rapid infiltration of water from the surface through highly conductive fracture networks and an increase in the elevation of the regional water table. The first mechanism is a site-scale or subregional issue and is not addressed by this research project. Elevation of the water table may occur due to increased recharge to the regional carbonate system along stream channels and mountain fronts in topographically closed basins 100 km to the north and northeast of YM. Even if elevation of the regional water table does not saturate the repository block, the reduced thickness of the unsaturated zone has the potential to diminish travel times within the vadose zone. In addition, travel times in the saturated zone and the location of potential discharge areas for dissolved radionuclides downgradient from YM are performance-related issues addressed by this research project. The primary objectives of this research project are to: (i) analyze existing conceptual models and develop new conceptual models of the regional hydrogeologic flow regime in the Death Valley region that contains YM, and (ii) construct numerical models of regional flow that may be used to assess the potential for the water table beneath YM to rise in response to wetter climatic conditions.

Predictions made with numerical models will be used by the U.S. Department of Energy (DOE) in its license application to demonstrate that the YM site meets the overall performance standards outlined in 10 CFR 60.112 and the geologic subsystem performance standard defined in 10 CFR 60.113(a)(2). In addition, the DOE may choose to use numerical models to demonstrate the absence or influence of potentially adverse conditions including: the effects of future pumping on the regional flow system [10 CFR 60.122(c)(2)]; the potential for deleterious changes to the hydrologic system [10 CFR 60.122(c)(5)]; the potential for changes to the hydrologic conditions resulting from climate change [10 CFR 60.122(c)(6)]; the potential for water table rise [10 CFR 60.122(c)(22)]; and the presence and influence of favorable conditions, including the clear absence of fully saturated pathways connecting the repository to the water table [10 CFR 60.122(b)(8)(ii)]. Understanding of the regional hydrogeologic system developed in this project will be used to guide review of the DOE license application and associated prelicensing submittals, and to assess the adequacy of the models used by the DOE to demonstrate compliance with the regulatory requirements and environmental standards.

Understanding of the regional hydrogeologic system gained from this research project will also be used to construct specific Compliance Determination Methods outlined in the License Application Review Plan (LARP) (Nuclear Regulatory Commission, 1994). Literature reviews and hydrogeologic data gathered in Task 1 of the project will provide information that may be directly used to assess the description of individual systems and characteristics of the site (LARP Section 3.1) and, in particular, the description of the hydrologic and geochemical systems (LARP Sections 3.1.2 and 3.1.3, respectively). Evidence gleaned from literature reviews and data analyses in conjunction with conceptual and numerical models of the regional flow regime developed in this research project will be directly used to determine whether the applicant has

provided convincing evidence of the presence or absence of favorable hydrogeologic conditions and potentially adverse hydrogeologic conditions (LARP Sections 3.2.1.1, 3.2.2.1, 3.2.2.3, 3.2.2.6, 3.2.2.8, 3.2.2.9, 3.2.2.11, and 3.2.4.2). Flow models developed in this project will also be used to confirm that velocity fields and travel times within the saturated zone estimated by the DOE are accurate enough to demonstrate compliance with the Ground Water Travel Time performance objective (LARP Section 3.3).

Compliance Determination Strategies (CDSs) for the LARP sections listed previously have been developed but will not be finalized until a thorough review and integration of the various LARP sections have been conducted. However, the Regional Hydrogeology Research Project will be instrumental in resolving specific technical uncertainties identified during the CDS development process. Key Technical Uncertainties (KTUs) that pose a high risk of noncompliance with the total-system or subsystem performance requirements may require that the Nuclear Regulatory Commission conduct independent research to resolve the issue. Development of a conceptual groundwater flow model that is representative of the YM site groundwater system has been identified as a KTU that must be addressed in LARP Sections 3.2.2.1, 3.2.2.9, and 3.3.

The Regional Hydrogeology Research Project has been divided into five tasks: Task 1—Collect and analyze data and existing models; Task 2—Construct alternative conceptual models of key hydrogeologic processes in the Death Valley region of the Western Great Basin; Task 3—Construct and calibrate mathematical and numerical models of subsurface flow at local, basin, and regional scales; Task 4—Use geochemical data to evaluate and refine regional flow models; and Task 5—Apply models to analyze problems critical to repository performance. Current plans call for completion of Tasks 1 and 2 during the first 2 yr of the project with the remaining tasks to be initiated in the third year and completed by the fourth and final year of the project. Efforts during the past 6 mo have primarily focused on Tasks 2 and 3. The primary technical objectives of Task 2 are to: (i) critically evaluate geologic, hydrogeologic and geochemical data from the Death Valley region; and (ii) use data compiled in the computerized Geographic Information System (GIS) to construct alternative conceptual models of flow in the Death Valley region. The primary technical objectives of Task 3 are to: (i) develop numerical models of regional flow in the Death Valley region; and (ii) develop or acquire parameter estimation methods for automatically calibrating these flow models.

10.2 SIGNIFICANT TECHNICAL ACCOMPLISHMENTS

During the past 6 mo, research has focused on collecting and analyzing hydraulic, hydrostratigraphic, geochemical, and structural data in order to critically evaluate existing conceptual models of interbasin flow in the Death Valley region, as well as to develop new conceptual flow models. Efforts have been primarily directed toward developing estimates of average annual precipitation and average annual recharge and constructing a map of steady-state water levels in the Death Valley region. Because estimating areal recharge and constructing the regional steady-state water level both represent a great deal of effort, only the former is reported herein. Obtaining reasonably accurate initial estimates of the distribution and magnitude of natural recharge is essential for constructing and calibrating numerical models of the regional flow system. The areal distribution of recharge will be used to define the number and extent of the areal source terms in the numerical flow model. In addition, estimates of the magnitude of recharge are needed to provide the prior information used to stabilize the inverse problem, as well as to provide initial parameter estimates for the optimization algorithm used in the automatic calibration routine.

10.2.1 Spatial Distribution of Average Annual Precipitation

The Death Valley region lies within the portion of the Basin and Range physiographic province between 114 to 118° west longitude and 36 to 38° north latitude. A physiographic map with the boundaries of the Death Valley regional hydrogeologic system as defined by Bedinger et al. (1989) is shown in Figure 10-1. The Death Valley regional hydrogeologic system, as defined here, lies wholly within the Great Basin hydrographic basin, although the location of the hydrogeologic divide separating it from the Las Vegas valley hydrographic basin, which is influent to the Colorado River, is not precisely known. Climatologists and biogeographers have delineated two distinct deserts within the Death Valley region: (i) the Great Basin Desert to the north, and (ii) the Mojave Desert to the south. The Great Basin Desert is a cold desert and receives most of its annual precipitation as snow during the winter. The Mojave

Desert is a hot desert receiving most of its annual precipitation as rain during both winter and summer.

Prevailing winds at these latitudes are the westerlies, which steer winter storms generated by low-pressure centers located in the western Pacific Ocean across the Great Basin. Of five primary winter weather types that affect the Pacific coast, only the San Diego Low and the Tonopah Low produce significant winter precipitation in southern Nevada. San Diego Low systems are produced when a zone of high pressure develops over the Pacific northwest, displacing the storm track southward and driving low pressure centers onshore along the United States-Mexico border (U.S. Department of Energy, 1991). San Diego Low frontal systems generally move slowly through southern California, southern Nevada, and western Arizona, increasing the duration of precipitation (U.S. Department of Energy, 1991). Tonopah Lows develop in the lee of the Sierra Nevada from storms that are spawned in the Gulf of Alaska and driven south by the Canadian High before moving onshore (U.S. Department of Energy, 1991). Tonopah Lows may produce precipitation in southern Nevada if sufficient atmospheric moisture is available from the Pacific or from snowmelt (U.S. Department of Energy, 1991; Trimble, 1989). During July and August, moisture from the Gulf of Mexico, the Gulf of California, and the Pacific Ocean west of Baja California is driven northward into southern Nevada by a westward expansion of the Bermuda High. This so-called Southwest Monsoon sometimes generates mesoscale convective complexes in Arizona and New Mexico that may very occasionally intrude into southern Nevada (U.S. Department of Energy, 1991). These mesoscale convective complexes produce southern Nevada's heaviest summertime rainfall and provide the greatest chances of flash flooding, hail, and high winds (U.S. Department of Energy, 1991). However, summer precipitation more often comes from isolated convective thunderstorm cells of limited areal extent and duration.

10.2.1.1 Estimation of Orographic Precipitation

The spatial distribution of average annual precipitation within the Death Valley region can be estimated well taking only synoptic and mesoscale effects into consideration. The predominant mesoscale effect is orographic precipitation resulting from the extreme relief of Basin and Range topography. Only after the orographic effect is subtracted from the measured average annual precipitation do the secondary, synoptic effects become apparent. According to French (1983), average annual precipitation in the western and northwestern portion of the Death Valley region is depleted relative to that in the southern and southeastern portions primarily due to the rain shadow produced by the Sierra Nevada during the winter. However, because the southern and southeastern areas lie within the Mojave Desert where summer convective storms are more prevalent, the rain shadow may reflect more than one synoptic effect. French (1983) developed a simple logarithmic model to express the altitude dependence of average annual precipitation (AAP) within southern Nevada. French's general model is

$$\log\left[\hat{A}\,(x_i)\right] = a + b \cdot E\,(x_i) \qquad (10\text{-}1)$$

where $\hat{A}$ is the predicted average annual precipitation at location $x_i=(x_i,y_i)$, E is the elevation, a and b are fitted parameters. Using ordinary least squares (OLS) to fit this equation to measurements from 64 precipitation stations in southern Nevada, 32 of which were located on the Nevada Test Site (NTS), French (1983) obtained the relationship

$$\log\left[\hat{A}\,(x_i)\right] = 0.446 + 0.0000786 \cdot E\,(x_i) \qquad (10\text{-}2)$$

where $\hat{A}$ is given in inches, and E is given in feet above mean sea level. Based on the correlation coefficient given by French (1983), the coefficient of determination for Eq. (10-2) is $R^2=0.581$. When elevation is given in meters above mean sea level, precipitation is given in millimeters, and the natural logarithm is used instead of the base ten logarithm. Eq. (10-2) may be rewritten

$$\hat{A}\,(x_i) = \exp\left[4.262 + 0.000594 \cdot E\,(x_i)\right] \qquad (10\text{-}3)$$

French (1983) also fitted separate logarithmic models to data from rainfall stations in the Sierra Nevada rain shadow (deficit stations), as well as to data from rainfall stations in the southwest portion of Nevada where the rain shadow effect, if it occurs, is obscured by the increase in summer precipitation (excess stations). French's analysis suggests that, on the basis of average annual precipitation, southern Nevada, south of 38.5° north latitude, can be divided into a precipitation deficit zone to the west of the potential rain shadow boundary shown in Figure 10-1 and a precipitation excess zone to the east. The transition zone between the Sierra Nevada rain

shadow zone, or winter precipitation source zone, and the summer moisture source zone, is an 80-km wide north-south strip that includes most of the NTS.

Hevesi et al. (1992) reanalyzed the precipitation-elevation relationship developed by French and chose to exclude those precipitation stations with less than 8 yr of record. The 42 precipitation stations having records with 8 or more years that were selected by Hevesi et al. (1992) are shown in Table 10-1. Using OLS to fit Eq. (10-1) to the 42 measurements of average annual precipitation, Hevesi et al. (1992) obtained

$$\hat{A}(x_i) = \exp[4.32 + 0.00059 \cdot E(x_i)] \qquad (10\text{-}4)$$

where $\hat{A}$ is given in mm, and E is given in meters above mean sea level. Hevesi et al. (1992) note that a scatterplot comparison of the 42 data points with Eq. (10-4) indicates that there is increased variability of the measured data with increasing altitude. The authors attribute this increased variability to: "1. the small number of stations below [600 m], 2. a rain-shadow effect caused by the location of stations on the lee of slopes of higher topography or adjacent to blocking ranges, 3. regional trends in AAP, such as the west-to-east increase hypothesized by French (1983), 4. an increase in elevations of basins from north to south, 5. increased measurement error with increased elevation because of increasing amounts of snow, and 6. increased variability of annual precipitation with increased precipitation." The data in Table 10-1 clearly show that the standard deviations of the AAP measurements are not constant. When the variance of the independent variable is nonconstant (heteroscedasticity), OLS is no longer a minimum variance estimator and will produce suboptimal estimates of the regression coefficients (Draper and Smith, 1981). Generalized least squares (GLS) may be used to explicitly incorporate the variance of the independent variable into the regression equations (Seber and Wild, 1989). The exponential model obtained using GLS for the 42 stations selected by Hevesi et al. (1992) is

$$\hat{A}(x_i) = \exp[4.351 + 0.000468 \cdot E(x_i)] \qquad (10\text{-}5)$$

Plots of Eq. (10-4), Eq. (10-5), and the point measurements of average annual precipitation at the 42 locations with their associated error bars are shown Figure 10-2. It is readily apparent from Figure 10-2 that the shape of Eq. (10-5) is more influenced by measurements with small variances than is Eq. (10-4). Because the standard deviation of the annual precipitation is positively correlated with the average annual precipitation, ($\rho = 0.74$, where ρ is the Pearson correlation coefficient), Eq. (10-5) predicts lower precipitation values at higher elevations than does Eq. (10-4).

If elevation and average annual precipitation are indeed highly correlated, it is reasonable to assume that the areal distribution of average annual precipitation can be estimated accurately from elevation data alone. However, as was noted earlier, the areal distribution of average annual precipitation is also controlled by synoptic effects. Examining the spatial structure of the residuals of measured annual average precipitation minus the orographic effect predicted by either Eq. (10-4) or Eq. (10-5) should reveal the synoptic patterns identified by French (1983). As is shown in Figure 10-3 for Eq. (10-5), negative residuals tend to cluster in the area identified by French (1983) as the potential rain shadow zone, while positive residuals occur more frequently in the zone most affected by summer precipitation from the Southwest Monsoon. Standard procedures for estimating the spatial distribution of rainfall, such as Thiessen polygons, spline surface fitting, or kriging, do not explicitly account for the strong orographic effect observed in southern Nevada. However, one spatial estimation method that does explicitly account for correlation between measured variables of different types is cokriging.

10.2.1.2 Estimation Based on Co-Regionalization

Hevesi et al. (1992) used cokriging to estimate AAP at unsampled locations from the 42 measurements of average annual precipitation, and 1,531 additional measurements of ground surface elevations manually extracted from 1:250,000 scale topographic maps (Caliente, Death Valley, Goldfield, and Las Vegas). The authors first constructed sample, direct- and cross-semivariograms for measured AAP, and elevation. They then performed cross-validation to select the final model direct- and cross-semivariograms from among sets of alternative models. Based on the sample semivariogram computed by Hevesi et al. (1992) for measured AAP, it appears that this variable may be treated as a stationary random function, although for reasons discussed later, this observation is somewhat counterintuitive. The paucity of AAP data precluded computing accurate, directional sample semivariograms, and statistical isotropy had to be assumed. Sample semivariograms of elevation

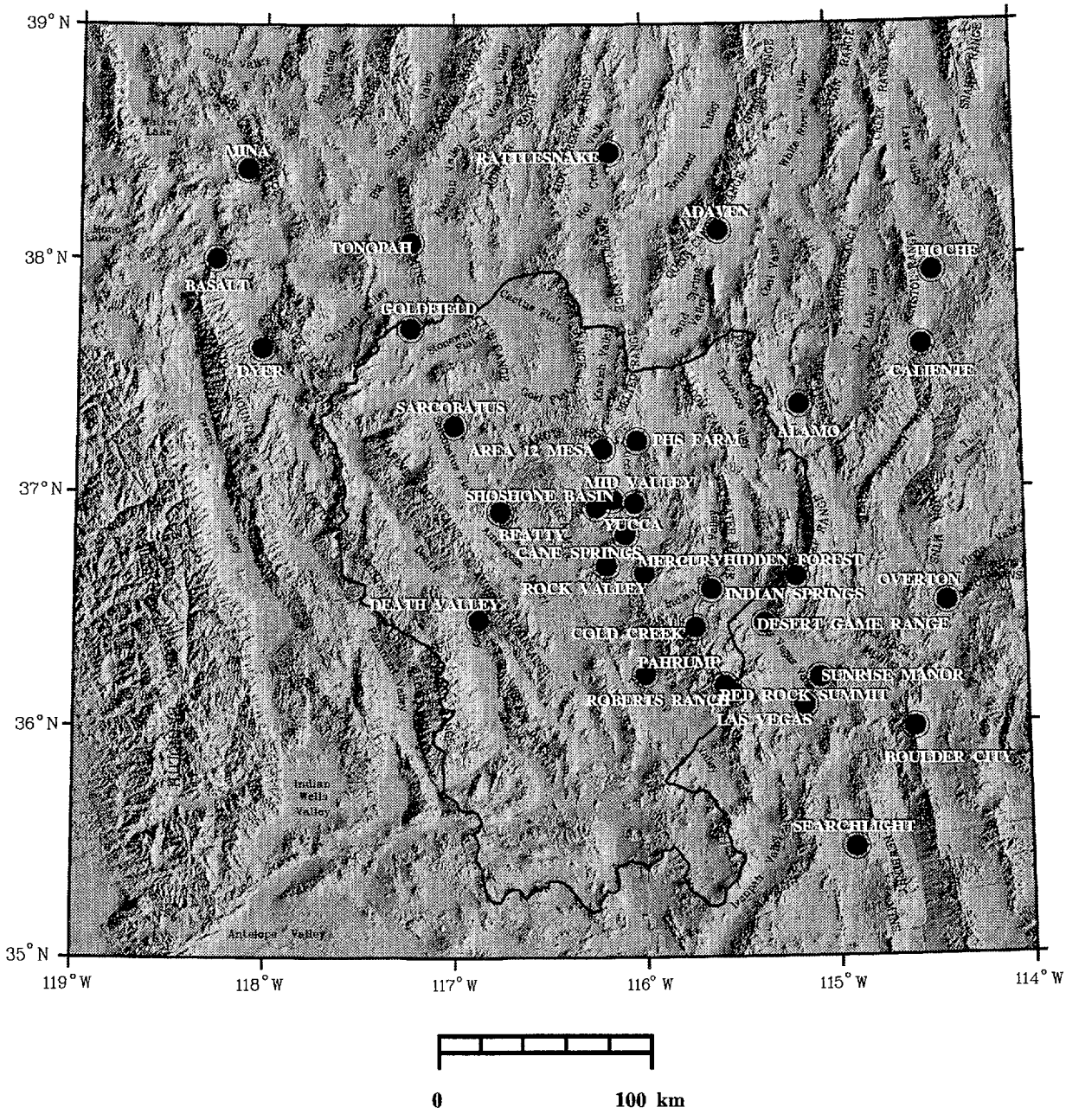

Figure 10-1. Physiographic map and locations of precipitation stations in the Death Valley region

Table 10-1. Precipitation stations in southern Nevada (after Hevesi et al., 1992)

Precipitation Station	X (m)	Y (m)	Elevation (m)	Record Length (yr)	AAP (mm)	σ_{AAP}
Rock Valley	571477	4059803	1036	8	157	23
Desert Rock Airport	587903	4052634	1005	15	157	17
Mercury	589385	4056310	1149	13	159	18
4JA	563978	4070837	1043	16	119	15
Cane Springs	580272	4074747	1219	21	208	21
Well 5B	592156	4072981	938	19	128	12
Shoshone Basin	566792	4087499	1725	12	225	25
Mid Valley	574151	4091332	1420	13	226	23
Yucca	584585	4089544	1194	25	177	17
40 MN	563756	4100456	1469	18	202	18
Tippipah Springs 2	572648	4100527	1517	20	245	23
BJY	584456	4102523	1241	22	177	17
Area 12 Mesa	569503	4115256	2282	17	295	31
PHS Farm	585797	4119179	1391	8	193	22
Little Feller 2	562189	4107877	1572	8	229	36
Adaven	624217	4219539	1905	47	321	16
Alamo	662317	4136958	1048	26	128	10
Boulder City	716377	3984526	769	50	139	9
Caliente	719152	4166016	1343	51	231	11
Cold Creek	613593	4030745	1828	8	230	33
Hidden Forest	660934	4055467	2301	9	320	27
Las Vegas Airport	665043	3994509	658	33	104	8
Sunrise Manor	672351	4007634	554	32	106	8
Overton	731299	4044195	371	26	91	13
Pioche	724110	4201242	1865	44	313	16
Red Rock Summit	632002	3999496	1981	8	270	36

Table 10-1. Precipitation stations in southern Nevada (after Hevesi et al., 1992) (Cont'd)

Precipitation Station	X (m)	Y (m)	Elevation (m)	Record Length (yr)	AAP (mm)	σ_{AAP}
Roberts Ranch	627448	4003200	1859	8	354	47
Searchlight	689009	3926628	1078	50	185	14
Basalt	388755	4206366	1935	15	142	17
Beatty	522268	4085491	1082	47	159	12
Death Valley	511918	4033668	–51	18	69	7
Desert Game Range	646379	4033013	890	42	106	8
Dyer	410244	4163603	1516	31	125	9
Goldfield	479459	4172350	1734	39	136	12
Indian Springs	619255	4049239	955	25	116	16
Lathrop Wells	553630	4056012	663	21	85	11
Mina	403923	4248677	1387	53	115	7
Pahrump	589883	4008279	822	20	126	16
Rattlesnake	572688	4255867	1802	20	121	13
Sarcobatus	500000	4126063	1225	14	90	13
Tonopah Airport	492719	4213046	1654	29	163	10
Tonopah City	479561	4213068	1857	22	126	11

indicated strong zonal anisotropy presumably resulting from the general north-northwest to south-southeast alignment of basin and range physiographic features in the Walker Lane. In addition, two distinct correlation structures were observed in the sample semivariogram. These two structures were assumed to correspond to the local spatial variability of elevation within basins, and the regional variability of elevation between basins and ranges (Hevesi et al., 1992). In order to simplify semivariogram model fitting, the authors assumed that the elevation field was statistically isotropic and stationary within a radius of 61,000 m. Because of the strong positive correlation observed between precipitation and elevation, it is not surprising that the sample cross-semivariogram for these variables exhibits a rather long correlation length (approximately 67,000 m). Hevesi et al. (1992) note that, between 67,000 and 128,000 m, the sample cross-semivariogram shows a distinct negative slope that may result from the clustering of precipitation stations along the northwest to southeast alignment of the physiographic features of the Walker Lane.

Hevesi et al. (1992) selected a model semivariogram for AAP consisting of a nugget and a spherical structure with a range of 58,000 m. For elevation, the authors selected a nested semivariogram, consisting of a nugget, a Gaussian structure with a range of 18,500 m, a spherical structure with a range of 21,300 m, and a linear structure with a range of 82,300 m. An appropriate and consistent model cross-semivariogram cannot be selected using cross-validation alone since the complete model of statistical structure, which consists of the two direct-semivariograms and the cross-semivariogram, must be positive definite. Thus, in addition to the requirement that each model semivariogram be positive definite, the Cauchy-Schwartz condition

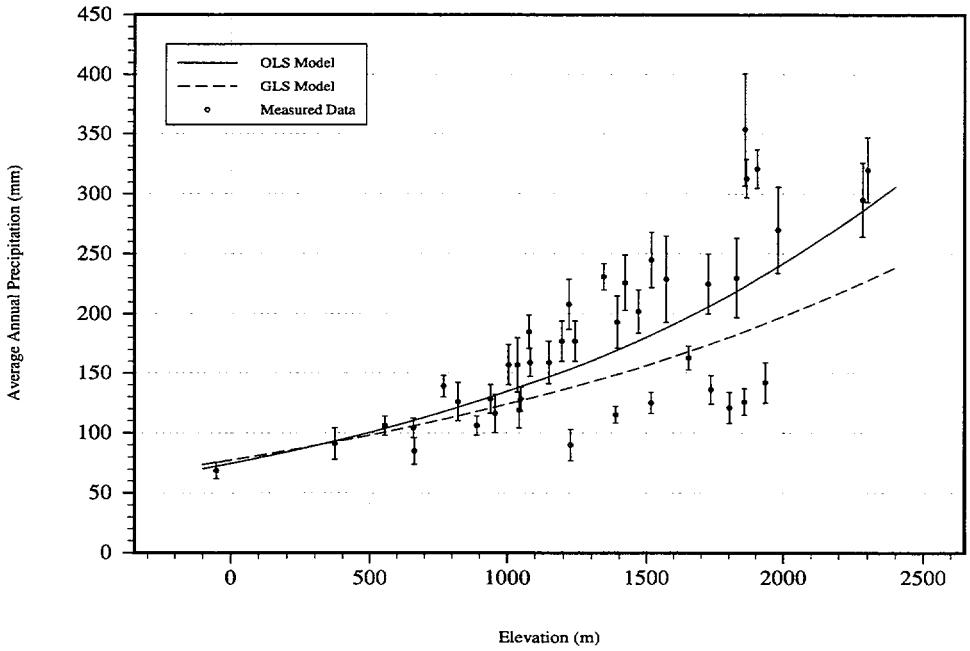

Figure 10-2. Average annual precipitation as a function of elevation in the Death Valley region

$$\gamma_{ij}(h) \leq [\gamma_{ii}(h)\,\gamma_{jj}(h)]^{1/2} \qquad (10\text{-}6)$$

must be satisfied for all lags h, where $\gamma_{ij}(h)$ is the model cross-semivariogram, $\gamma_{ii}(h)$ and $\gamma_{jj}(h)$ are the model direct-semivariograms. The final model cross-semivariogram selected by Hevesi et al. (1992) was a nested model consisting of a Gaussian structure with a range of 18,600 m, and a spherical structure with a range of 58,000 m.

On the basis of detailed cross-validation analysis of cokriging, kriging, and six other spatial interpolation procedures, Hevesi et al. (1992) concluded that those methods that use elevation data generally produced more accurate estimates than those using AAP data alone. However, of the three methods that use elevation data to estimate AAP (log-linear regression, linear regression, and cokriging), cokriging produced the most accurate results, with the accuracy increasing as the radius of the cokriging neighborhood increased. In addition, the authors concluded that due to the relatively large distances separating precipitation stations in the Death Valley region, the strong positive correlation between AAP and elevation is more important for estimating AAP than the spatial correlation of AAP itself.

Because average annual precipitation is strongly controlled by elevation and, to a much lesser extent, by the Sierra Nevada rain shadow effect, it is difficult to accept the hypothesis that AAP is statistically stationary, even though stationarity is what its sample semivariogram appears to suggest. The sample semivariogram for elevation, which largely determines average annual precipitation, is clearly not stationary over the entire Death Valley region. Hevesi et al. (1992) acknowledge that nonstationary or nonintrinsic random functions can be modeled using universal kriging or universal cokriging; however, they also correctly point out that either the form of the drift function or the model semivariogram must be known *a priori*. Clearly, it would be desirable to use a spatial estimation procedure that is applicable to nonintrinsic functions, since neither AAP nor elevation is stationary.

10.2.1.3 Nonintrinsic Function Estimation Using an External Drift and Residual Kriging

A hybrid nonintrinsic co-estimation procedure was developed for estimating average annual precipitation within the Death Valley region and is described in the following section. This hybrid method combines the relatively simple technique of kriging with an external drift (Deutsch and Journel, 1992) with residual kriging

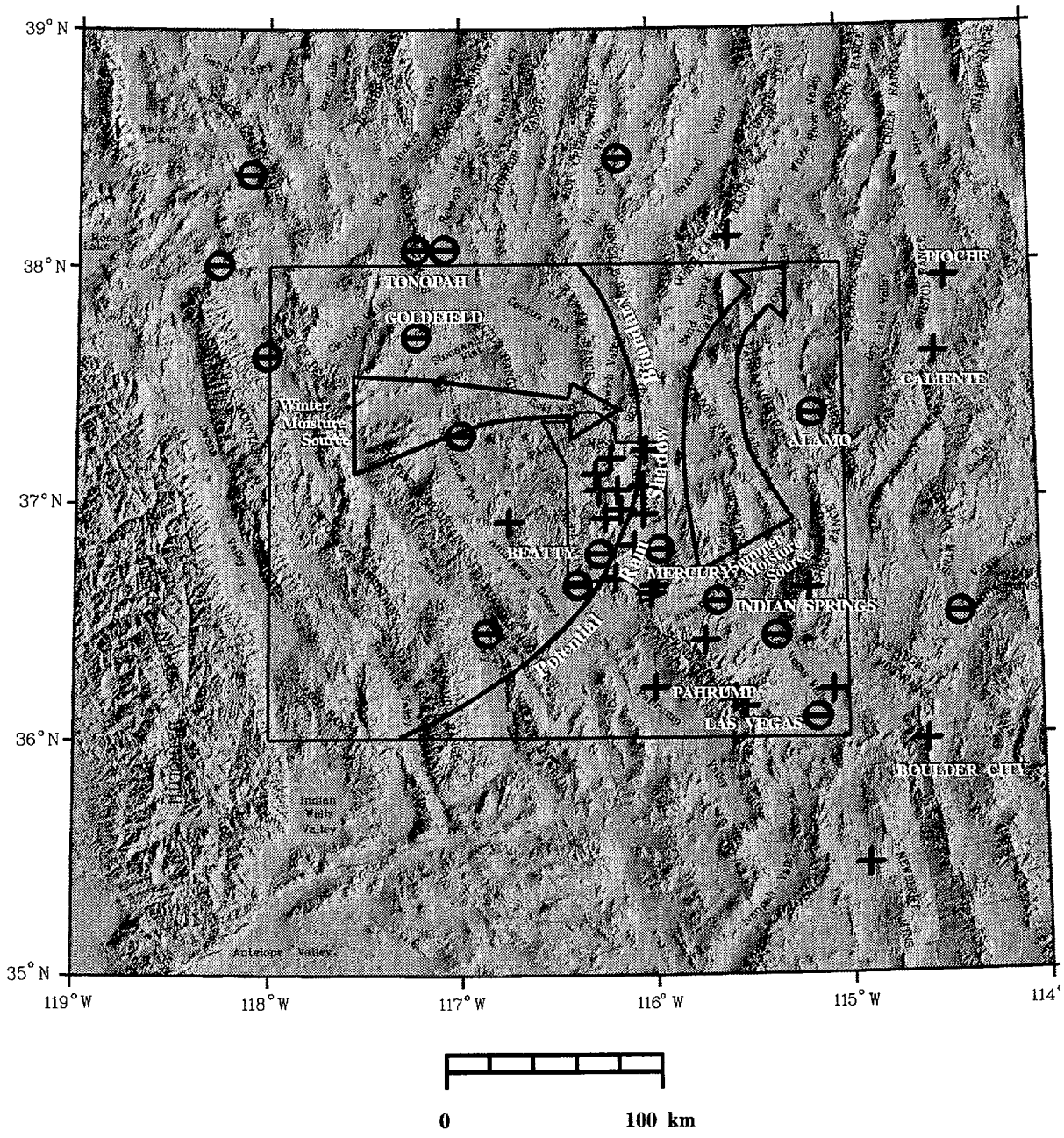

Figure 10-3. Location and sign of residuals of average annual precipitation after orographic effect has been subtracted. (a) OLS orographic model

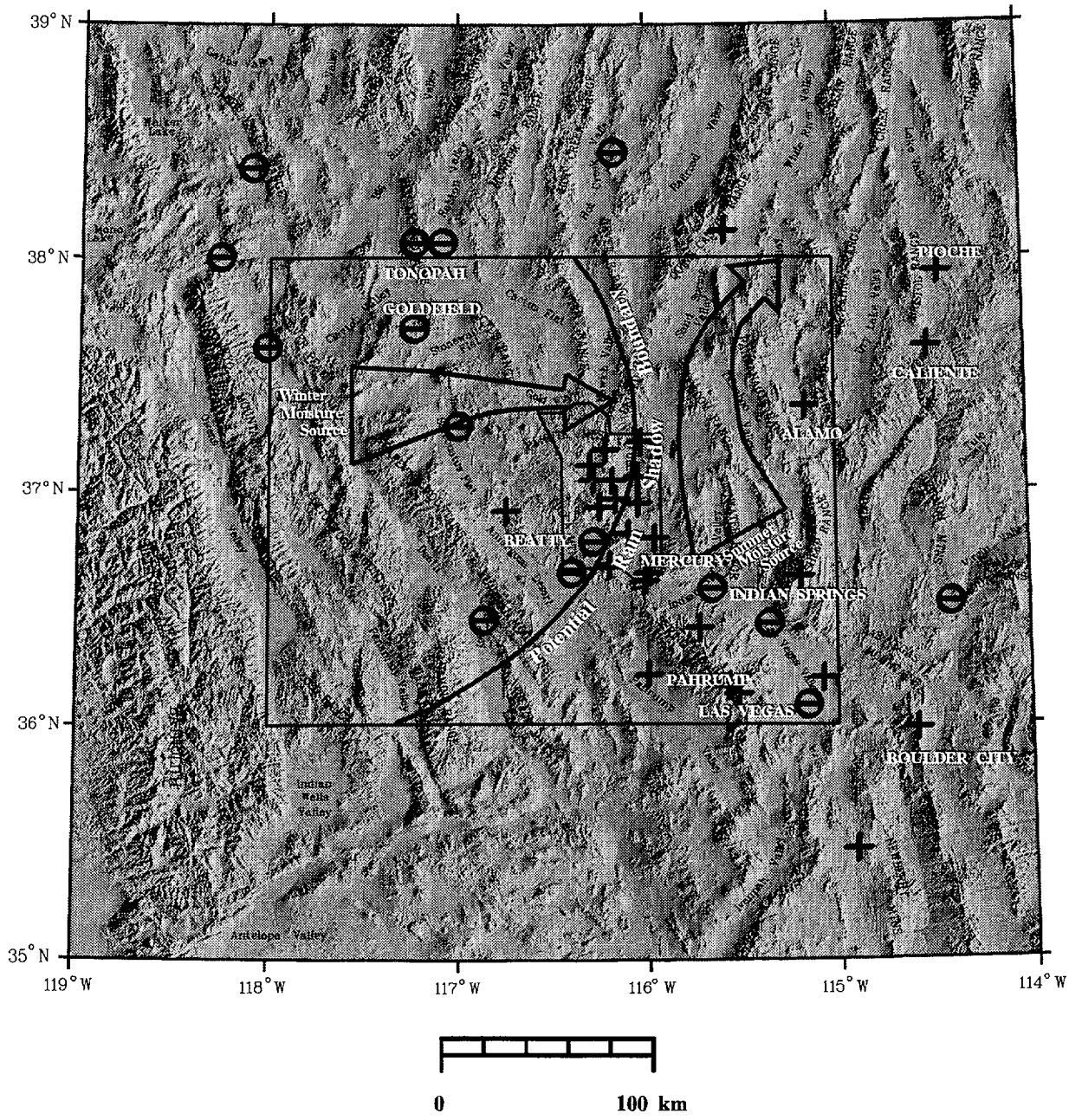

Figuure 10-3 (Cont'd). Location and sign of residuals of average annual precipitation after orographic effect has been subtracted. (b) GLS orographic model

of nonintrinsic functions (Neuman and Jacobson, 1984). As described by Deutsch and Journel (1992), kriging with an external drift variable is a straightforward extension of kriging with a trend, where the trend is restricted to a simple two-term equation. Moreover, kriging with an external drift accounts for co-regionalization among variables without adding the computational burden of cokriging. However, the secondary variable used in the external drift must be measured at every point in the domain at which an estimate of the primary variable is required. This requirement poses no problem if elevation is used to estimate $\hat{A}$ since elevation measurements can be obtained at 30-m intervals from digital elevation maps (DEM) produced by the U.S. Geological Survey.

Let $Z(\boldsymbol{x})$ be the random function for AAP, the primary variable, and $Y(\boldsymbol{x})$ be the random function for elevation, the secondary or external variable. The drift model for the primary variable is given by

$$\mathrm{E}\{Z(\boldsymbol{x})\} = m(\boldsymbol{x}) = a + b \cdot Y(\boldsymbol{x}) \qquad (10\text{-}7)$$

which is the same as Eq. (10-4) or Eq. (10-5). Thus the random function for AAP is

$$Z(x) = m(\boldsymbol{x}) + R(\boldsymbol{x}) = a + b \cdot Y(\boldsymbol{x}) + R(\boldsymbol{x}) \qquad (10\text{-}8)$$

where $R(\boldsymbol{x})$ is the random function with zero mean commonly called the residual component. Although the influence of the external trend model can be accounted for and the kriging weights estimated using universal kriging if the covariance structure is already known, Isaaks and Srivastava (1989) contend that "... it is wiser to choose the trend based on an understanding of the genesis of the phenomenon, subtract this trend from the observed samples to obtain residuals, do the estimation on the residuals, and add the trend back at the end." Since the orographic phenomenon is well understood and the coefficients of the external trend are readily obtained by regression, no benefit is gained from constructing and solving the more complex universal kriging system instead of the simple residual kriging system for the random function $R(\boldsymbol{x}) = Z(\boldsymbol{x}) - [a + b \cdot Y(\boldsymbol{x})]$. However, the spatial map of the orographic residuals (Figures 10-3a and 10-3b), which reflect the synoptic effects of the Sierra Nevada rain shadow and the Southwest Monsoon, suggest that the random function $R(\boldsymbol{x})$ is also nonstationary. This lack of stationarity is confirmed by Figures 10-4a and 10-4b which show the sample semivariograms for $\hat{R}_{ols}(\boldsymbol{x}_i) = Z(\boldsymbol{x}_i) - [a_{ols} + b_{ols} \cdot Y(\boldsymbol{x}_i)]$, and $\hat{R}_{gls}(\boldsymbol{x}_i) = Z(\boldsymbol{x}_i) - [a_{gls} + b_{gls} \cdot Y(\boldsymbol{x}_i)]$, where *ols* refers to the regression equation obtained using ordinary least squares, *gls* refers to the regression equation using generalized least squares, and *i* is an index that refers to the precipitation station location. It is clear that neither sample semivariogram attains a fixed sill, although the semivariogram for the GLS regression equation increases at a much lower rate than that for the OLS regression equation. Here again the physical phenomena that produce the trend (the Sierra Nevada rain shadow and Southwest Monsoon effects) are well understood, and straightforward residual kriging is suggested.

The procedure used to extract the trend from the rain shadow random function is similar to the residual kriging approach developed by Neuman and Jacobson (1984), except that iterative refinement of the average sample semivariogram based on the correlation structure of the resulting residuals is not pursued. A series of polynomial trend surfaces of increasing order were fitted to $\hat{R}_{ols}(\boldsymbol{x}_i)$ and $\hat{R}_{gls}(\boldsymbol{x}_i)$ until stationarity was observed in the sample semivariogram for the residuals

$$\hat{S}_{ols}(\boldsymbol{x}_i) = \hat{R}_{ols}(\boldsymbol{x}_i) - \sum_{j=1}^{N_p} \alpha_j f_j(\boldsymbol{x}_i) \qquad (10\text{-}9)$$

where $N_p = 1/2\,(m+1)\,(m+2)$, m is the order of the polynomial, $\alpha_j, j = 1, \ldots, N_p$ are coefficients obtained by regression, $f_j(\boldsymbol{x}), j = 1, \ldots, N_p$ are prescribed basis function, and $\boldsymbol{x} = (x, y)$ is the location vector [a formula similar to Eq. (10-9) is used for the GLS orographic model]. For example, a second-order polynomial trend surface is given by $m = 2$, $N_p = 6$, and $\{f_j\} = \{1, x, y, x^2, xy, y^2\}$. Sample semivariograms for $\hat{S}$ determined after fitting first-, second-, and third-order polynomial trend surfaces to $\hat{R}$ are shown for the OLS and GLS orographic models in Figures 10-5a and 10-5b, respectively. As the degree of the polynomial trend surface increases from 1 to 3, the presence of a sill becomes more apparent for the sample semivariograms, and the value of the sill decreases. It appears that a third-order polynomial trend must be removed before $\hat{S}_{ols}$ is stationary, while only a second-order trend surface must be removed to make $\hat{S}_{gls}$ stationary.

During early efforts, an attempt was made to fit model semivariograms to the sample semivariograms for $\hat{S}_{ols}$ and $\hat{S}_{gls}$ using statistical measures obtained from cross-validation. The cross-validation measures

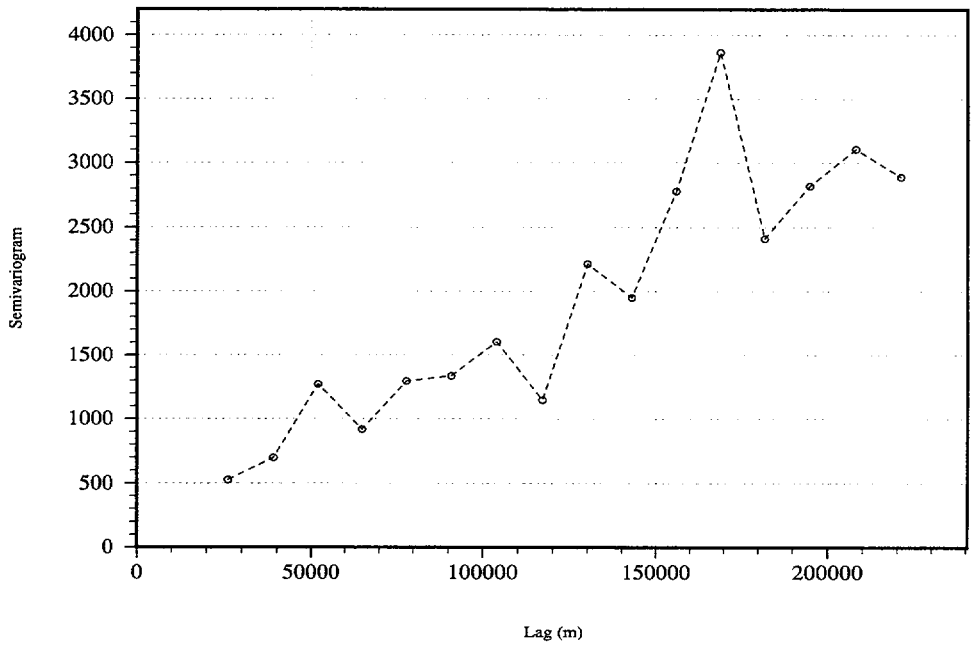

(a)

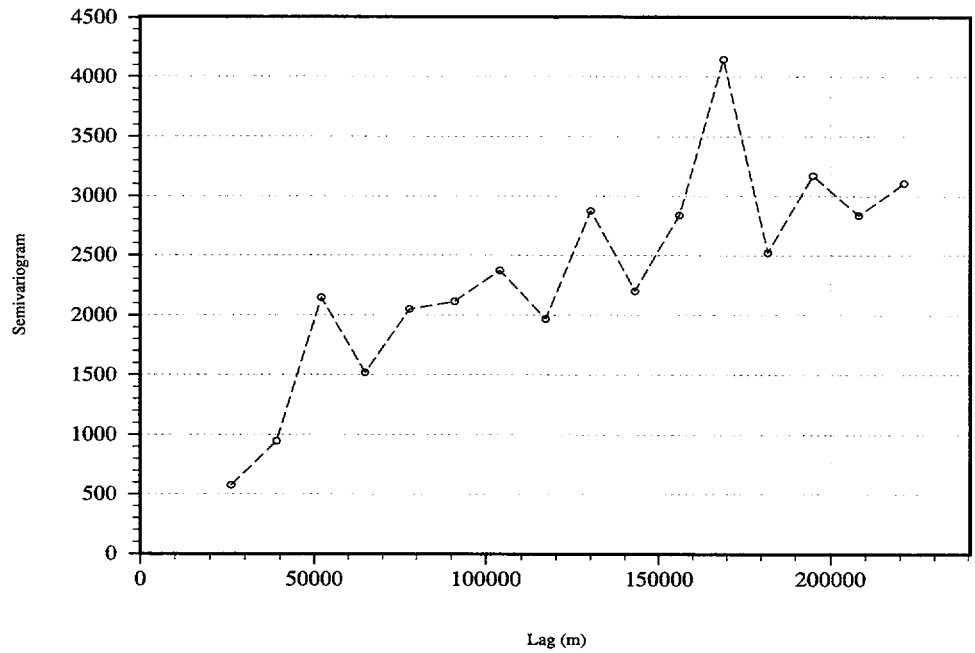

(b)

Figure 10-4. Sample semivariograms for (a) $\hat{R}_{ols}$;(b) $\hat{R}_{gls}$

$$\text{RMSE} = \frac{1}{s^2 nk=1} \sum^{n} \left[S^*(x_k) - \hat{S}(x_k) \right]^2 \quad (10\text{-}10)$$

and

$$\text{MSE} = \frac{1}{n} \sum_{k=1}^{n} \frac{\left[S^*(x_k) - \hat{S}(x_k) \right]}{\sigma_K^2(x_k)} \quad (10\text{-}11)$$

were used to assess the relative accuracy and consistency of the estimates $S^*(x_k)$ obtained at the measurement location k, when data from location k is excluded from the kriging equations. Here s^2 is the sample variance of $\hat{S}$, n is the number of measurement points remaining after point k is excluded, and σ_K^2 is the kriging variance. According to Hevesi et al. (1992), estimates are considered accurate if RMSE is close to zero, and the calculated estimation variances are deemed to be consistent with the RMSE if SMSE is in the range $1 \pm 2(2/n)^{0.5}$. Comparison of alternative semivariogram models based on these cross-validation measures indicated that, for the OLS orographic model, a spherical semivariogram with a sill of 1,080, and a range of 10 m or less was optimal, while for the GLS orographic model a spherical semivariogram with a sill of 1,800 and a range of 10 m or less was optimal. Clearly, the extremely short ranges of these so-called optimal model semivariograms are much shorter than the ranges that may be reasonably inferred from the sample semivariograms shown in Figures 10-5a and 10-5b. Moreover, it appears that in this case use of these cross-validation measures would lead to the adoption of incorrect models of the statistical structure of the random field. Ultimately the model semivariograms were selected by equating the sill to the sample variance and estimating the range using nonlinear least squares. Spherical models were selected for both the OLS and GLS orographic models. The model semivariogram for the OLS orographic model had a sill of 1,080 and a range of 69,600 m. The model semivariogram for the GLS orographic model had a sill of 1,800 and a range of 76,100 m. Sample and model semivariograms for the OLS and GLS orographic models are shown in Figures 10-6a and 10-6b, respectively.

Final estimates of AAP were obtained by adding together the kriged estimates of the rain shadow residual, $S^*(x)$, the mean rain shadow effect, $\sum \alpha_j f_j(x)$, and the mean orographic effect, $\hat{A}(x)$. The estimated mean annual precipitation at any location x is given by

$$\tilde{A}(x) = a + b \cdot E(x) + \sum_{j=1}^{N_p} \alpha_j f_j(x) + S^*(x) \quad (10\text{-}12)$$

For this preliminary study, AAP was estimated within that portion of the Death Valley region between 36 to 38° north and 114 to 117° west. Each 1° DEM consists of a 1,201×1,201 grid of elevation measurements for a total of 1,442,401 grid points. To reduce computational burden, less than 10 percent of the measurements along each grid direction were retained in order to produce a final grid with dimensions 301×201 (60,501 measurements) for the 3×2° area considered. Gray-scale isohyetal maps of the estimated average annual precipitation due to orographic effects for this area are shown for the OLS and GLS models in Figures 10-7a and 10-7b, respectively. Similar maps of $\tilde{A}$, are shown for the OLS and GLS models in Figures 10-8a and 10-8b, respectively. It is clear from Figures 10-7a and 10-7b that the OLS model for the orographic precipitation effect predicts a larger overall $\hat{A}$ within this portion of the Death Valley region than is predicted by the GLS model. The increase in orographic precipitation predicted by the OLS model is most apparent in the northeast. The rain shadow effect is evidenced by a pronounced increase in the area of darker shaded regions in the eastern portion of model area, between the maps for $\hat{A}$ (Figures 10-7a and 10-7b) and the maps for $\tilde{A}$ (Figures 10-8a and 10-8b). Only for the GLS model is there a noticeable increase in the area of lighter shaded regions in the western portion of the map when the rain shadow effect is incorporated.

10.2.2 Spatial Distribution of Average Annual Recharge

In order to construct a regional scale flow model of the Death Valley system's hydrogeologic regime, the locations of natural system boundaries and areas of recharge and discharge must be identified. Since the groundwater system for the Death Valley region is composed by a number of topographically closed basins that are hydraulically connected at depth by the highly transmissive Paleozoic carbonate aquifer,

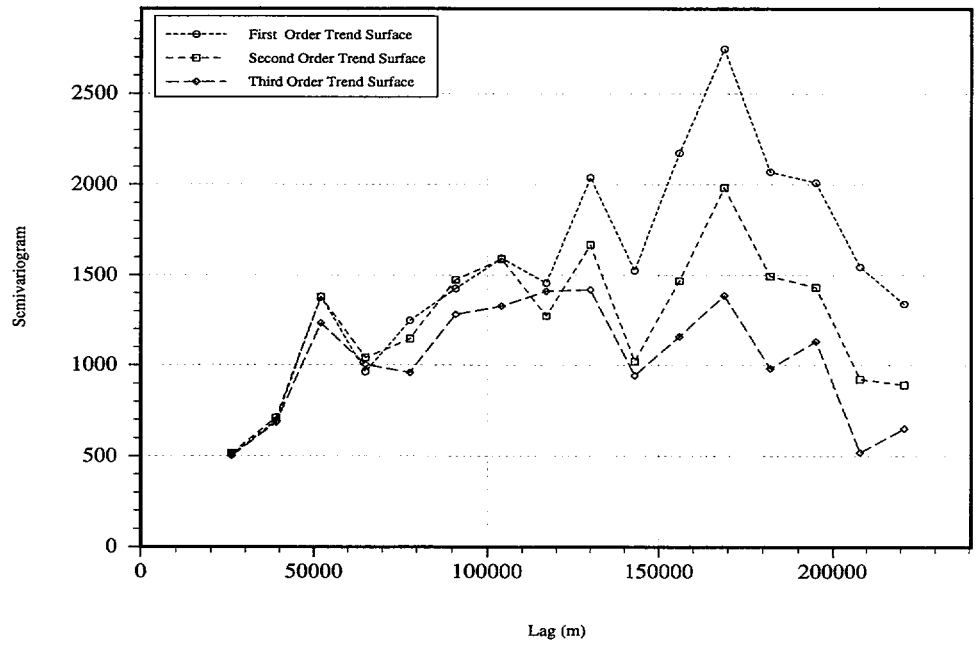

(a)

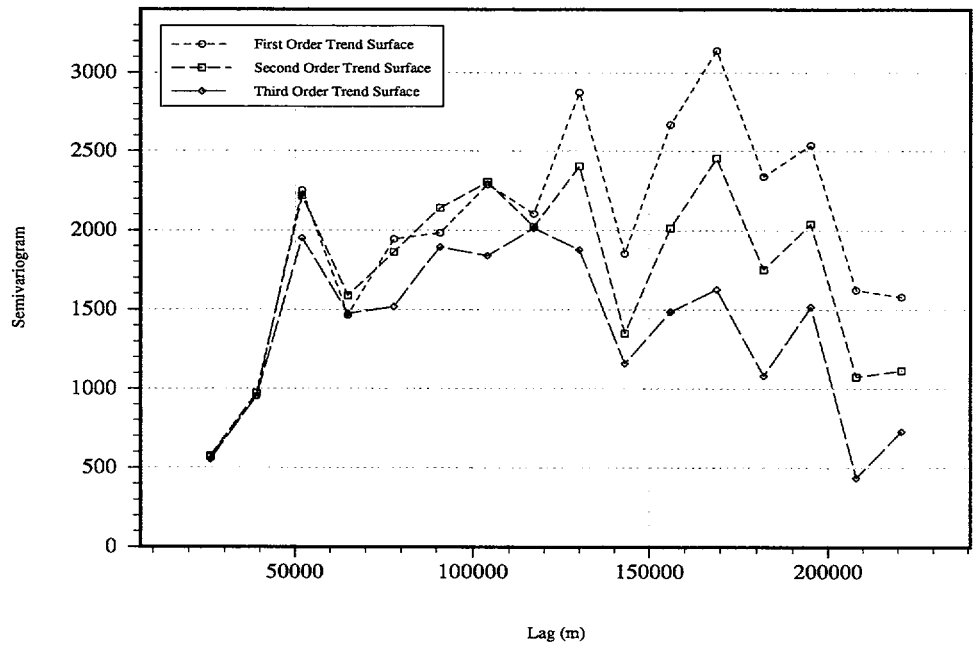

(b)

Figure 10-5. Sample semivariograms of $\hat{R}$ residuals after subtraction of first, second, and third order polynomial drifts (a) $\hat{S}_{ols}$; (b) $\hat{S}_{gls}$

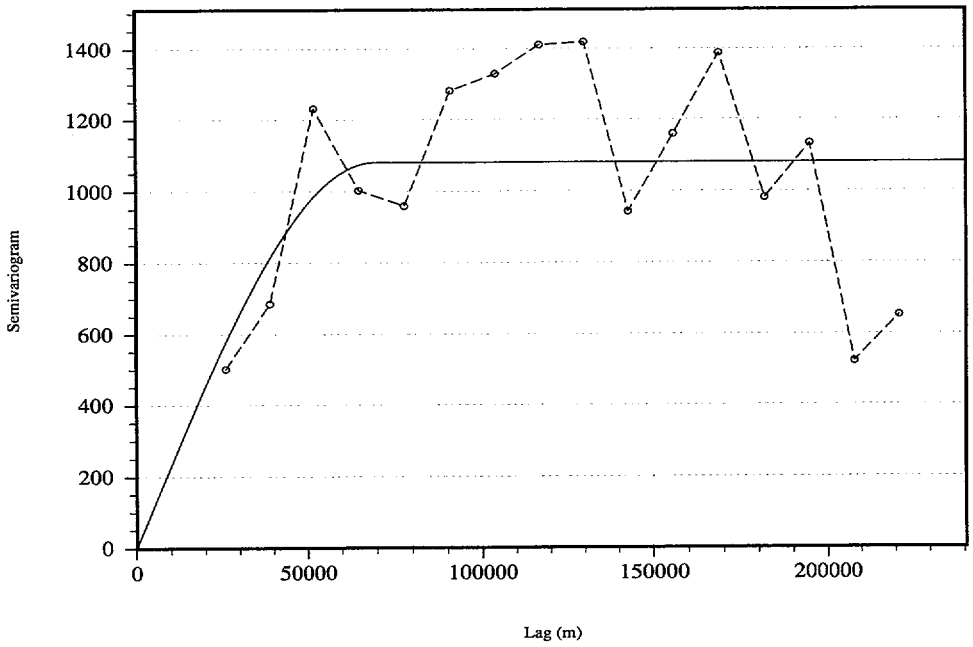

(a)

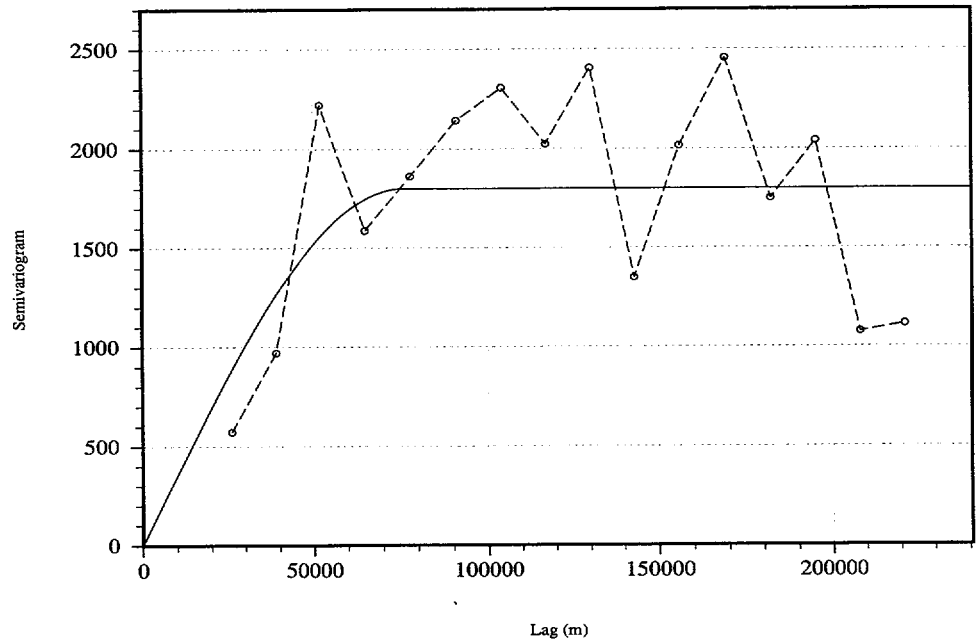

(b)

Figure 10-6. Sample and model semivariograms of $\hat{R}$ residuals. (a) $\hat{S}_{ols}$ after subtraction of a third order polynomial drift; (b) $\hat{S}_{gls}$ after subtraction of a second order polynomial drift

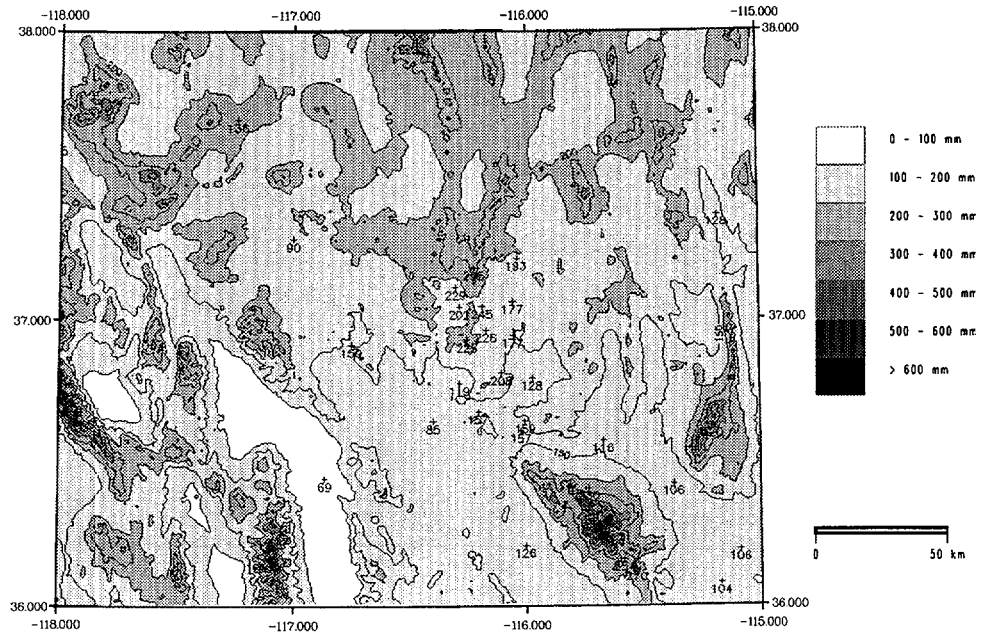

(a)

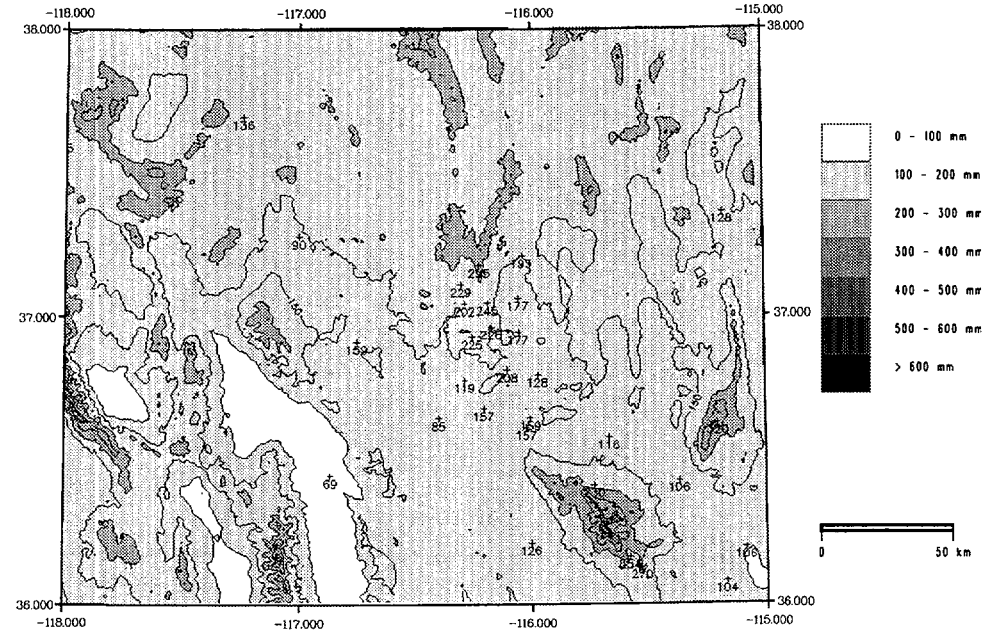

(b)

Figure 10-7. Map of estimated orographic precipitation $\hat{A}$. (a) OLS model; (b) GLS model

the extent of the region may be fixed if a boundary across which no water is transported can be delineated. If these zero-flux boundaries can be identified, the nature of the hydrogeologic regime can be largely determined by the location and magnitude of the internal recharge and discharge zones. Water leaves the Death Valley groundwater system primarily by evapotranspiration of water discharged by springs in the Ash Meadows, Oasis Valley, and Furnace Creek Ranch areas. Recharge to the regional system is presumed to occur primarily along the upper reaches of stream channels that drain the higher mountain ranges. While groundwater discharge can be at least roughly estimated by measuring spring discharge and calculating the area and water use of native vegetation and agricultural crops dependent on the spring discharge, estimating the location and magnitude of natural recharge is extremely difficult. Direct measurement of recharge to shallow aquifers can be made using lysimeters; however, this method is probably not practical for estimating recharge to the extremely deep Paleozoic carbonate aquifer. Straightforward application of the water budget method is also impractical since estimates of evapotranspiration must be obtained for the entire region. Empirical techniques are often the only methods that can be easily used to obtain rough predictions of recharge, although their derivation is often not carefully documented and their reliability is often in question.

Watson et al. (1976) conducted a statistical evaluation of the empirical formula developed by Maxey and Eakin (1949) to estimate groundwater recharge for basins in Nevada. In the Maxey-Eakin method, recharge is estimated from specific percentages of the mean annual precipitation. According to Watson et al. (1976), Maxey and Eakin defined five mean annual precipitation zones (>20 in., 15–20 in., 12–15 in., 8–12 in., and <8 in.), based on Hardman's (1936) precipitation map of Nevada. The fixed percentage from each precipitation zone that is recharged to a basin, which is shown in Table 10-2, was determined by assuming that each hydrologic basin is in equilibrium so that total basin recharge could be equated to the estimated basin discharge. As pointed out by Watson et al. (1976), "[t]he predictive equations derived relate discharge to precipitation in each zone and, therefore, only give values of discharge." However, the assumption of equilibrium makes estimated recharge equivalent to estimated discharge. Using multiple regression, Watson et al. (1976) determined the coefficients of the equation

$$D = \beta_0 + \sum_{i=1}^{5} \beta_i X_i \qquad (10\text{-}13)$$

where D is the basin discharge, X_i is the product of mean annual precipitation and area for the i th Hardman zone in the given basin, and β_i is a coefficient that represents the fraction of total precipitation in zone i that is contributed to basin discharge. When the intercept β_0 is eliminated by subtracting the volume of subsurface outflow to adjoining basins from D, the β_i correspond closely to the Maxey-Eakin percentages. The large range of the 95 percent confidence intervals obtained by Watson et al. (1976) for the β_i indicates that neither Eq. (10-13) nor the Maxey-Eakin formula, are highly reliable. The authors assert ". . . that neither of these predictive equations can be used for anything more than a first approximation to recharge." Regardless of the accuracy of these equations, Watson et al. (1976) recognize that in the absence of other data, this simple approach may be the only practical method to estimate recharge in Nevada.For future numerical modeling work that will be conducted in this research project, estimates of recharge must be obtained by some procedure. Even though statistically based inversion methods will be used to calibrate the numerical flow model, prior estimates of all parameters, including the location and magnitude of recharge, are required both to regularize the inverse problem, and to provide initial guesses for the optimization routine. Because there are currently few alternative procedures for obtaining prior estimates of recharge within the Death Valley region, the Maxey-Eakin formula will be used; final estimates of recharge being obtained from the model calibration results. Prior estimates of mean annual

Table 10-2. Maxey-Eakin Recharge (from Watson et al., 1976)

Hardman Zones	Maxey-Eakin Recharge (%)
> 20 in. (490 mm)	25
15–20 in. (381–490 mm)	15
12–15 in. (305–381 mm)	7
8–12 in. (203–305 mm)	3
< 8 in. (203 mm)	0

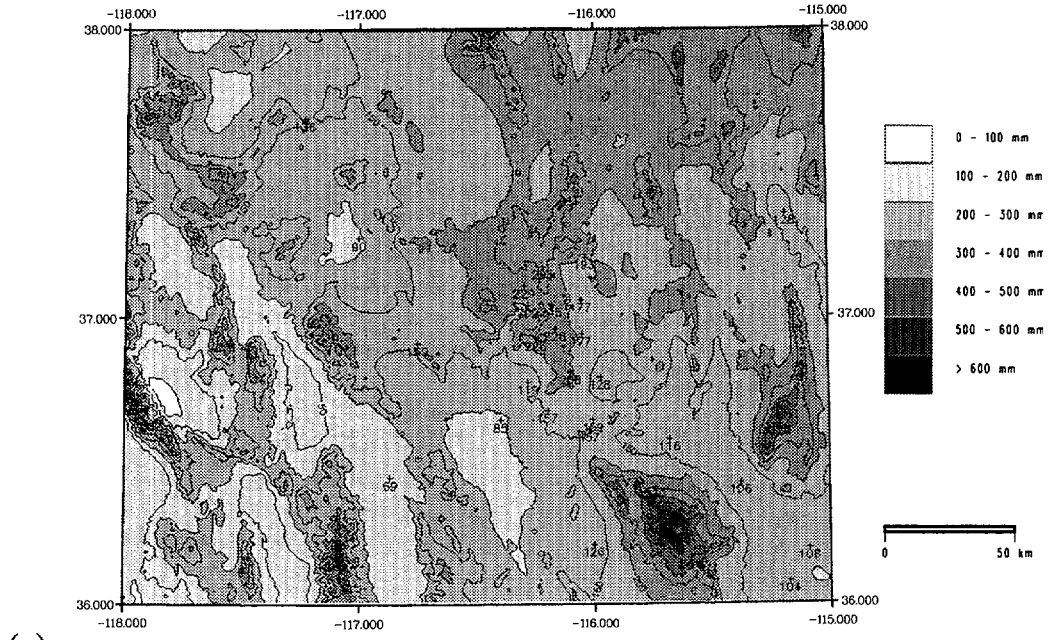

(a)

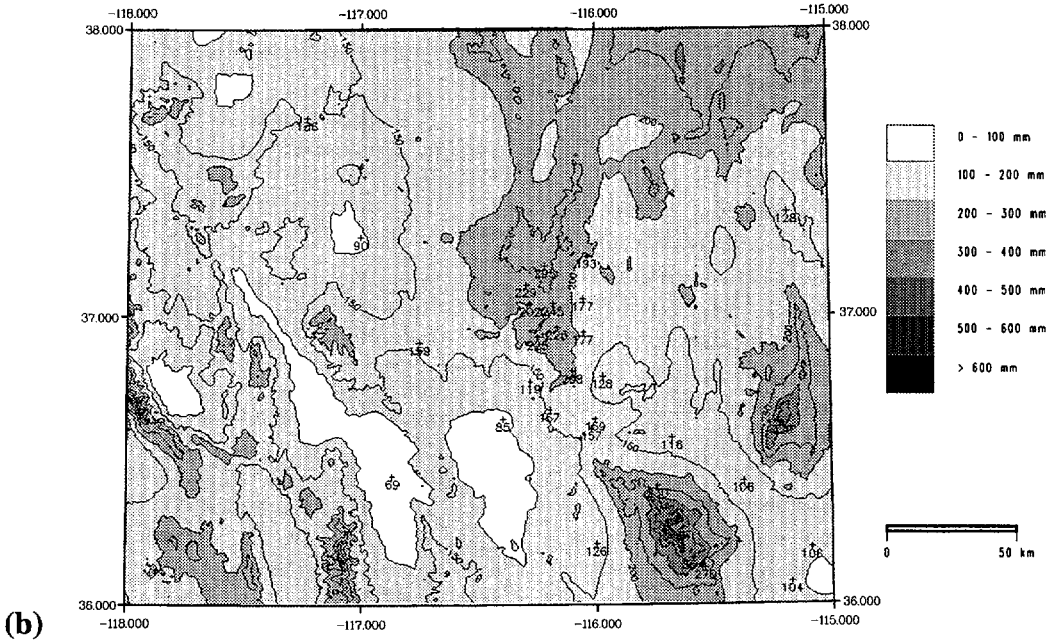

(b)

Figure 10-8. Map of estimated average annual precipitation $\tilde{A}$. (a) OLS model; (b) GLS model

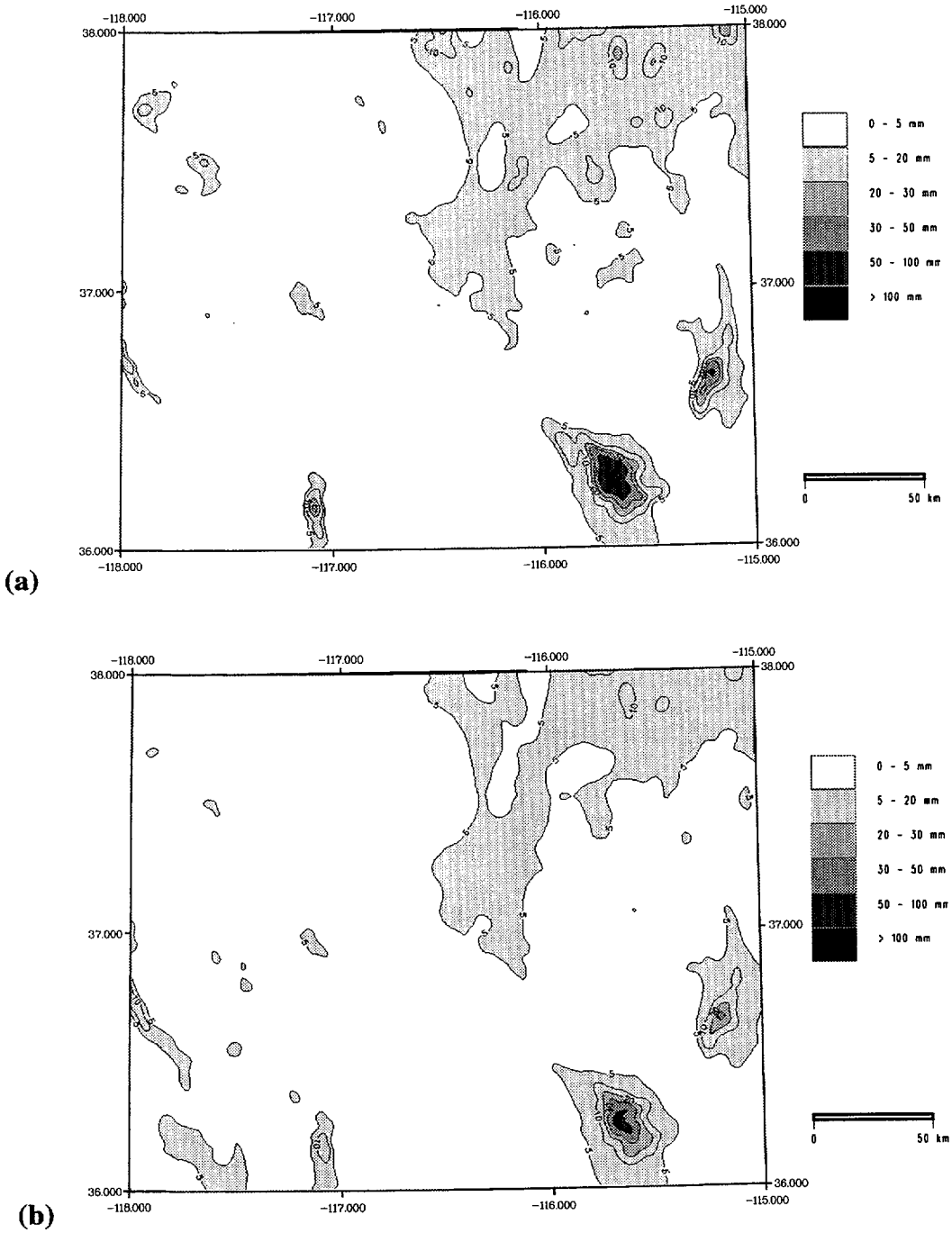

Figure 10-9. Map of Maxey-Eakin recharge. (a) OLS model; (b) GLS model

recharge based on the isohyetal maps in Figures 10-8a and 10-8b, and the Maxey-Eakin formula are shown in Figures 10-9a and 10-9b, respectively. The area within which the average annual precipitation was estimated does not cover the entire Death Valley region, so it is incorrect to compare the total estimated recharge to the cumulative discharge at Ash Meadows, Oasis Valley, and Furnace Creek Wash.

10.3 ASSESSMENT OF PROGRESS

During the past 6 mo, significant progress has been made in acquiring basic hydrogeologic data, developing new data analysis procedures, and constructing new map coverages for the regional hydrogeologic processes ARC/INFO database. Efforts have continued toward assessing the potential for using measurements of the orientation of the maximum horizontal component of the *in situ* stress tensor to determine the direction of the maximum principal component of the transmissivity tensor for the fractured, Paleozoic carbonate aquifer. Work is proceeding on using this technique to revise the flow direction map for the fractured tuff aquifer below YM. Recent geochemical modeling work has focused on development of a thermodynamic basis to permit use of vein mineralogy to interpret variations in groundwater conditions at the time of mineral precipitation. The sign of variations of pressure and/or temperature at the time of mineral precipitation may then be used to infer aspects of the direction of fluid flow. Detailed analyses have been conducted of hydrographs from each of the boreholes in the Death Valley region at which water level measurements have been recorded. Approximate steady-state water levels have been determined for each borehole, and two preliminary water level contour maps for the regional system have been constructed. The first water level contour map was constructed using the minimum tension gridding algorithm provided in the EarthVision software package. The second water level contour map was hand drawn. These water level maps, in conjunction with hydrochemical facies maps and fault maps, will be used to infer the boundaries of local groundwater flow subsystems.

As reported in Section 10.2, considerable effort during the past 6 mo has been devoted to developing a simple and accurate method for estimating average annual precipitation and average annual recharge within the Death Valley region. A new co-estimation procedure for average annual precipitation, which makes use of the relative abundance of elevation data from DEMs, was developed that combines residual kriging with an external drift function and polynomial trend surface fitting. An especially appealing aspect of the procedure is its use of drift models that are based on the well-understood, physical phenomena of orographic precipitation and leeward rain shadow effects. Models of the orographic precipitation effect were fitted to available precipitation data using OLS and GLS. Measurements of AAP with large standard errors are given less weight in the GLS regression procedure than in the OLS procedure. Because AAP measurements obtained from precipitation stations located at higher altitudes in southern Nevada tend to have larger standard errors due to their relatively short record lengths, and because AAP increases exponentially with elevation, using the GLS model yields generally lower $\hat{A}$ estimates than OLS. The application of GLS is indeed appropriate if heteroscedasticity in the errors is the result of some fundamental physical process. However, for the AAP record in southern Nevada, it appears that heteroscedasticity is an artifact of either the relatively short records of the high elevation precipitation stations or increased measurement error due to precipitation occurring as snow. It is tempting to select the OLS model because its higher AAP estimates yield larger estimates of areal recharge, which should produce a flow and transport model that is more conservative from the standpoint of radiologic safety. The method is still under development, and its accuracy has not been compared to cokriging or other, more traditional, spatial interpolation procedures using either cross-validation or ground truth tests.

10.4 PLANS FOR THE NEXT REPORTING PERIOD

During the next reporting period, efforts will focus on the development of a three-dimensional hydrostratigraphic model of the Death Valley region. Effort will also continue to be directed toward studying the stress-hydraulic anisotropy relationship in fractured rocks, as well as the complementary study devoted to using geochemical methods to estimate the depth at which waters discharged through springs from the Paleozoic carbonate aquifer originate. Work will continue on the development and testing of the procedure reported in Section 10.2.1.3 for estimating AAP and recharge. In addition, work will commence on building and automatically calibrating a relatively simple numerical flow model of the Death Valley region.

10.5 REFERENCES

Bedinger, M.S., K.A. Sargent, and W.H. Langer. 1989. *Studies of Geology and Hydrology in the Basin and Range Province, Southwestern United States, for Isolation of High-Level Radioactive Waste–Characterization of the Death Valley Region, Nevada, and California.* U.S. Geological Survey Professional Paper 1370-F. Washington, DC: U.S. Geological Survey.

Draper, N., and H. Smith. 1981. *Applied Regression Analysis, Second Edition.* New York City, NY: John Wiley & Sons: 709.

Deutsch, C.V., and A.G. Journel. 1992. *GSLIB-Geostatistical Software Library and User's Guide.* New York City, NY: Oxford University Press: 340.

French, R.H. 1983. Precipitation in Southern Nevada. *American Society of Civil Engineers Journal of Hydraulic Engineering* 109(7): 1,023–1,036.

Hardman, G. 1936. *Nevada precipitation and acreages of land by rainfall zones.* University of Nevada Experimental Station Mimeograph Paper. Reno, NV: University of Nevada.

Hevesi, J.A., J.D. Istok, and A.L. Flint. 1992. Precipitation estimation in mountainous terrain using multivariate statistics. Part I: Structural analysis. *Journal of Applied Meteorology* 31(7): 661–676.

Isaaks, E.H., and R.M. Srivastava. 1989. *An Introduction to Applied Geostatistics.* New York City, NY: Oxford University Press: 61.

Maxey, G.B., and T.E. Eakin. 1949. *Ground Water in White River Valley, White Pine, Nye, and Lincoln Counties, Nevada—Water Resources Bulletin No. 8.* Carson City, NV: State of Nevada Office of the State Engineer.

Neuman, S.P., and E.A. Jacobson. 1984. Analysis of nonintrinsic spatial variability by residual kriging with application to regional groundwater levels. *Mathematical Geology* 16(5): 499–521.

Nuclear Regulatory Commission. 1994. *License Application Review Plan for the Review of a License Application for a Geologic Repository for Spent Nuclear Fuel and High-Level Radioactive Waste.* NUREG-1323. Washington, DC: Nuclear Regulatory Commission.

Seber, G.A.F., and C.J. Wild. 1989. *Nonlinear Regression.* New York City, NY: John Wiley & Sons: 768.

Trimble, S. 1989. *The Sagebrush Ocean.* Reno, NV: University of Nevada Press: 248.

Watson, P., P. Sinclair, and R. Waggoner. 1976. Quantitative evaluation of a method for estimating recharge to the desert basins of Nevada. *Journal of Hydrology* 31: 335–357.

U.S. Department of Energy. 1991. *Study Plan for Study 8.3.1.2.1.1–Characterization of the Meteorology for Regional Hydrology: Revision 0.* Las Vegas, NV: U.S. Department of Energy, Yucca Mountain Site Characterization Project Office.

THIS PAGE INTENTIONALLY LEFT BLANK